DEVELOPMENT OF COMPACT, DEPLOYABLE SENSORS USING COLD ATOM INTERFERENCE

DISSERTATION

Eric A. Imhof,

AFIT-ENP-DS-17-J-073

DEPARTMENT OF THE AIR FORCE
AIR UNIVERSITY

AIR FORCE INSTITUTE OF TECHNOLOGY

Wright-Patterson Air Force Base, Ohio

The views expressed in this dissertation are those of the author and do not reflect the official policy or position of the United States Air Force, the Department of Defense, or the United States Government.

AFIT-ENP-DS-17-J-073

DEVELOPMENT OF COMPACT, DEPLOYABLE SENSORS USING COLD ATOM INTERFERENCE

DISSERTATION

Presented to the Faculty

Graduate School of Engineering and Management

Air Force Institute of Technology

Air University

Air Education and Training Command

in Partial Fulfillment of the Requirements for the

Degree of Doctor of Philosophy in Applied Physics

Eric A. Imhof,

MS in Applied Physics - Air Force Institute of Technology (2013)

BS in Physics - University of Virginia (2011)

June 2017

AFIT-ENP-DS-17-J-073

DEVELOPMENT OF COMPACT, DEPLOYABLE SENSORS USING COLD ATOM INTERFERENCE

DISSERTATION

Eric A. Imhof, M.S., B.S.

Committee Membership:

Dr. Glen P. Perram
Chair

Dr. Matthew B. Squires
Member

Dr. David E. Weeks
Member

Dr. Benjamin F. Akers
Member

AFIT-ENP-DS-17-J-073

Abstract

This dissertation makes three distinct contributions to the field of compact cold atom interferometry.

First, a two-dimensional grating magneto-optical trap (2D GMOT) is demonstrated, in which a single laser and a planar diffraction grating produce a slow, high flux beam of ^{87}Rb atoms. This configuration increases experimental access when compared with a traditional 2D MOT. The output flux is several hundred million rubidium atoms/s at a mean velocity of 19.0(2) m/s. The velocity distribution has a 3.3(17) m/s standard deviation. The atomic beam from the 2D GMOT is used to demonstrate loading of a three-dimensional grating MOT (3D GMOT) with $2.02(3)\times10^8$ atoms. Methods to improve flux output are discussed.

Second, a method to produce uniform magnetic fields of arbitrary direction from a single planar microchip is developed. Chip-based fields reduce the dependence of cold atom devices on large current-carrying coils external to the vacuum chamber. A chip is fabricated that demonstrates equivalent magnetic field uniformity to the widely-used Helmholtz coil pair. These results are used to propose a novel magnetic trap conveyor to move atoms along the surface of the chip without the use of an externally-supplied field.

Third, using a thermal gas, the signal of a trapped atom interferometer is modeled. This interferometer uses two short laser pulses, separated by time T, which act as phase gratings for the matter waves. Near time $2T$, there is an echo in the cloud's density due to the Talbot-Lau effect. The model uses the Wigner function approach and includes a weak residual harmonic trap. The analysis shows that the residual potential limits the interferometer's visibility, shifts the echo time, and alters its time dependence. Loss of visibility can be mitigated by optimizing the initial trap frequency just before the interferometer cycle begins.

To my family, especially my wife

Acknowledgments

First and foremost, I would like to thank my research advisor, Dr. Matthew Squires. This dissertation is only possible because of your seven years of steadfast commitment to my growth as a scientist and person. Hopefully, my effort has rewarded that investment. You gave me ample independence while providing capable, enthusiastic guidance. I have tried to emulate the patience, resolve, and good humor with which you approach science and the other aspects of life. With your trust, I have gained a more clear concept of my goals and path forward.

The instruction and encouragement of the Cold Atom Group at the Air Force Research Laboratory has been instrumental to this work. Thank you Dr. Spencer Olson, Dr. Brian Kasch, Dr. James Stickney, Dr. Chris Erickson, Dr. Benjamin Stuhl, Dr. Gretchen Phelps, Dr. John Burke, Mr. Stacey Schramm, Dr. Rudy Kohn, Dr. Nathan Lemke, Dr. Matthew Bigelow, Dr. Robbie Robertson, Dr. Maxwell Gregoire, Mr. Kyle Martin, Ms. Jordan Armstrong, Lt. Evan Carlson, Lt. Bethany Kroese, Lt. Michael Bishop, Capt. Gordon Lott, and Dr. Mayer Landau.

My committee members, Prof. Glen Perram, Prof. David Weeks, and Prof. Benjamin Akers shepherded me through my time at AFIT. The evidence of your capable teaching is distributed throughout this document. In particular, I am grateful for my committee chairman, Prof. Glen Perram, whose poise and understanding kept this work going through the trials of the 2013 budget sequestration.

Finally, my family has been the foundation of my life over the course of this work. I am not allowed to use names, so to my wife, parents, brothers, sisters, and new nephew, thank you.

Eric A. Imhof

Table of Contents

Page

Page

List of Figures

Figure Page

Figure Page

List of Tables

List of Symbols (in approximate order of appearance)

Symbol	Definition
h	Planck's constant (6.62607×10^{-34} J s)
m	Mass (kg)
k_B	Boltzmann's constant (1.38065×10^{-23} J/K)
$\mathcal{T}$	Temperature (°K)
$\mathcal{T}_c$	Critical temperature of a Bose-condensed gas (°K)
n_b	Density of a Bose-condensed gas (m^{-3})
r	Radial distance (m)
$\mathcal{R}$	Radius of imaginary sphere locating axial currents to create uniform fields (m)
ψ	Stationary energy state of the quantum wave function in position space
E	Energy (J)
$\hbar$	Reduced Planck's constant (1.05457×10^{-34} J s)
ω	Angular frequency of light (s^{-1})
$\hat{\boldsymbol{\epsilon}}_{0,1}$	Unit vectors describing direction of light propagation
$\mathbf{p}$	Momentum (kg·m/s)
$\mathbf{k}$	Wave vector of light (m)
c	Speed of light (2.99792×10^8 m/s)
τ_{sp}	Spontaneous re-emission time (s)
$\mathcal{F}$	Force (kg·m/s^2)
t	Time (s)
Γ	Spontaneous emission rate (s^{-1})
I	Laser intensity (W/m^2)
I_{sat}	Saturation intensity (W/m^2)
Δ	Laser detuning = $\omega - \omega_0$ (s^{-1})

Symbol	Definition
$\mathbf{v}$	Velocity (m/s)
$\boldsymbol{\mu}$	Magnetic dipole moment (A·m^2)
$\mathbf{B}$	Magnetic field (kg/A·s^2)
$\mathbf{J}$	Electronic angular momentum (J·s)
$\mathbf{I}$	Nuclear angular momentum (J·s)
$\mathbf{F}$	Total electronic and nuclear angular momentum (J·s)
m_F	Quantum number describing the projection of total angular momentum state $\mathbf{F}$ onto $\mathbf{B}$
g_F	g-factor of the total angular momentum state F
μ_B	Bohr magneton (9.27401×10^{-24} A·m^2)
σ^-, π, σ^+	Transitions in which $m_{F'} - m_F = -1, 0, +1$, respectively
$\mathbf{E}$	Electric field (V/m)
λ	Wavelength (m)
V	Potential energy (J)
$\Psi(x,t)$	Full wave function in position space
β	Harmonic potential curvature (s^{-2})
δ_q	Quantum phase shift (s^{-1})
$\hat{H}$	Hamiltonian operator
e	Electron charge (1.60218×10^{-19} A·s)
Ω	Rabi frequency (s^{-1})
χ	Stationary energy state of the quantum wave function in momentum space
a	Acceleration (m/s^2)
g	Local Earth acceleration due to gravity (9.80665 m/s^2)
I_{chip}	Current on atom chip (A)
μ_0	Permeability of free space (1.25664×10^{-6} kg m/A^2 s^2)
R_{coil}	Radius of magnetic coil (m)

Symbol	Definition
α_{m_F}	Relative transition strength to the m_F state
φ	Angle between beam direction and local magnetic field
s	Polarization indexing integer
θ	Diffraction angle
$P_{\pm}$	Beam intensity fraction in the right and left circular polarizations
N	Atom number
τ_{trap}	MOT lifetime (s)
$R_{capture}$	Capture rate of the MOT (s^{-1})
η	2D GMOT atomic distribution (s/m^2)
A	Atoms per meter in 2D GMOT (m^{-1})
σ	2D GMOT speed distribution (m/s)
Φ	Flux of 2D GMOT (s^{-1})
$\mathcal{N}$	Number of turns of a magnetic coil
I_{coil}	Current of a magnetic coil (A)
D	Separation between two magnetic coils (m)
ζ	Magnetic scalar potential ($kg \cdot m/ (A \cdot s^2)$)
I_p	Current of wire pair for planar magnetic field sources (A)
b	Spacing of wire pairs
L	Loop side length
S	Talbot-Lau interferometer signal
$\mathcal{I}$	Talbot-Lau echo signal strength

DEVELOPMENT OF COMPACT, DEPLOYABLE SENSORS
USING COLD ATOM INTERFERENCE

I. Introduction

1.1 Context

Currently, clouds of atoms with sub-milliKelvin temperatures are being dropped from 110 m towers [1] and launched in sounding rockets [2–5]. Similar experiments are making parabolic flights [6] and being prepped for the International Space Station [7, 8]. Nations around the world are investing in efforts to create and measure cold atoms in harsh, real-world environments [9–11].

Why?

Cold atoms provide one of the most direct methods of probing the quantum world, in which it is impossible to know both a particle's position and momentum with absolute certainty. Specifically, for a gas with density n_b, atomic mass m, and temperature $\mathcal{T}$, the average uncertainty in position is

$$\lambda_{th} = \frac{h}{\sqrt{2\pi m k_B \mathcal{T}}}, \tag{1.1}$$

where h is Planck's constant and k_B is Boltzmann's constant.

As the gas cools, λ_{th} increases. Taken to the extreme, the position uncertainty becomes larger than the average separation between particles. Below a critical temperature,

$$\mathcal{T}_c = \left(\frac{n_b}{2.6124}\right)^{2/3} \frac{h^2}{2\pi m k_B}, \tag{1.2}$$

the gas, now called a Bose-Einstein Condensate (BEC), can no longer be described by the locations of distinct constituents. Instead, a wave-like function gives the probability of finding one of the many indistinguishable particles at a given coordinate. Describing the probability as a wave leads to unexpected results. For example, Fig. 1.1, reproduced from [12], shows the observed interference between two overlapped BECs. Remarkably, these images were captured with a laser and a simple CCD camera.

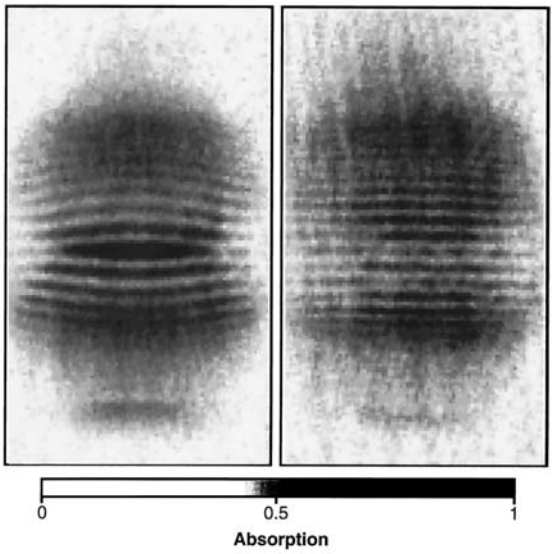

SCIENCE • VOL. 275 • 31 JANUARY 1997

Figure 1.1: Density modulation of two overlapped atomic BECs, reproduced from a seminal early demonstration in [12].

By harnessing this and similar effects, cold atoms have enabled the premier measurements of basic quantities such as time [13, 14], fine structure constant [15, 16], mass [17], and gravity [18–20]. These successes raise hopes for applications outside the laboratory environment such as gravitational wave detection aboard a constellation of satellites [21] and improving the Global Positioning System (GPS) [22].

1.2 Problem Statement

The potential of cold atoms is apparent to the highest levels of Air Force leadership. In 2010, Secretary of the Air Force Michael B. Donley and Air Force Chief of Staff Gen. Norton A. Schwartz commissioned the Air Force *Technology Horizons* survey [23]. They wrote,

> *Technology Horizons* presents a clearly articulated and credible assessment of the strategic environment and enduring realities we face. It outlines a set of overarching themes that defines attributes our future Air Force systems will need to prevail... We believe the Air Force must boldly move forward to advance these technologies through the dedicated, creative, and focused efforts of our science, technology, engineering, and mathematics workforce. The future is ours to shape.

Their list of the top ten Air Force research priorities over the next 20 years include precision navigation in GPS-denied environments.

> Widespread dependence of critical Air Force and other DOD systems on GPS for precision navigation and timing functions has caused potential adversaries to exploit GPS jamming as an asymmetric advantage. Key systems will thus need GPS independence or augmentation to allow their use in such environments.

To meet that need, the Cold Atom Group at the Air Force Research Laboratory (AFRL) is focused on development of strategic grade inertial measurement devices using cold atom interference [24–27]. We have demonstrated BEC in a compact experiment as well as coherent splitting of the matter wave. This dissertation reports my series of efforts to improve that system and its successors. First, I fabricate a cold atomic beam that reduces the device's total laser power and increases experimental access. Second, I create uniform magnetic fields of arbitrary direction from planar sources to remove the need for external current-carrying coils. Third, I investigate a confined atom interferometry technique that operates at non-condensed temperatures to reduce the number of cooling stages before a measurement is made.

1.3 Outline of this Dissertation

Chapter 2 provides a brief history of compact cold atomic physics. The contributions of this dissertation will be detailed in context with the broader field. Then, Chapter 3 briefly discusses the range of products, methods, and techniques that support our experiments.

Chapter 4 explains the main experimental effort of this dissertation, a novel method to create a cold atom beam called a Two-Dimensional Grating Magneto-Optical Trap (2D GMOT). In an ultra-high vacuum chamber, a dilute gas of ^{87}Rb is illuminated by a broad beam of laser light. After passing through the gas, the light is directed back into the chamber by diffraction from two reflective gratings. Under proper conditions of laser beam polarization and detuning, the light provides optical forces which cool and trap in two dimensions, forming an atom beam along the third.

This atom beam allows the source gas to be separated from a second, lower pressure chamber in which a 3D GMOT is created. Like the 2D GMOT, the 3D GMOT creates optical forces to cool and trap atoms, but this time in all three dimensions. Locating the 3D GMOT in a lower pressure chamber reduces cold atom loss due to collisions with background room-temperature atoms. Indeed, this process shows the highest atom number in a 3D GMOT so far reported.

While matter-wave interference is possible after the GMOT stage, better measurements can be achieved with even colder atoms. Subsequent cooling stages require precise magnetic fields created by co-axial pairs of current-carrying coils. Each pair provides a large volume of uniform field. In particular, if the coils rest on an imaginary sphere of radius $\mathcal{R}$, the field is constant and unidirectional for points r if $(r/\mathcal{R})^4 << 1$.

Despite the uniformity afforded by coils, there are significant downsides to their use. Coils are bulky, blocking access to the experimental chamber. Additionally, they are heavy and waste significant power creating field within a larger volume than necessary. Thus, coils often require complicated structures to dissipate heat.

In response, many experiments use atom chips, which capture atoms in magnetic traps formed by currents flowing on a planar microchip. Atom chips enable precision current placement by lithographic methods and are more easily cooled through techniques borrowed from the electronics industry.

However, most atom chip designs still rely on a global uniform bias field provided by external coils. Chapter 5 details a framework to create the same uniform fields from planar structures. The resulting chips are tested and shown to be analogous to coil-based sources. These results are then applied to demonstrate a fully planar, movable, bias-free magnetic trap to convey cold atoms along the chip surface.

With the magnetic control developed by the Cold Atom Group, a promising interference technique is possible. Most matter interferometers split the atom cloud with processes that either require ultra-cold temperatures or free propagation of the atoms. Ultra-cold temperatures raise the necessary experimental resources while unconstrained motion necessitates large devices, especially on Earth where atoms fall with gravity.

However, the Talbot-Lau interferometer has been shown to operate at non-BEC temperatures while being magnetically confined. Ideally, the atoms are trapped by a magnetic field along two dimensions, while being allowed to split and recombine along a free third direction. In reality, eliminating the field gradient along the third direction is exceedingly difficult.

The question posed was how much of this remnant field could be tolerated. Chapter 6 describes the use of the Wigner function to investigate signal loss from a small, harmonic potential. The model suggests an optimized sequence for loading atoms into the interferometer. Finally, Chapter 7 summarizes the main results of this work and discusses expected avenues of future research.

To improve clarity, lengthy derivations throughout this dissertation have been compiled into a series of appendices.

Page intentionally left blank

II. Background

2.1 Introduction

The allure of the very cold precedes its scientific study. In 1558, Giambattista della Porta published a book titled *Natural Magic* [28]. In an appendix called *The Chaos*, he described the mixing of saltpeter (potassium nitrate) with snow, producing a "mighty cold" that was twice as cold as either substance. In the summer of 1620, Cornelius Drebbel used the technique to cool the Great Hall of Westminster Abbey, to the astonishment of King James I [29].

Rigorous scientific study began with Robert Boyle's *New Experiments and Observations Touching Cold* in 1665 [30]. By 1703, Guillaume Amontons, experimenting with expanding gasses, predicted the existence of an absolute zero temperature [31]. Throughout the eighteenth and nineteenth centuries, progressively lower temperatures were achieved, including the liquefaction of ammonia (239.9°K), chlorine (239.2°K), oxygen (90.2°K), and hydrogen (20.3°K). In 1908, the Cryogenic Laboratory led by Heike Kamerlingh Onnes became the "coldest spot on earth" by liquifying Helium at 4.2°K [32].

Until relatively recently, liquid Helium represented the lowest temperature in physics, taken as low as 2 mK with the latest dilution refrigerators [33]. This chapter outlines recently invented techniques that enable further cooling. Then, a description is given for how these techniques are applied in the Air Force Research Laboratory's Cold Atom Sensor (CAS). Finally, my contributions to the CAS and the broader field are introduced.

2.2 Radiation Force

Several modern cooling methods rely heavily on the force radiation can apply to matter. These developments were inspired in 1970, when Ashkin [34] proposed that

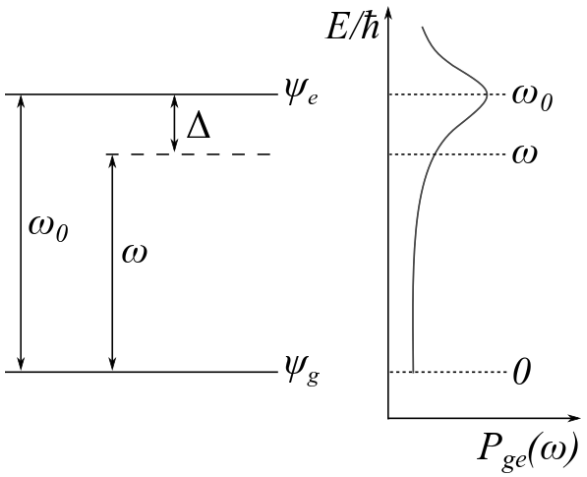

Figure 2.1: Energy levels of a two-level atom at rest with ground state ψ_g and an excited state ψ_e separated by energy $E = \hbar\omega_0$. The probability a photon with frequency ω drives a transition from $\psi_g \rightarrow \psi_e$ is shown as $P_{ge}(\omega)$ in blue.

radiation pressure could be useful to "separate, velocity analyze, or trap neutral atoms." Therefore, this section provides a brief theoretical overview of the radiation force.

Consider the two-level approximation of an atom, shown in Fig. 2.1. The atom's electronic ground state ψ_g and an excited state ψ_e are separated by energy $E = \hbar\omega_0$. A photon can drive the electron from $\psi_g \rightarrow \psi_e$ with a probability P_{ge} dependent on its frequency ω. When the atom absorbs a photon traveling along the $\hat{\boldsymbol{\epsilon}}_0$ direction, its momentum changes by an amount

$$\mathbf{p}_{photon} = \hbar\mathbf{k}, \tag{2.1}$$

where $\mathbf{k} = (\omega/c)\,\hat{\boldsymbol{\epsilon}}_0$, the wavevector of the photon. After an average time τ_{sp}, the atom spontaneously re-emits a photon in a random direction $\hat{\boldsymbol{\epsilon}}_1$. The atom's momentum shifts again by an amount $\hbar k$, this time in the $-\hat{\boldsymbol{\epsilon}}_1$ direction. The process is illustrated in Fig. 2.2.

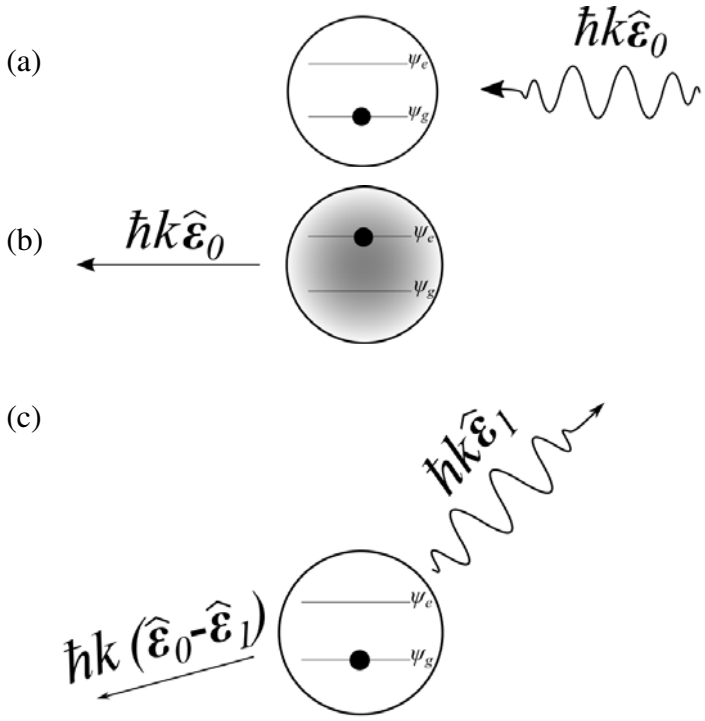

Figure 2.2: A two-level atom's momentum changing during the absorption ($(a) \rightarrow (b)$) and re-emission (c) of a photon.

Over many scattering events, each absorption continues to provide an average momentum change of $\hbar\mathbf{k}$. However, the average momentum change from re-emission is zero due to the random direction of each re-emitted photon, as seen in Fig. 2.3. As a result, the average force on the atom from monochromatic light with intensity I is

$$\begin{aligned} \mathcal{F} = \frac{d\mathbf{p}}{dt} &= \hbar\mathbf{k} \times (\text{steady state rate of photon absorption}) \\ &= \hbar\mathbf{k}\frac{\Gamma}{2}\frac{I/I_{sat}}{1 + I/I_{sat} + 4\Delta^2/\Gamma^2}, \end{aligned} \tag{2.2}$$

where $\Delta = \omega - \omega_0$ is called the detuning of the photon from the atomic resonance, $\Gamma = 1/\tau_{sp}$ is the natural line width of the transition, and I_{sat} is the saturation intensity, defined as the intensity of resonant (i.e. $\omega = \omega_0$) light at which the atom spends $1/4$ of its time in the excited state [35] (for the $\sigma^{\pm}$ transitions used in later sections, $I_{sat} = \hbar\omega^3\Gamma/12\pi c^2$ [36]). The force is plotted as a function of detuning in Fig. 2.4. Further derivations are covered in many textbooks [37, 38].

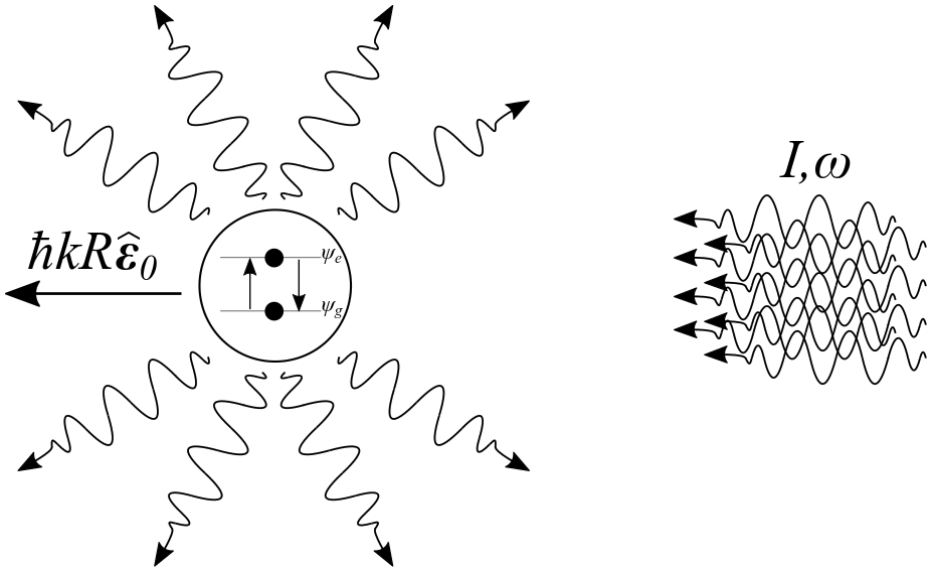

Figure 2.3: Average force on a two-level atom due to scattering from a beam of photons with intensity I and frequency ω.

2.3 Slowing and Cooling

Soon after Ashkin's proposal, light was used to partially slow an atom beam [35, 39–41]. Atoms with velocity $\mathbf{v} = v\hat{\mathbf{v}}$ encountered light traveling in $-\hat{\mathbf{v}}$, Doppler shifting the light in the frame of the atoms to

$$\omega' = \omega + kv. \tag{2.3}$$

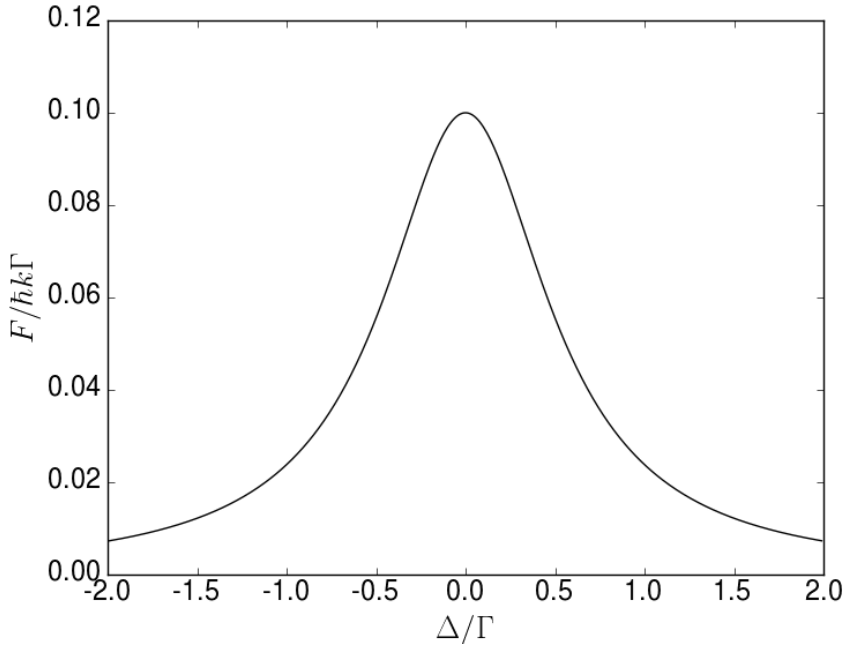

Figure 2.4: Scattering force from Eq. (2.2) for typical values associated with the ^{87}Rb $5^2S_{1/2} \rightarrow 5^2P_{3/2}, F = 2 \rightarrow F' = 3$ transition with circularly polarized light.

Accordingly, ω was tuned to target the peak of the atom beam's speed distribution. As these atoms slowed, the frequency was ramped downwards to maintain resonance and continue the slowing process. While the frequency changed, new atoms entering the beam did not experience the ideal cooling force, resulting in a pulsed output of slow atoms.

To create continuous slowing, tapered solenoids were built that added a varied magnetic field along the atom beam. Through the Zeeman shift introduced in the next section, the magnetic field adjusted the atomic energy levels to maintain resonance. The light never had to change frequency. In principle, atoms could be stopped, but the experimental design prevented measurement of low velocities. According to Bill Phillips in his 1995 Nobel prize lecture,

> [Slow atoms exiting the solenoid] always continued to absorb enough light while traveling from the solenoid to the detection region so as to stop before

reaching the detector. By shutting off the cooling laser beam and delaying observation until the slow atoms arrived in the observation region, we were able to detect atoms as slow as 40 m/s with a spread of 10 m/s, corresponding to a temperature (in the atoms rest frame) of 70 mK. [42]

In 1975, an alternative design was proposed by Hänsch and Schawlow [43]. Instead of trying to bring a directed atom beam to rest, the low velocity range of a free gas could be cooled towards $v = 0$. In one dimension, if red-detuned light was applied along both $\pm\hat{\mathbf{v}}$, a slow atom would be Doppler-shifted onto resonance with the light opposing its motion, while being shifted away from resonance with co-propagating light. If the light in each direction had intensity I, the radiation force then becomes

$$\mathcal{F} = \left[\hbar k \frac{\Gamma}{2} \frac{I/I_{sat}}{1 + 2I/I_{sat} + 4(\Delta - kv)^2/\Gamma^2} - \hbar k \frac{\Gamma}{2} \frac{I/I_{sat}}{1 + 2I/I_{sat} + 4(\Delta + kv)^2/\Gamma^2}\right] \hat{\mathbf{v}}, \tag{2.4}$$

as shown in Fig. 2.5 for $\omega < \omega_0$. Notice that the force only opposes the atomic velocity for a narrow range of kv/Γ, typically corresponding to a few m/s. This low end of the thermal velocity distribution is concentrated around $v = 0$ by

$$\mathcal{F} \approx \frac{8\hbar k^2 \Delta}{\Gamma} \frac{I/I_{sat}}{\left(1 + 2I/I_{sat} + 4\Delta^2/\Gamma^2\right)^2} \, v. \tag{2.5}$$

The cooling force from Eq. (2.5) is often referred to as optical molasses because the atom slows as if moving through a viscous fluid. Just as a particle in a fluid cannot slow to zero velocity because collisions cause it to undergo random Brownian motion, so the atom's discrete photon absorption/re-emission process causes it to be heated as well, reaching a steady state with the cooling power Fv. A gas of atoms with average kinetic energy $k_B\mathcal{T}/2$ finds equilibrium when

$$\mathcal{T} = -\frac{\hbar\Gamma}{8k_B} \frac{1 + 2I/I_{sat} + 4\Delta^2/\Gamma^2}{\Delta/\Gamma}. \tag{2.6}$$

If $2I << I_{sat}$, the minimum temperature is obtained for $\Delta = -\Gamma/2$, yielding

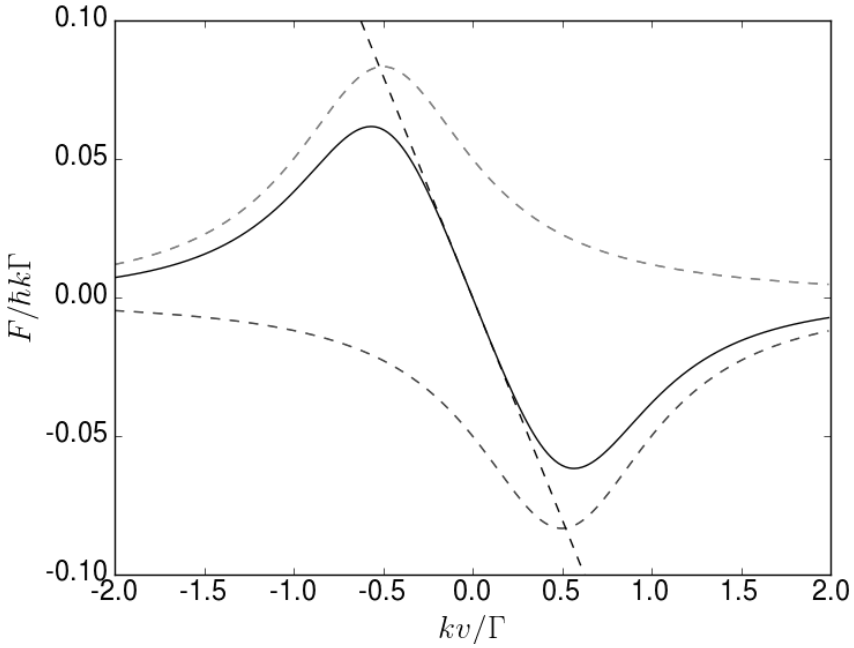

Figure 2.5: A laser beam traveling in $-\hat{\mathbf{v}}$ (blue dashed) is more absorbed by an atom with positive velocity, while a beam traveling in $+\hat{\mathbf{v}}$ (red dashed) is more absorbed by an atom with negative velocity. The black solid curve shows the combined force from Eq. (2.4), the dashed line is the approximation for $kv << \Delta = -\Gamma/2$ from Eq. (2.5).

$$\mathcal{T}_{Doppler} = \frac{\hbar\Gamma}{2k_B}, \tag{2.7}$$

referred to as the Doppler limit. Fig. 2.6 shows the force curve at the Doppler limit (solid black, $\Delta = -\Gamma/2$) compared to non-optimized cooling. The dashed blue curve shows $\Delta = -1.5\Gamma$ and the dashed red curve shows $\Delta = -0.1\Gamma$. Notice that the restoring linear region is steepest for the optimized case. In 1985, Steven Chu reached the Doppler limit with 10^6 Na atoms/cm^3 at a mean temperature of $\sim 240\ \mu$K, work partially responsible for his share of the 1995 Nobel prize in physics [44, 45].

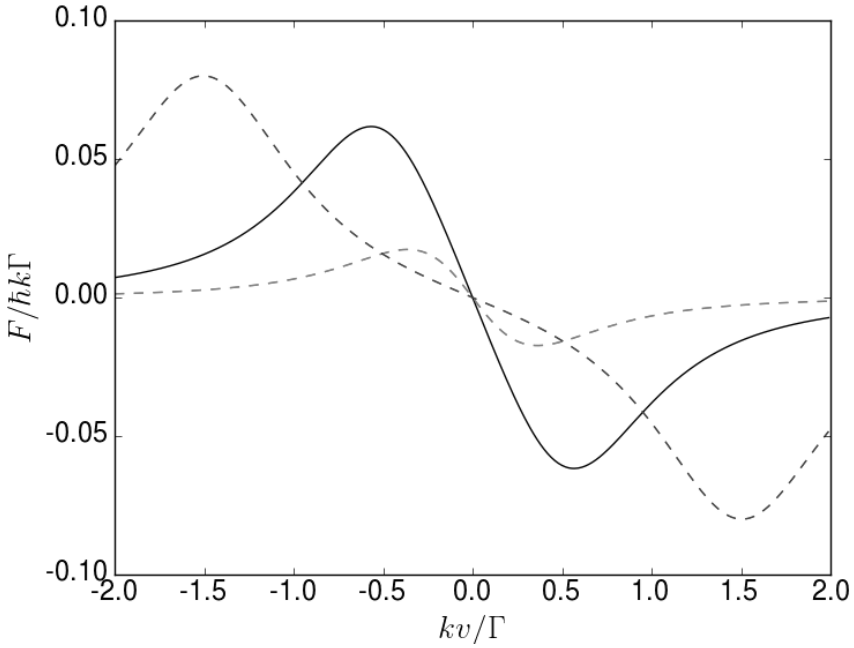

Figure 2.6: The effect of detuning on total cooling power. The solid black curve shows $\Delta = -\Gamma/2$, corresponding to the Doppler limit, while the dashed blue curve shows $\Delta = -1.5\Gamma$ and the dashed red curve shows $\Delta = -0.1\Gamma$. The steep linear region of the optimized curve corresponds to the maximal cooling force.

2.4 Magnetic Trapping

2.4.1 Static Trap

Doppler cooling raised the possibility of confining atoms in a magnetic field, inspired by the 1978 trapping of cold neutrons [42, 46]. Simple schemes took advantage of the atom's magnetic dipole moment $\boldsymbol{\mu}$ experiencing a force in a magnetic field $\mathbf{B}$,

$$\boldsymbol{\mathcal{F}} = -\boldsymbol{\mu} \cdot \nabla \mathbf{B}. \tag{2.8}$$

The atom's magnetic moment arises from its nuclear angular momentum $\mathbf{I}$ and electronic angular momentum $\mathbf{J}$. These angular momenta can be thought of as currents

of charge flowing around the atom, creating a small magnetic field. Their combination $\mathbf{F} = \mathbf{I} + \mathbf{J}$ form states defined by the quantum numbers (F, m_F). The energies of these states vary with magnetic field by

$$V_{Zeeman} = m_F g_F \mu_B B, \tag{2.9}$$

called the Zeeman shift, where g_F is the effective Landé g-factor and μ_B is the Bohr magneton. Thus, the projection of $\boldsymbol{\mu}$ along $\mathbf{B}$ is $m_F g_F \mu_B$. Eq. (2.9) implies atoms in positive $m_F g_F$ states can be captured at minima of the magnetic field.

Suppose the magnetic field is zero at the atom cloud location and increases in magnitude for all directions to a maximal value B_{max}. A cloud of temperature $\mathcal{T}$ is contained if

$$B_{max} >> \frac{3k_B\mathcal{T}}{2m_F g_F \mu_B}. \tag{2.10}$$

For atoms at the Doppler limit ($\sim$ 240 μK) with $m_F g_F = 1$, B_{max} must be much greater than $\sim$ 5 Gauss. In practice, if B_{max} is $\sim 3\times$ greater, a significant fraction of the Boltzmann distribution is captured.

Unfortunately, such a simple magnetic trap is subject to rapid atom loss due to atomic transitions to untrapped (i.e. $m_F g_F \leq 0$) states [47]. These transitions are caused because the atom is moving through a spatially variant field. In the moving frame, the field can be recast as a time-dependent perturbation. Because the unperturbed atomic states form a complete set, they can be used to describe the state of the perturbed atom as well. In most regions of the trap, the Hamiltonian changes slowly and the likelihood of finding the atom in a state other than its original is negligible. However, near the zero of the magnetic field, the probability of a transition becomes significant.

Specifically, using the quantum adiabatic approximation [48], state numbers are conserved so long as the Hamiltonian's rate of change is less than the frequency associated with changing from state $i \rightarrow f$

$$\omega_{fi} = \frac{E_f - E_i}{\hbar}, \tag{2.11}$$

where $E_{i,f}$ are the energies of the unperturbed Hamiltonian. For the changing magnetic field, the adiabatic condition implies

$$\frac{1}{|B|}\frac{\partial \mathbf{B}}{\partial t} << \frac{g_F m_F \mu_B B}{\hbar}. \tag{2.12}$$

If the field has a zero point, atoms will experience an abrupt change in field direction, violating adiabaticity and inducing transitions to untrapped states. These are called Majorana losses, named for the physicist who first considered them [49]. Methods to overcome these losses will be discussed later.

2.4.2 Magneto-Optical Trap

The difficulties of the static magnetic trap prompted efforts to trap atoms with the radiation force. Initial hopes were dampened in 1983 by Ashkin and Gordon, who proved

> an optical radiation Earnshaw theorem: A small dielectric particle cannot be trapped by using only the scattering force of optical radiation pressure. [50]

However, the theorem assumes the radiation force is proportional to light intensity. The addition of an external, position-dependent magnetic field can alter this strict proportionality [51], leading to Dalibard's elegant Magneto-Optical Trap (MOT), demonstrated by Raab in 1987 [52].

A simplified understanding of the MOT considers a $F = 0 \rightarrow F' = 1$ transition, such that the ground state is defined by $(F, m_F) = (0, 0)$ and the possible excited states have $(F', m_{F'}) = (1, 1)$, $(1, 0)$, and $(1, -1)$. The excited state can have angular momentum along $\mathbf{B}$, while the ground state does not. Therefore, to conserve angular momentum,

transitioning to state $m_{F'}$ requires the absorbed photon be polarized with an appropriate spin. If the photon is traveling along the magnetic field direction, a left (right) circular polarization drives a transition to the $m_{F'} = +1$ (-1) state, as shown in Fig. 2.7. For a photon traveling opposite the magnetic field vector, the reverse is true. Excitations where $m_{F'} - m_F = -1, 0, +1$ are referred to as σ^-, π, and σ^+ transitions, respectively, seen in Fig. 2.8.

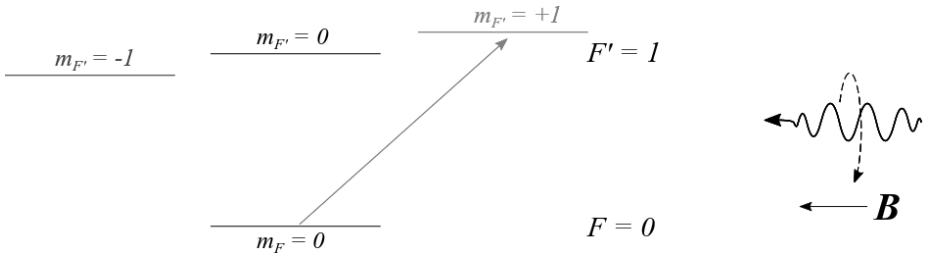

Figure 2.7: A left hand circularly polarized photon traveling along the magnetic field vector must drive a $m_{F'} - m_F = +1$ transition to conserve angular momentum.

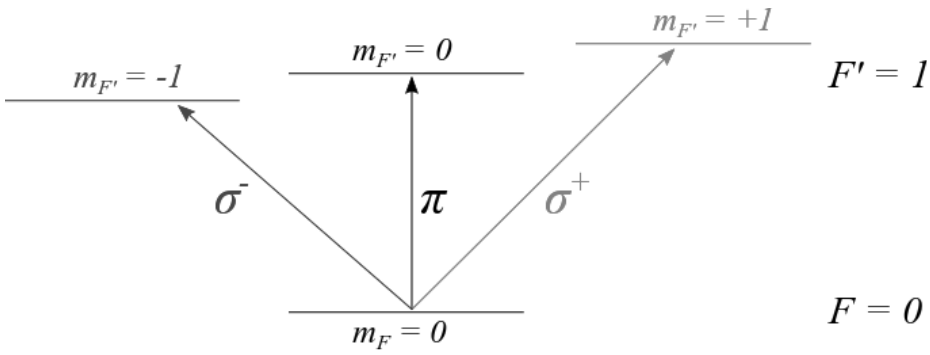

Figure 2.8: Transitions to the $m_{F'} = -1, 0, +1$ states are referred to as σ^-, π, and σ^+, respectively.

Consider a one-dimensional system in which the atom is illuminated by two beams from both the $\pm\hat{\mathbf{z}}$ directions. Each beam is red detuned by Δ from ω_0 and given left hand

circular polarization. Apply a linear magnetic field of the form $\mathbf{B} = Gz\hat{\mathbf{z}}$, such that the field is zero and changes direction at the origin.

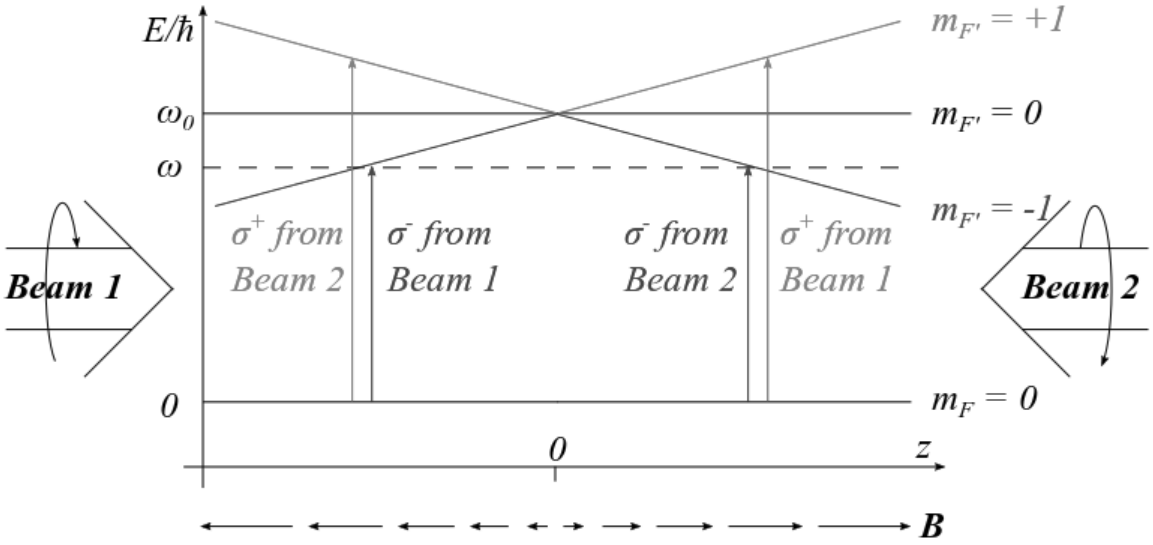

Figure 2.9: Origin of the position-dependent force in a Magneto-Optical Trap. Circular polarization gives each beam angular momentum. Conservation of angular momentum requires Beam 1 to drive only σ^+ transitions for $z < 0$ and only σ^- transitions for $z > 0$. The reverse holds for Beam 2. Because of the laser detuning and Zeeman energy shift, σ^- transitions are more likely, resulting in a net optical force towards the origin.

The energy levels of the $m_{F'} = \pm 1$ states now change linearly with the absolute value of position because of Eq. (2.9), as seen in Fig. 2.9. If the atom is located at $z < 0$, Beam 1 drives σ^- transitions while Beam 2 drives σ^+. On the other hand, if $z > 0$, Beams 1 and 2 switch roles. Accordingly, σ^- transitions are only driven by the beam which would push the atom towards the origin.

As distance from the origin increases, the Zeeman effect makes σ^- transitions more likely than π or σ^+. This preferential scattering creates a position-dependent, restoring

force centered around the origin. The combination of both beams can be captured as another adjustment to the radiation force equations from Eq. (2.4)

$$\mathcal{F} = \left[\hbar k\frac{\Gamma}{2}\frac{I/I_{sat}}{1+2I/I_{sat}+4(\Delta-kv-\alpha_z z)^2/\Gamma^2} - \hbar k\frac{\Gamma}{2}\frac{I/I_{sat}}{1+2I/I_{sat}+4(\Delta+kv+\alpha_z z)^2/\Gamma^2}\right]\hat{\mathbf{z}}, \tag{2.13}$$

where $\alpha_z = (m_{F'}g_{F'} - m_F g_F)\mu_B G/\hbar$. For $z < 0$, the left term is from Beam 1 and the right term is from Beam 2. For $z > 0$, the roles of each term reverse. However, the symmetry of this simplified case allows the force to be written in this intuitive form. In cases where the magnetic field and **k** vectors do not align, more complicated equations are necessary, as will be shown in Chapter 4.

2.5 Polarization Gradient Cooling

With Doppler cooling and magneto-optical trapping, cold atom physics made dramatic progress in little more than a decade. Then, in 1988, Lett reported something unexpected.

> We have measured the temperature of a gas of sodium atoms released from 'optical molasses' to be as low as 43±20 μK. Surprisingly, this strongly violates the generally accepted theory of Doppler cooling which predicts a limit of 240 μK. [53]

The explanation for this unexpected cooling helped Claude Cohen-Tannoudji win a share of the 1995 Nobel prize in physics [54].

Cohen-Tannoudji's simplest theoretical demonstration uses an atomic transition where the ground state has total angular momentum $F = 1/2$ and the excited state $F' = 3/2$ [55]. The two ground states are then $m_F = \pm 1/2$. Detuned light interacting with the atom causes AC-Stark shifts in the ground states that differ according to the light's polarization.

Suppose two counter-propagating beams in $\hat{\mathbf{z}}$ with perpendicular linear polarizations illuminate the atom. The combined electric field of the light can be written

$$\begin{aligned}\mathbf{E} &= E_0 \cos(\omega t - kz)\,\hat{\mathbf{x}} + E_0 \cos(\omega t - kz)\,\hat{\mathbf{y}} \\ &= E_0 (\cos\omega t \cos kz)(\hat{\mathbf{x}} + \hat{\mathbf{y}}) + E_0 (\sin\omega t \sin kz)(\hat{\mathbf{x}} - \hat{\mathbf{y}})\,. \end{aligned} \tag{2.14}$$

At $z = 0$, the total electric field will be linearly polarized

$$\mathbf{E} = E_0 (\cos\omega t)(\hat{\mathbf{x}} + \hat{\mathbf{y}})\,. \tag{2.15}$$

However, at $z = \lambda/8 \rightarrow kz = \pi/4$, the total electric field will be circularly polarized

$$\mathbf{E} = E_0 \sin(\omega t + \pi/4)\,\hat{\mathbf{x}} - E_0 \cos(\omega t + \pi/4)\,\hat{\mathbf{y}}. \tag{2.16}$$

Further, the electric field at $z = 3\lambda/8 \rightarrow kz = 3\pi/4$ will be circularly polarized with the opposite handedness.

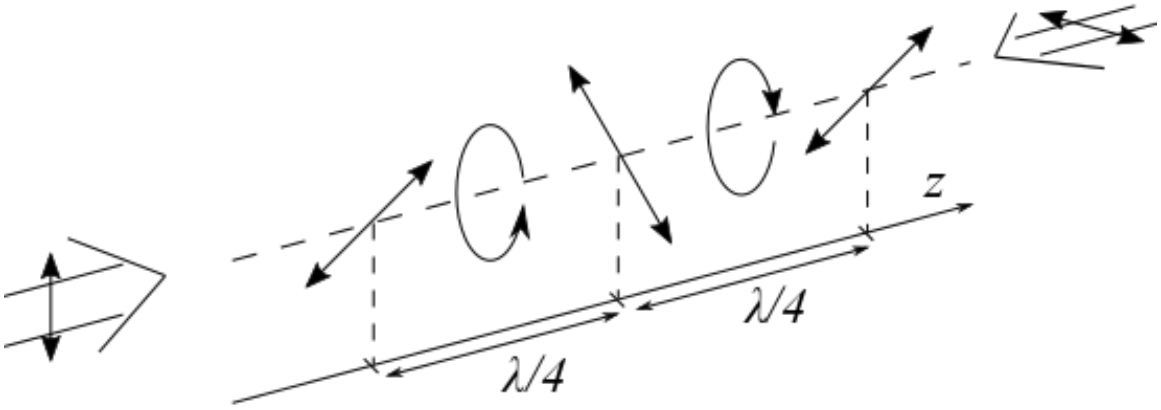

Figure 2.10: Two counter-propagating beams with orthogonal polarizations create a polarization gradient over the scale of half a wavelength.

The pair of perpendicularly polarized beams thus creates a polarization gradient in which the light field changes from linear to circular polarization over an eighth of a wavelength, as seen in Fig. 2.10. Accordingly, the energies of the two ground states

oscillate in space within the same period, as shown in Fig. 2.11. In addition, optical pumping dictates that light polarized to drive σ^+ (σ^-) transitions will accumulate atoms preferentially into the $m_F = +1/2$ ($m_F = -1/2$) state.

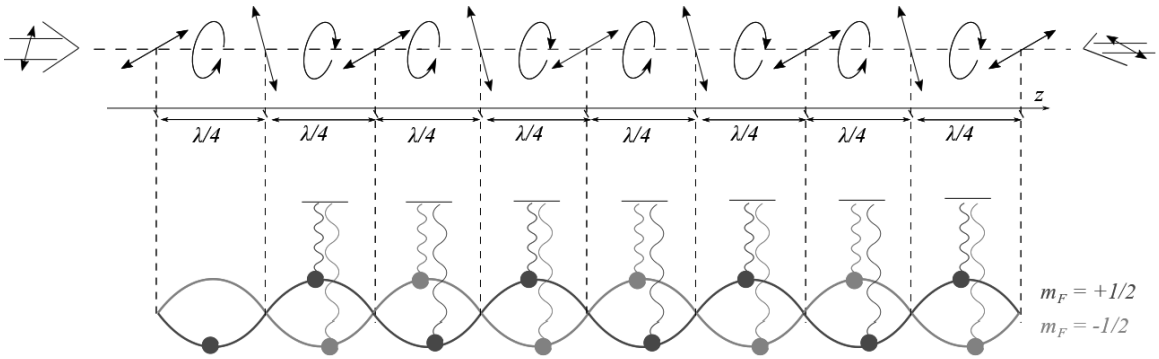

Figure 2.11: An atom's ground state energy levels split based on the polarization of its local light field. Optical pumping continually places the atom in its lower energy state, requiring it to lose kinetic energy as it climbs the next potential hill.

If the atom starts at $z = \lambda/8$, the field is circularly polarized to pump it into the $m_F = -1/2$ state. Suppose the atom then travels approximately $\lambda/4$ in the optical pumping time τ_{OP}, slowing as it climbs the potential energy gradient caused by the varying polarization. Reaching $z = 3\lambda/8$, the atom is optically pumped to the $m_F = +1/2$ state by light of the opposite circular handedness. The atom must then repeat the cycle of slowing, only to be pumped back to the original $m_F = -1/2$ state.

As the cycle repeats, a new average force can be written

$$\mathcal{F}(v) = 3\hbar k^2 \frac{\Delta}{\Gamma} \frac{v}{1 + (v/v_{crit})^2}, \tag{2.17}$$

with critical velocity

$$v_{crit} = \frac{\Gamma}{9k} \frac{I/I_{sat}}{1 + 4(\Delta/\Gamma)^2}. \tag{2.18}$$

The damping force from polarization gradient cooling (PGC) is approximately an order of magnitude larger than that of Doppler cooling, leading to a new temperature limit

$$\mathcal{T}_{sub-Doppler} = \frac{\hbar\Gamma^2}{4k_B|\Delta|}\frac{I}{I_{sat}}, \tag{2.19}$$

which corresponds roughly to the AC-Stark shift between the two ground energy levels. The sub-Doppler temperature is often on the same order of magnitude as the recoil temperature

$$\mathcal{T}_{recoil} = \frac{\hbar^2k^2}{2mk_B}, \tag{2.20}$$

for atomic mass m, defined for the average kinetic energy associated with the scattering of a single photon.

A similar polarization gradient exists for pairs of counter-propagating, circularly polarized beams interacting with more complicated spin structures. Circular polarization allows PGC to be performed using the same laser beams as the MOT, simplifying the path to cold clouds of atoms with single μK temperatures.

PGC requires a true zero magnetic field over the size of the cloud. Otherwise, the AC Stark shift would be washed out by the Zeeman shift from the remnant field. Particularly, the magnetic field must be such that

$$V_{Zeeman} << V_{AC}, \tag{2.21}$$

where the AC-Stark shift is

$$V_{AC} = \frac{\hbar\Gamma^2 I}{8\Delta I_{sat}}. \tag{2.22}$$

Thus,

$$B << \frac{\hbar\Gamma^2 I}{8m_F g_F \mu_B |\Delta| I_{sat}}. \tag{2.23}$$

Using typical values for ^{87}Rb, the remnant field must be much less than 0.14 Gauss.

Typical Earth and stray laboratory fields are on the order of 0.1 Gauss, and must therefore be cancelled with a uniform bias field. In practice, knowing the direction of the remnant field is difficult, requiring the ability to create uniform fields of arbitrary direction.

2.6 Magnetic Trapping Reconsidered

After PGC, static trapping becomes possible for significantly lower magnetic fields. A 20 μK cloud with $(m_F, g_F) = (2, 2)$ requires B_{max} be much greater than only ~ 0.1 Gauss. Meanwhile, Majorana losses can be avoided by creating non-zero magnetic minima so atoms can always adiabatically follow the field. An early example is the Ioffe-Pritchard trap [56, 57]. The trap begins with four equal currents flowing in $\pm\hat{\mathbf{x}}$, called Ioffe bars, creating the magnetic field seen in Fig. 2.12. The field, called a 2D quadrupole or 2D waveguide, has the form $\mathbf{B} = G(y\hat{\mathbf{y}} - z\hat{\mathbf{z}})$ for small displacement around the origin. Two current-carrying coils are then placed co-axially around the Ioffe bars, as seen in Fig. 2.13. These coils create a $\hat{\mathbf{x}}$ field along what was the line of magnetic field zero at $(y, z) = (0, 0)$. The field peaks at each coil, creating a non-zero local minimum between them.

Through the early 1990's, several groups realized magnetic trapping enabled even colder temperatures than PGC. By applying radiation with radio frequency ω_{RF}, atoms experiencing a certain magnetic field were resonant with transitions to untrapped states [58, 59], as seen in Fig. 2.14. By setting ω_{RF} to correspond with a large magnetic field, only the hottest atoms had enough kinetic energy to be ejected from the trap. The remaining atoms then collisionally thermalized to a lower temperature. Ramping ω_{RF} to lower frequencies continually targeted the hottest edge of the thermal distribution, forcing the remaining atoms to ever lower temperatures.

This process, aptly named evaporative cooling, made possible a new form of matter first predicted in 1924-1925. Bose [60] and Einstein [61] derived that a gas of

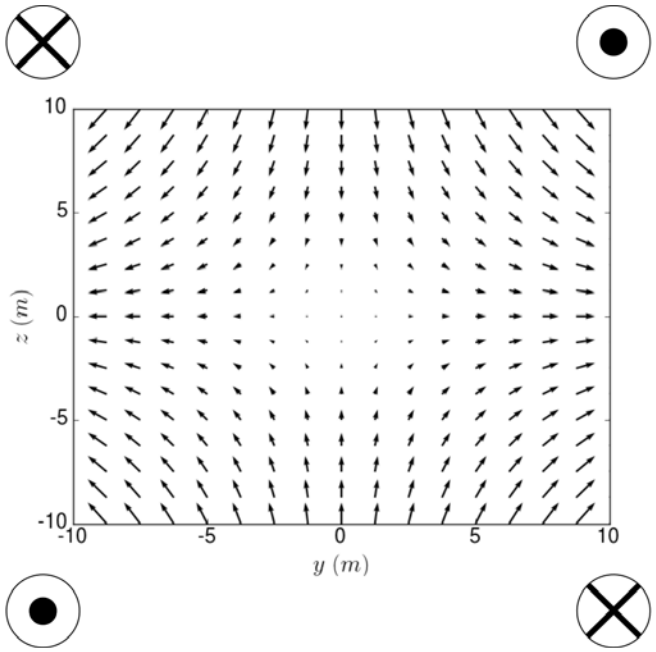

Figure 2.12: Magnetic field produced in the yz plane by four Ioffe bars in $\hat{\mathbf{x}}$.

indistinguishable bosons with density n_b and mass m would significantly populate the ground energy state below a critical temperature

$$\mathcal{T}_c = \left(\frac{n_b}{\zeta(3/2)}\right)^{2/3} \frac{2\pi\hbar^2}{mk_B}, \tag{2.24}$$

where ζ is the Riemann zeta function, for which $\zeta(3/2) = 2.6124$. Cornell and Wieman at Colorado-Boulder and Ketterle at MIT were able to demonstrate the first Bose-Einstein Condensates (BEC) [62, 63], for which they shared the 2001 Nobel prize in physics [64, 65].

2.7 Cold Atom Interferometry

As atoms populate an increasingly narrow range of energy states, quantum dynamics must be considered. Using a two photon process called the stimulated Raman transition [66–69], interference can be observed between momentum states $\chi_n(p)$ with energies E'_n.

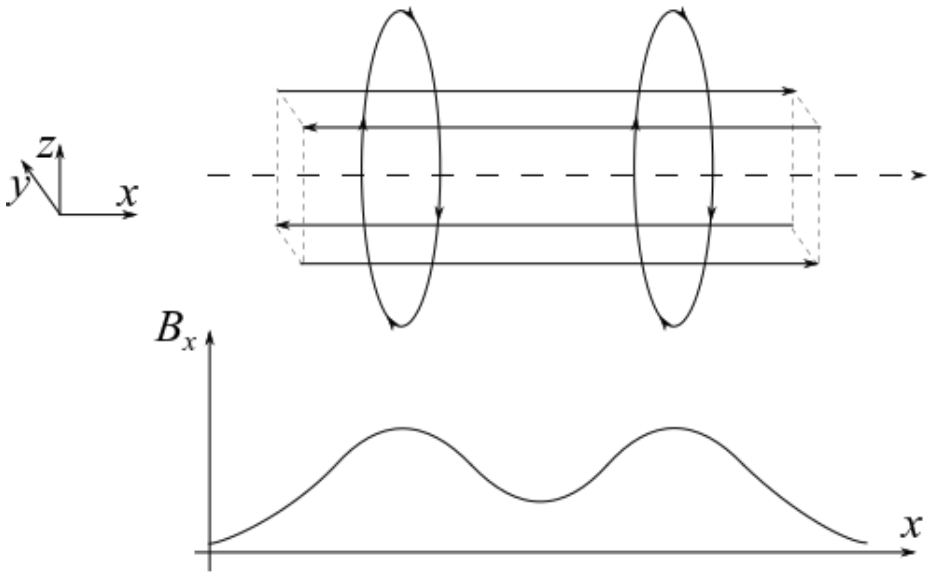

Figure 2.13: The Ioffe-Pritchard trap. Two coils placed along the Ioffe bars create a magnetic field along $\hat{\mathbf{x}}$. The field peaks at each coil and is minimal between them.

During a stimulated Raman transition, two counter-propagating lasers with frequency ω_1 and ω_2 interact with an atom in state $\chi_1(p)$, characterized by momentum expectation value p_0 and energy E_1'. The atom can absorb an ω_2 photon and emit an ω_1 photon via stimulated emission. The result is an atom in χ_2 with additional momentum $\hbar\mathbf{k}_{eff} = \hbar(\omega_1 - \omega_2)/c$ along the ω_1 beam direction. The state change is illustrated in Fig. 2.15. The duration of the Raman pulse determines the likelihood that the atom transitions from χ_1 to χ_2.

The interferometry process, Fig. 2.16, begins with an atom in state χ_1. A laser pulse at time $t = 0$ transitions the atom from its original χ_1 state into an equal superposition of χ_1 and χ_2. The resulting states will spatially separate as half of the probability distribution begins to move along the ω_1 beam direction. After time T, a second laser pulse transitions the χ_1 state to χ_2 and the χ_2 state to χ_1. The two halves of the probability distribution overlap again at time $t = 2T$, at which point a final laser pulse is applied. After a

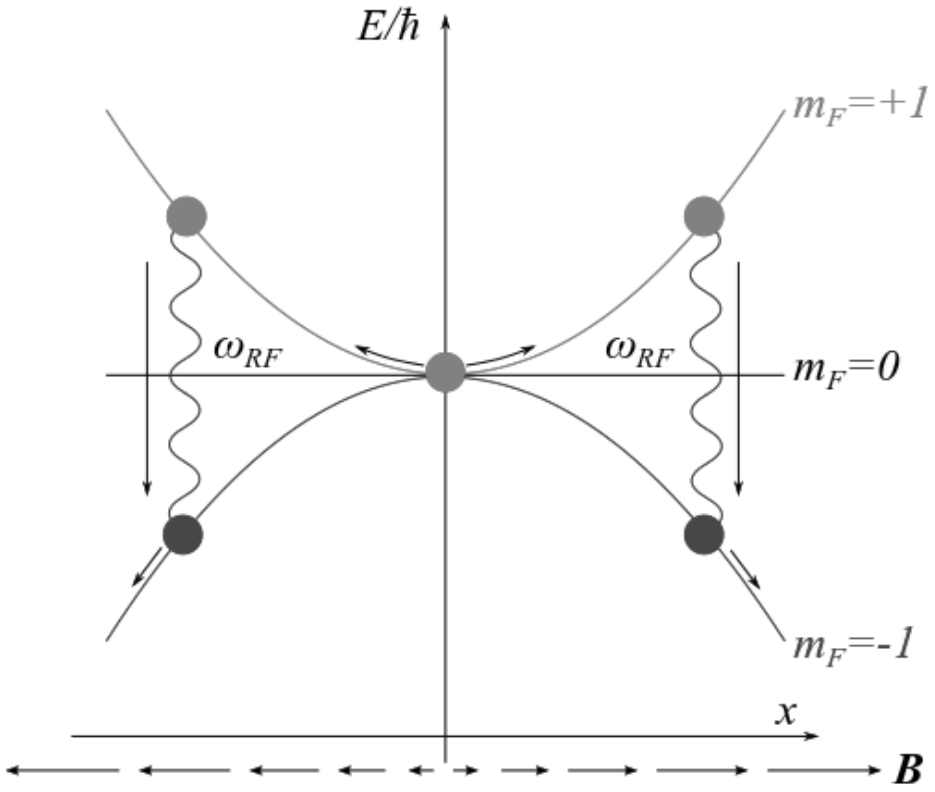

Figure 2.14: A RF frequency couples a trapped and anti-trapped state for a particular magnitude of the magnetic field. Adjusting the RF field allows selective removal of the most energetic atoms.

measurement time t_m, the probability distribution separates again, and the final location of the atom is found by absorption imaging.

In a cold cloud, the above interferometry process occurs simultaneously for each atom. As a result, the final distribution of the atom cloud measures the full probability function. The measured ratio of atoms in each state depends on the difference in accumulated phase between the two paths of the interferometer. The phase can be separated into two parts, one due to free evolution and the other to the Raman pulses themselves [70–72]. If the interferometer is used to measure a uniform acceleration a, then the free evolution phase difference is zero. On the other hand, the phase difference from the cloud locations

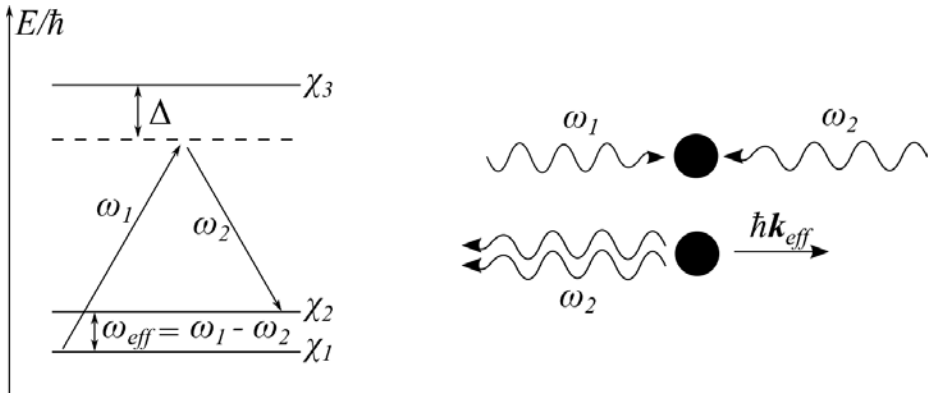

Figure 2.15: Level structure and absorption/emission process for the stimulated Raman transition.

within the Raman beams is $k_{eff}aT^2$. The first interferometer of this kind separated laser-cooled atoms by 2.4 mm to measure local gravity to a resolution of $\Delta g/g = 10^{-6}$. The current state-of-the-art achieves separation by tens of cm to measure gravity routinely at $\Delta g/g = 10^{-9}$ [73–75].

2.8 From the Lab to the Real-World

Following the first cold atom gravity measurement in 1991, national and defense applications were quickly recognized. Grants from the Air Force Office of Scientific Research and the Office of Naval Research showed immediate interest in accelerometers and frequency standards [76, 77]. Rapid progress resulted in multiple efforts by the Defense Advanced Research Projects Agency (DARPA) [22]. A specific focus was placed on outperforming GPS for certain disruptive capabilities [23].

To achieve these goals, the sensitivity of the Raman interferometer had to be improved. One route attempted to increase k_{eff}. Recently, 102 individual $\hbar k_{eff}$ momentum transfers were demonstrated [78]. Another route attempts to increase T [24]. However, atoms on Earth fall due to gravity, so long interferometer times require large devices.

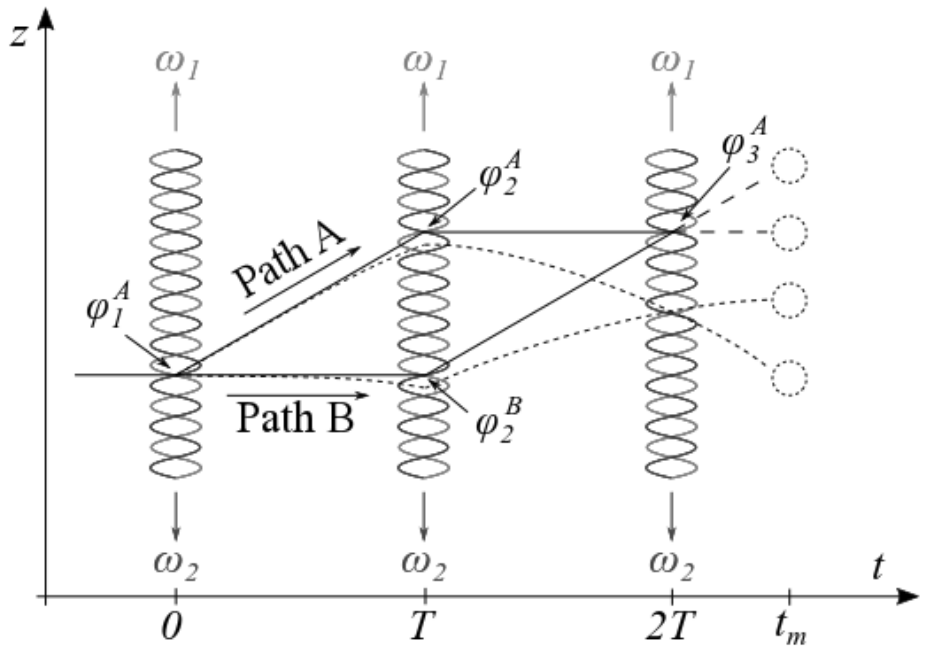

Figure 2.16: Stimulated Raman transitions creating interference between two momentum states to measure uniform acceleration. If the acceleration is zero, the atom can follow the paths drawn as solid lines. If the acceleration is along $-z$, the atom follows the dashed paths.

Accordingly, there has been a push for confined atom interferometry, in which the atoms are held at a constant height [79]. To that end, the DARPA effort created 10^5 condensed atoms in < 3.8 seconds in a compact ($\sim$ 1 m^3) system [47, 80]. A critical new component of this rapid, compact device was the atom chip. The atoms were held in a magnetic trap partially created by currents flowing across a microchip placed near the atom cloud, as depicted in Fig. 2.17. The atom chip enabled more precise field shape, higher efficiency by reducing the distance from the current to the atoms, and simplified cooling of the magnetic field source using techniques borrowed from the electronics industry. A few common atom chip structures are detailed below [81].

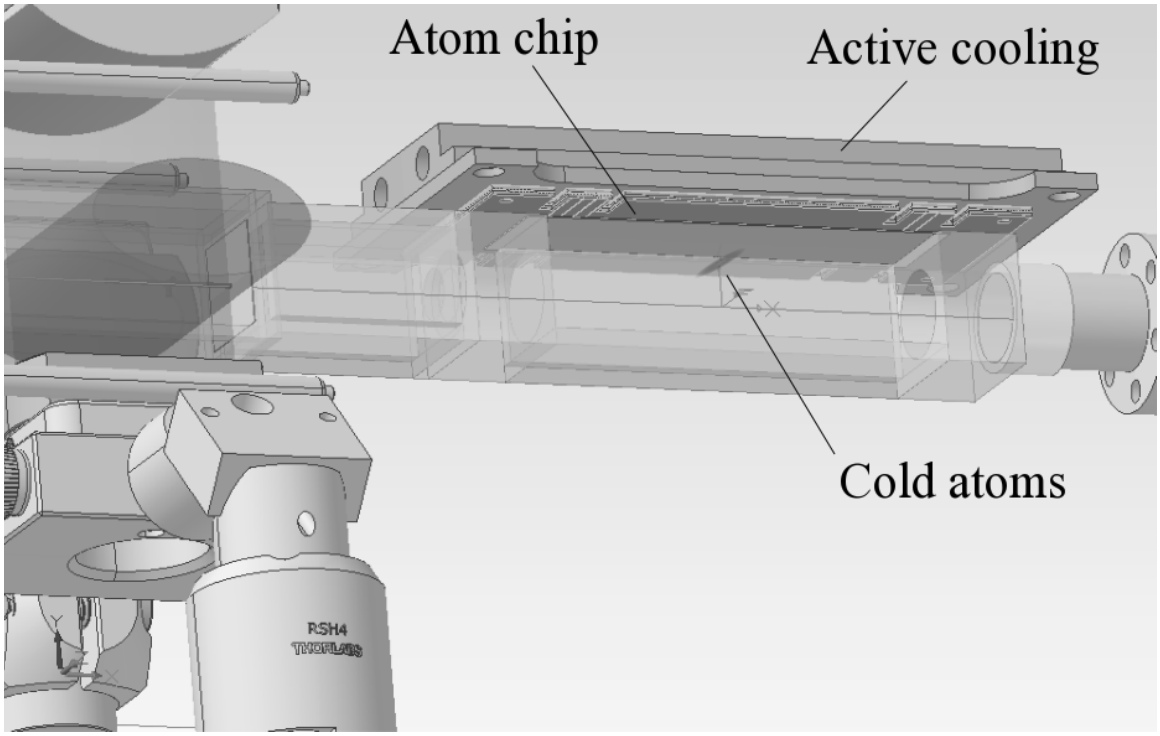

Figure 2.17: Cold atoms captured using magnetic fields generated from currents on an atom chip.

2.8.1 Single Wire Guide

Suppose the chip sits in the xy plane. An infinite length wire with current I_{chip} along $\hat{\mathbf{x}}$ produces a magnetic field

$$\mathbf{B} = \frac{\mu_0 I_{chip}}{2\pi r_{chip}} \left(\hat{\mathbf{x}} \times \hat{\mathbf{r}}_{chip} \right), \tag{2.25}$$

where μ_0 is the magnetic permeability of free space and $\mathbf{r}_{chip}$ is the radial vector from the wire to the field point. If a uniform bias field $\mathbf{B}_{bias} = B_{bias}\hat{\mathbf{y}}$ is applied as in Fig. 2.18, then a line of magnetic field zero points will form where

$$(y_1, z_1) = \left(0, \frac{\mu_0 I_{chip}}{2\pi B_{bias}} \right). \tag{2.26}$$

Near the line of zeros, the magnetic field is linear with a form $\mathbf{B} = G\left[(z - z_1)\hat{\mathbf{y}} + (y - y_1)\hat{\mathbf{z}}\right]$, which is similar to the field produced by the Ioffe bars in Fig. 2.12 except the axes of the field are angled by 45° from $\hat{\mathbf{z}}$. Accordingly, this field is referred to as a rotated 2D quadrupole, or a rotated 2D guide.

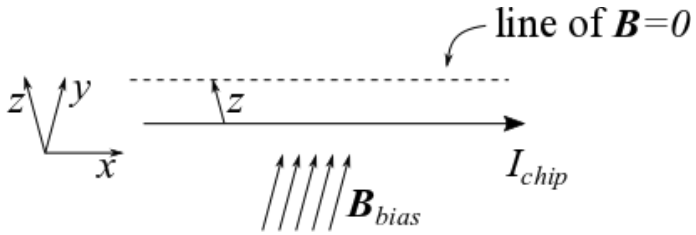

Figure 2.18: A uniform bias field creates a line of $\mathbf{B} = 0$ along a current-carrying wire.

2.8.2 U-Wire Quadrupole

Place two additional infinite wires co-planar with the first, with equal currents running in the $\pm\hat{\mathbf{y}}$ directions, separated by a distance w, as depicted in Fig. 2.19(a). These extra wires provide axial confinement. What was the line of zeros now has an $\hat{\mathbf{x}}$ field component that is maximal in magnitude above each wire. This configuration produces a trap that is linear in three dimensions with the magnetic field minimum being zero. The three-wire system is often approximated by a single U-shaped wire, as seen in Fig. 2.19(b). The linear trap is useful for MOT formation.

2.8.3 Z-Wire Trap

If the two additional wires had co-propagating currents, as in Fig. 2.19(c), an analog to the Ioffe-Pritchard trap is formed, creating a non-zero magnetic minimum. The $\hat{\mathbf{x}}$ field component peaks over each $\hat{\mathbf{y}}$ wire and is minimal between them. This three-wire trap is usually approximated by a single Z-shaped wire, as shown in Fig. 2.19(d).

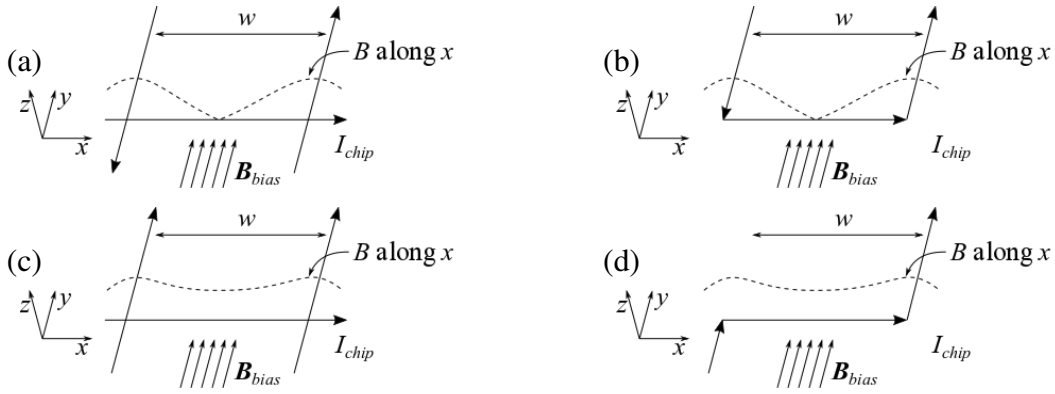

Figure 2.19: Two parallel infinite wires add field along x axis to create two types of 3D traps. Pairs of counter-propagating currents (a) create a zero field point along x, approximated by (b) a U-shaped wire. Alternatively, co-propagating currents (c) create a non-zero magnetic minimum, approximated by (d) a single bent Z-shaped wire.

2.9 The AFRL Cold Atom Sensor

Like the compact DARPA device, the Cold Atom Group at the Air Force Research Laboratory (AFRL) is pursuing magnetic confinement of an interferometer using atom chips. The group's main experiment, the cold atom sensor (CAS), shown in Fig. 2.20, represents the latest developments in that effort.

To aid viewing, Fig. 2.21 omits the vacuum pumping apparatus and removes components obscuring the experimental chambers. Two lasers apply trapping and cooling along $\pm\hat{\mathbf{y}}$ and $\pm\hat{\mathbf{z}}$ to create a two-dimensional Magneto-Optical Trap (2D MOT). The resulting cold atom beam travels into a lower pressure chamber where two counter-propagating lasers along $(\hat{\mathbf{y}} \pm \hat{\mathbf{x}})/\sqrt{2}$ retro-reflect from a mirror positioned above the chamber. Another laser pair propagates in $\pm\hat{\mathbf{z}}$. The resulting 3D MOT is labeled. After the 3D MOT is created, three pairs of nested current-carrying coils cancel the magnetic field at the 3D MOT location so PGC can begin. Once PGC is complete, the coils provide

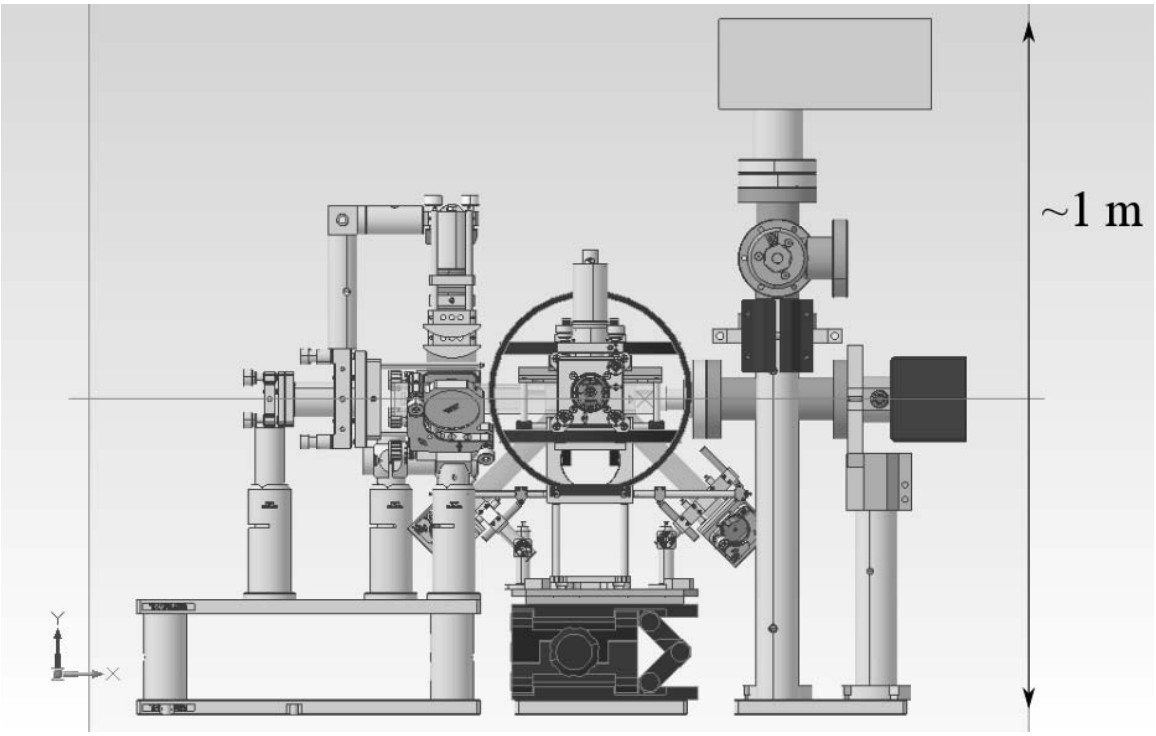

Figure 2.20: A current state-of-the-art system designed by the Air Force Research Laboratory to investigate future deployable cold atom sensors.

the bias field necessary to capture the atoms in a Z-wire trap created by an atom chip above the 3D MOT mirror. A RF coil (not shown) evaporatively cools the magnetic trap to Bose condensation.

2.10 My Contributions

My contributions to the AFRL CAS are the subject of this dissertation. The advancements described reduce the necessary components, size, weight, and power consumption of the CAS to those seen in Fig. 2.22. By designing a new geometry to laser cool atoms, five lasers are replaced with two, without losing operational performance. In addition, I fabricated several new atom chips to replace the fields of external magnetic coils. Removing these coils will significantly increase optical access for future experiments.

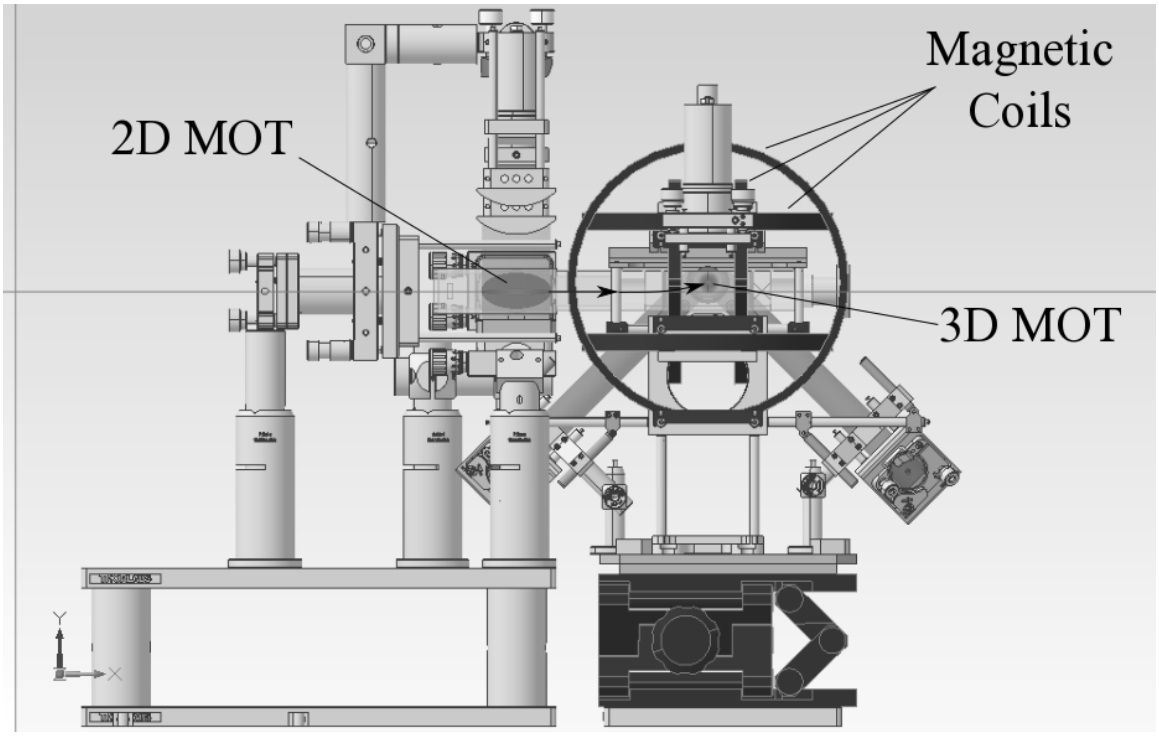

Figure 2.21: The CAS with its vacuum pumps and some optics removed for clarity.

Then, I introduce a theoretical effort to model a promising confined interferometer. The interference mechanism produces a useful signal with non-condensed atoms, enabling less stringent requirements for the laser and power supply systems. However, this method is subject to rapid signal loss due to small magnetic fields along the splitting axis. My model puts limits on how much magnetic field is tolerable and proposes new methods to improve signal quality. These contributions are more explicitly introduced in sections 2.10.1 through 2.10.3 below.

2.10.1 Grating Magneto-Optical Traps

The ease of the one-dimensional models for laser cooling often makes the initial cooling stage an afterthought. Lasers simply approach the trap in both directions along each cardinal axis. While effective, surrounding the experiment with optics on all sides has unintended consequences.

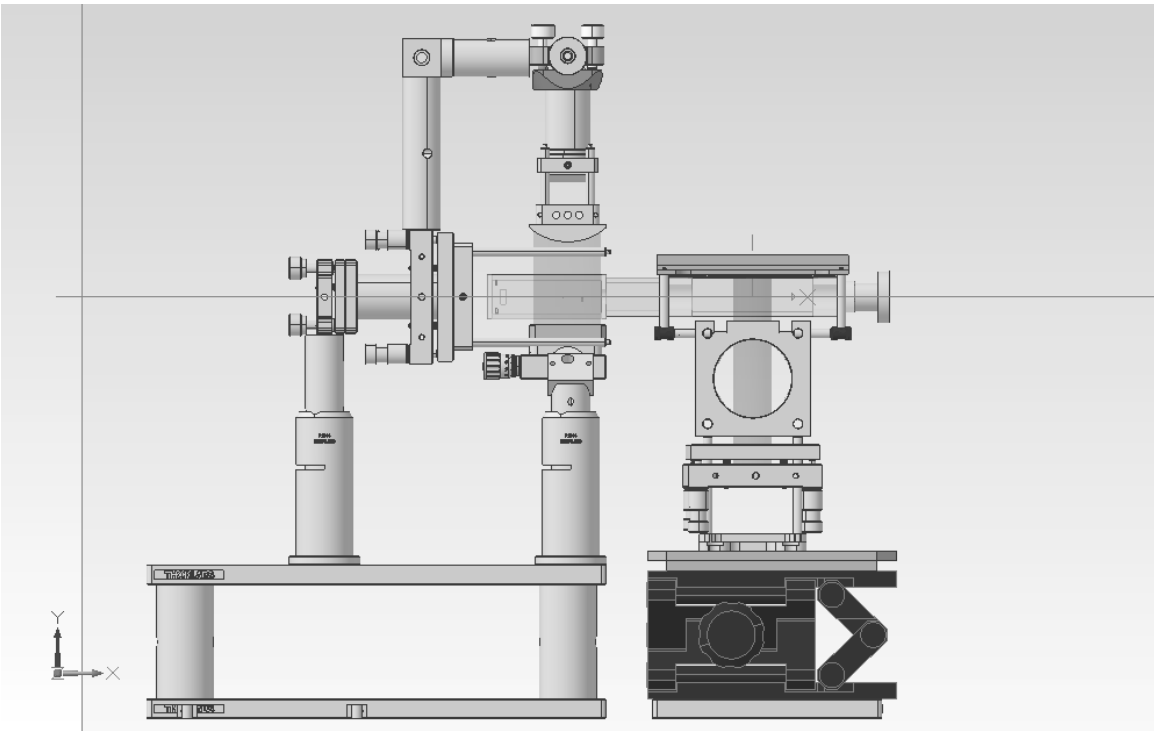

Figure 2.22: The AFRL CAS incorporating improvements explained in this dissertation. The 2D and 3D MOT now require a single laser beam each. The magnetic coils have been removed in favor of a more elaborate atom chip. Requirements on the laser and power supply systems (not shown) are reduced by using a high temperature interferometry sequence.

First, optical access is severely reduced. As seen in Fig. 2.20, beam launchers block other necessary components such as imaging cameras, magnetic field sources, or interferometry beams. Second, the cooling light must be broken into several beams. Multiple beams require significantly more optical components which can misalign under vibration or thermal variation, and add size, weight, and cost. Additionally, optical power is used inefficiently. Only one laser beam is required for laser cooling if its power is properly recycled.

Alternative MOT designs have been proposed, with a sample of the trade space shown in Fig. 2.23. Many, such as the pyramid and mirror MOT, rely on advantageous mirror placement to recycle optical power. Both suffer from optical access concerns. The focusing MOT provides access through the transverse directions at the expense of weak trapping along those directions. The prism MOT is promising in that its atom number scales like typical MOTs with good transverse access, but requires two beams and the prism structure might cause unwanted obstruction for later experimental stages.

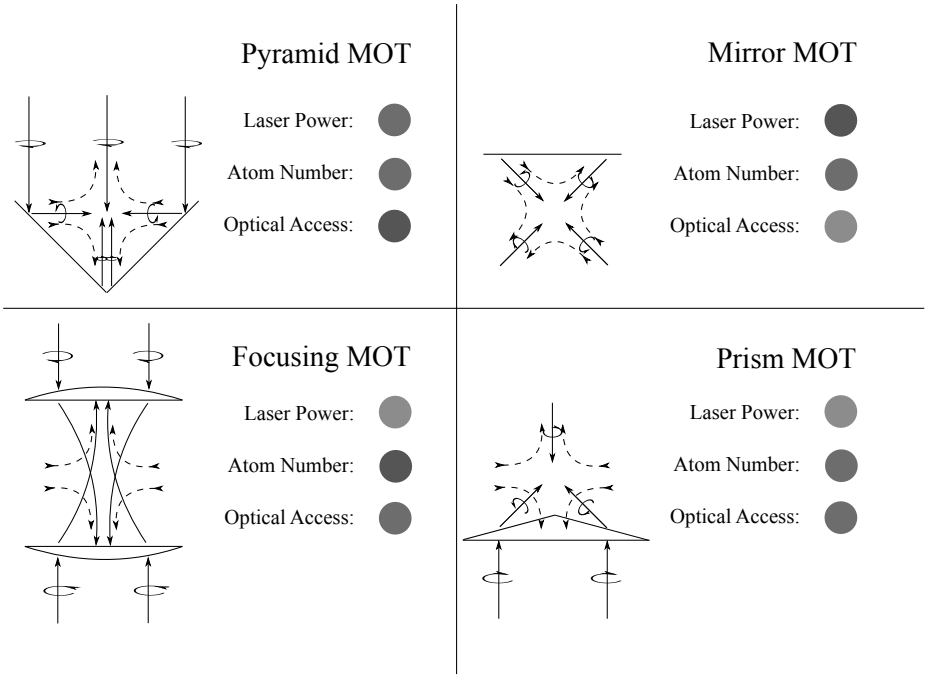

Figure 2.23: Some common 3D MOT configurations.

Recently, a three-dimensional Grating Magneto-Optical Trap (3D GMOT) was demonstrated that satisfies many needs of a deployable system [82, 83]. Like the prism MOT, a single beam approaches downward towards the zero of a magnetic quadrupole, illustrated in Fig. 4.1(c). However, instead of a second beam refracting upward through a prism, the downward beam is diffracted upwards by a set of planar reflective gratings. The

resulting 3D GMOT shows comparable atom number scaling to standard six-beam MOTs [84] and is able to achieve sub-Doppler cooling [85].

A similar principle can be used to form a two-dimensional GMOT (2D GMOT), as illustrated in Fig. 4.1(a), resulting in a cold atomic beam. Adapting from the 3D to the 2D case requires different theoretical considerations and conditions on grating efficiency, laser intensity, and polarization, which are detailed in Chapter 4. After demonstrating the first 2D GMOT, shown in Fig. 4.1(b), the atom beam is characterized and used to load a 3D GMOT with the highest atom number reported so far in a grating-based system, as seen in Fig. 4.1(d).

2.10.2 Planar Sources of Localized Magnetic Fields

While atom chips are commonly used in cold atom experiments, they often require uniform bias magnetic fields to operate, as discussed for the common structures in Sec. 2.8. These bias fields are typically created with large external coils.

The CAS uses coils, as seen in Fig. 2.24, despite the obvious obstruction they cause. In large part, coils are used because they are a simple, effective way to create large volumes of uniform magnetic fields with moderate strength. For that reason, these field sources can be found across many scientific disciplines.

But coils have become a significant burden to our experiments. In addition to their bulk, they are heavy and labor-intensive to fabricate. Their cylindrical form requires specially designed cooling structures that further exacerbate size, weight, power, and cost concerns. We wondered, would it not be simpler just to make all the necessary fields with the atom chip?

Atom chips are lightweight and easily manufactured, as will be discussed in Chapter 2. Their planar surfaces enable excellent heat transfer to a range of well-tested devices such as thermo-electric coolers and micro-channel cold plates. Additionally, the chips rest on only one of the vacuum chamber walls, enabling optical access from many angles.

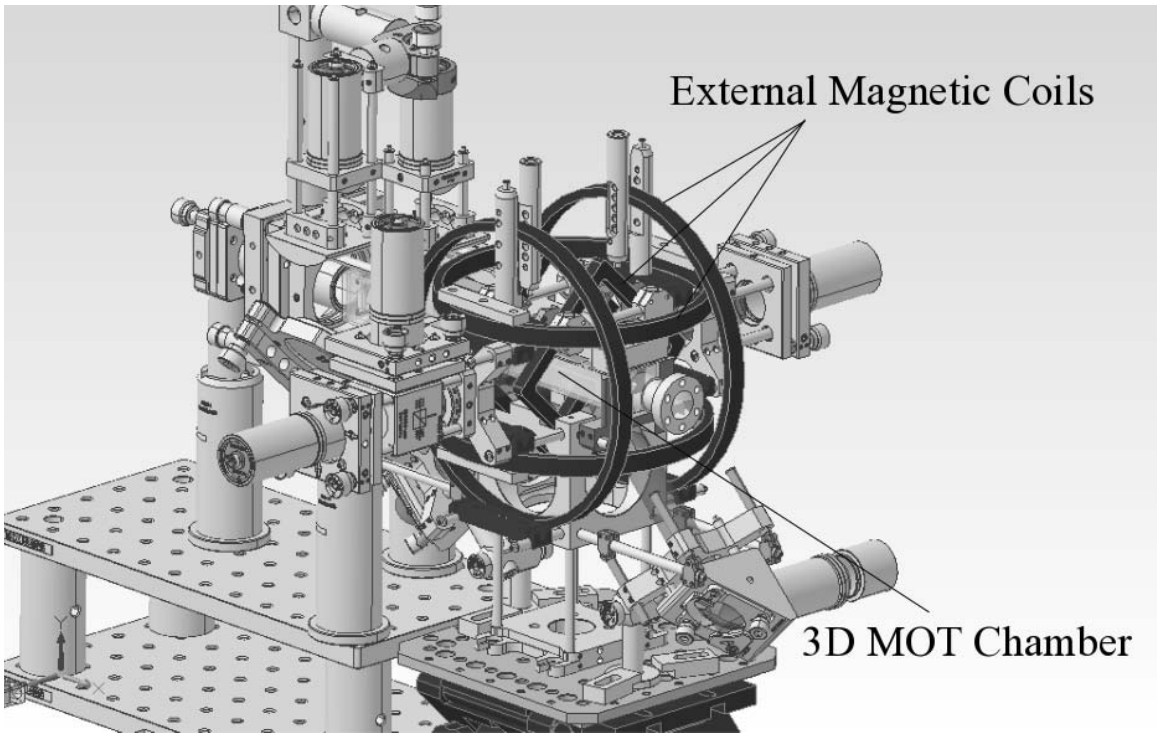

Figure 2.24: The external magnetic coils required by the CAS. These coils can be replaced by the atom chips designed in Chapter 5. As a result, increased optical access is given to the 3D MOT chamber.

Motivated by these benefits, Chapter 5 investigates the theory of uniform magnetic field generation in coil-based systems and applies a similar framework to the design of large volume uniform fields from planar sources. A model is developed by which pairs of parallel infinite currents eliminate successive unwanted orders of a magnetic field expansion. Based on the model, an atom chip is designed, fabricated, and tested with a magnetic probe. The field produced by the chip shows excellent agreement with simulations. The results are considered in the context of a real-world application, a magnetic trap conveyor to move atoms along the chip surface.

2.10.3 Talbot-Lau Interference Modeled Through the Wigner Function

The magnetic control provided by atom chips enables a matter-wave interference technique that operates at a higher temperature than BEC in a compact device. Most so-called "thermal" techniques, such as the Raman pulse interferometer discussed in Sec. **??**, change the internal state of the interrogated atoms to achieve coherent splitting. Because it is difficult to control multiple states with a magnetic field, atoms are then allowed to propagate freely, necessitating a large system. The most sensitive devices use a 10-meter long apparatus [24].

Single internal state splitting has allowed atoms to be trapped for the duration of the interferometer cycle, reducing the apparatus length to a few millimeters [79]. Unfortunately, most of these techniques require BEC and thus cooling stages that increase power consumption, decrease possible repetition rates, and lower atom numbers (see double-well potentials [86], optical lattices [87], and standing wave pulses [88, 89]).

One single-state technique has been shown to work at thermal (i.e. non-condensed) temperatures [90–92]. These interferometers, in the Talbot-Lau configuration, confine the atomic sample in two directions and allow free propagation in the third. The atoms split and recombine along the third direction.

However, due to the finite size of the device and uncontrollable external fields, there remains a residual potential along the splitting axis. Unfortunately, the residual potential and other field imperfections reduce coherence times [89, 93, 94].

With our atom chips, a high degree of control over the residual field is achieved, though small defects still remain [26]. Chapter 6 analyzes the effect of a remnant harmonic potential using a Wigner function approach. The model predicts the interference signal's decay while suggesting an optimized approach to loading the interferometer potential from a magnetic trap.

2.11 Conclusion

In this chapter, the foundation of theoretical and experimental concepts underlying this dissertation were presented. Laser cooling, magnetic trapping, condensation, and interference of atoms were discussed. A brief history was given as to how these techniques led to the Air Force Research Laboratory Cold Atom Group and its cold atom sensor experiment. Finally, my contributions were placed in context of improvements made to the CAS and the broader field of cold atoms. A novel laser-cooling geometry, called the grating magneto-optical trap was introduced to reduce optical power and increase experimental access. To further increase access, planar magnetic field sources were proposed. These sources replace external coils with currents on the atom chip. With increased magnetic field control, a promising interferometer is examined using the Wigner function. These contributions require a range of supporting experimental systems to be discussed in the following chapter.

Page intentionally left blank

III. Supporting Experimental Apparatus

3.1 Introduction

Several subsystems, methods, and laboratory techniques support the experiments discussed in this dissertation. To avoid obscuring later results, these details have been gathered together into this chapter.

3.2 Laser System

3.2.1 Requirements

We use ^{87}Rb, an alkali metal atom which has a single valence electron. The $5^2S_{1/2} \rightarrow 5^2P_{3/2}$ manifold, depicted in Fig. 3.1, is of particular interest for cold atom systems. The transition broadly exists near wavelength $\lambda = 780.241$ nm with $\Gamma = 38.11 \times 10^6$ Hz .

Selection rules dictate that the $F' = 3$ state can only decay back to the $F = 2$ state. Accordingly, the $F = 2 \rightarrow F' = 3$ transition at $\lambda_c = 780.246\ 021$ nm approximates the two-level atom used to discuss laser cooling. However, a laser red-detuned from this transition has a small but non-zero probability of driving transitions to the $F' = 1$ or 2 excited states. These states can decay to the $F = 1$ ground state, at which point the atom would no longer interact with the laser.

To ensure the cooling process continues, atoms that decay to the $F = 1$ ground state are repumped back to the $F' = 2$ state, from which they can decay to the ground $F = 2$ state and continue absorbing $F = 2 \rightarrow F' = 3$ light. The $F = 2 \rightarrow F' = 2$ repump transition occurs at $\lambda_{rp} = 780.232\ 683$ nm.

After the completion of laser cooling (MOT+PGC), the atoms populate various m_F levels of the $F = 2$ ground state, with a small fraction in $F = 1$. The goal is to populate a single magnetically trappable m_F state.

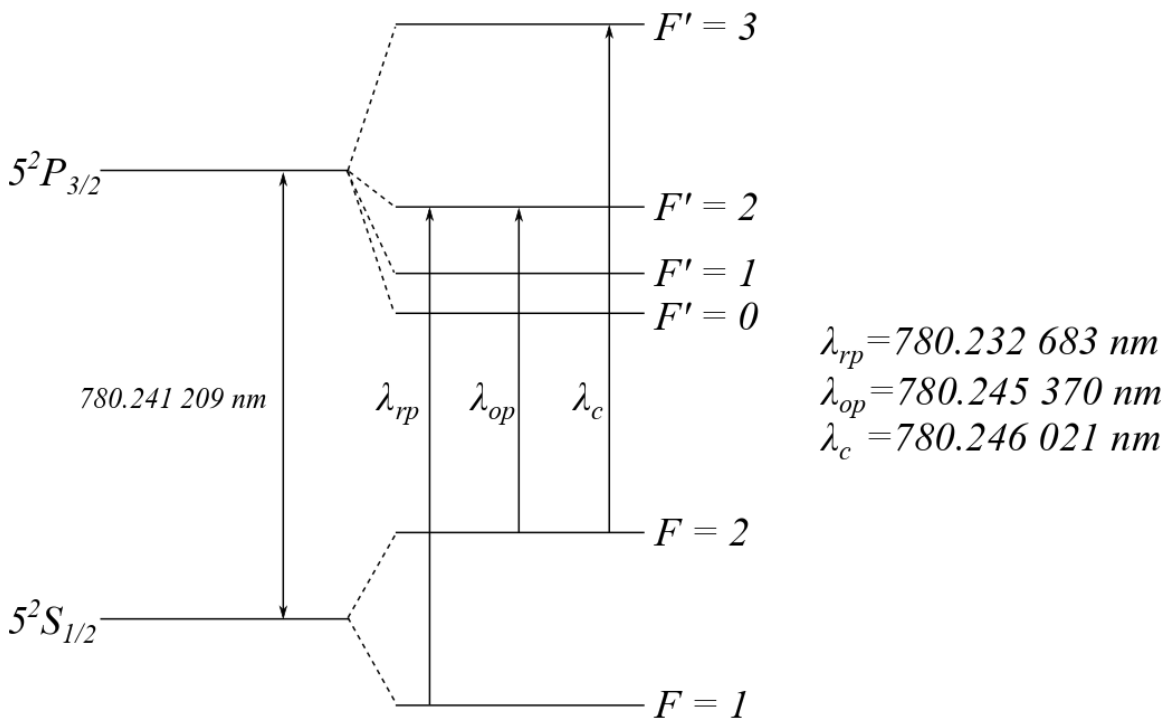

Figure 3.1: The energy levels of the $5^2S_{1/2} \rightarrow 5^2P_{3/2}$ manifold in ^{87}Rb, showing transitions of particular use for cold atom experiments.

One option is to apply circularly polarized cooling light (and some repump to clear the $F = 1$ ground state) to drive σ^+ transitions until the atoms occupy the $F' = 3$, $m_{F'} = 3$ excited state, as seen in Fig 3.2(a). However, that state can decay to $F = 2$, $m_F = 2$ and absorb again. These scattering events would add heat to PGC-cooled atoms. Instead, circularly polarized light on the $F = 2 \rightarrow F' = 2$ transition optically pumps atoms to the $F = 2$, $m_F = 2$ ground state, seen in Fig. 3.2(b),which cannot absorb further. This so-called "dark state" can be magnetically trapped. Optical pumping light has wavelength $\lambda_{op} = 780.245\ 370$ nm.

Simply generating these three discrete wavelengths of light does not provide adequate experimental capability. PGC continuously ramps the detuning of cooling light from $\Delta \approx -3\Gamma \rightarrow -11\Gamma$. Additionally, certain steps are optimized for total optical power.

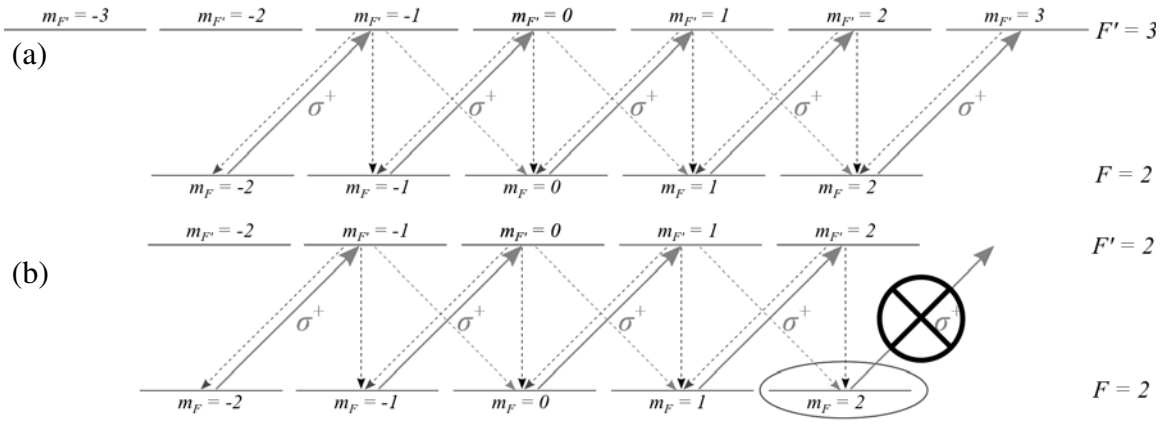

Figure 3.2: Optical pumping where circularly polarized light drives σ^+ transitions from $F \rightarrow F'$ (solid red arrows). The atom can decay to any state m_F such that $m_{F'} - m_F = -1, 0, 1$ (dashed arrows). Note that in (a) the $F = 2 \rightarrow F' = 3$ case, the atom will be pumped to the $m_F = 2 \rightarrow m_{F'} = 3$ transition, which can continue to absorb and re-emit photons. In (b) the $F = 2 \rightarrow F' = 2$ case, if the atom decays from $m'_F = 2 \rightarrow m_F = 2$, it can no longer absorb on a σ^+ transition.

3.2.2 Layout and Design

The laser system is designed to provide stable, constant power repump light and tunable, variable power cooling light, as shown in Fig. 3.3. The cooling light can be adjusted to optical pumping and imaging frequencies after laser cooling completes.

Fig. 3.4 shows the main frequency reference, a thermally stabilized diode laser from Vescent Photonics called the Heterodyne Agile Laser (HAL). The HAL incorporates an internal vapor cell and locks to the repump transition using saturated absorption spectroscopy. The output power is only $\approx$ 3 mW, which is amplified using a tapered amplifier (BoosTA) from Toptica Photonics. The resulting $\approx$ 100 mW are split and coupled into two polarization-maintaining fibers. The output of one fiber is used for laser cooling.

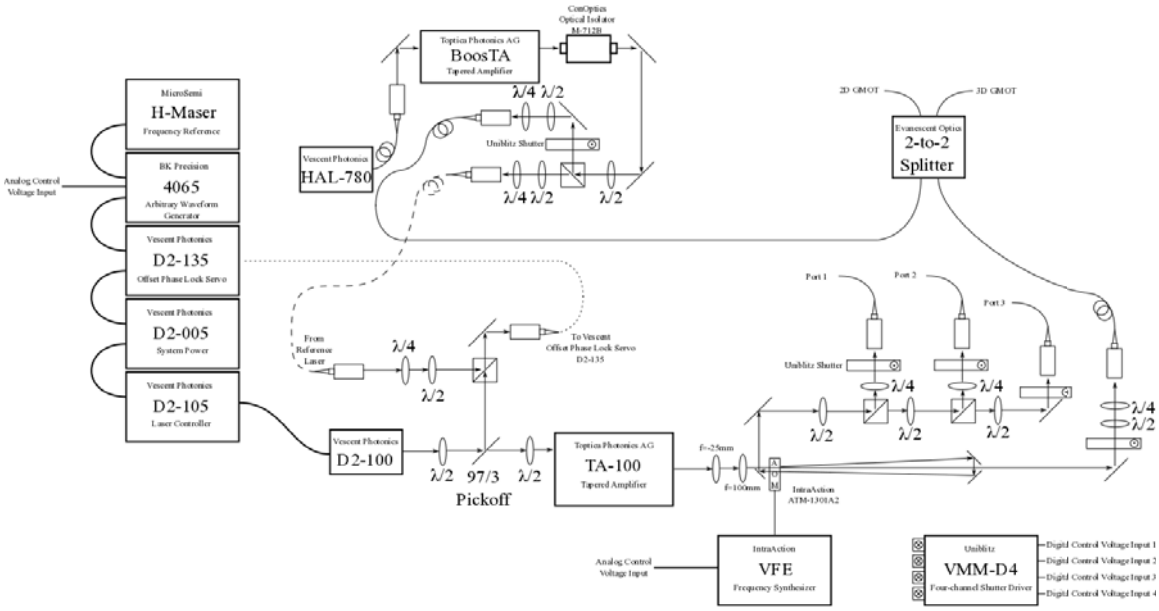

Figure 3.3: A schematic of the full laser system to provide two fiber coupled beams containing stable, constant power repump light and tunable, variable power cooling light.

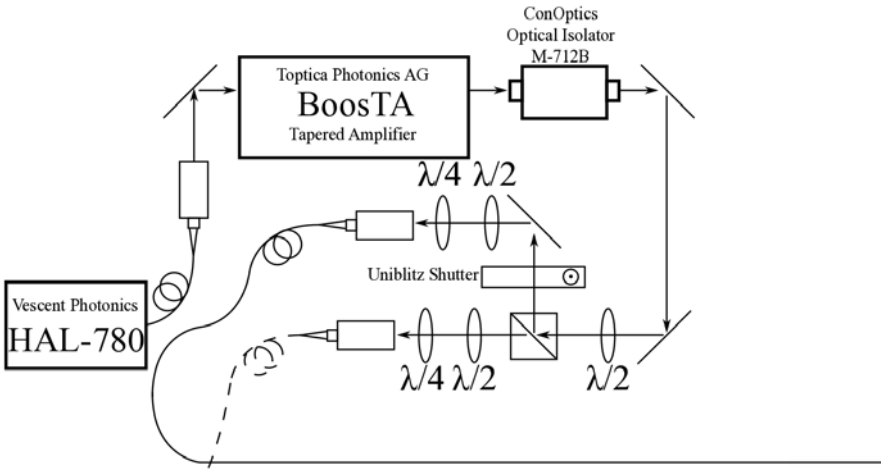

Figure 3.4: Repump light is amplified and fiber coupled for use in laser cooling and as a reference to lock the cooling light.

The other fiber (shown as a dashed line) is routed to the locking setup of the cooling laser in Fig. 3.5. The fiber's repump light has its polarization matched with the output of a second laser from Vescent Photonics. The second laser (D2-100) will provide cooling light and outputs $\approx$ 20 mW, 3% of which is picked off and mixed with the reference repump light on a beamsplitter. Both beams are coupled to another fiber which routes to a series of electronics, shown in Fig. 3.6.

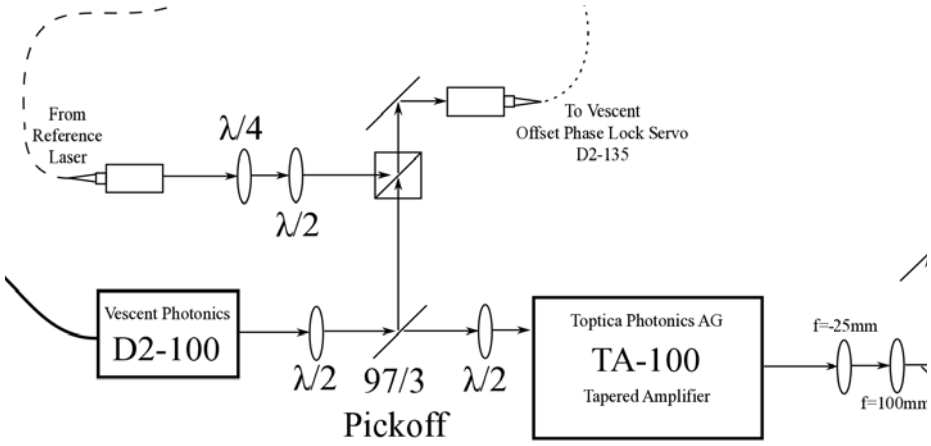

Figure 3.5: The reference repump light is combined with light from the cooling laser, creating an optical beat note used to lock the cooling light.

The fiber carrying the beat note between the two laser outputs is connected to the Offset Phase Lock Servo (D2-135) from Vescent. The servo divides the beat note frequency by 64 so it can be compared to an externally-supplied stable radio frequency. The error between the beat note and the stable frequency is used to adjust the cooling laser output via the D2-105 Laser Controller. The stable RF frequency is sourced from a BK Precision 4065 Arbitrary Waveform Generator running at $\approx$ 102.292 MHz, which is stabilized to the 10 MHz output of a Hydrogen Maser from MicroSemi. The waveform generator frequency,

and hence the cooling light's detuning from repump, can be controlled externally by an analog DC voltage input to the BK Precision 4065.

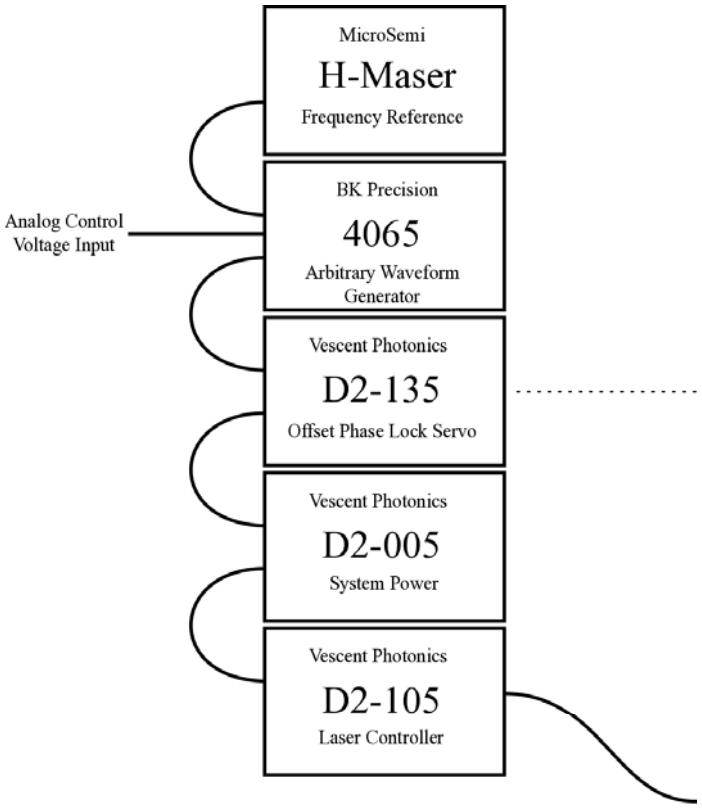

Figure 3.6: The beat note is input into an electronics box (D2-135). The desired frequency offset between the repump and cooling light is generated (4065 and H-Maser) and compared to the beat note. The error signal from the comparison is used to control the cooling laser (D2-105).

The now-locked cooling laser is amplified by another tapered amplifier (TA-100 from Toptica) which outputs $\approx$ 250 mW before being broken into multiple beams, as shown in Fig. 3.7. The output of the TA is passed through a double passed acousto-optic modulator (AOM) in the bowtie configuration. In this setup, the first order beam is routed back through the AOM such that the frequency remains unchanged. However, the double pass provides

extremely fast variable power control, adjusting the ratio of light in the zeroth and first order beams on the μs timescale. The power of the AOM is controlled via an IntraAction model VFE Frequency Synthesizer with analog external voltage control. At its extreme, the double pass provides $\approx$ 60 dB extinction of the first order beam.

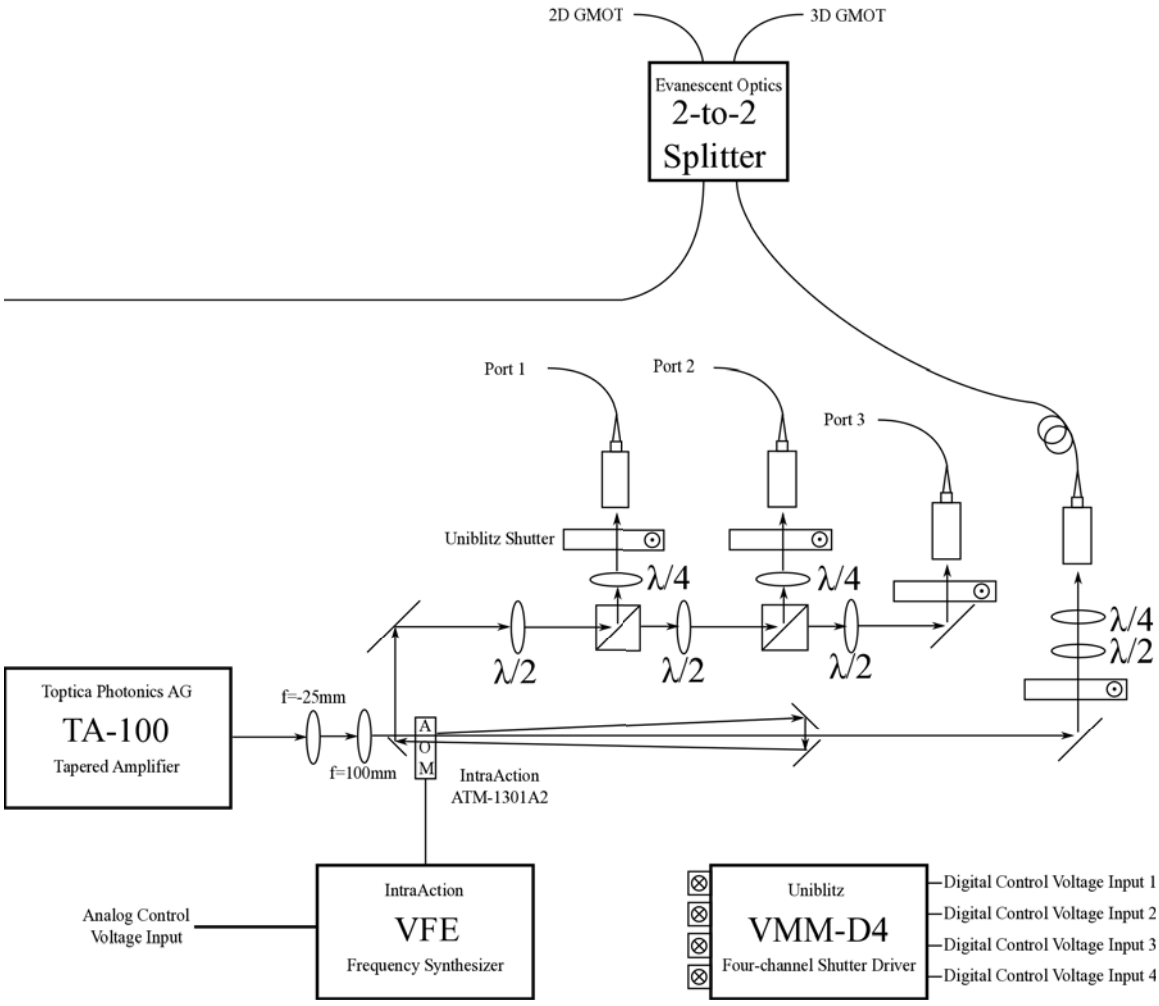

Figure 3.7: The locked cooling light is amplified and split into several ports, with the power in each controlled via an analog controlled double-passed AOM and a series of digitally controlled shutters.

The zeroth order light is fiber coupled into one arm of a polarization-maintaining, single mode 2-to-2 fiber splitter from Evanescent Optics. The other arm contains the amplified repump light coupled previously. The output arms of the splitter produce two polarized, Gaussian mode beams containing both cooling and repump frequencies. These will form the main beams for the 2D and 3D GMOTs discussed later.

The first order light is directed through a series of waveplates and polarizing beam splitters which adjust the power directed into three output fiber coupling ports. These ports serve a range of purposes, including the provision of absorption imaging light and frequency monitoring. Their original purpose was to provide the capability of creating traditional 2D and 3D MOTs. As the GMOT parameters were optimized, these ports were gradually shuttered off until the GMOTs could operate independently. The shutters for these ports, as well as those for the main cooling and repump light, are operated via a Uniblitz VMM-D4 four channel driver with digital external voltage control.

3.3 Magnetic Sources

As seen in Sec. 2.4.2, the 2D and 3D MOT require linear magnetic fields that go to zero where the laser beams intersect. For the 2D MOT whose atom beam travels along $\hat{\mathbf{x}}$, four NdFeB permanent magnets are arranged as seen in Fig. 3.8. Each magnet (K&J Magnetics part number BX842) has volume $38.10 \times 3.18 \times 6.35$ mm^3, magnetized through the 38.10×6.35 mm^2 plane with a remnant field $B_r = 1.3$ Tesla. Like the Ioffe bars, a 2D quadrupole field forms along $\hat{\mathbf{x}}$. The magnets are epoxied onto cage rods and placed in a tip/tilt optics mount, as seen in Fig. 3.9. Adjusting the magnetic structure moves the 2D MOT location until it is aligned with a small exit pinhole leading to the 3D MOT chamber.

The 3D MOT requires a linear magnetic field along three axes. As discussed in Chapter 5, a 3D quadrupole is created using two coils, as seen in Fig. 3.10. These coils

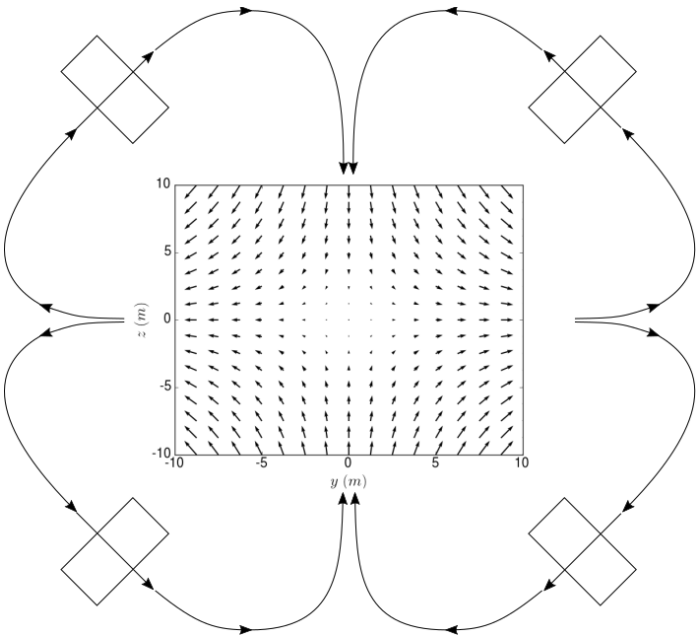

Figure 3.8: Four permanent magnets are oriented to create a 2D quadrupole field along $\hat{\mathbf{x}}$

have radius R_{coil} and are placed co-axially at $z = \pm R_{coil}/2$. Each carries current I_{coil} in opposite directions.

The coils are held in place with cage rods placed around the 3D MOT chamber, as shown in Fig. 3.11(a). Each is wound with 130 turns of 18 gauge magnet wire and is 11.2 mm in height. The inner diameter is 57 mm and the outer diameter is 76 mm. When energized with 3 A, these coils create a 9.5 Gauss/cm gradient near $z = 0$ along the $\hat{\mathbf{z}}$ axis. When the two coils carry current in the same direction, they create a constant $\hat{\mathbf{z}}$ field. With a 0.1 A current, a 2 Gauss field is formed.

Typical Earth and stray laboratory fields are on the order of 0.1 Gauss. As discussed in Sec. 2.5, these background fields must be cancelled for PGC. Two additional coil pairs are placed along $\hat{\mathbf{x}}$ and $\hat{\mathbf{y}}$, such that adjusting the currents in each pair creates a cancelling field in any direction, as shown in Fig. 3.11(b). Thus, the experiment requires four independent current controls: the upper $\hat{\mathbf{z}}$ coil, the lower $\hat{\mathbf{z}}$ coil, a pair of $\hat{\mathbf{x}}$ coils, and a pair of $\hat{\mathbf{y}}$ coils.

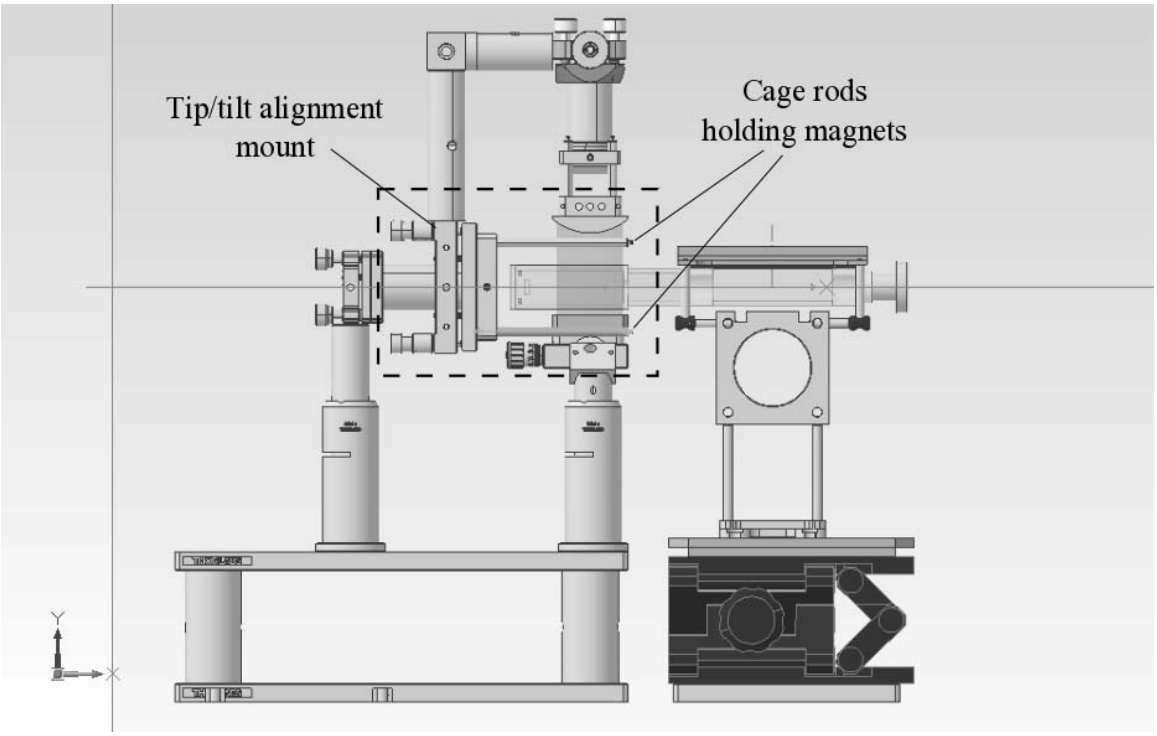

Figure 3.9: The mounting and alignment of the 2D MOT magnets.

3.4 Timing and Control

In addition to accurate lasers and magnetic field, these experiments require precision timing. For example, PGC uses a controlled analog frequency ramp from $\Delta = -3\Gamma \rightarrow -11\Gamma$ in 12 ms. Further, the camera used for absorption imaging triggers in 50 μs and must be coincident with the imaging light being shuttered on.

The lab uses a home-built solution, written in Python, that controls and synchronizes various hardware interfaces called the Arbitrary Waveform Generator, or Arbwave. Arbwave can be programmed to output signals using two systems. The DIO-64 from Viewpoint Systems is capable of delivering 50 ns pulses on 64 independent channels. A National Instruments DAQ multifunction I/O module outputs 16 simultaneous analog channels.

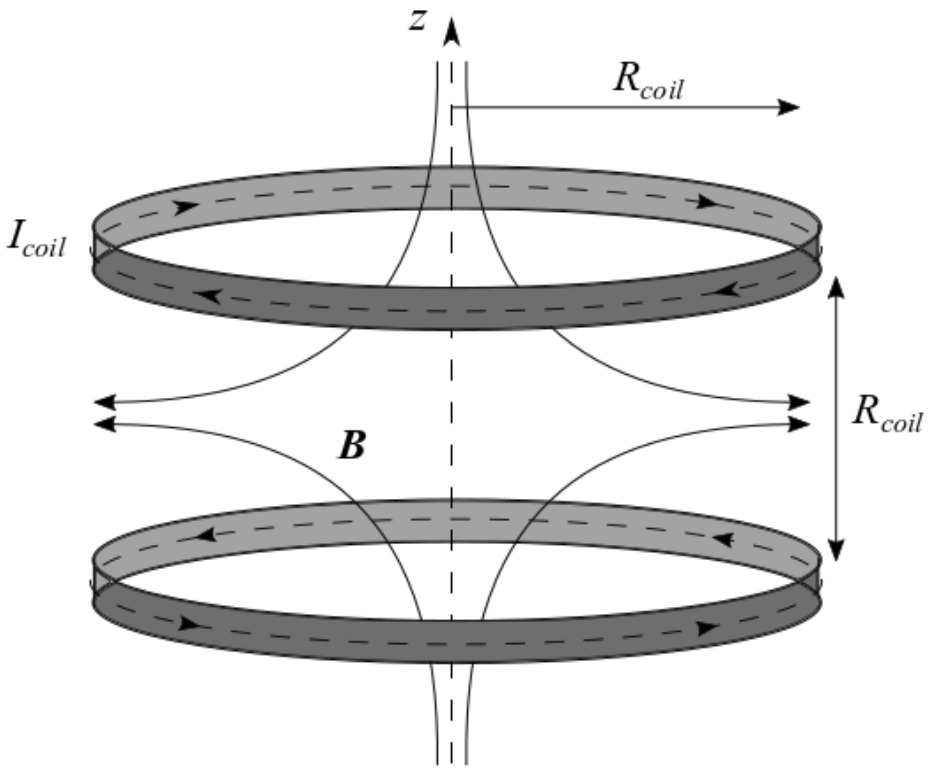

Figure 3.10: Two coils with counter-propagating currents separated by their radius create a linear field at their midpoint.

Shutters for the repump, cooling, imaging, and other light ports are controlled digitally. Each shutter was calibrated against a photodiode to determine the delay between the Arbwave signal and shutter operation, as shown in Fig. 3.12 for the repump beam. The dashed curve is the scaled-down voltage from Arbwave and the solid curve is the photodiode voltage. The calibration results are shown in Table 3.1.

The GMOT experiment's magnetic fields are created by an array of Helmholtz coils connected to KEPCO 20V, 10A bipolar operational power supplies, controlled via analog voltages (part number BOP 20/10). The current, delay, and ringing of these coils was found using four point measurements of voltage across an inline power resistor, with a typical

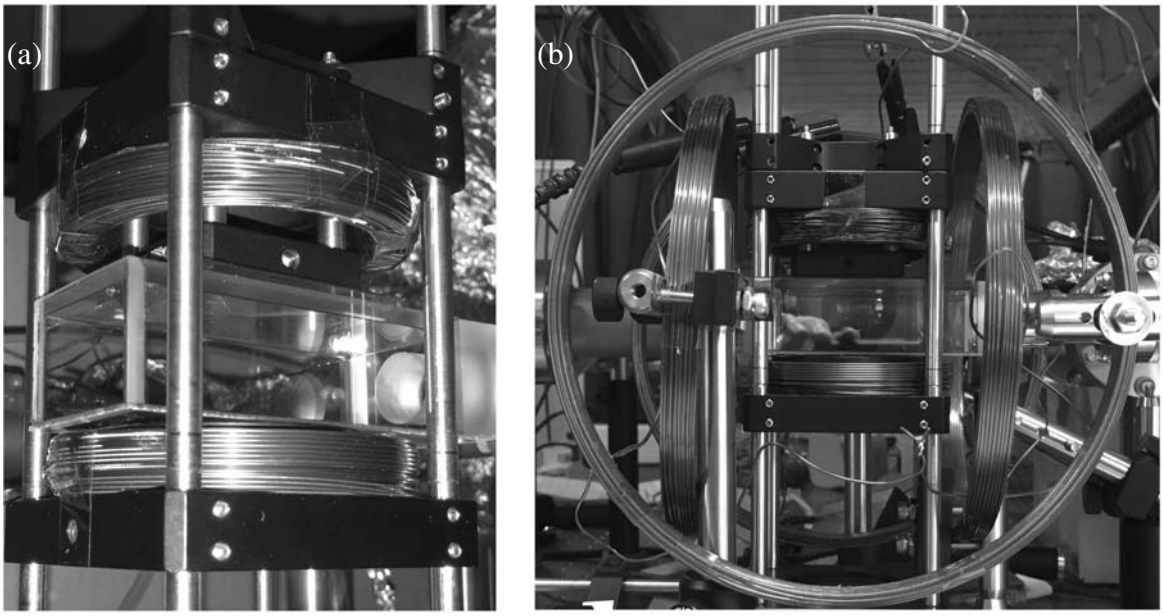

Figure 3.11: When the coils in (a) are used for the 3D MOT, the upper and lower coil carry opposite direction currents. The coils carry current in the same direction for PGC to cancel background $\hat{\mathbf{z}}$ fields. Additional coils are added (using red wire) to cancel $\hat{\mathbf{x}}$ and $\hat{\mathbf{y}}$ background fields.

Beam	On delay (ms)	Full on time (ms)	Off delay (ms)	Full off time (ms)
Repump	1.1	1.7	1.4	2.5
Cooling	1.6	2.3	0.7	1.4
Block/Imaging (Port 1)	1.6	2.2	1.0	1.8
Push (Port 2)	1.6	2.4	0.6	1.4

Table 3.1: Shutter response times.

response shown in Fig. 3.13. The current had no noticeable delay within the resolution of the scope (1 μs), and full on/off times were 55 ± 5 μs.

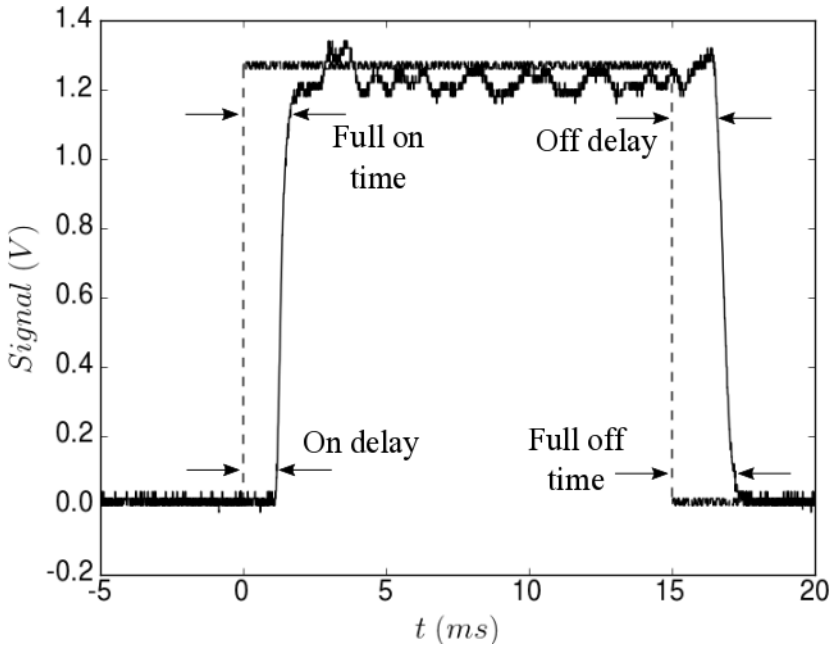

Figure 3.12: Photodiode signal of the repump beam (solid) compared to the digital signal provided by Arbwave (dashed).

Arbwave adjusts the cooling laser frequency via an analog signal to the 4065 Arbitrary Waveform Generator referencing the lock. Control voltages were calibrated against cooling light with a Bristol Instruments 621 wavelength meter.

Despite these controls, background fields emanating from 60 Hz power line fluctuations are a well-known systematic issue in cold atom devices. A 60 Hz trigger, sketched in Fig. 3.14, switches from low to high voltage when the phase of the AC power line changes sign. The trigger is connected to Arbwave via the DIO-64, allowing experimental runs to always begin at the same phase of the 60 Hz fluctuation.

The 120 V AC signal is met by an 11 kΩ power resistor, bringing the current to $\approx$ 11 mA. An external BAW75V silicon small signal diode prevents reverse current flow from damaging a 4N35 optocoupler. The optocoupler drives the gate of an internal transistor

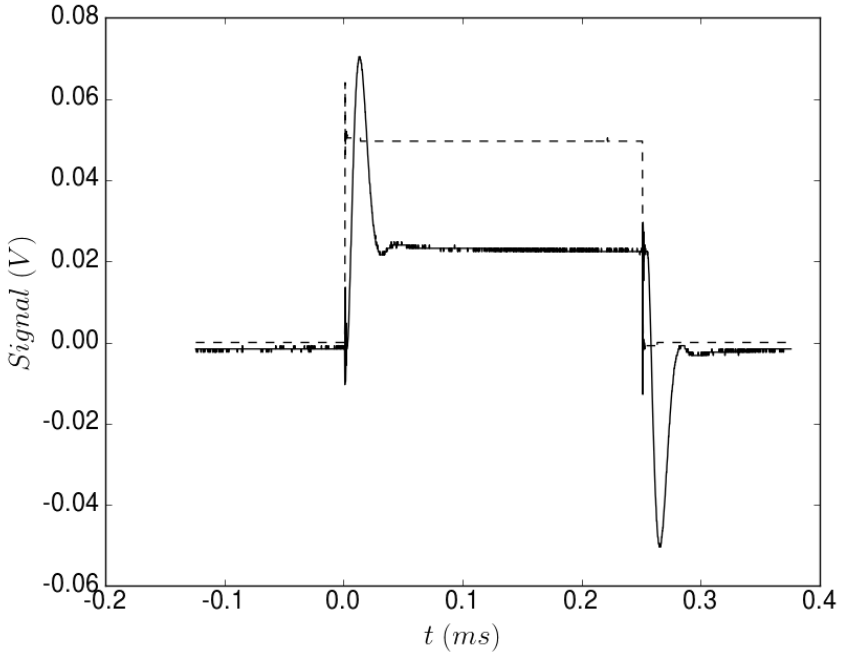

Figure 3.13: Typical magnetic coil response (solid) to a digital signal from Arbwave (scaled, dashed).

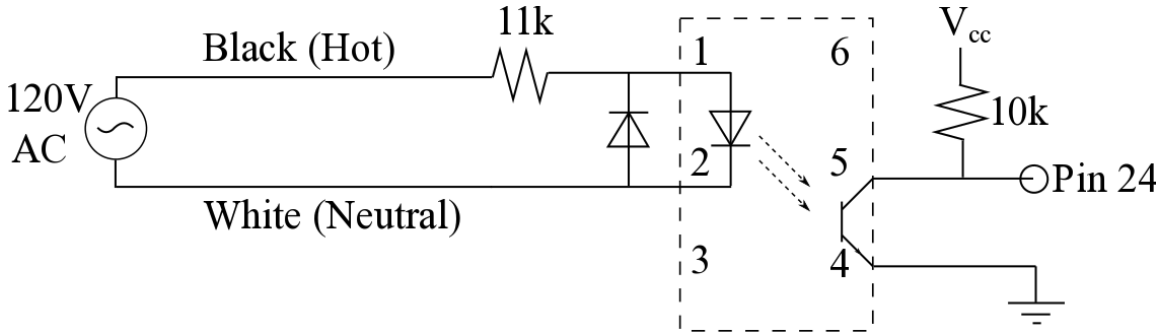

Figure 3.14: A circuit to trigger Arbwave to begin an experimental run in phase with the 60 Hz oscillation of the lab power lines.

to switch the voltage of the external triggering pin (24) on the DIO-64 board, starting an experimental run.

3.5 Vacuum System

Compact, cold atom systems typically use transparent vacuum chambers to maintain optical access. The choice of material includes quartz, silicate, borosilicate, sapphire, or even diamond. These optical surfaces are often treated for anti-reflection, making bonding them into useful structures difficult as treatments fail at high temperature.

Few low temperature bonding techniques exist. Optical contact bonding requires significant polishing, anodic bonding requires high voltages and difficult seals, and glass frit is untested at our pressures. Instead, AFRL has opted to fabricate chambers from polished borosilicate using a NASA-certified low-outgassing epoxy, 353-ND from Epo-Tek. These chambers have been evacuated to pressures on the order of 10^{-10} Torr.

Via a glass-to-metal seal, the chambers are connected to more traditional ultra-high vacuum (UHV) components. Stainless steel tubes are connected via Con-Flat flanges with copper gaskets. Several pumps are attached to the system, including an Edwards nXDS dry scroll pump and EXT75DX turbomolecular pump, a Varian 40 l/s ion pump, and a titanium sublimation pump. Once sealed and evacuated, the system is baked at ≈ 200 °C for several days to reduce outgassing of adsorbed particles, in particular water and H_2.

A source of Rb must be placed inside the chamber prior to evacuation. The vapor pressure of Rb at room temperature is $\approx 4 \times 10^{-7}$ Torr, significantly higher than the ideal $10^{-8} - 10^{-9}$ Torr of Rb needed for laser cooling [95]. Common practice is to use a Rubidium getter. These dispensers contain alkali metals in the form of a chromate salt of the type Rb_2CrO_4. Resistive heating from an applied current evaporates Rb into the chamber [96].

To apply current through the chamber walls, the dispensers are formed into a ring as shown in Fig. 3.15. The ring is then inductively heated by an AC coil outside the vacuum cell. Adjusting the distance between the dispenser ring and the heating coil reduces the inductive coupling, allowing manual control of the Rb vapor density.

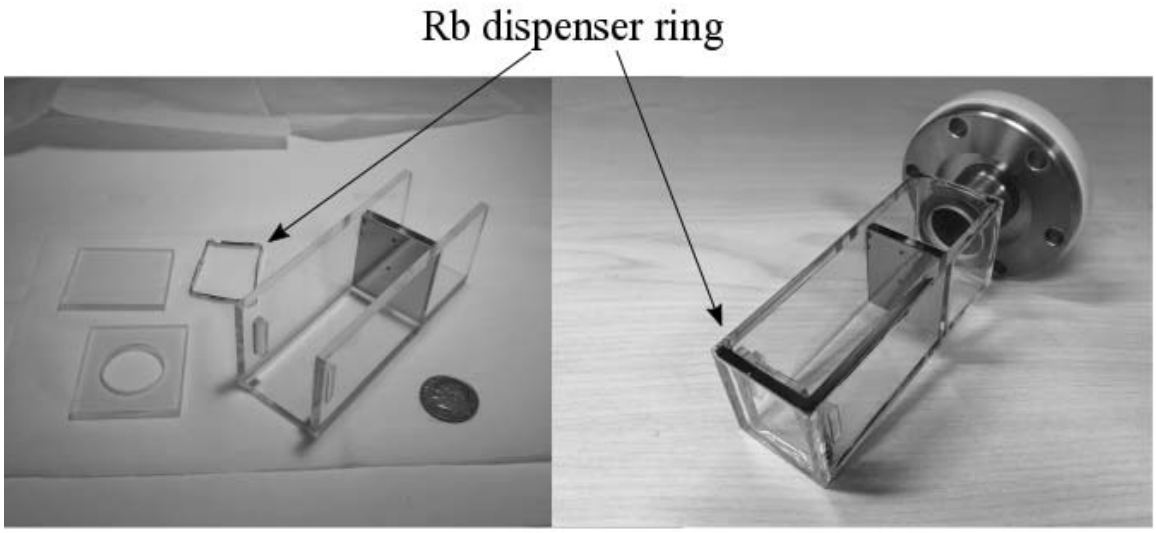

Figure 3.15: Rb dispensers formed into a ring so they can be inductively heated within the vacuum system.

The induction heater fabricated for this purpose is shown in Fig. 3.16, from [97]. It allows operation with a DC power supply and just two N-type MOSFETs (100 V, 35 A). The primary difficulty of the heater's construction is that the work coil is composed of two inductors L_1. At their midpoint, a choke inductor L_2 ($\approx$ 2 mH) connects to $+V$. The current flows through L_2 and then alternately through the upper or lower L_1, depending on the switching transistors. Components must be selected to handle the large currents heating the work coil. In the diagram, R are 220Ω, 0.6 W resistors, D are 40V, 1A Schottky diodes, and C is a 330 nF, 400 V polypropylene capacitor.

Prior AFRL experiments noted that the Rb chromate dispensers release undesirable levels of remnant gas. The remnant gas lowered the trap lifetime by increasing background chamber pressure. We developed a cleaner dispenser using Highly Oriented Pyrolytic Graphite (HOPG). Usually used as a calibration surface for electron microscopy, HOPG consists of carbon atoms in stacked parallel layers like sheets of graphene. Heat can force

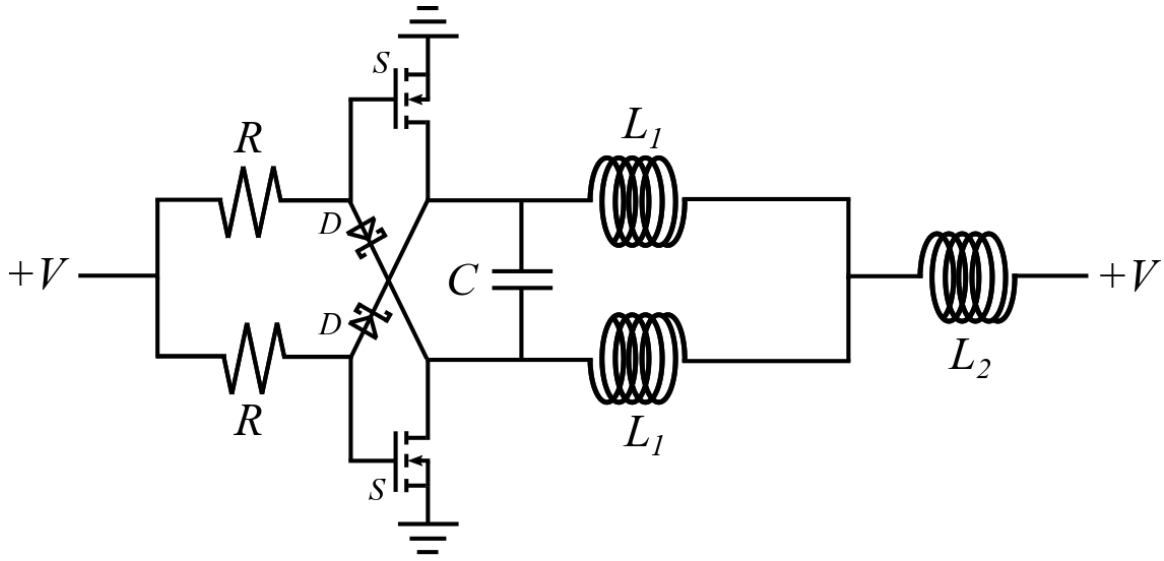

Figure 3.16: The circuit diagram of the induction heater used to release Rb from the getters and HOPG into the vacuum chamber.

Rb atoms between these layers. In practice, the 1 mm thick HOPG samples swell to ≈ 3 mm once loaded. The loaded HOPG samples were reheated and tested by a residual gas analyzer. The Rb re-emerged with order of magnitude lower vapor pressures of remnant gas. The GMOT experiment described below was the first operational test of the HOPG source and its success validates future use of HOPG for cold atom devices.

3.6 Atom Chip Design and Manufacture

The size, weight, and power of the magnetic coils are identified as a major source of inefficiency in the CAS. Instead, bias and quadrupole fields can be created using currents on an atom chip as discussed in later chapters.

The atom chips are cut from blanks of direct-bonded Copper (DBC) on an Aluminum Nitride substrate (AlN) obtained from Stellar Ceramics (part number: 5475-C840-D) [98]. AlN is a ceramic with a particularly high thermal conductivity (≈ 300 W/(m·K)), capable of forming a eutectic bond with copper that has strong thermal and mechanical connection.

The DBC method enables particularly thick copper layers as high as 305 μm. Using an A-Series fiber laser micro-machining mill from Oxford Lasers, features as small as 20 μm are cut into the DBC. The channels between features are cleared of copper in an etching solution of HCl/H_2O_2 or cupric chlorate and then cleaned with vinegar. In testing, wires with a 200×200 μm^2 cross-section carried currents as high as 200 A for single ms pulses.

Chip designs are drawn in DXF format using a range of programs, including Inkscape and AutoCAD. The DXF drawings are converted to specialized G-Code commands run by the mill with in-house software. Completed chips are placed outside the vacuum chamber, separated by a thin silicon or borosilicate membrane. Ex-vacuo chips allow rapid prototyping, as chips can be replaced without breaking vacuum [27].

3.7 Conclusion

In this chapter, the requirements of laser cooling ^{87}Rb were discussed and our optical layout was detailed. MOT and PGC magnetic field sources were described. The experimental timing and control system was shown with typical calibrations of shutters and power supplies. An overview of the ultra-high vacuum systems and Rb sources used was presented. Finally, the design and manufacture of atom chips were considered. In the following chapter, these supporting systems are used to demonstrate a novel geometry for laser cooling.

Page intentionally left blank

IV. Initial Cooling: Grating Magneto-Optical Traps

4.1 Introduction

This chapter details the demonstration of the first 2D GMOT, seen in Fig. 4.1(a)-(b). The 2D GMOT is used to load a 3D GMOT, seen in Fig. 4.1(c)-(d). The 3D GMOT is the first to be loaded by an atom beam and has the highest atom number so far reported.

This chapter will be organized as follows: the theory considerations for adapting from the 3D to the 2D case will be detailed. The design and characteristics of a 2D GMOT with Doppler cooling along the atom beam axis (the $2D^+$ configuration [99]) are then presented. Finally, the loading rates, lifetime, and atom number of the combined $2D^+$ to 3D GMOT system are reported.

4.2 Theory and Design

Unlike most common MOT configurations, the GMOT wavevectors are not aligned with the magnetic field axes. Accordingly, specific conditions for intensity and polarization must be considered when selecting gratings. These conditions differ between the 2D and 3D GMOT case. A more detailed derivation of the following results is given in Appendix A.

Each atom in a MOT scatters light from multiple off-resonant laser beams with wavevectors $\mathbf{k}_j$ and polarization vectors $\hat{\boldsymbol{\epsilon}}_j$. Assuming the atom absorbs from $F = 0 \rightarrow F' = 1$, a circularly polarized beam drives transitions to the $m_F = -1, 0, +1$ excited states with relative strengths $\alpha_{m_F}(\varphi, \hat{\boldsymbol{\epsilon}}_j)$ that depend on the beam's polarization and angle with respect to the local magnetic field φ. For a beam whose polarization is labeled by $s = +1$ for right circular or $s = -1$ for left, these strengths are $\alpha_{\pm 1} = (1 \mp s\cos\varphi)^2/4$ and $\alpha_0 = (\sin^2\varphi)/2$. The average force from a single beam j, of intensity I_j, on an atom with velocity $\mathbf{v}$ in a magnetic field $\mathbf{B}$ is

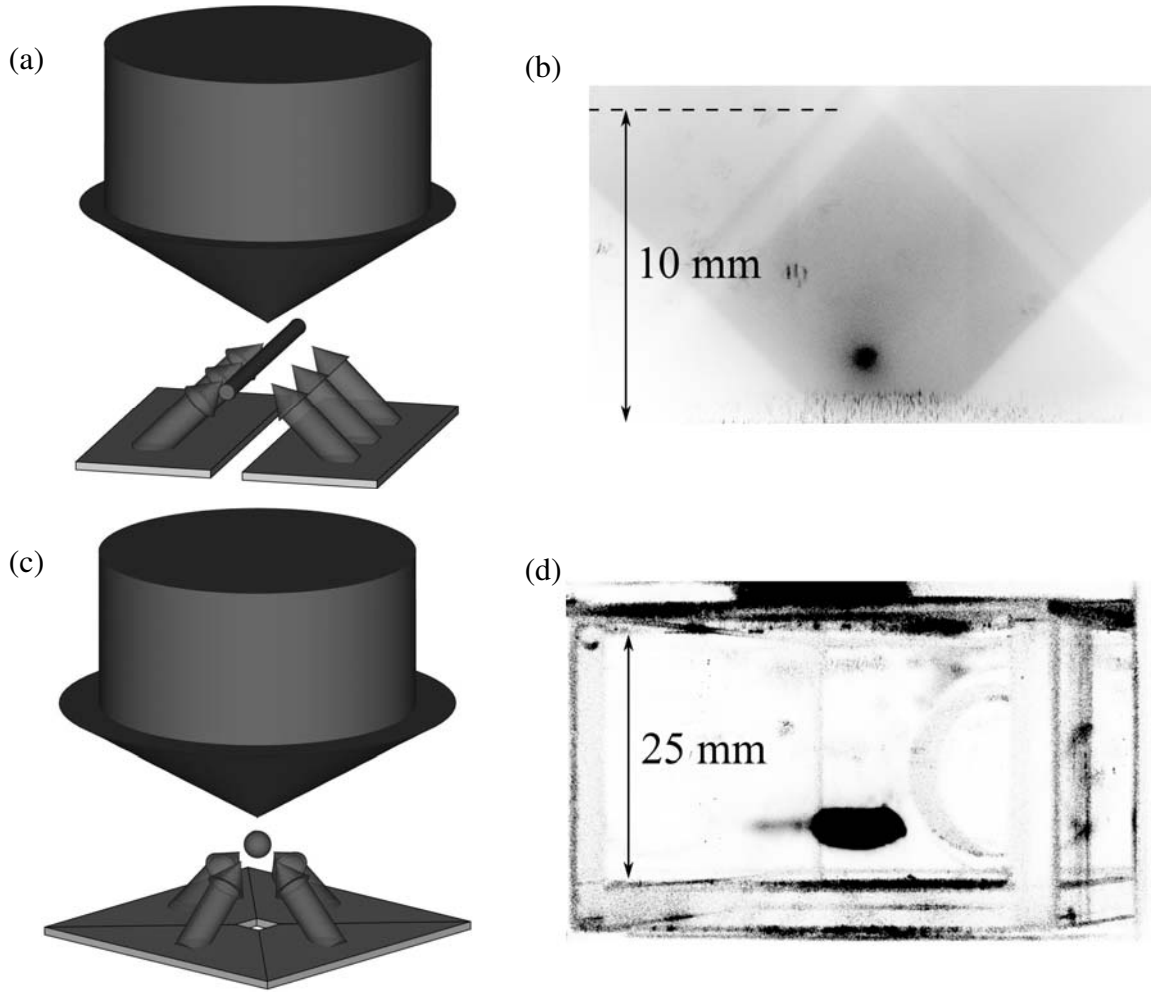

Figure 4.1: (a) A laser beam impinges on a series of diffraction gratings to form a 2D GMOT. (b) Inverted greyscale fluorescence of the 2D GMOT viewed along its axis. (c) A schematic of a 3D GMOT and (d) its corresponding inverted fluorescence image.

$$\mathcal{F}_j = \hbar \mathbf{k}_j \frac{\Gamma}{2} \frac{I_j}{I_{sat}} \sum_{m_F=-1,0,1} \frac{\alpha_{m_F}(\varphi, \hat{\boldsymbol{\epsilon}}_j)}{1 + \frac{\sum_j I_j}{I_{sat}} + \frac{4(\Delta - \mathbf{k}_j \cdot \mathbf{v} - \mu_F m_F B/\hbar)^2}{\Gamma^2}}, \tag{4.1}$$

where Γ is the natural linewidth and $\Delta = \omega_L - \omega_0$, the detuning of the laser frequency from the transition. I_{sat} is the saturation intensity and $\mu_F = g_F \mu_B$. In the limit of small Doppler and Zeeman shifts, the force becomes

$$\mathcal{F}_j \approx \hbar \mathbf{k}_j \frac{\Gamma}{2} \frac{I_j}{I_{sat}} \left[K + C \left(\mathbf{k}_j \cdot \mathbf{v} - \frac{\mu_F s}{\hbar} \frac{\mathbf{k}_j \cdot \mathbf{B}}{|\mathbf{k}_j|} \right) \right], \tag{4.2}$$

where $K = (1 + \sum_j I_j / I_{sat} + 4\Delta^2/\Gamma^2)^{-1}$, $C = 8\Delta K^2/\Gamma^2$[100].

For most MOT configurations, lasers approach the trap along the principal axes of the magnetic field. Accordingly, $|\hat{\mathbf{k}}_j \cdot \hat{\mathbf{B}}| = 1$, so trapping is optimized for pure circular polarization. In a GMOT, the wavevector of each diffracted beam is not aligned with the magnetic field. Therefore, the optimal light field does not have pure circular polarization. Gratings are selected which balance the necessary contributions of each transition to form a trap. These requirements differ between the 2D and 3D GMOT, as shown in the following.

A circularly polarized beam with intensity I_1, normally incident on a grating, will diffract upwards at an angle θ from normal ($+\hat{\mathbf{y}}$) with intensity I_{up}, as shown in Fig. 4.2. The incident beam has $\mathbf{k}_1 = -|k|\hat{\mathbf{y}}$ and s = +1, denoting pure circular polarization. The magnetic field $\mathbf{B} = G(x\hat{\mathbf{x}} - y\hat{\mathbf{y}})$ has gradient G and is centered on the beam overlap region. The resulting force from beam 1 is

$$\mathcal{F}_1 \approx -\hbar k \frac{\Gamma}{2\pi} \frac{I_1}{I_{sat}} \left[K + C \left(-k v_y - \frac{\mu_F G}{\hbar} y \right) \right] \hat{\mathbf{y}}. \tag{4.3}$$

In general, gratings do not preserve polarization. The diffracted beams will have a fractional intensity $P_+ I_{up}$ in the $s = +1$ polarization and $P_- I_{up}$ in the $s = -1$ polarization. Summing over the polarizations, the total force in $\hat{\mathbf{x}}$ is

$$\mathcal{F}_x \approx \hbar k C \Gamma \sin^2\theta \frac{I_{up}}{I_{sat}} \left(k v_x + (P_- - P_+) \frac{\mu_F G}{\hbar} x \right) \hat{\mathbf{x}}. \tag{4.4}$$

Similarly,

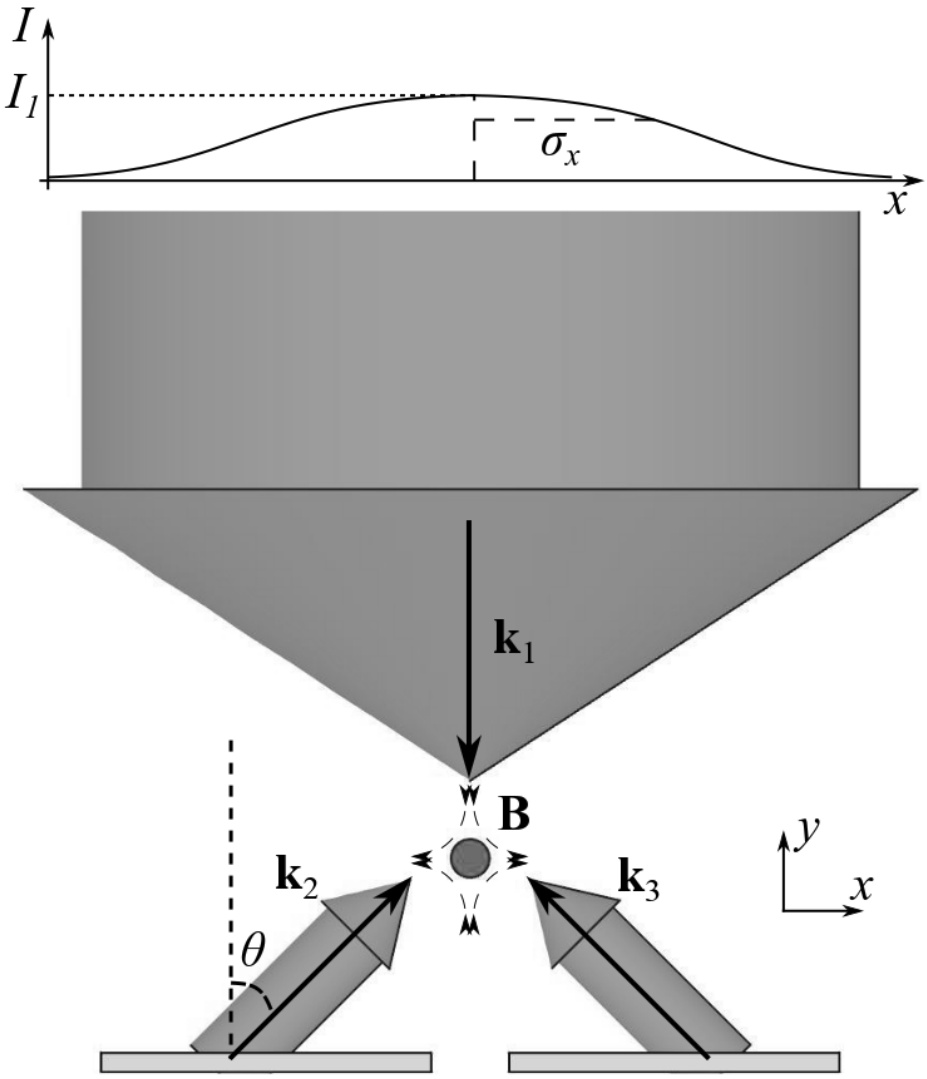

Figure 4.2: The input intensity profile, **k** vectors, and **B** field to model a 2D GMOT.

$$\begin{aligned}\mathcal{F}_y \approx\ & \hbar k \Gamma K \cos\theta \frac{I_{up}}{I_{sat}} \\ & + \hbar k \Gamma C \cos\theta \frac{I_{up}}{I_{sat}} \left(k v_y \cos\theta + 2(P_+ - P_-) \frac{\mu_F G}{\hbar} y \cos\theta \right) \\ & - \hbar k \frac{\Gamma}{2} \frac{I_1}{I_{sat}} \left[K + C \left(-k v_y - \frac{\mu_F G}{\hbar} y \right) \right] \hat{\mathbf{y}}. \end{aligned} \tag{4.5}$$

The constant terms (i.e. those $\propto K$) represent an intensity mismatch that will shift the trap center if not properly balanced. In particular, a trap will only form at the field zero if

$$I_{up} = \frac{I_1}{2\cos\theta}. \tag{4.6}$$

Then,

$$\mathcal{F}_x \approx \hbar k C \frac{\Gamma}{2}\frac{I_1}{I_{sat}}\frac{\sin^2\theta}{\cos\theta}\Big(kv_x + (P_- - P_+)\frac{\mu_F G}{\hbar}x\Big)\hat{\mathbf{x}}, \tag{4.7}$$

$$\begin{aligned}\mathcal{F}_y \approx \hbar k C \frac{\Gamma}{2}\frac{I_1}{I_{sat}}\Big(&kv_y(1+\cos\theta)\\ &+ \frac{\mu_F G}{\hbar}y\Big(1 + (P_+ - P_-)\cos\theta\Big)\Big)\hat{\mathbf{y}}.\end{aligned} \tag{4.8}$$

Note that because Δ is negative, these forces perform trapping and cooling.

Eq. (4.6) shows the ideal intensity balance between the three beams of the 2D GMOT. However, a subtle distinction separates Eq. (4.6) from the necessary grating efficiency. Gratings compress the diffracted beam area with respect to the originally incident light. Thus, a perfectly efficient grating (i.e. 100% of input power directed into the first order) would produce $I_{up} = I_1/\cos\theta$. As a result, satisfying Eq. (4.6) requires a grating efficiency of 50%, independent of θ. If not, the resulting intensity imbalance manifests as an offset in the trap location from the field zero along the axis normal to the gratings [101]. In general, for a GMOT with N diffracted beams, the ideal grating efficiency is $1/N$.

The relatively high ($1/N = 50\%$) efficiency requirements of the 2D GMOT preclude many grating types. Any grating without a preferred direction would have to diffract practically all power into the ± 1 orders. Asymmetric (e.g. blazed) gratings are therefore preferable.

Custom non-directional etched gratings have been fabricated to this standard for the 3D GMOT [84, 102, 103], albeit with considerable design time and fabrication cost. Such gratings often require e-beam lithography for small ($\approx$ 500 nm) feature sizes.

Manufacturing large area gratings requires significant time in high-demand clean room facilities, motivating our experiment to investigate the option of using replicated blazed gratings.

Replicated gratings are inexpensive and readily available, but confined to existing master gratings. Additionally, replicated gratings are not designed to minimize residual specular reflections (normal to the grating plane), which can undermine trap performance by driving anti-trapping transitions in the atoms. To avoid reflected light, GMOT systems with blazed gratings have gaps between the gratings which are aligned with the central axis of the input laser.

In addition to intensity balance, the polarization of the diffracted beams significantly effects the GMOT forces. In particular, maximizing trapping in the x direction requires $P_- = 1$ and $P_+ = 0$, as shown in Fig. 4.3(a). However, this polarization minimizes trapping in the y direction.

Fig. 4.3 shows the effect of imperfect polarization on the trapping forces by adjusting the ratio of P_+ to P_- within the 50% diffraction efficiency constraint. Fig. 4.3(a)-(d) show $(P_+, P_-) = (0, 1), (0.1, 0.9), (0.2, 0.8)$, and $(0.3, 0.7)$, respectively. The linear approximation of $\mathcal{F}_x$ from Eq. (4.7) is shown as a dashed line. The force along y increases at the expense of the x trapping strength. Equal trapping strength along each axis can be achieved for $P_- - P_+ = \cos\theta$. For the case of $\theta = 45^o$, equal trapping in the $\hat{\mathbf{x}}$ and $\hat{\mathbf{y}}$ directions is achieved for $P_- \approx 0.85$ and $P_+ \approx 0.15$.

4.3 Experimental Setup

We operate with ^{87}Rb, cooled on the $5^2S_{1/2} \rightarrow 5^2P_{3/2}$, $F = 2 \rightarrow 3$ transition at $\lambda = 780.246$ nm. Thus, Eq. (4.1) must be modified to account for a different set of m_F states and g_F factors. However, the simplified theory guides our choice of two test gratings.

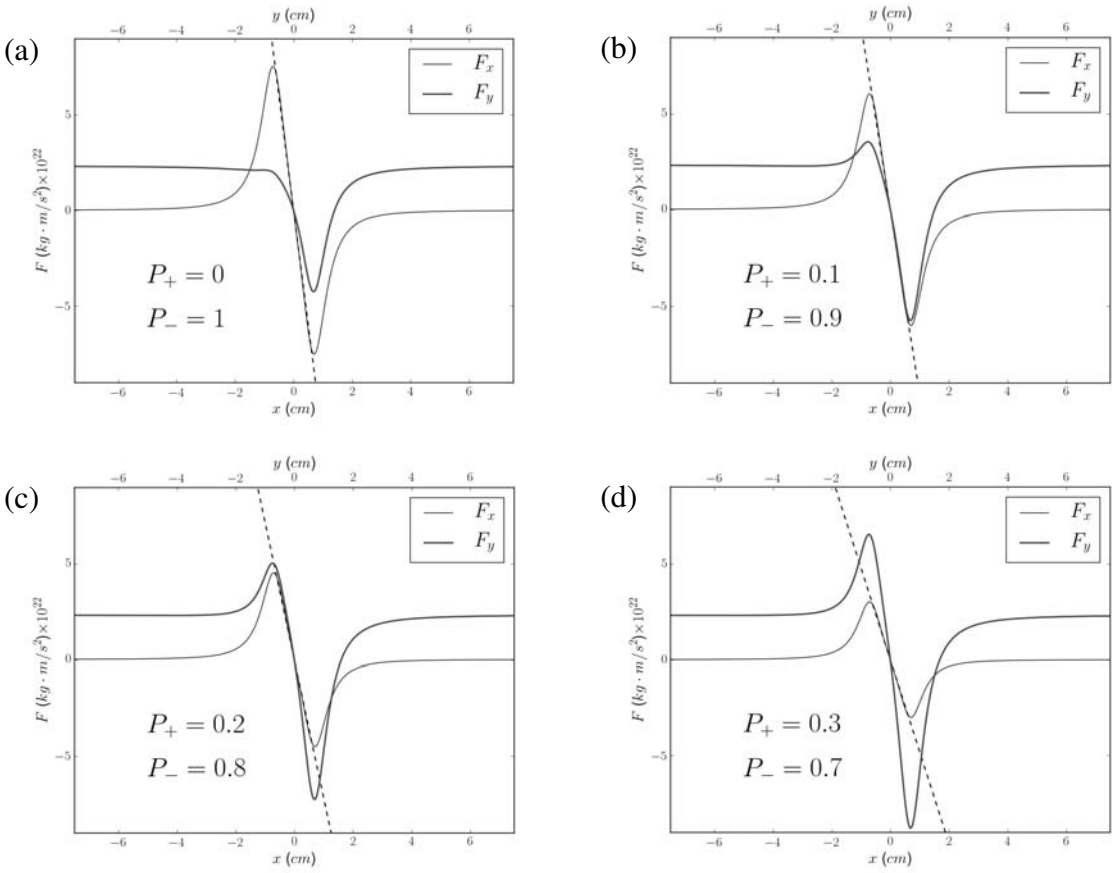

Figure 4.3: Trapping forces in a 2D GMOT for varying polarizations of the diffracted beams, assuming 50% total efficiency. Thin black curves show $\mathcal{F}_x$ and thick blue curves show $\mathcal{F}_y$. Dashed black lines are the linear approximation of $\mathcal{F}_x$ from Eq. (4.7). Plots (a)-(d) show $(P_+, P_-) = (0, 1), (0.1, 0.9), (0.2, 0.8)$, and $(0.3, 0.7)$, respectively.

Fig. 4.4 shows the theoretical diffraction efficiencies of two commercially produced ruled gratings with different groove spacings and blaze angles for the case of normal incidence. The efficiencies depend on both wavelength and incident polarization. The results for the polarization parallel and perpendicular to the groove direction combine to give the average efficiency, shown as the thick blue curve. Fig. 4.4(a) shows a grating $G1$ with 900 grooves/mm and 1000 nm blaze wavelength. At the transition, $G1$ provides equal

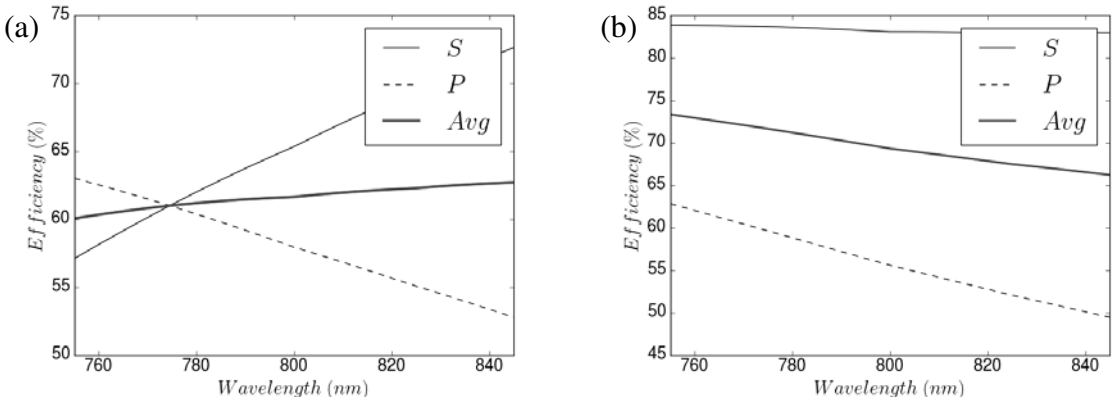

Figure 4.4: Grating efficiencies as a function of wavelength at normal incidence for two gratings of interest in magneto-optical trapping. Figure (a) shows efficiencies for grating $G1$ with 900 grooves/mm and an 1000 nm blaze wavelength, while (b) shows grating $G2$ with 830 g/mm and an 800 nm blaze.

linear polarization efficiencies near 60%. A different grating $G2$ (Fig. 4.4(b)), with 830 grooves/mm and an 800 nm blaze, diffracts a small fraction of its power into the opposing circular handedness.

Equal linear polarization should result in a circularly polarized diffracted beam. However, as discussed above, pure circular polarization does not provide equal trapping strength along each axis. $G2$'s imperfect polarization should aid trapping along the x direction. Both gratings $G1$ and $G2$ were tested but only $G2$ produces a 2D GMOT.

While $G1$ is unsuccessful in this experiment, it should be noted that the input light has a Gaussian intensity profile (see Fig. 4.2). As a result, the diffracted intensity is further diminished compared to the peak input intensity along the central axis. If the input light had a more uniform profile, we expect $G1$ to create a trap. Similarly, it is possible that $G2$ diffracts too strongly for a uniform intensity profile.

We measure the overall diffraction efficiency of $G2$ at 68% with $P_+ = 0.061$ and $P_- = 0.939$ using a Thorlabs TXP polarimeter. Because the gratings are located outside of the vacuum cell, the optical surfaces of the glass chamber modify the intensity and polarization of the diffracted beams. As a result, the overall efficiency of $G2$ drops to 64%, with $P_+ = 0.066$ and $P_- = 0.934$.

For the 2D GMOT, two 17.5×38 mm^2 rectangular gratings are placed with their blazes facing towards the central axis, separated by a 5 mm gap. For the 3D GMOT, four trapezoidal gratings are combined to produce a 38×38 mm^2 square with a 4×4 mm^2 gap at its center, as shown in Fig. 4.5. Again, all the blazes point towards the central axis. However, because the 3D gratings produce $N = 4$ diffracted beams, the 3D GMOT requires an efficiency closer to 25%. To reduce the diffracted beam power, a 0.1 ND filter is placed between the 3D gratings and the vacuum chamber wall.

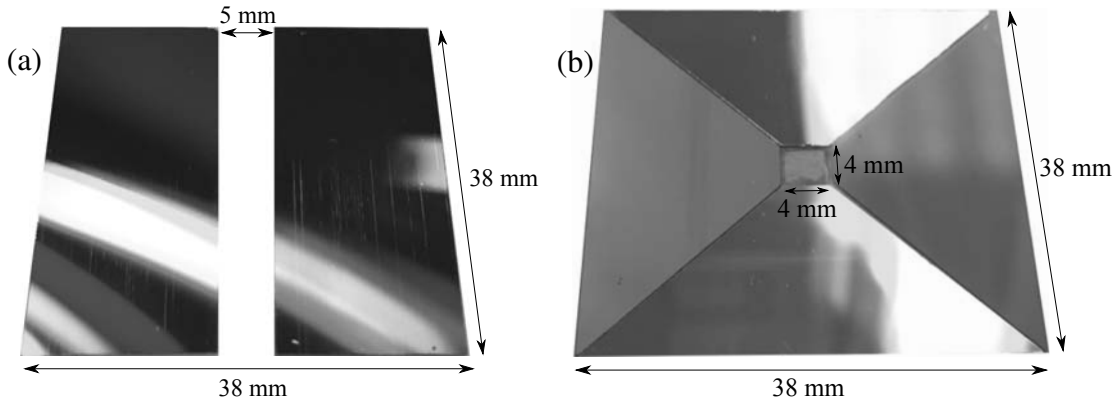

Figure 4.5: The gratings used for the (a) 2D GMOT and (b) 3D GMOT.

The experiment uses two epoxied glass vacuum cells [27] separated by a mini-conflat flange cross, as shown in Fig. 4.6. All cell walls are anti-reflection coated on both sides of the glass for 780 nm. The system pressure is 2×10^{-9} Torr as measured by a residual gas analyzer on a pumping station a few meters from the experimental chambers. The 2D

GMOT is produced in a chamber $30 \times 40 \times 72$ mm^3, which is capped by a silicon reflector with a 1 mm diameter pinhole. The atom beam travels through the pinhole, then through a second filtering (3 mm) pinhole in the copper gasket of the conflat cross. The atoms are then collected on the opposing side of the cross in a 3D GMOT in a $25 \times 40 \times 85$ mm^3 chamber.

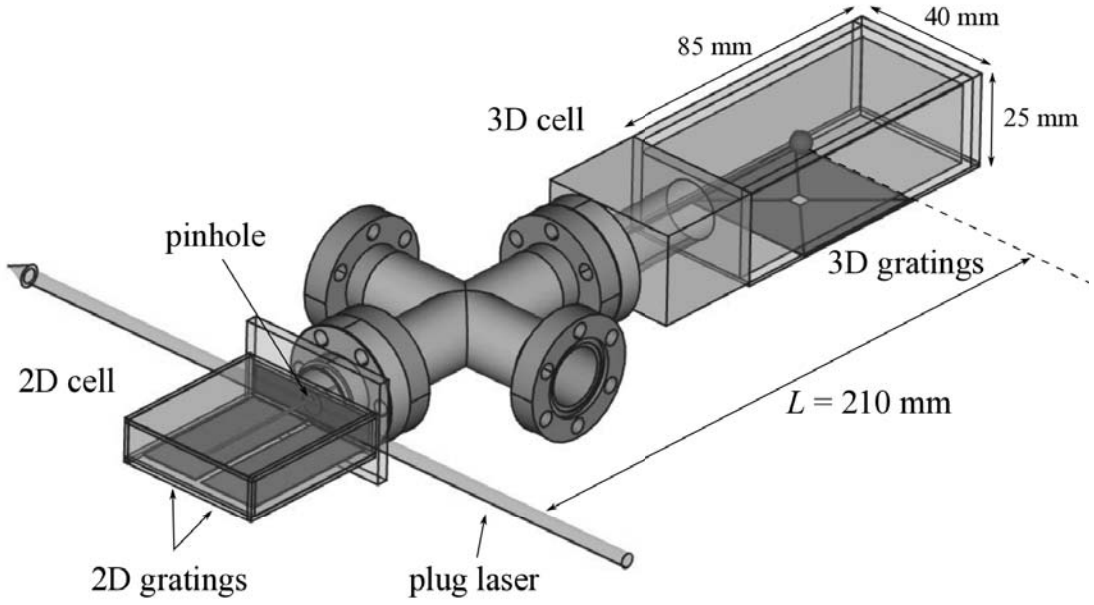

Figure 4.6: The experimental setup for a 2D GMOT loading a 3D GMOT. Input lasers, push laser, and magnetic field sources omitted for clarity.

A single cooling laser beam is input into each chamber with 11.0 mW/cm^2 light red detuned from the cycling transition and 3.8 mW/cm^2 at the repump transition for ^{87}Rb. The light is emitted from a single mode, polarization-maintaining fiber and expanded through

a negative lens. A wide-angle quarter wave plate provides circular polarization to the expanding beam, which is then reflected from a two inch mirror and collimated with a 100 mm focal length lens.

A push laser beam is directed along the 2D GMOT axis to provide enhanced cooling, using 3.3 mW of cooling light in a beam with a 4 mm waist. The beam is retro-reflected from the silicon reflector. We refer to the 2D GMOT with a push beam as a $2D^+$ GMOT.

Four permanent neodymium magnets are arranged along the corners of the $2D^+$ GMOT chamber, as was done in Fig. 2.21 and Fig. 3.8. These magnets create an extended quadrupole magnetic field with a 20 Gauss/cm gradient. They are positioned via a three axis translation stage and a tip-tilt mirror mount to aid alignment of the $2D^+$ GMOT with the silicon pinhole. The 3D GMOT magnetic fields are produced by an anti-Helmholtz coil pair, centered by cage rods that align the 3D GMOT optics. At 1.2 A current, they provide an axial gradient of 10 Gauss/cm.

4.4 Diagnostics

A more detailed description of the theory underlying this section is presented in Appendix B. The 3D GMOT fluorescence is monitored using a photodiode (Thorlabs PDA100A). Light from the GMOT is collected using a $f = 25.4$ mm lens positioned $2f$ from the trap and the sensor surface. Switching the 3D GMOT's magnetic field on produces a rising fluorescence signal proportional to the number of captured atoms. The 3D GMOT atom number $N(t)$ is approximately described by the capture rate $R_{capture}$ and trap lifetime τ_{trap}

$$N(t) = \tau_{trap} R_{capture} \left(1 - e^{-t/\tau_{trap}}\right). \tag{4.9}$$

The $2D^+$ GMOT beam is characterized by monitoring the 3D GMOT fluorescence as a function of time. An 8 mW plug laser beam is positioned just before the exit pinhole, as seen in Fig. 4.6. The plug laser acts via radiation pressure to misalign the atomic beam

from the 3D GMOT, effectively reducing $R_{capture}$. If the plug beam is turned off for a short period, the 3D GMOT will grow as atoms traverse the distance L from the exit pinhole to the capture volume of the 3D trap, as shown in Fig. 4.7.

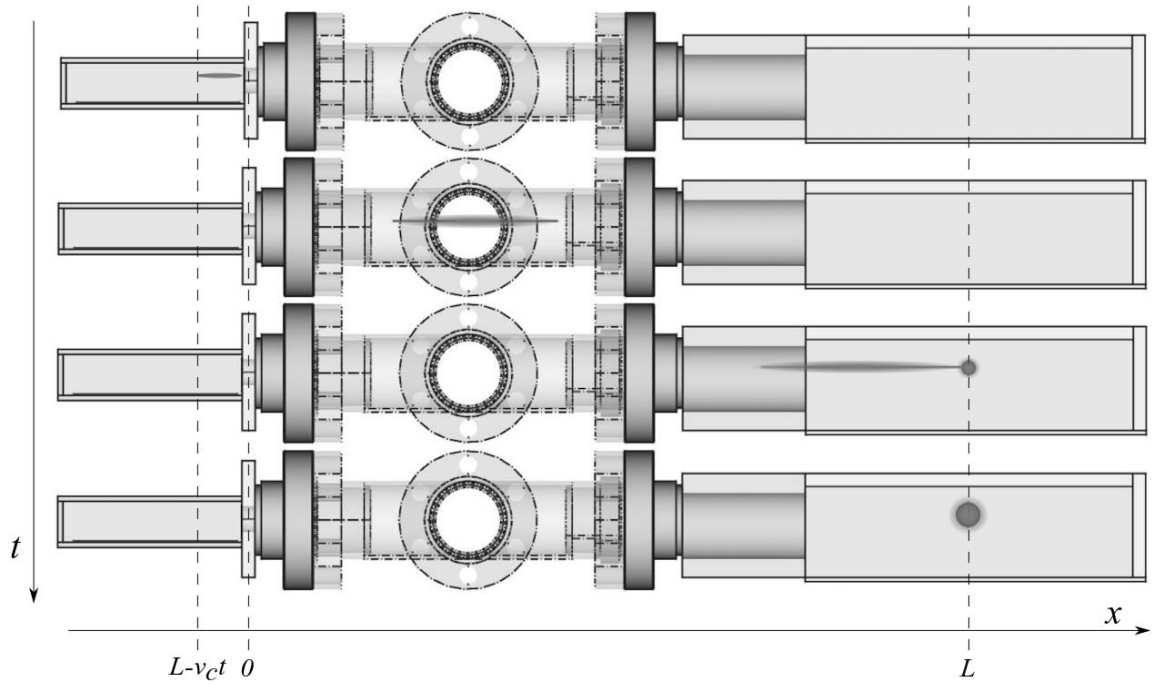

Figure 4.7: A short pulse of the $2D^+$ GMOT is released at $t = 0$, traverses a distance L, and is captured in a 3D GMOT, which grows as a function of time.

Two models are used to analyze the $2D^+$ GMOT flux using the transient response of the 3D GMOT. The first model assumes the atoms start at the exit pinhole of the 2D chamber with a singular speed v_0 and that the number of atoms reaching the capture volume per unit time is $R_{capture}$. The atom number will be zero for times $0 < t < T = L/v_0$, and then grow linearly according to

$$N(t) = R_{capture}(t - T). \tag{4.10}$$

In the second model, the $2D^+$ GMOT before the plug beam is turned off is described as a distribution of atoms in position and velocity

$$\eta(z, v) = \frac{A}{\sigma\sqrt{2\pi}} \exp\left(-\frac{(v - v_0)^2}{2\sigma^2}\right), \tag{4.11}$$

where A represents the number of atoms/m in the beam, weighted by a normal distribution in velocity with peak v_0 and spread σ. That is, the density of atoms with velocities between v_1 and v_2 is given by $A\int_{v_1}^{v_2} \exp\left[-(v - v_0)^2/2\sigma^2\right]/\sigma\sqrt{2\pi}\, dv$. The normal distribution represents a low temperature approximation of the thermal velocity distribution.

When the plug beam is turned off, the 3D GMOT grows as atoms reach the capture volume in time t with $v < v_c$, the capture velocity of the trap. For $t << \tau_{trap}$, loss terms can be neglected. Defining the exit pinhole to be at $z = 0$,

$$\begin{aligned} N(t) &= \int_{L-v_c t}^{0} \int_{(L-z)/t}^{v_c} \eta(z, v)\, dv\, dz \\ &= A\frac{\sigma t}{\sqrt{2\pi}}\left(\exp\left[-\frac{(v_0 - \frac{L}{t})^2}{2\sigma^2}\right] - \exp\left[-\frac{(v_c - v_0)^2}{2\sigma^2}\right]\right) \\ &+ \frac{A}{2}(v_0 t - L)\left(\mathrm{erf}\left[\frac{v_0 - \frac{L}{t}}{\sigma\sqrt{2}}\right] + \mathrm{erf}\left[\frac{v_c - v_0}{\sigma\sqrt{2}}\right]\right). \end{aligned} \tag{4.12}$$

The distribution $\eta(z, v)$ leads to a more experimentally useful result, the flux $\Phi(v)dv$, defined as the number of atoms exiting the pinhole at velocity v per unit time. The normal approximation for η yields

$$\Phi(v) = v\eta(z, v) = \frac{A}{\sigma\sqrt{2\pi}}\, v \exp\left(-\frac{(v - v_0)^2}{2\sigma^2}\right). \tag{4.13}$$

4.5 Results

Fig. 4.8 shows the rise in atom number when the 3D magnetic coils were switched on. The solid curve is a fit to Eq. (4.9) in which $R_{capture} = 9.97(5) \times 10^7$ atoms/s and $\tau_{trap} = 2.03(2)$ seconds. The steady state MOT number was $2.02(3) \times 10^8$ atoms. Note that

the uncertainty listed here is from the statistical fit to the data using the fluorescence to atom number calibration discussed in Appendix B. This calibration depends on several factors such as photodiode response time, temperature dependence, mechanical vibration, and faith in the manufacturer's specifications. Further, fluctuations in the power and frequency of the push beam are known to cause variations in $R_{capture}$. Thus, the atom numbers reported should be used only for order of magnitude comparisons to other MOT systems.

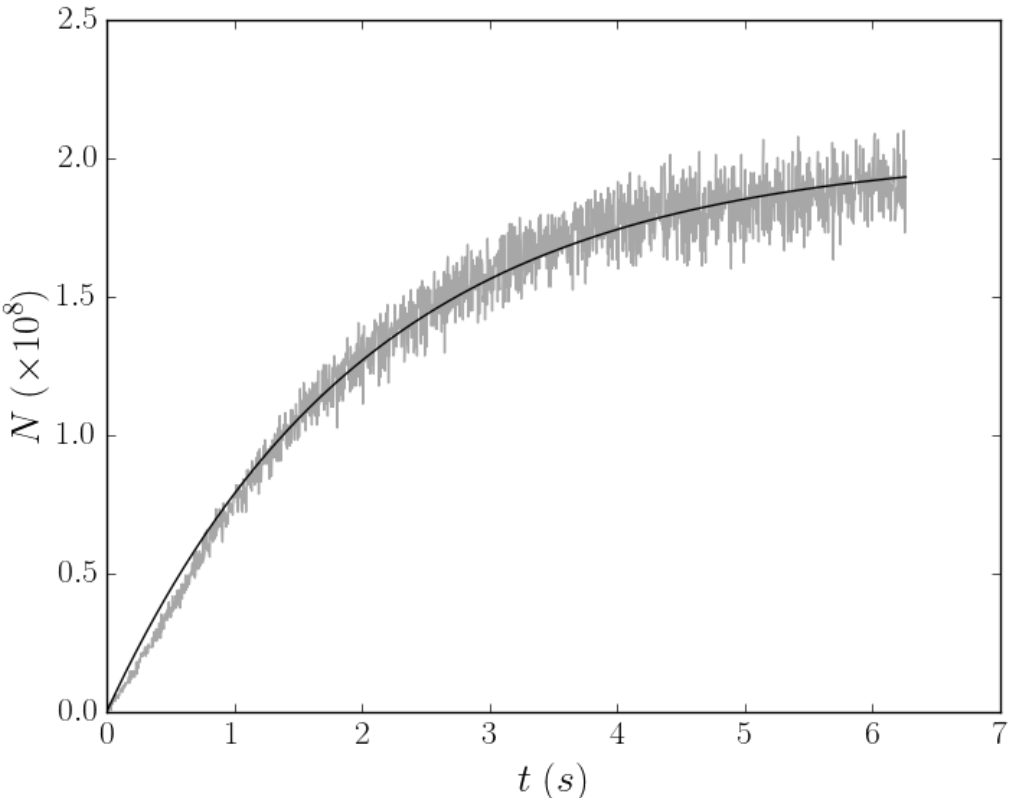

Figure 4.8: Atom number vs. time after 3D GMOT magnetic field is switched on.

The plug beam was then applied to reduce $R_{capture}$. The plug beam was turned off for 197 ms and the resulting 3D GMOT growth is shown in Fig. 4.9. The data was collected by an average of 16 independent runs and then smoothed using a centered simple moving

average. The dashed line uses Eq. (4.10) with $R_{capture} = 7 \times 10^7$ atoms/s and $T = 11.0$ ms. The solid curve is a fit using Eq. (4.12) with $A = 3.51(5) \times 10^6$ atoms/m, $\sigma = 3.3(17)$ m/s, and $v_0 = 19.0(2)$ m/s.

It should be noted that the plug beam used detuned light and did not act as a perfect shutter. Because some flux continued to feed the 3D GMOT, the reported values for $R_{capture}$ represent the fraction of atomic flux that was affected by the plug beam.

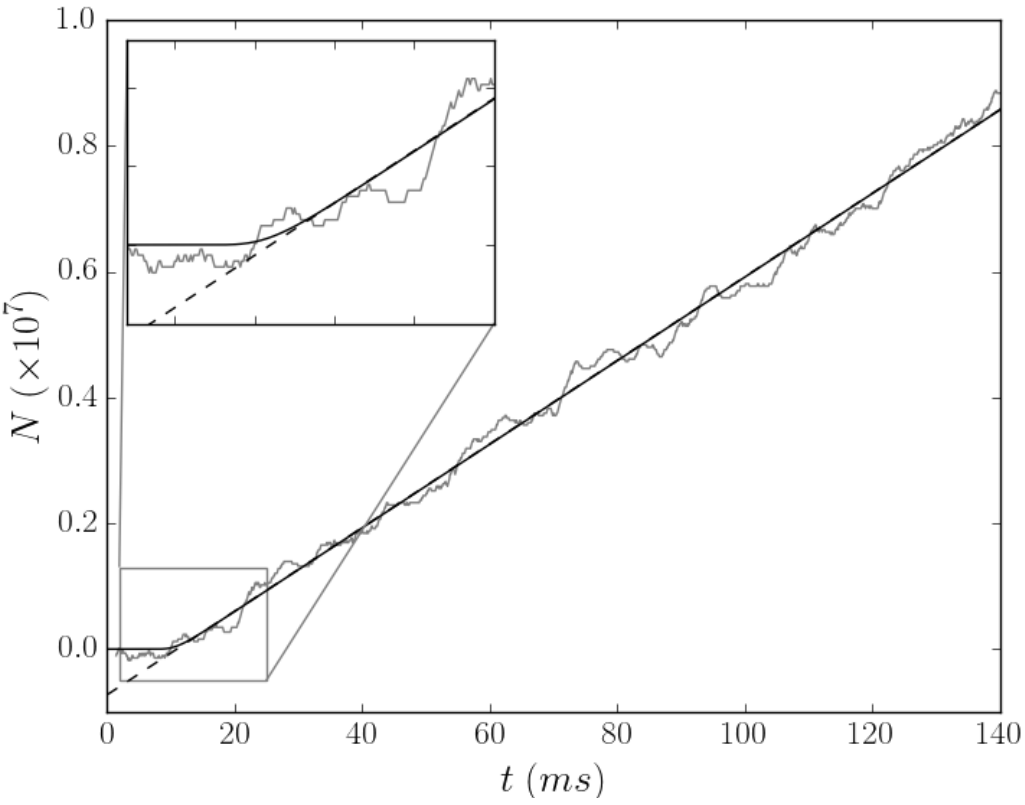

Figure 4.9: 3D GMOT atom number vs. time as plug laser beam is turned off, allowing the $2D^+$ GMOT to load the 3D GMOT. The dashed line assumes no spread in the velocity distribution of the $2D^+$ GMOT, as in Eq. (4.10). The solid curve is a fit using Eq. (4.12), which accounts for a range of velocities.

Assuming typical atom beam divergence as discussed in [99], it is likely that only $\approx$ 25% of the $2D^+$ GMOT beam actually entered the capture volume of the 3D GMOT. Using Eq. (4.13), we therefore estimate the total flux at the pinhole to be $> 4 \times 10^8$ atoms/s.

4.6 Comparisons and Outlook

Traditional $2D^+$ MOT's have typical flux values near 10^9 atoms/s [99], and in extreme cases are as high as 10^{11} atoms/s [104]. However, high flux $2D^+$ MOT's form across 10 cm lengths or higher and saturate with laser intensities near 20 mW/cm^2. By comparison, the $2D^+$ GMOT reported here forms over a length of several mm with 11 mW/cm^2 laser intensity. The short beam length is expected, as circular Gaussian beams cause the input intensity profile to vary significantly, limiting the range over which optimal cooling parameters are achieved. Future work will employ beam shaping techniques to create a top hat intensity profile within the trap region. A top hat intensity profile will also help make more effective use of available laser power.

Increasing the $2D^+$ GMOT length allows atoms with higher longitudinal velocities to be collimated into the MOT beam [104–106]. Assuming the pressure is low enough that collisions are negligible, the flux should scale linearly with increased length.

Both the $2D^+$ GMOT and 3D GMOT should benefit from higher laser intensity, which acts to raise the capture velocity. Prior work has shown that $2D^+$ GMOT flux is maximal near 20 mW/cm^2, while the 3D GMOT atom number saturates with input intensities near 50 mW/cm^2 [84]. Both are significantly higher than the maximal 11 mW/cm^2 produced by our laser system. Despite the difference, the loaded 3D GMOT described here shows the highest atom number reported so far in a grating based system, likely due to the improved vacuum quality of the 3D GMOT chamber.

These results encourage further development and integration of gratings into future cold atom experiments. In particular, gratings are easily integrated into atom chip designs, in which magnetic fields are created with currents on microchips instead of large coil-based

systems. GMOTs specifically aid alignment of atomic clouds with small chip features, further suggesting their use in field-deployable devices.

Page intentionally left blank

V. State-Preparation: Planar Sources of Uniform Fields

5.1 Introduction

As seen in Chapter 2, two magnetic field types are particularly necessary for cold atom systems. First, the MOT requires a linear field with gradient G that extends over the capture volume of the trap. In two dimensions, such a field can be written as

$$\mathbf{B}_{2D} = G\left(y\hat{\mathbf{y}} - z\hat{\mathbf{z}}\right), \tag{5.1}$$

called a 2D quadrupole. In three dimensions, the field is

$$\mathbf{B}_{3D} = G\left(x\hat{\mathbf{x}} + y\hat{\mathbf{y}} - 2z\hat{\mathbf{z}}\right), \tag{5.2}$$

called a 3D quadrupole. Second, PGC can only operate when the Zeeman energy shift is less than the AC Stark shift. Thus, a uniform field must be applied to cancel background Earth and laboratory fields. If the stray background field points in some unknown direction $\hat{\boldsymbol{\epsilon}}_B$, then the uniform field must be

$$\mathbf{B}_{uniform} = -C_B\hat{\boldsymbol{\epsilon}}_B, \tag{5.3}$$

for some constant C_B. By far, the most common route to satisfy these requirements is the Helmholtz/Anti-Helmholtz coil pair, introduced below.

Consider two coaxial coils of radius R_{coil} with $\mathcal{N}$ turns and current I_{coil} placed at $z = \pm D/2$, as seen in Fig. 5.1. The field along the $\hat{\mathbf{z}}$ axis is

$$\mathbf{B}_z = \frac{\mu_0 \mathcal{N} I_{coil} R_{coil}^2}{2}\left[\frac{1}{\left[R_{coil}^2 + (z - D/2)^2\right]^{3/2}} + \frac{1}{\left[R_{coil}^2 + (z + D/2)^2\right]^{3/2}}\right]\hat{\mathbf{z}}. \tag{5.4}$$

To determine the separation D that creates a uniform field over the largest volume possible, Taylor expand around the point $z = 0$,

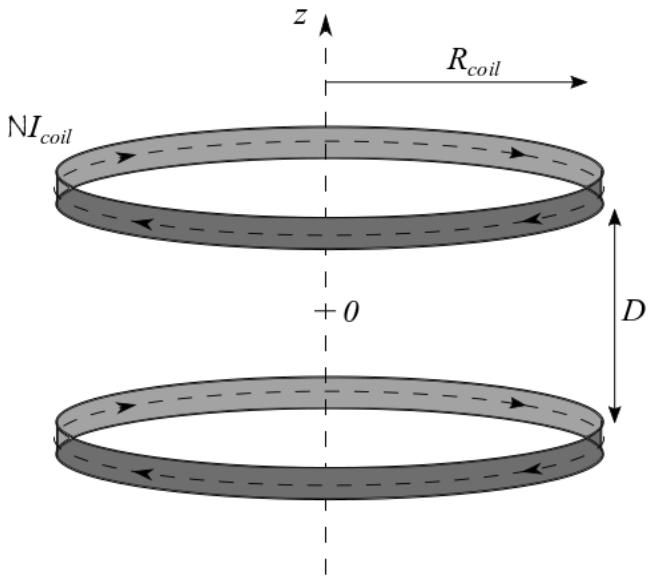

Figure 5.1: Two coils with equal current separated by a distance D produce a magnetic field along their common axis. The most uniform field between the coils is found by the Helmholtz condition that $D = R_{coil}$.

$$B_z(z) \approx B_z\Big|_{z=0} + \frac{dB_z}{dz}\Big|_{z=0} z + \frac{1}{2}\frac{d^2B_z}{dz^2}\Big|_{z=0} z^2 + \frac{1}{6}\frac{d^3B_z}{dz^3}\Big|_{z=0} z^3 + \cdots \tag{5.5}$$

where

$$\begin{aligned}
B_z\Big|_{z=0} &= \frac{\mu_0 \mathcal{N} I_{coil} R_{coil}^2}{\left[R_{coil}^2 + (D/2)^2\right]^{3/2}}, \\
\frac{dB_z}{dz}\Big|_{z=0} &= 0, \\
\frac{d^2B_z}{dz^2}\Big|_{z=0} &= -\frac{\mu_0 \mathcal{N} I_{coil}}{2}\frac{6(R_{coil}^2 - D^2)}{\left[R_{coil}^2 + (D/2)^2\right]^{7/2}}, \\
\frac{d^3B_z}{dz^3}\Big|_{z=0} &= 0.
\end{aligned} \tag{5.6}$$

Clearly, the second derivative is zero when $D = R_{coil}$, known as the Helmholtz condition. Then, the field is uniform to fourth order, or $(z/R_{coil})^4 << 1$, with $B_z\Big|_{z=0} = \mu_0 \mathcal{N} I_{coil}/(5/4)^{3/2}R$.

To create the 3D quadrupole field, suppose the coil at $z = -D/2$ carries current $-I_{coil}$. Then,

$$\begin{aligned}
B_z\Big|_{z=0} &= 0, \\
\frac{dB_z}{dz}\Big|_{z=0} &= \frac{\mu_0 \mathcal{N} I_{coil} R_{coil}^2}{2} \frac{3D}{\left[(D/2)^2 + R_{coil}^2\right]^{5/2}}, \\
\frac{d^2B_z}{dz^2}\Big|_{z=0} &= 0, \\
\frac{d^3B_z}{dz^3}\Big|_{z=0} &= -\frac{\mu_0 \mathcal{N} I_{coil} R_{coil}^2}{2} \frac{15D\left(3R_{coil}^2 - D^2\right)}{\left[(D/2)^2 + R_{coil}^2\right]^{9/2}}.
\end{aligned} \tag{5.7}$$

Applying the Helmholtz condition to this situation creates what are called anti-Helmholtz coils. The resulting field is only linear to third order, or $(z/R_{coil})^3 << 1$.

Typical large MOT capture volumes are $\sim$ 8 cm^3, so an anti-Helmholtz coil with $R_{coil} \approx 5$ cm is usually sufficient. An equal-sized Helmholtz pair provides a uniform field over a $\sim$ 12 cm^3 volume, more than necessary for PGC.

Due to its simplicity, the Helmholtz coil pair is seen across a broad swath of scientific endeavors. Silicon crystal growth, electron microscopy, and magnetic resonance imaging are just a few applications that use either Helmholtz coils or their more engineered cousins, to be described below.

Unfortunately, coils do have drawbacks. Active cooling is difficult, limiting the currents that can be used, and therefore the magnetic field strength. Prior versions of the AFRL cold atom sensor pumped externally chilled water through hollow copper coils to raise the field capacity. In some applications, strong fields require superconducting wire. Specialized structures are developed to funnel liquid nitrogen or helium through the device.

In addition, each coil pair produces a uniform field along one axis only. To create a magnetic field of arbitrary direction, three coil pairs are nested along each of the cardinal axes, as shown in Fig 5.2. If the innermost pair must fit around an obstruction, such as a

vacuum chamber, coils often define the maximal required size of the system. The coil nest also significantly blocks optical and experimental access.

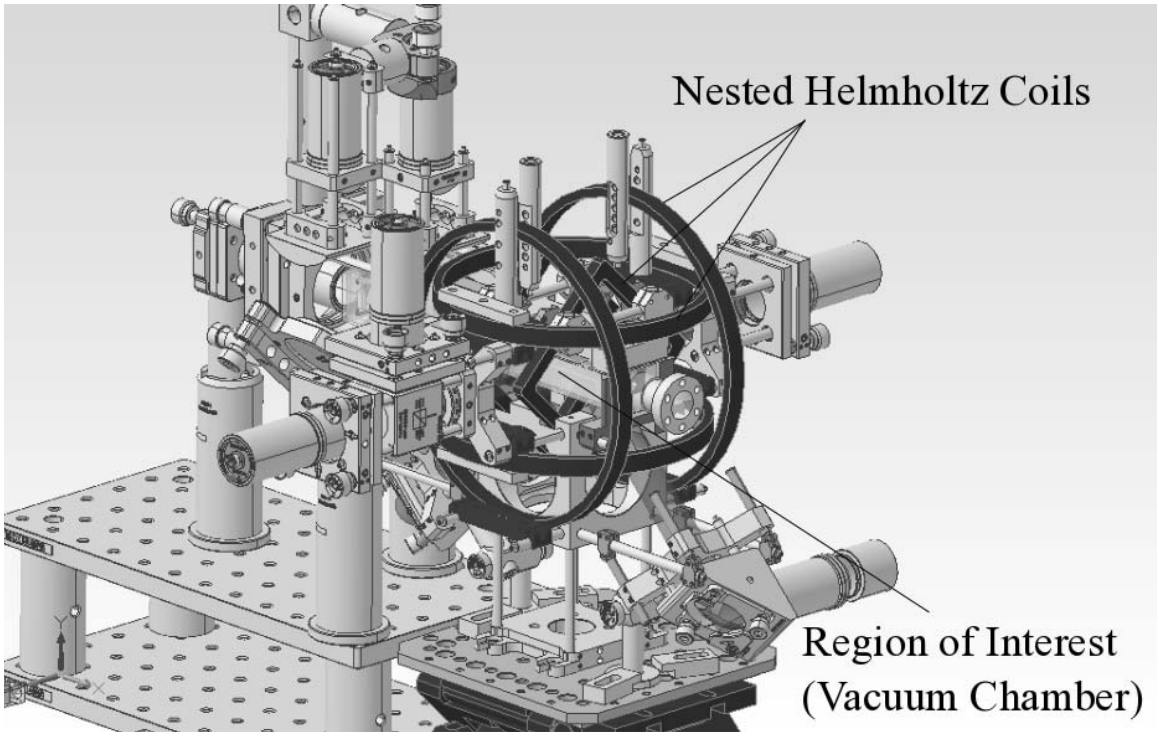

Figure 5.2: Three orthogonal Helmholtz coils nested around the vacuum chamber of the AFRL cold atom sensor. Space limitations require the innermost pair to be approximated by square coils.

Recognizing these challenges, we wondered if all the necessary magnetic fields of our experiment could be formed by a combination of atom chips. Chips can be actively cooled with a series of well-tested electronics techniques (e.g. thermal paste, thermo-electric coolers, cold plates). The added weight of additional chips is minimal compared to the equivalent coils. Chips are comparatively less labor-intensive to fabricate. Finally, optical access is opened to all but one surface of the vacuum chamber.

To motivate the creation of uniform and linear gradient fields from planar structures, a more general consideration of coil-based magnetic field sources is introduced. Using a similar framework, we optimize, design, and test chips that produce uniform **B** fields of arbitrary direction to the same mathematical order as the Helmholtz pair. Similarly, chips are shown to generate equivalent linear gradient fields to the anti-Helmholtz pair. Then, a magnetic trap conveyor is proposed that does not require an externally-supplied uniform field. The conveyor is capable of three-dimensional translation of the atom cloud using only three independent currents.

5.2 Multipole Expansion of the Axially Symmetric Magnetic Field

In 1951, Milan Garrett detailed methods to create precision fields in axially symmetric (e.g. coil) systems [107, 108]. His derivations show that the Helmholtz (anti-Helmholtz) coil pair is just one of a class of configurations to produce uniform (linear gradient) fields. His methods are summarized to motivate later derivations for planar systems.

5.2.1 Field Equations

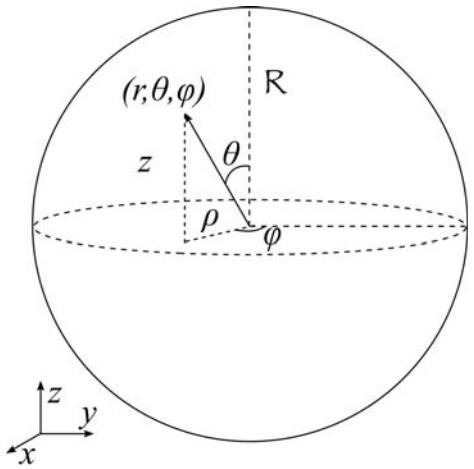

Figure 5.3: Coordinate and variable definition for analysis of axially symmetric fields.

Consider a spherical coordinate system with points defined by (r, θ, φ), as seen in Fig. 5.3. Alternatively, points can be described in cylindrical coordinates by (ρ, φ, z), where $\rho = r \sin\theta$ and $z = r\cos\theta$. Static magnetic fields are generated by currents I_{coil} with $\mathcal{N}$ turns around a common axis of revolution $\hat{\mathbf{z}}$. These currents lie on the surface of an imaginary sphere of radius $\mathcal{R}$, depicted in Fig. 5.4.

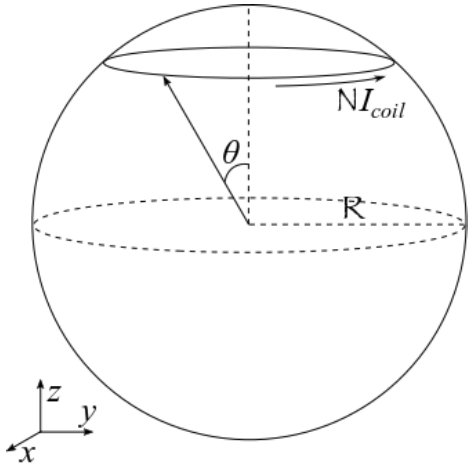

Figure 5.4: A single coil with $\mathcal{N}$ turns and current I_{coil} on a sphere of radius $\mathcal{R}$ produces a field described by associated Legendre polynomials with coefficients h_n.

For $r \neq \mathcal{R}$,

$$\nabla \times \mathbf{B} = 0, \tag{5.8}$$

implying the existence of a magnetic scalar potential ζ such that

$$\mathbf{B} = -\nabla\zeta. \tag{5.9}$$

The axial symmetry implies ζ is independent of φ and equal to

$$\zeta(r,\theta) = \mathcal{R}\sum_{n=1}^{\infty}\frac{h_n}{n+1}\left(\frac{\mathcal{R}}{r}\right)^{n+1}P_n(\cos\theta), \quad r > \mathcal{R}$$
$$\zeta(r,\theta) = -\mathcal{R}\sum_{n=1}^{\infty}\frac{h_n}{n}\left(\frac{r}{\mathcal{R}}\right)^{n}P_n(\cos\theta), \quad r < \mathcal{R} \tag{5.10}$$

where $P_n(\cos\theta)$ are the Legendre polynomials and h_n are coefficients defined by the boundary conditions.

The scalar potential gives the magnetic field along $\hat{\mathbf{z}}$ and $\hat{\boldsymbol{\rho}}$ as

$$(a)\ \mathbf{B}_z(r,\theta) = \sum_{n=1}^{\infty}h_n\left(\frac{\mathcal{R}}{r}\right)^{n+2}P_{n+1}(\cos\theta)\,\hat{\mathbf{z}}, \quad r > \mathcal{R}$$
$$(b)\ \mathbf{B}_z(r,\theta) = \sum_{n=1}^{\infty}h_n\left(\frac{r}{\mathcal{R}}\right)^{n-1}P_{n-1}(\cos\theta)\,\hat{\mathbf{z}}, \quad r < \mathcal{R}$$
$$(c)\ \mathbf{B}_\rho(r,\theta) = -\sum_{n=1}^{\infty}\frac{h_n}{n+1}\left(\frac{\mathcal{R}}{r}\right)^{n+2}P^1_{n+1}(\cos\theta)\,\hat{\boldsymbol{\rho}}, \quad r > \mathcal{R}$$
$$(d)\ \mathbf{B}_\rho(r,\theta) = \sum_{n=2}^{\infty}\frac{h_n}{n}\left(\frac{r}{\mathcal{R}}\right)^{n-1}P^1_{n-1}(\cos\theta)\,\hat{\boldsymbol{\rho}}, \quad r < \mathcal{R} \tag{5.11}$$

where $P^1_n(\cos\theta)$ are associated Legendre polynomials of degree n and order 1. Each coil, located on the sphere by θ_i, has source coefficients

$$h_n = -\frac{\mu_0 \mathcal{N} I_{coil}}{2\mathcal{R}}\sin\theta_i P^1_n(\cos\theta_i), \tag{5.12}$$

for positive integers n.

5.2.2 Uniform Axial Fields

A uniform axial field through the $(n_{max}-1)$ order is defined as $h_1 \neq 0$ and $h_n = 0$ for $1 < n \leq n_{max}$. If so, the field is constant within a radial volume $(r/\mathcal{R})^{n_{max}-1} << 1$, as seen in Eq. (5.11)(b). Place $M/2$ equal current coils on the sphere such that

$$P^1_{M+1}(\cos\theta) = 0, \tag{5.13}$$

and place $M/2$ more coils symmetrically below the equator. Then $n_{max} = 2M + 1$. That is, the field will be uniform through the $2M^{th}$ order.

For the Helmholtz case of $M = 2$, Eq. (5.13) implies $\cos\theta = 1/\sqrt{5}$. The radius of each coil is then

$$R_{coil} = \rho = \frac{2\mathcal{R}}{\sqrt{5}}, \tag{5.14}$$

while the height of the coil above the equator is

$$z = \frac{\mathcal{R}}{\sqrt{5}}. \tag{5.15}$$

The coil below the equator is found at $-z$, implying the total separation is $2z = 2\mathcal{R}/\sqrt{5} = R_{coil}$, as seen in Fig. 5.5. Note these results match the Helmholtz condition, $R_{coil} = D$.

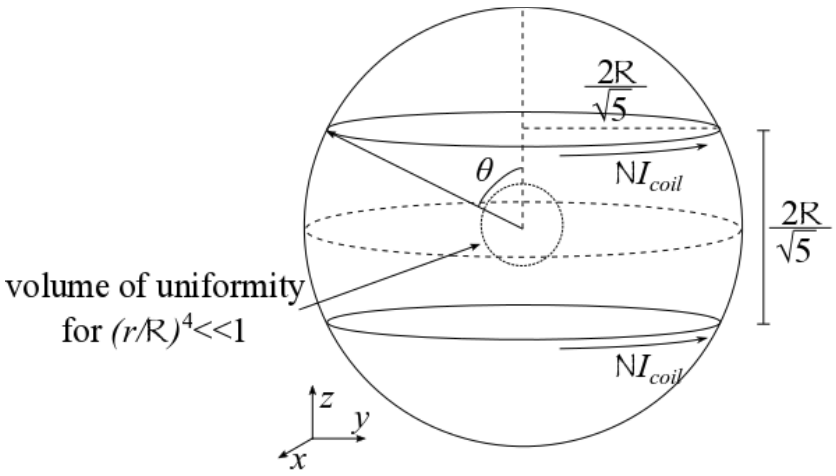

Figure 5.5: The Helmholtz pair making a uniform field for volume $(r/\mathcal{R})^4 << 1$, shown as a special case of coils placed on a sphere of radius $\mathcal{R}$.

Clearly, the Helmholtz coil pair is a specific case of a broader method to create uniform fields. Indeed, various combinations can be found throughout literature, including the Maxwell's coils ($M = 3$) [109], McKeehan's coils ($M = 4$) [110], and Sauter's coils ($M = 6$) [111].

5.2.3 Linear Gradient Fields

In Garrett's approach, the linear gradient magnetic field requires coils below the equator to carry negative current. In order to set $h_1 = 0$, $h_2 \neq 0$, and $h_n = 0$ for $2 < n \leq n_{max}$, place $M/2$ coils above the equator such that

$$P^1_{M+2}(\cos\theta) = 0. \tag{5.16}$$

Then, the first non-zero coefficient other than the linear term is h_{2M+2}. Note in particular that the coil locations for the linear gradient field are not the same as those found for the uniform field.

5.3 Analogous Expansion for a Planar System

Garrett's method requires coil pairs symmetrically placed about the equator of an imaginary sphere. Similarly, our method requires parallel, co-planar, infinite wire pairs be symmetric about a common axis. These pairs create uniform or linear gradient fields by successively eliminating undesired orders of the field expansion.

To begin, consider the magnetic field of a single infinite wire parallel to $\hat{\mathbf{x}}$ located at $(y, z) = (bd, d)$ with current I_p,

$$\mathbf{B} = \frac{\mu_0 I_p}{2\pi}\left[f(y,z)\hat{\mathbf{y}} + g(y,z)\hat{\mathbf{z}}\right], \tag{5.17}$$

where

$$\begin{aligned} f(y,z) &= \frac{-(z-d)}{(y-bd)^2 + (z-d)^2} \\ g(y,z) &= \frac{y-bd}{(y-bd)^2 + (z-d)^2}. \end{aligned} \tag{5.18}$$

A two-dimensional Taylor expansion around $(y, z) = (0, 0)$ gives

$$f(y,z) \approx \frac{1}{d(1+b^2)} + \frac{2b}{d^2(1+b^2)^2}y + \frac{1-b^2}{d^2(1+b^2)^2}z + \frac{1}{2}\left[\frac{6b^2-2}{d^3(1+b^2)^3}y^2 + 2\frac{2b(3-b^2)}{d^3(1+b^2)^3}yz - \frac{6b^2-2}{d^3(1+b^2)^3}z^2\right] + \cdots$$
$$g(y,z) \approx \frac{-b}{d(1+b^2)} + \frac{1-b^2}{d^2(1+b^2)^2}y - \frac{2b}{d^2(1+b^2)^2}z + \frac{1}{2}\left[\frac{2b(3-b^2)}{d^3(1+b^2)^3}y^2 - 2\frac{6b^2-2}{d^3(1+b^2)^3}yz - \frac{2b(3-b^2)}{d^3(1+b^2)^3}z^2\right] + \cdots \tag{5.19}$$

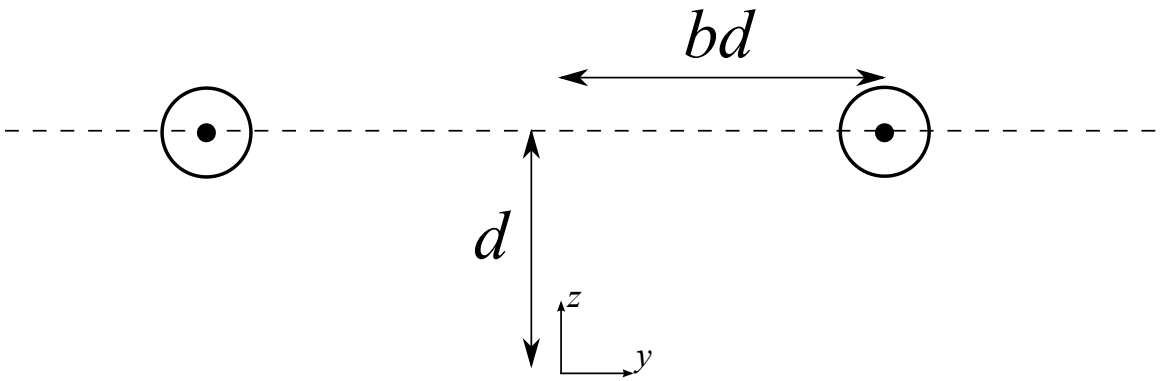

Figure 5.6: A pair of co-propagating currents in the $z = d$ plane at locations $y = \pm bd$.

Clearly, several terms have similar coefficients. If two wires with equal currents are placed at $y = \pm bd$, as seen in Fig. 5.6, each wire produces its own Taylor series like Eq. 5.19. The total field adds these two series together, resulting in greatly simplified expressions for the $\hat{\mathbf{y}}$ and $\hat{\mathbf{z}}$ field components,

$$f_{++}(y,z) \approx \frac{2}{d(1+b^2)} + \frac{2(1-b^2)}{d^2(1+b^2)^2}z + \frac{2(3b^2-1)}{d^3(1+b^2)^3}(y^2-z^2) + \cdots, \tag{5.20}$$
$$g_{++}(y,z) \approx \frac{2(1-b^2)}{d^2(1+b^2)^2}y - \frac{4(3b^2-1)}{d^3(1+b^2)^3}yz + \cdots. \tag{5.21}$$

Similarly, if the wire at $y = +bd$ carries positive current, and the wire at $y = -bd$ carries negative current, then

$$f_{-+}(y,z) \approx \frac{4b}{d^2(1+b^2)^2}y - \frac{4b(b^2-3)}{d^3(1+b^2)^3}(yz) + \cdots, \tag{5.22}$$

$$g_{-+}(y,z) \approx -\frac{2b}{d(1+b^2)} - \frac{4b}{d^2(1+b^2)^2}z - \frac{2b(b^2-3)}{d^3(1+b^2)^3}(y^2-z^2) + \cdots. \tag{5.23}$$

Thus, at the origin, co-propagating current pairs create purely $\hat{\mathbf{y}}$ fields while counter-propagating pairs create purely $\hat{\mathbf{z}}$ fields. But this logic can be taken further. The $\hat{\mathbf{y}}$ field can be made uniform to second order by choosing $b = 1$. Naïvely, the same could be said for selecting $b = 0$ for the $\hat{\mathbf{z}}$ field. However, that case is trivial because then the two counter-propagating currents cancel.

Using two wire pairs with spacings b_1 and b_2, a non-trivial solution can be constructed for the $\hat{\mathbf{z}}$ field. Assuming the first pair has current I_p and the second pair has current $-I_p$, the $\hat{\mathbf{z}}$ field is uniform to second order in y and z if

$$\frac{4b_1}{d^2(1+b_1^2)^2}y - \frac{4b_2}{d^2(1+b_2^2)^2}y = 0$$

$$\rightarrow b_1^4(-b_2) + b_1^2(-2b_2) + b_1(1+2b_2^2+b_2^4) - b_2 = 0. \tag{5.24}$$

The solutions to this quartic equation in b_1 are lengthy and do not significantly contribute to this discussion. Rather, we postulate that generally for $N+1$ wire pairs, N orders can be non-trivially eliminated. This statement is not proven, though it is strongly suggested by our similar work examining one-dimensional fields [26].

5.4 Manipulating Fields From Planar Sources

5.4.1 Uniform ŷ Fields Through Second Order

Having shown the first order field can be eliminated with two wire pairs, consider the requirements for creating a uniform $\hat{\mathbf{y}}$ field through the second order ($N = 2$). Accordingly, $N + 1 = 3$ wire pairs are needed. The corresponding conditions are

$$\sum_{i=1}^{3} I_i \left(\frac{1}{1+b_i^2} \right) \neq 0,$$
$$\sum_{i=1}^{3} I_i \left(\frac{(1-b_i^2)}{(1+b_i^2)^2} \right) = 0,$$
$$\sum_{i=1}^{3} I_i \left(\frac{3b_i^2-1}{(1+b_i^2)^3} \right) = 0. \tag{5.25}$$

In rectilinear coordinates, solving this system analytically is not tractable. While we expect a cleaner formulation exists in cylindrical functions, our coordinates more closely match the planar system's geometry. Many solutions are easily found using numerical methods. Which solution to choose depends on the particular application.

In this case, the uniform field is generated by an atom chip, so overall size is a factor. Thus, b_i is arbitrarily required to be less than three. Also, in order to control the $\hat{\mathbf{y}}$ field with a single power supply, all currents are set to equal magnitude, $|I_i| = I_p$. Initial solutions had difficulty with the $b = 0$ case, which implies a single wire of current $2I_p$. Instead, a central wire with current I_p is placed at $b = 0$. Under these constraints, searching for the maximal field strength gives the spacings

$$(b_1, b_2, b_3) = (0, 0.431, 0.869),$$

for currents

$$(I_1, I_2, I_3) = I_p(-1/2, 1, -1).$$

The resulting field has strength

$$B_z^{(0)} = \frac{\mu_0}{2\pi} \sum_{i=1}^{4} \frac{I_i}{d} \frac{2}{1+b_i^2} = 0.23 \frac{\mu_0 I_p}{\pi d}. \tag{5.26}$$

This solution is illustrated in Fig. 5.7(a), which shows a contour plot of the magnetic field strength. The locations of the wires (white circular regions along $z/d = -1$) are seen

with respect to the region over which uniformity is achieved (dashed box). The volume of interest is shown more clearly in Fig. 5.7(b), where each side is of length d.

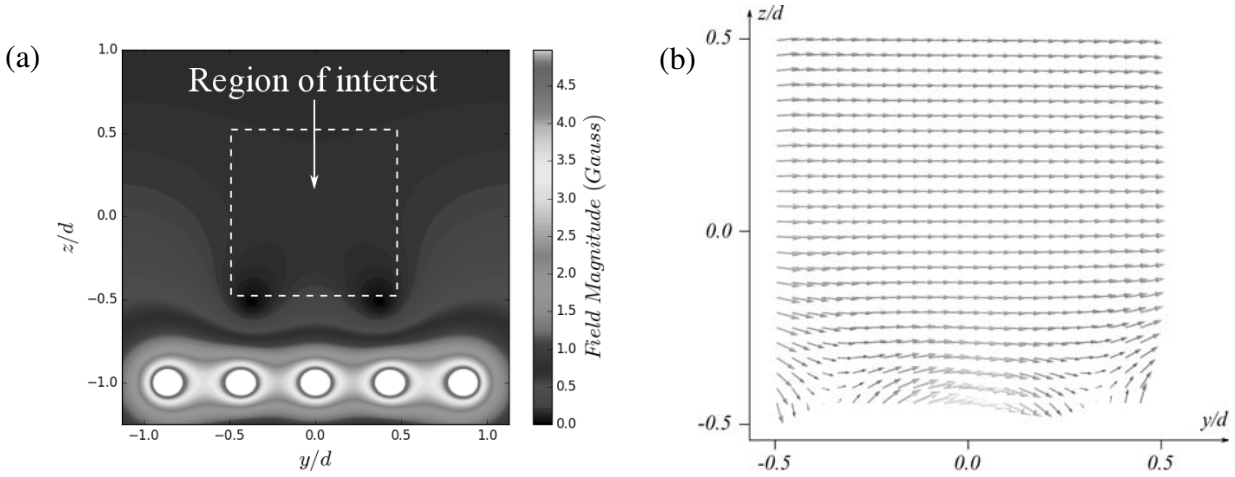

Figure 5.7: (a) A contour plot of the planar system to produce a uniform $\hat{\mathbf{y}}$ field. The wires are the white circular regions along the lower section of the plot, while dashed box shows the central region over which the field is uniform. A zoomed in vector plot of the region of interest is shown in (b). The plots use $I_p = 1$ A.

Another method of visualizing this process is shown in Fig. 5.8. In Fig. 5.8(a), the common coefficient of the first order

$$c^{(1)}(b) = I_i \frac{(1-b^2)}{(1+b^2)^2}$$

is plotted as a solid curve for $I_i = I_p$. The dashed curve presents the case of $I_i = -I_p$. Each point represents a single wire pair in the given solution. The $b = 0$ wire lies on a dotted curve representing $I_i = -I_p/2$ in accordance with the constraints given above. Note that the three individual wire coefficients sum to zero. Fig. 5.8(b) repeats the process for the

common coefficient of the second order

$$c^{(2)}(b) = I_i \frac{3b_i^2 - 1}{(1 + b_i^2)^3}.$$

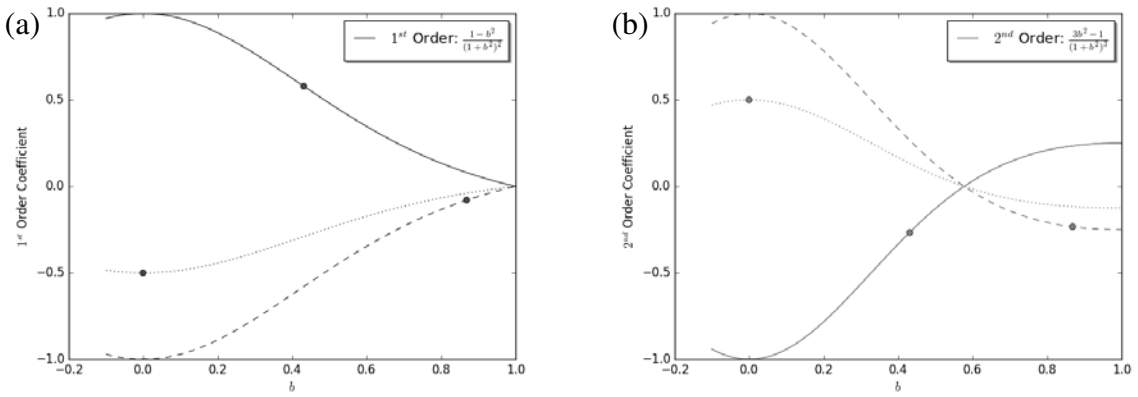

Figure 5.8: The common coefficients of the (a) first and (b) second order fields as a function of wire pair spacing for co-propagating currents. The case of positive current is plotted with a solid curve, while negative current is dashed. The dotted curve represents negative half current, corresponding to the $b = 0$ wire. Each point represents a single wire pair in the given solution. Note the three individual wire coefficients sum to zero for each order.

5.4.2 Uniform $\hat{z}$ Fields Through Third Order

Helmholtz coils provide field uniformity to fourth order, i.e. $(r/\mathcal{R})^4 << 1$. Here, equivalent uniformity (i.e. $(r/d)^4 << 1$) is demonstrated for the planar system. The demonstration simultaneously shows a key advantage of planar field sources. On a second layer of the same chip as the uniform $\hat{\mathbf{y}}$ field wires from the previous section, pairs of counter-propagating currents create a uniform $\hat{\mathbf{z}}$ field. Thus, arbitrary directionality can be achieved from a single planar source.

The uniform $\hat{\mathbf{z}}$ field to fourth order is produced by solving

$$\sum_{i=1}^{4} I_i \left(\frac{b_i}{1+b_i^2} \right) \neq 0,$$
$$\sum_{i=1}^{4} I_i \left(\frac{b_i}{(1+b_i^2)^2} \right) = 0,$$
$$\sum_{i=1}^{4} I_i \left(\frac{b_i(b_i^2-3)}{(1+b_i^2)^3} \right) = 0,$$
$$\sum_{i=1}^{4} I_i \left(\frac{b_i(b_i^2-1)}{(1+b_i^2)^4} \right) = 0. \tag{5.27}$$

Note that the third order condition is introduced without derivation. This condition is a natural extension of the Taylor series performed in Eq. (5.19). Using the same single current and size requirements as the $\hat{\mathbf{y}}$ field case, the maximal field solution is

$$(b_1, b_2, b_3, b_4) = (0.071, 0.870, 0.644, 2.980),$$

for currents

$$(I_1, I_2, I_3, I_4) = I_p(1, 1, -1, -1).$$

The resulting field has strength

$$B_z^{(0)} = \frac{\mu_0}{2\pi} \sum_{i=1}^{4} \frac{I_i}{d} \frac{2b_i}{1+b_i^2} = 0.19 \frac{\mu_0 I_p}{\pi d}, \tag{5.28}$$

illustrated in Fig. 5.9. Note that this field is slightly weaker than the uniform $\hat{\mathbf{y}}$ field shown previously. In canceling one higher order, the added wire pair subtracts from the remnant field, as seen in Fig. 5.10. This is a key weakness of the planar system in comparison to Garrett's coils, in which each additional coil adds field to the central region. This comparative weakness is further detailed below for the fabricated test chip. However, it should be noted that extra coils have the drawback of further obstructing optical access.

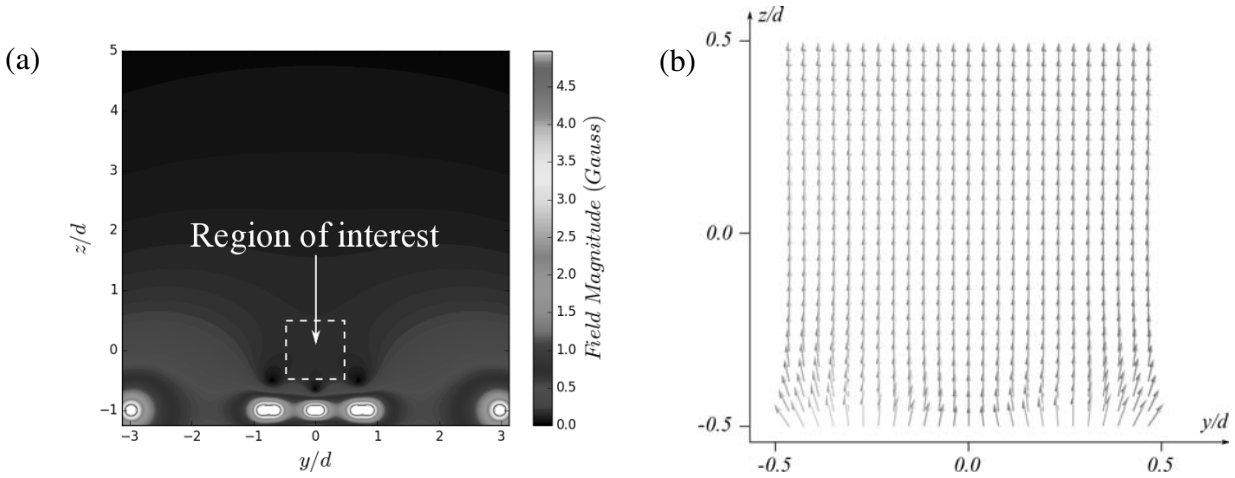

Figure 5.9: (a) A contour plot of the planar system to produce a uniform $\hat{\mathbf{z}}$ field. The wires are the white circular regions along the lower section of the plot, while dashed box shows the central region over which the field is uniform. A zoomed in vector plot of the region of interest is shown in (b). The plots use $I_p = 1$ A.

5.4.3 Linear Gradient Planar Fields

As in the axial case, linear gradient fields can be created by allowing the combined first order to be non-zero, while canceling the zeroth and higher orders. To match the performance of the anti-Helmholtz pair, only the zeroth and second order must be eliminated.

For example, using pairs of co-propagating wires, the conditions are

$$\begin{aligned}
\sum_{i=1}^{3} I_i \left(\frac{1}{1+b_i^2} \right) &= 0, \\
\sum_{i=1}^{3} I_i \left(\frac{(1-b_i^2)}{(1+b_i^2)^2} \right) &\neq 0, \\
\sum_{i=1}^{3} I_i \left(\frac{3b_i^2-1}{(1+b_i^2)^3} \right) &= 0.
\end{aligned} \tag{5.29}$$

Eq.'s (5.20) and (5.21) show these requirements produce a rotated 2D quadrupole field

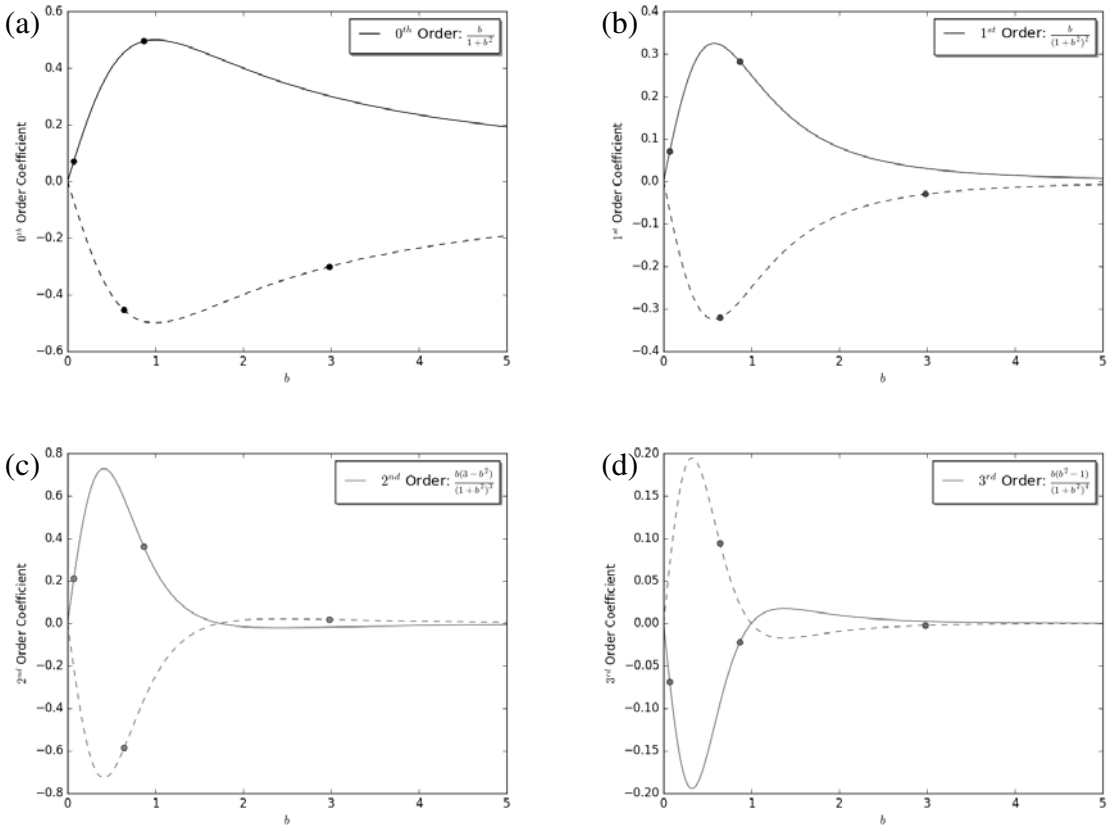

Figure 5.10: The common coefficients of the (a) zeroth, (b) first, (c) second, and (d) third order fields as a function of wire pair spacing for counter-propagating currents. The case of positive current is plotted with a solid curve, while negative current is dashed. Each point represents a single wire pair in the given solution. Note the four individual wire coefficients sum to zero for the first, second, and third orders.

$$\mathbf{B} \approx G\left[z\hat{\mathbf{y}} + y\hat{\mathbf{z}}\right]. \tag{5.30}$$

Fig. 5.11 depicts such a field where

$$(b_1, b_2, b_3) = (0, 0.414, 1.352)$$

for currents

$$(I_1, I_2, I_3) = I_p(-1/2, 1, -1).$$

The rotation arises because the field of the outer wire pairs is canceling the field of the central wire, which is along $\hat{\mathbf{y}}$ at the origin. By contrast, as seen in Eq.'s (5.22) and (5.23), pairs of counter-propagating wires create standard 2D quadrupole fields

$$\mathbf{B} \approx G\left[y\hat{\mathbf{y}} - z\hat{\mathbf{z}}\right], \tag{5.31}$$

under the conditions

$$\begin{aligned}
\sum_{i=1}^{4} I_i \left(\frac{b_i}{1 + b_i^2}\right) &= 0, \\
\sum_{i=1}^{4} I_i \left(\frac{b_i}{(1 + b_i^2)^2}\right) &\neq 0, \\
\sum_{i=1}^{4} I_i \left(\frac{b_i(b_i^2 - 3)}{(1 + b_i^2)^3}\right) &= 0,
\end{aligned} \tag{5.32}$$

because the field of the inner wire pair is along $\hat{\mathbf{z}}$ at the origin. One such system is given by

$$(b_1, b_2, b_3) = (-2.981, 0.752, 0.185),$$

for currents

$$(I_1, I_2, I_3) = I_p(1, 1, -1).$$

The resulting linear gradient field is shown in Fig. 5.12.

5.5 Finite Wire Optimization

The process of transitioning the infinite wire pair model to a realistic atom chip will be shown for the case of the uniform $\hat{\mathbf{z}}$ field. The considerations and methods are similar for the uniform $\hat{\mathbf{y}}$ and linear gradient fields.

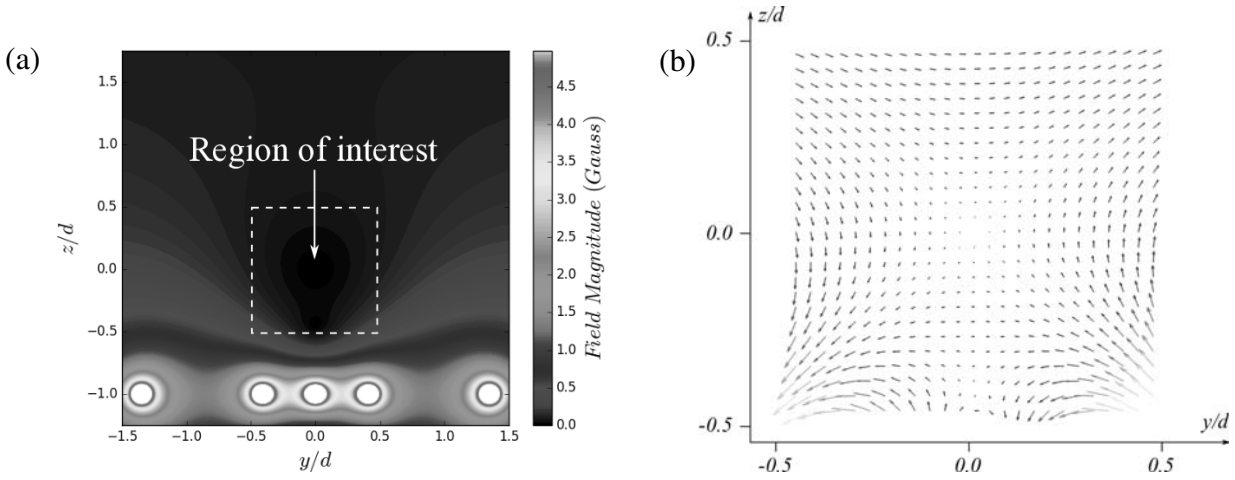

Figure 5.11: (a) A contour plot of the planar system to produce a rotated 2D quadrupole field. The wires are the white circular regions along the lower section of the plot, while dashed box shows the central region over which the field is linear. A zoomed in vector plot of the region of interest is shown in (b). The plots use $I_p = 1$ A.

The uniform $\hat{\mathbf{z}}$ field to third order requires three infinite wire pairs. However, on a realistic atom chip, wire lengths are finite. Additionally, wire leads attached to the chip create fields that are difficult to model.

To approximate the infinite wires, consider three rectangular loops of current. The incoming and outgoing current leads can then be placed together to minimize their long-range magnetic field. One loop is centered at $y = 0$ with width $w_1 d$. Two more are placed symmetrically around the $y = 0$ axis, centered at $(x, y) = (0, cd)$ with width w_2, as depicted in Fig. 5.13.

As the loop length $L \to \infty$, the magnetic field of these three loops should align with the infinite wire pair model. To reduce Ohmic heating of the chip, the loop length should be minimized to the extent possible because each loop dissipates power

$$P_i = I_p^2 \frac{\rho_\Omega (4L + 2w_i)}{A_{wire}}, \tag{5.33}$$

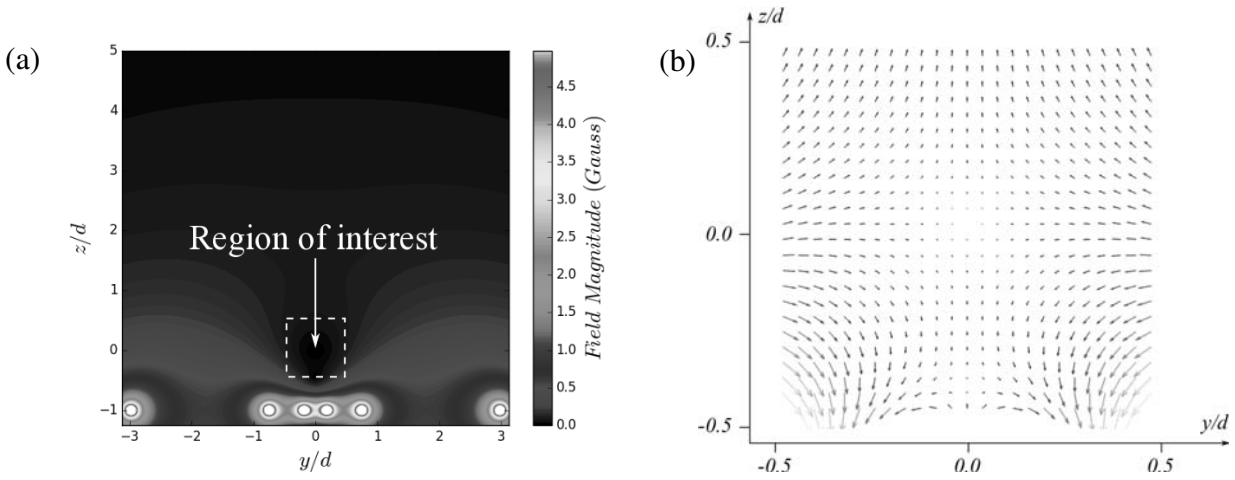

Figure 5.12: (a) A contour plot of the planar system to produce a standard 2D quadrupole field. The wires are the white circular regions along the lower section of the plot, while dashed box shows the central region over which the field is linear. A zoomed in vector plot of the region of interest is shown in (b). The plots use $I_p = 1$ A.

where ρ_Ω is the resistivity of the chip material (copper) and A_{wire} is the wire's cross-sectional area.

To find the minimal acceptable loop length, a simulation calculates the magnetic field vector $\mathbf{B}$ at one hundred points within a cubic volume of interest with side length $d/2$, centered at the origin. Each loop is constructed of four finite current segments where the field of a single segment flowing from point a to b is given by

$$\mathbf{B} = \frac{\mu_0 I_p}{\pi} \frac{(r_b + r_a)}{r_b r_a + \mathbf{r}_b \cdot \mathbf{r}_a} (\hat{\mathbf{r}}_b \times \hat{\mathbf{r}}_a), \tag{5.34}$$

where $\mathbf{r}_{a,b}$ are vectors from a and b to the field point, respectively.

The simulation uses a genetic algorithm with 50 generations of 100 individuals each to search for the most uniform field at a given loop length L. A single-valued merit function judges each individual. The merit function calculates the average angular deviation $\bar{\theta}$ of $\mathbf{B}$

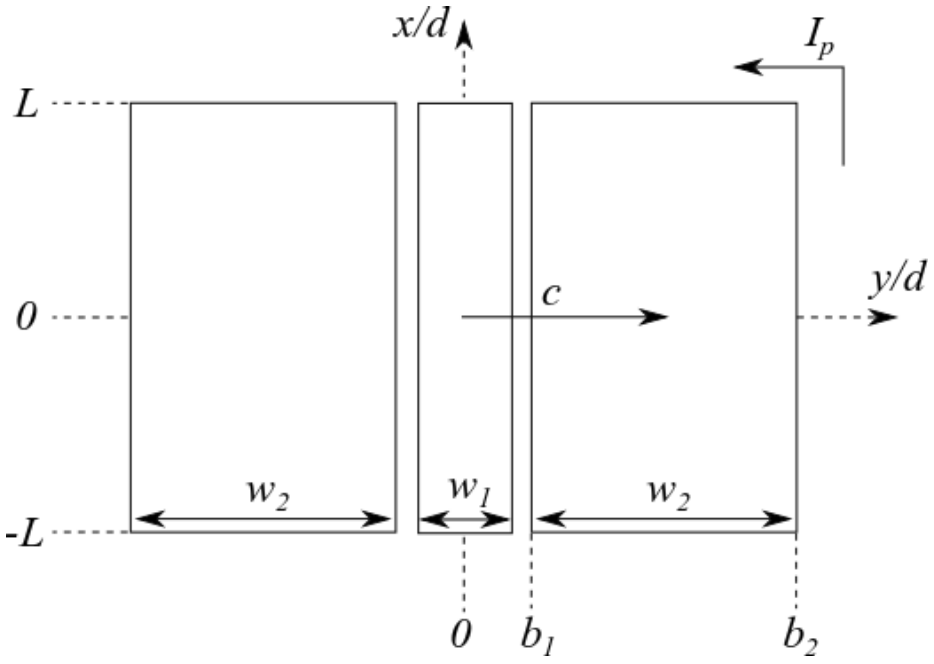

Figure 5.13: Characteristic loop parameters for optimization of the planar uniform $\hat{\mathbf{z}}$ field chip to third order.

from $\hat{\mathbf{z}}$ at each point in the volume of interest. For uniform fields, $\nabla \cdot \mathbf{B} = 0$ implies the magnetic field is also constant when $\bar{\theta} = 0$.

Using $\bar{\theta}$, the simulation steps through a range of possible L. At each value, the individual with the smallest average angular deviation is plotted in Fig. 5.14. The red solid line shows the equivalent infinite wire solution with three counter-propagating current pairs. Clearly, increasing loop length reaches a point of diminishing returns for $L \gtrsim 5d$.

5.6 Results

The $L = 5.2d$ solution results in an average angular deviation $\bar{\theta} = 0.529$ degrees from a true uniform $\hat{\mathbf{z}}$ field at a distance d from the chip surface. The optimization calls for the central loop to have width $w_1 = 0.2892d$ and the two outer loops to be centered at $c = \pm 1.3040d$ with widths $w_2 = 0.7377d$. The resulting chip is drawn in Fig. 5.15 for

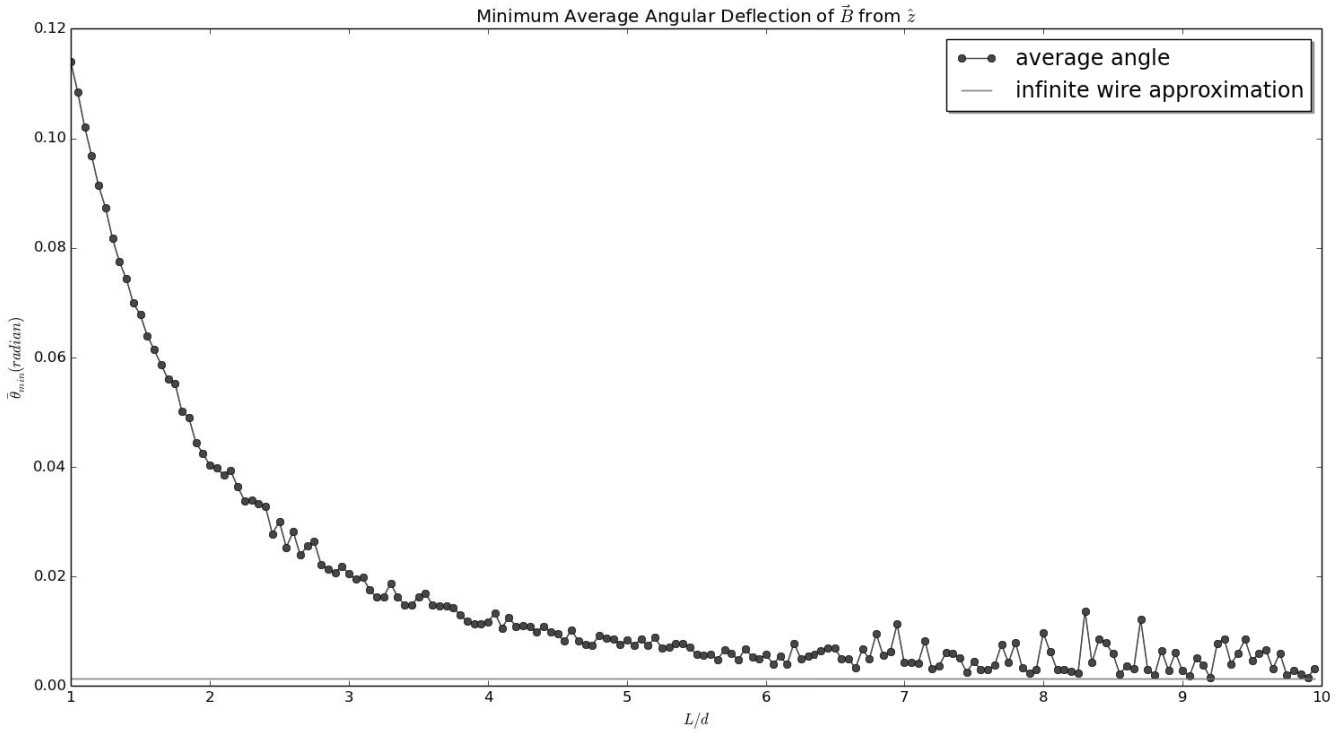

Figure 5.14: The minimum average angular deviation of the optimized magnetic field as a function of chip length.

the case of $d = 5$ mm with 500 micron wide wires. Using the techniques described in Chapter 3, a DBC/AlN chip was fabricated as shown in Fig. 5.16.

The field produced by the chip was measured using an Ametes MFS-3A three axis magnetic field sensor from GMW Associates. Once the sensor was properly positioned over the chip surface, an initial reading of the background laboratory magnetic field was taken. Then, the wires were energized with current $I_p = 15$ A. The chip was scanned across the sensor with a three axis linear translation stage with 0.0254 mm precision. The background field was subtracted from each measurement. The results are shown compared to the simulated field in Figs. 5.17 and 5.18.

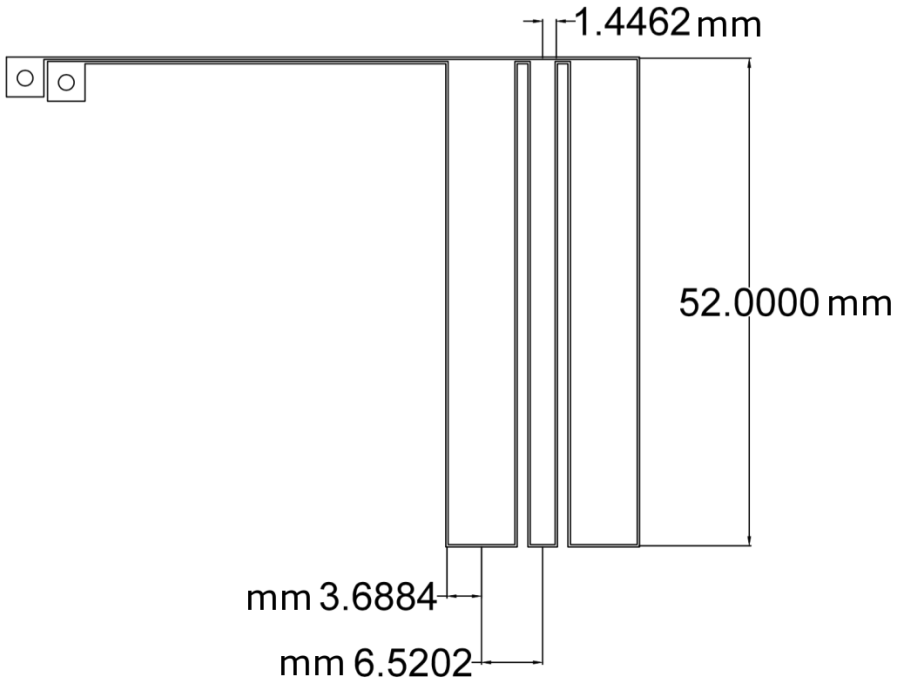

Figure 5.15: The chosen design for creating a uniform bias field parallel to the chip normal.

Within the volume of interest, the magnetic field was $\sim$ 3 Gauss. By comparison, a single turn Helmholtz coil with current $I_{coil} = 15$ A and radius $R_{coil} = d = 5$ mm provides a field

$$B^{(0)} \approx \frac{\mu_0 \mathcal{N} I_{coil}}{(5/4)^{3/2} R_{coil}} = 27 \text{ Gauss.} \tag{5.35}$$

The Helmholtz pair provides an order of magnitude higher field per turn. Further complicating matters, implementing multiple turns on a chip is challenging given the narrow gap between loops. However, the ease by which chips are cooled enables higher current capacity than free-space coils, reducing the discrepancy of maximal output field.

Further, recall that the CAS has external Helmholtz coils with radius $R_{coil} \sim 5$ cm, creating a uniform field over a $\sim$ 12 cm^3 volume. That volume is excessive considering

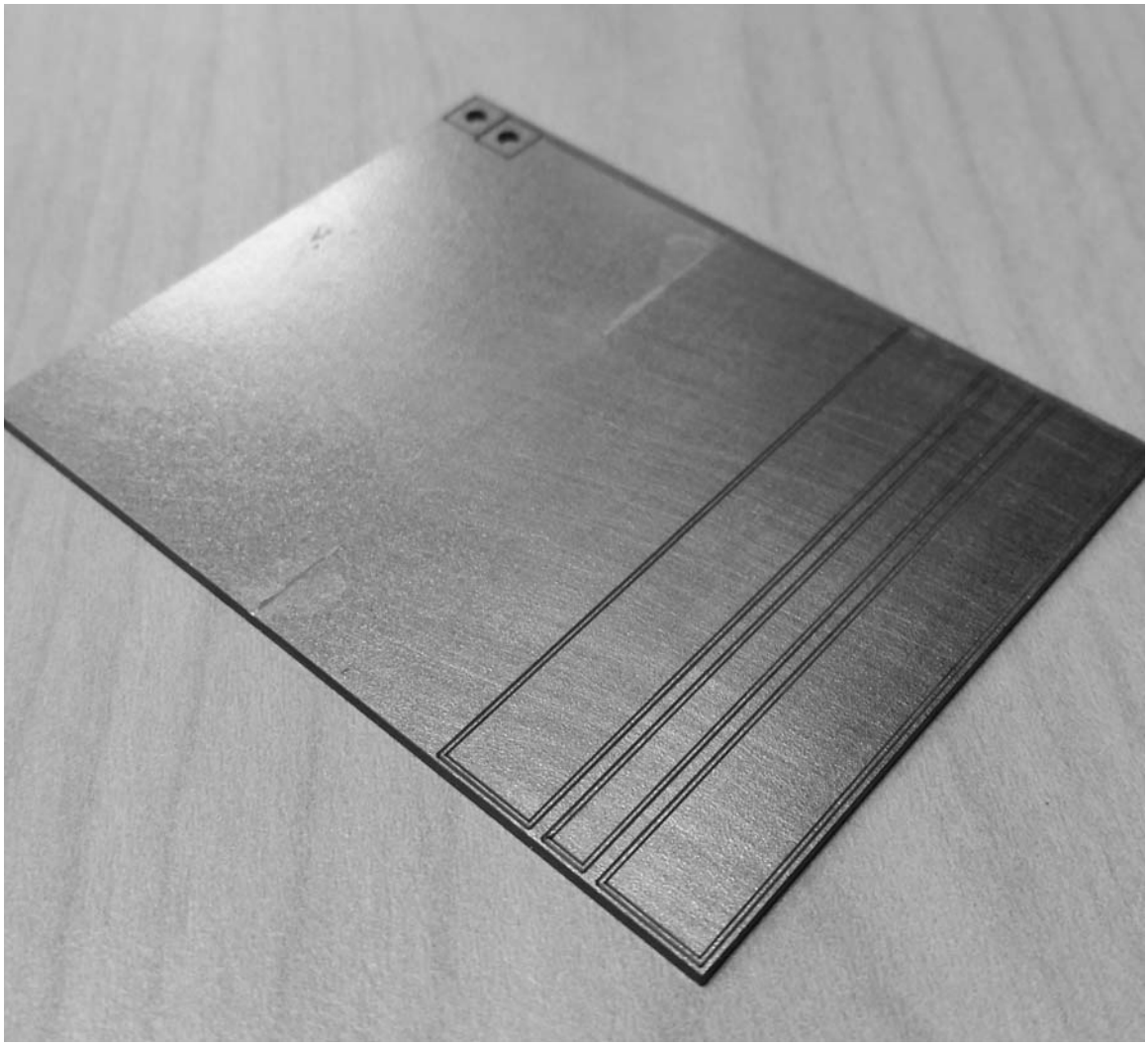

Figure 5.16: A fabricated chip for creating a uniform bias field parallel to the chip normal.

the atom cloud is only a few mm across during PGC. The smaller volume of uniformity created by the $d = 5$ mm chip is adequate. Meanwhile, the lower source-to-atom distance creates an equivalent field strength to that of the coils.

5.7 Application: Cold Atom Transport

Another application where the planar uniform field holds promise is the magnetic trap conveyor, which moves atoms controllably along a chip surface, as demonstrated in

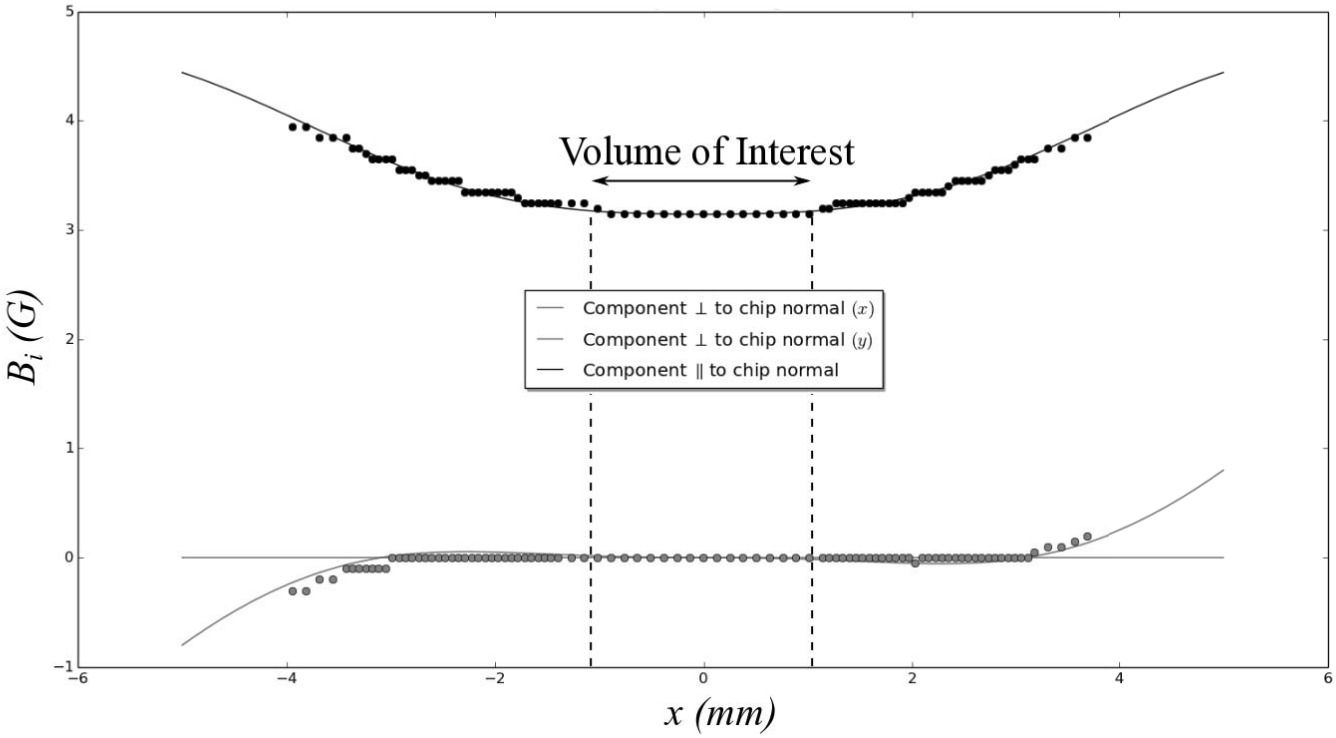

Figure 5.17: The magnetic field as predicted and measured as a function of x (transverse to the chip normal).

2005 [112]. The scheme is depicted in Fig. 5.19. Qualitatively, a central current I_0 and a bias field $\mathbf{B}_{bias}$ create a line of magnetic field zeros as in Eq. (2.26). Two other currents I_a and I_b flow back and forth along I_0, offset by a quarter period. The crossing currents oscillate in time according to

$$(I_a, I_b) = I_{peak}(\cos \Upsilon(t), -\sin \Upsilon(t)), \tag{5.36}$$

resulting in local magnetic field minima which move across x, as shown in Fig. 5.20, reproduced from [112].

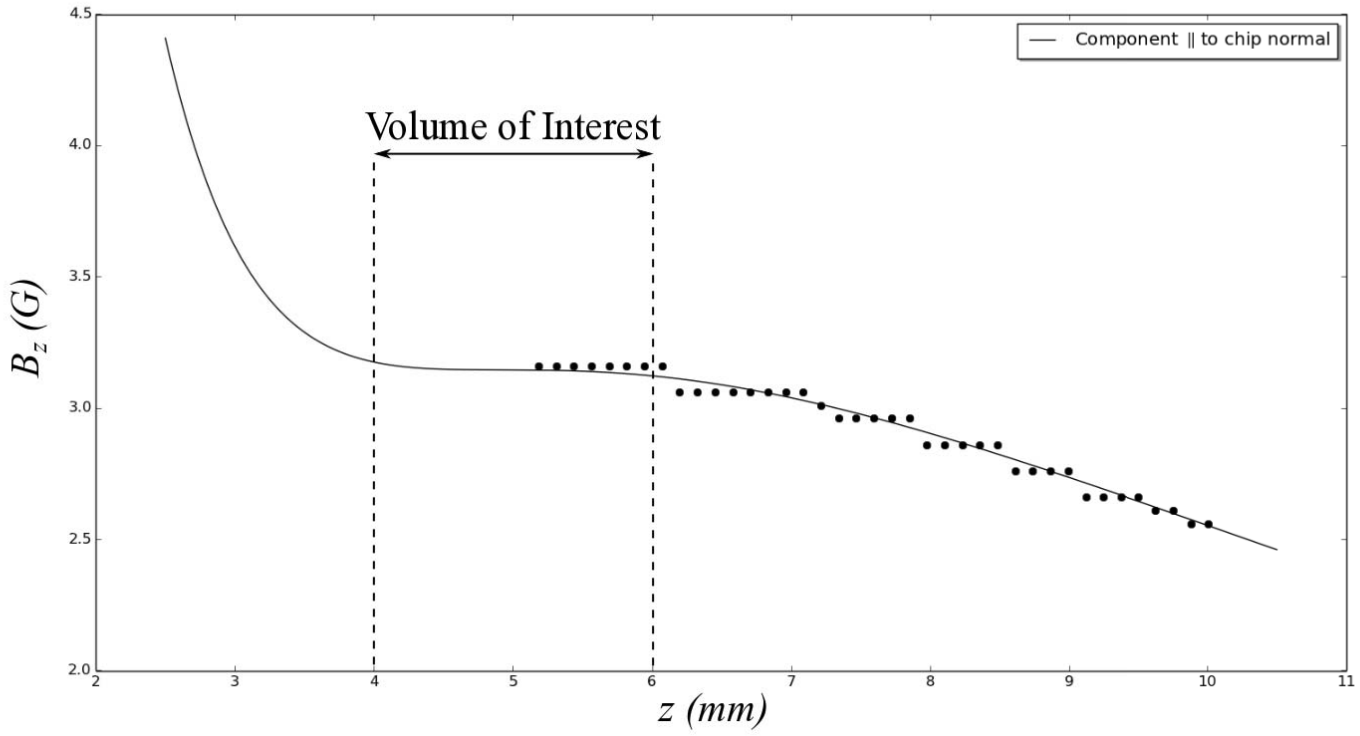

Figure 5.18: The magnetic field as predicted and measured as a function of z (parallel to the chip normal).

In the experiment, the central current was $I_0 = 2$ A, the peak oscillating current was $I_{peak} = 1$ A, and the bias field magnitude was $B_{bias} = 17.5$ Gauss. Using Eq. (2.26), the resulting traps were just $d = 200$ microns from the chip surface. If the bias field is formed by the uniform $\hat{\mathbf{y}}$ field chip, the required current is

$$17.5 \text{ Gauss} = 0.23\frac{\mu_0 I_p}{\pi d} \rightarrow I_p = 3.8 \text{ A}. \tag{5.37}$$

This current is easily achieved with standard power supplies.

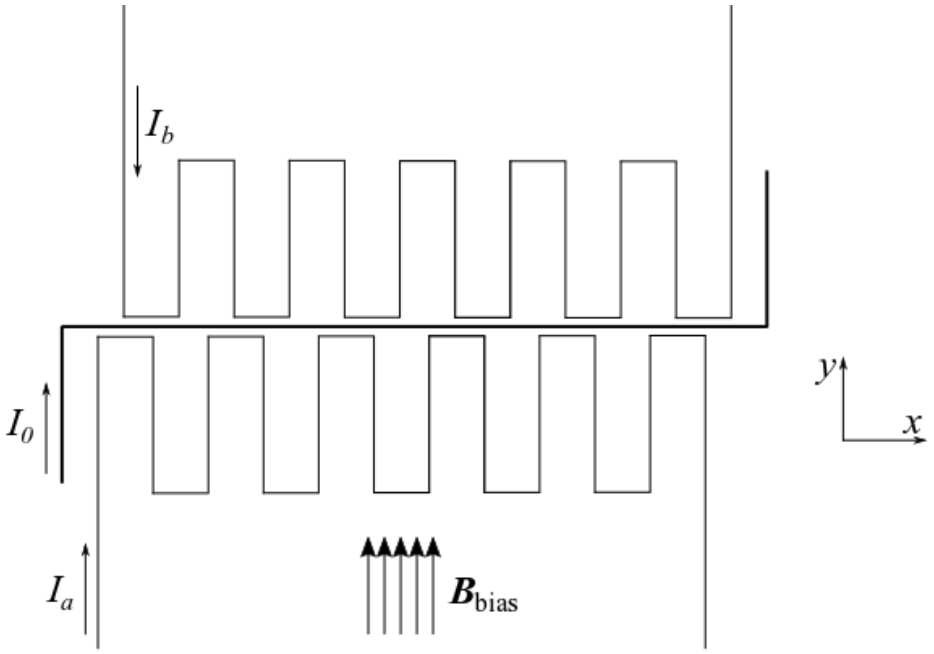

Figure 5.19: A chip to translate cold atoms along a current I_0 flowing in $\hat{\mathbf{x}}$, as shown in [112].

5.7.1 Bias-Free Atom Conveyor

The uniform $\hat{\mathbf{y}}$ field chip could produce the necessary bias above. However, a conveyor can be constructed that does not rely on a bias field at all. Our design is sketched in Fig. 5.21.

On a first layer, four wires are aligned in the $\hat{\mathbf{x}}$ direction to create an aligned linear gradient field such as Fig. 5.12. A second layer consists of a series of equally spaced wires along the $\hat{\mathbf{y}}$ direction (colored blue), each with alternating current directions. That is, each wire is located at position $x = nl$ for integers n, with currents $I_{n,1} = I_y(-1)^n \mathcal{U}(t)$. Another set of $\hat{\mathbf{y}}$ wires (colored red) is placed at positions $x = nl + l/2$. These have currents $I_{n,2} = I_y(-1)^n \mathcal{V}(t)$, where

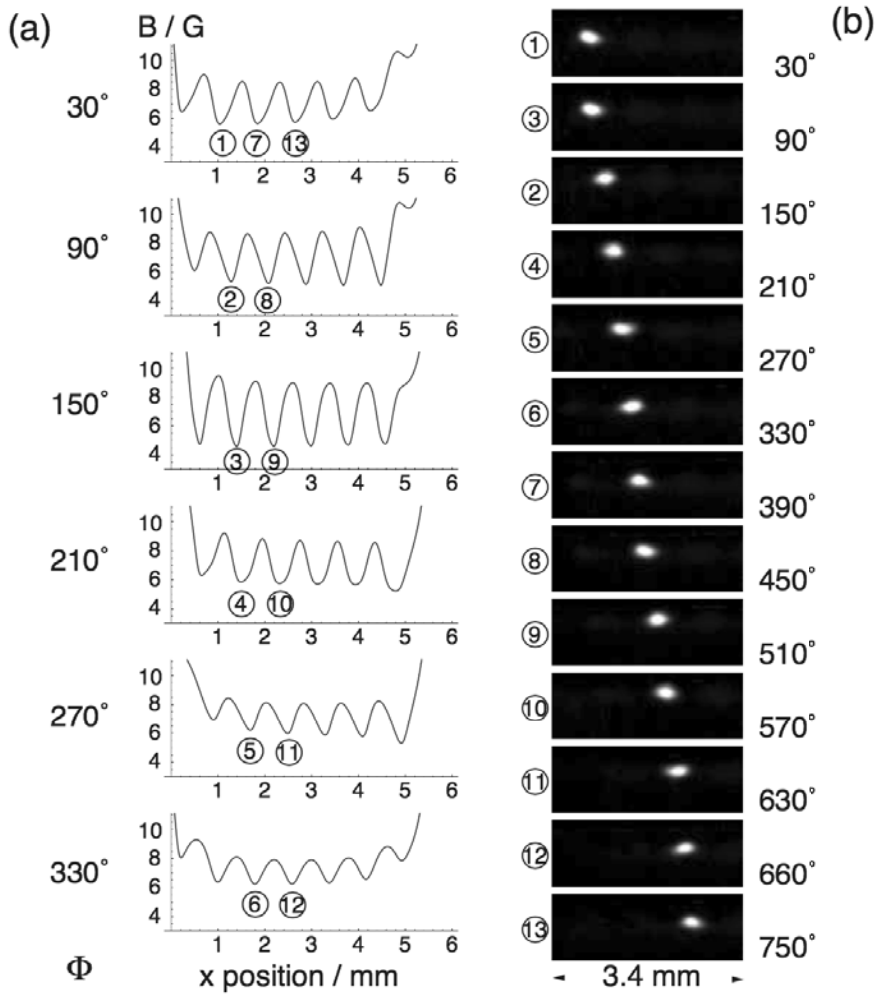

Figure 5.20: Translation of cold atoms via the chip in Fig. 5.19. (a) shows the magnetic potential, (b) shows absorption images of translated cold atoms. Reproduced from [112].

$$\mathcal{U}(t) = \cos(\pi x_0(t)/l),$$
$$\mathcal{V}(t) = \sin(\pi x_0(t)/l). \tag{5.38}$$

The locations of the minimum field points are dependent on both the $\hat{\mathbf{x}}$ and $\hat{\mathbf{z}}$ components of the $\hat{\mathbf{y}}$ crossing wires. However, if the guide wire currents are much stronger than the crossing wire currents, then the $\hat{\mathbf{z}}$ components of the crossing wire field become

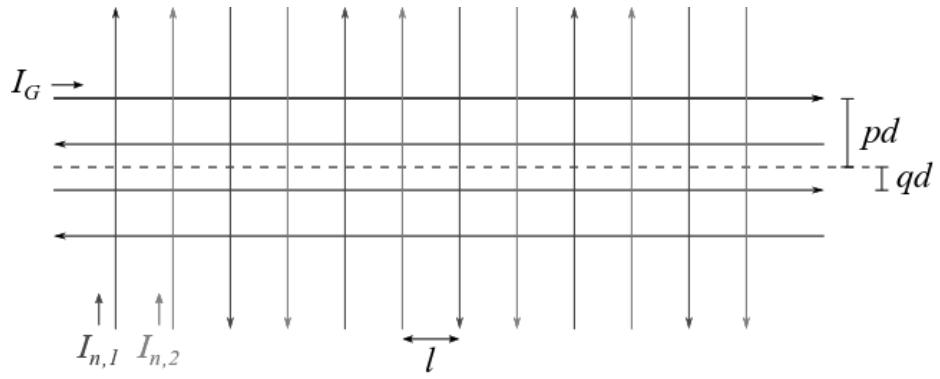

Figure 5.21: A chip design to translate atoms without the use of a global bias.

insignificant, enabling uniform translation of the magnetic trap at a fixed height $z = h$ from the chip surface.

The guide is thus a 2D quadrupole field with the maximum gradient possible. To find the maximal gradient, suppose the wires are located in the $z = d$ plane at $y/d = -p, -q, q, p$ with currents

$$\begin{aligned} I_{-p} &= I_G(1 - \Delta_I + \delta_I), \\ I_{-q} &= -I_G(1 + \Delta_I + \delta_I), \\ I_{+q} &= I_G(1 + \Delta_I - \delta_I), \\ I_{+p} &= -I_G(1 - \Delta_I - \delta_I), \end{aligned} \tag{5.39}$$

respectively, where I_G is called the guide current and $\Delta_I, \delta_I << 1$. As shown in Appendix C, if $p = 1/q$ and $q \approx \sqrt{2} - 1$, then the gradient of the linear field is maximized to

$$\mathbf{B}_G = \frac{\mu_0 I_G}{2\pi d^2}\Big[(y - y_0)\hat{\mathbf{y}} - (z - z_0)\hat{\mathbf{z}}\Big] \tag{5.40}$$

with $y_0 = \sqrt{2}\delta_I d$ and $z_0 = -\sqrt{2}\Delta_I d$.

Meanwhile, the first set of $\hat{\mathbf{y}}$ crossing wires creates a field at height $z = h$ from the chip surface

$$\mathbf{B}_{cross-wires} = \frac{\mu_0 I_y \mathcal{U}(t)}{2\pi} \left[\beta_x(x)\hat{\mathbf{x}} + \beta_z(x)\hat{\mathbf{z}}\right], \tag{5.41}$$

where

$$\begin{aligned}\beta_x(x) &= \frac{2\pi}{l}\sum_{n=0}^{\infty} e^{-k_n h}\cos(k_n x),\\ \beta_z(x) &= -\frac{2\pi}{l}\sum_{n=0}^{\infty} e^{-k_n h}\sin(k_n x).\end{aligned} \tag{5.42}$$

Derivation of these relations are detailed in Appendix D. The field of the second set of $\hat{\mathbf{y}}$ crossing wires is derived similarly such that the total crossing wire field is

$$\begin{aligned}\mathbf{B}_{c-w,x} &= \frac{\mu_0 I_y}{l}\left[\mathcal{U}(t)\sum_{n=0}^{\infty} e^{-k_n h}\cos(k_n x) + \mathcal{V}(t)\sum_{n=0}^{\infty} e^{-k_n h}\cos(k_n(x-l/2))\right]\hat{\mathbf{x}},\\ \mathbf{B}_{c-w,z} &= -\frac{\mu_0 I_y}{l}\left[\mathcal{U}(t)\sum_{n=0}^{\infty} e^{-k_n h}\sin(k_n x) + \mathcal{V}(t)\sum_{n=0}^{\infty} e^{-k_n h}\sin(k_n(x-l/2))\right]\hat{\mathbf{z}}.\end{aligned} \tag{5.43}$$

In the limit that $\pi h/l << 1$, then $e^{-k_n h} \to 0$ for $n \neq 0$. Keeping only the $n = 0$ terms and noting $k_0 = \pi/l$, then the field is

$$\begin{aligned}\mathbf{B}_{c-w,x} &= \frac{\mu_0 I_y}{l} e^{-\frac{\pi h}{l}}\left[\cos\left(\frac{\pi}{l}(x-x_0)\right)\right]\hat{\mathbf{x}},\\ \mathbf{B}_{c-w,z} &= -\frac{\mu_0 I_y}{l} e^{-\frac{\pi h}{l}}\left[\sin\left(\frac{\pi}{l}(x-x_0)\right)\right]\hat{\mathbf{z}}.\end{aligned} \tag{5.44}$$

When the guide field is added to the field from both sets of crossing wires, the magnetic potential energy is

$$V = -\mu_B m_F g_F \sqrt{C_1^2 + C_2^2\,(y-y_0)^2 + C_2^2\,(z-z_0)^2 + 2C_1C_2\,(z-z_0)\sin\left[\frac{\pi}{l}\Big(x - x_0(t)\Big)\right]} \tag{5.45}$$

where $C_1 = (\mu_0 I_y/l)e^{-\pi h/l}$ and $C_2 = \mu_0 I_G/(2\pi d^2)$. The minimums for the conveyor then occur at the positions

$$
\begin{aligned}
x_{min} &= \frac{(2n+1)l}{2} + x_0(t), \\
y_{min} &= \sqrt{2}\delta_I d, \\
z_{min} &= -\sqrt{2}\Delta_I d - \frac{2\pi d^2}{l} e^{-\frac{\pi h}{l}} \frac{I_y}{I_G}(-1)^n.
\end{aligned} \tag{5.46}
$$

Notice that the minimum of the trap can be independently controlled in the all three directions by varying Δ_I, δ_I, and $x_0(t)$. A contour plot showing these minima is given in Fig. 5.22. For the simulation, $h = d = l = 1$ mm. The guide current is $I_G = 10$ A and the crossing wire current is $I_y = 1$ A. The traps are of approximate depth C_1, so the trap depth is maximized for $l = \pi h \approx \pi d$. The traps were derived under the assumption that $z << d$, giving the following constraint on the currents

$$
\frac{z}{d} = \frac{2}{e}\frac{I_y}{I_G} << 1. \tag{5.47}
$$

5.8 Conclusion

Localized uniform fields of arbitrary direction can be produced by a multi-layer stack of planar currents. Similarly, linear gradient fields can be created on the same chip. These chips were shown to be a capable alternative to external coils in certain applications. For example, using a 15 A current, a 3 Gauss uniform field was created over a 16 mm^3 volume. This volume is comparable to that required for PGC of a cold atom cloud a few mm in diameter. Finally, an alternative magnetic conveyor was described that does not rely on a bias field at all. With these designs, the three external Helmholtz coil pairs can be removed to improve optical access and experimental efficiency of the AFRL cold atom device.

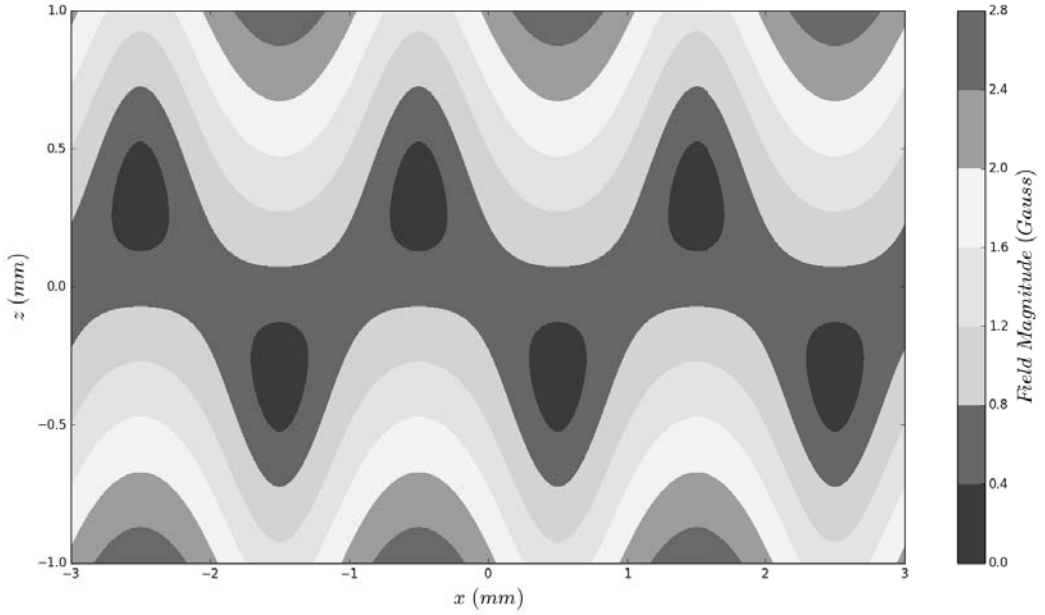

Figure 5.22: The magnetic field magnitude of the trap conveyor as a function of x and z at $y = 0$.

Page intentionally left blank

VI. Measurement Sequence: Coherence in a Magnetic Talbot-Lau Interferometer

6.1 Introduction

Thus far, this dissertation has examined methods to reduce the necessary size, weight, and power of laser cooling and magnetic trapping. However, these gains are quickly reversed if the following typical measurement sequence is used.

Most atom interferometers rely on a Raman pulse technique which changes the internal state of the interrogated atoms. Because of the difficulty in confining multiple states with a magnetic field, atoms are allowed to propagate freely, necessitating a large system. The most sensitive devices use a 10-meter long apparatus [24].

Single internal state splitting has allowed atoms to be trapped for the duration of the interferometer cycle, reducing the apparatus length to a few millimeters [79]. Techniques for confined splitting include double-well potentials [86], optical lattices [87], and standing wave pulses [88, 89]. However, these interferometers have used Bose-Einstein condensates, which require cooling stages that increase power consumption, decrease possible repetition rates, and lower atom numbers.

One single state technique has been shown to work at thermal (i.e., non-condensed) temperatures [90–92]. These interferometers, in the Talbot-Lau configuration, confine the atomic sample in two directions and allow free propagation in the third. In an ideal situation, the potential along the third direction would vanish. However, due to the finite size of the device and uncontrollable external fields, there is a residual potential along the waveguide.

Unfortunately, the residual potential and other field imperfections reduce coherence times [89, 93, 94]. Recent research has demonstrated a high degree of control over the residual field [26]. Here, we analyze the effect of a controlled residual potential in a Talbot-Lau interferometer with a gas of cold, thermal atoms using a Wigner function approach.

6.2 Interferometer Operation

To prepare the atomic gas for the interferometer cycle, a laser-cooled sample is loaded into a magnetic trap with frequencies $\omega_i^{(e)}$, where $i = (x, y, z)$. The collision rate is directly proportional to the geometric average of these trap frequencies $\bar{\omega}^{(e)} = (\omega_x^{(e)}\omega_y^{(e)}\omega_z^{(e)})^{1/3}$, so $\bar{\omega}^{(e)}$ should be made as large as possible to maximize the efficiency of the evaporative cooling. In typical atom chip experiments, the gas is evaporatively cooled in a trap with frequency $\bar{\omega}^{(e)} \sim 2\pi \times 200$ Hz.

Once the atoms are cooled to a temperature on the order of $\mathcal{T} \sim 10\,\mu$K, the potential is adiabatically transformed into a trap that tightly confines the atoms in the radial direction, with frequencies $\omega_y = \omega_z = \omega_\perp \sim 2\pi \times 200$ Hz; and in the axial direction, with frequency $\omega_x = \omega_0$. Just before the interferometer cycle starts, the potential is non-adiabatically transformed into a waveguide potential, while holding the radial trap frequency constant to reduce the effects of transverse excitations. In a realistic device, there remains a residual potential along the waveguide with frequency ω.

Once the atoms are loaded in the waveguide, the interferometer cycle begins. In this analysis, we considered the case of the trapped atom Talbot-Lau interferometer schematically shown in Figure 6.1. The figure traces the different paths that an initially stationary atom could experience when moving through the device. Time moves from left to right, and the displacement of the atom along the waveguide is shown in the vertical direction.

At time $t = 0$, the atomic cloud is illuminated with a short, standing wave laser pulse that acts as a diffraction grating. The pulse is sufficiently short that it is in the Kapitza-Dirac regime, i.e., the atoms do not move for the duration of the laser pulse. The pulse splits the wave function for each atom into several momentum states separated by the two photon recoil momentum $\delta P = 2\hbar k_l$, where k_l is the wave number of the laser beams.

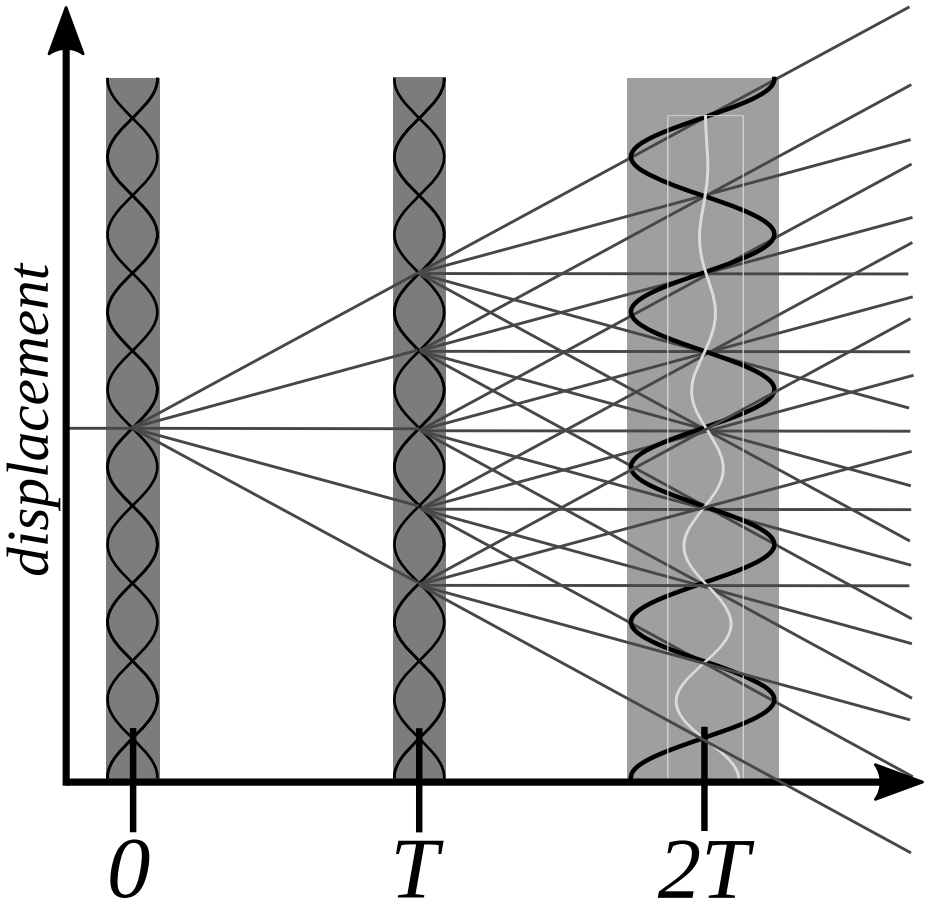

Figure 6.1: The schematic of a Talbot-Lau interferometer. An atomic cloud is split in space (vertical axis) by a laser pulse at time $t = 0$. The resulting diffracted orders separate and are further diffracted at $t = T$. At the recombination time $t = 2T$, the various orders overlap, allowing a probe laser to produce a back scattered signal from the periodic atomic distribution. Only two diffraction orders are shown because for typical laser pulses, higher orders are suppressed.

After the laser pulse, the atomic cloud propagates in the waveguide for a time T, at which point it is illuminated with a second laser pulse. The paths of the different momentum states are shown as blue lines between 0 and T. Ideally, the momentum of each mode should

be constant in time. However, the residual curvature along the waveguide will cause the paths to become curved (not shown in the figure), giving rise to decoherence.

For simplicity, it is assumed that the laser pulse at time T has the same strength and affects the atomic wave function in the same manner. Each of the momentum states that were populated after the first laser pulse are split into several modes. After the second laser pulse, the number of possible paths increases dramatically. However, near time $2T$, the different paths come together to form a density modulation that has the same period as the standing wave.

An extraordinary feature of a Talbot-Lau interferometer is that the location of the density echo is independent of the initial velocity of the atom. For example, if the initial atom in Figure 6.1 had some momentum, each of the diffracted orders would gain this additional momentum. After tracing out all possible paths, it is easy to show that the density modulation appears in exactly the same location as for the initially stationary atom. As a result, the density echo is still visible even when the initial atomic gas is relatively hot.

In the absence of external forces, the density echo will have the same relative phase as the standing wave laser pulse. However, if there is a force on the cloud, the echo will move in response to the force. By detecting the shift in the echo, it is possible to measure the force on the cloud.

This phase shift can be measured by reflecting a traveling wave off the density modulation. Due to the Bragg effect, there will be a strong backscattered signal for the duration of the echo. By heterodyning the back-reflected light with a reference beam, the phase of the density echo can be determined.

In this chapter, we present a theoretical model of a trapped Talbot-Lau interferometer that includes the decoherence due to the residual potential curvature. The Wigner function approach is used to model the dynamics of a thermal gas, which can be extended to include more complex laser pulse sequences [94]. For brevity, only the simple case of a two-pulse

interferometer is discussed. Our model predicts the amplitude of backscattered light for an arbitrary initial Wigner function and is then specialized to the case of an initial thermal distribution. Decoherence due to finite temperature and initial axial trap frequency are discussed. Finally, the model is used to determine the ideal axial frequency for a given initial phase space density and residual potential.

6.3 The Model

Following the prescription of [26], we assume that the potential is separable, i.e., $V(\boldsymbol{r}) = V(x) + V_\perp(r_\perp)$, and the k-vectors of the laser beams point in the x-direction. Collisions are neglected as we have previously analyzed the effects of collisions in a similar interferometer and do not expect atom-atom collisions to have a significant impact on the results [113]. We also ignore the mean field interaction, as it is mainly relevant for strongly interacting condensates, which we do not consider here. Inclusion of these terms may be possible, but are omitted to keep the discussion concise.

The Hamiltonian that governs the axial dynamics of the interferometer is one-dimensional and can be written as

$$H = \frac{P^2}{2M} + \frac{1}{2}M\beta X^2 + \hbar\Omega\cos(2k_l X), \tag{6.1}$$

where X and P are the canonical operators with commutation relation $[X, P] = i\hbar$, k_l is the wave number of the laser, M is the atomic mass, and β is the curvature of the residual potential. The parameter Ω is the frequency of the AC-stark shift due to the standing wave laser pulse, which depends on the intensity and detuning of the beam and is, in general, a function of time.

The Hamiltonian can be recast in the dimensionless form

$$H' = \frac{P'^2}{2} + \frac{1}{2}\beta' X'^2 + \Omega'\cos X', \tag{6.2}$$

where $P' = P/P_0$, $X' = X/X_0$, and $t' = t/t_0$ where $P_0 = 2\hbar k_l$, $X_0 = 1/2k_l$, and $t_0 = M/4\hbar k_l^2$. The other parameters in Equation (6.1) become $\beta' = \beta t_0^2$ and, $\Omega' = \Omega t_0$. The other important

dimensionless parameter is the cloud temperature $\mathcal{T}' = \mathcal{T}/\mathcal{T}_0$, where $\mathcal{T}_0 = 4\hbar^2 k_l^2/Mk_B$, where k_B is the Boltzmann constant. For ^{87}Rb where the standing wave laser is near the D2 transition, $t_0 = 5.3\,\mu$s, and $\mathcal{T}_0 = 1.4\,\mu$K. For the rest of this chapter, primes will be dropped for clarity, and unless otherwise stated, all introduced variables will be dimensionless.

Since the interferometer uses an incoherent gas, the state of the system cannot be written as a wave function. Instead, the system is described by the density operator ρ. The equation of motion for the density operator, in dimensionless form, is

$$i\dot{\rho} = [H, \rho], \tag{6.3}$$

where the dot denotes the time derivative and the brackets are the usual commutation operator. The density operator can be recast in terms of the Wigner function, which is defined as

$$f(x, p) = \frac{1}{\pi}\int d\xi \langle x + \xi|\rho|x - \xi\rangle e^{-2ip\xi} \tag{6.4}$$

where $|x\rangle$ are the eigenvectors of the coordinate operator, i.e., $X|x\rangle = x|x\rangle$. The Wigner function $f(x, p)$ can be interpreted as the probability density, however for non-classical states the Wigner function may be negative. As a result, $\int dx f = \mathcal{P}(p)$ is the momentum density of the cloud and $\int dp f = \rho(x)$ is the spatial density. Even when the Wigner function is negative, the densities, $\mathcal{P}$ and ρ are always positive.

It is worth noting that the Wigner approach works for pure states as well. In this case, it is defined as

$$f_{pure}(x, p) = \frac{1}{\pi}\int d\xi \psi^*(x + \xi)\psi(x - \xi)e^{-2ip\xi}. \tag{6.5}$$

We will find that the results of the incoherent process are easily extended to include the results of a pure state (BEC) interferometer.

Substituting Equation (6.4) into Equations (6.2) and (6.3), the equation of motion for the Wigner function is

$$\left(\frac{\partial}{\partial t} + p\frac{\partial}{\partial x} - \beta\frac{\partial}{\partial p}\right) f(x, p, t) = \Omega \sin x \left[f\left(x, p - \frac{1}{2}\right) - f\left(x, p + \frac{1}{2}\right)\right], \tag{6.6}$$

where the left side of the equation describes the motion of the distribution in the potential while the right side describes the interaction with the standing wave laser field.

Since the duration of the laser pulses τ_p is much shorter than the interferometer time T ($T \gg \tau_p$), the evolution of the distribution can be separated into relatively slow dynamics when the distribution is not being illuminated and fast dynamics when it is. Additionally, since each laser pulse is short $\tau_p \gg 1/\omega_0$ and strong $\Omega \gg \omega_0$, the pulses are in the Kapitza-Dirac regime, which occurs in the Raman-Nath limit. As a result, the coordinate and momentum derivatives in Equation (6.6) may be neglected during the pulse.

The dynamics of the distribution for the periods when the laser is off, $\Omega = 0$, are such that each part of phase space evolves classically. For simplicity, it is useful to write the classical equations of motion in the form

$$\dot{\boldsymbol{x}} = M\boldsymbol{x} \tag{6.7}$$

where $\boldsymbol{x} = (x, p)$ is the coordinate-momentum vector, and the matrix M is

$$M = \begin{pmatrix} 0 & 1 \\ -\beta & 0 \end{pmatrix}. \tag{6.8}$$

The solution to Equation (6.7) can be written as $\boldsymbol{x}(t) = U_t\boldsymbol{x}(0)$, where $U_t = \exp(Mt)$. By direct substitution, it can be shown that in between the laser pulses the distribution evolves as

$$f_f(\boldsymbol{x}) = f_i(U_{-t}\boldsymbol{x}). \tag{6.9}$$

The laser pulses are more involved and fundamentally quantum in nature (i.e., resulting in negative Wigner distributions). The effect of the laser pulse is to transform an initial Wigner distribution f_i into a final distribution f_f according to

$$f_f(\Omega \neq 0) = \sum_{nk=-\infty}^{\infty} (-i)^n J_k(\Xi) J_{n+k}(\Xi) e^{i(n+2k)x} f_i\left(x, p - \frac{n}{2}\right) \tag{6.10}$$

for the pulse area, $\Xi = \int d\tau\Omega(\tau)$, where the functions J_n are the Bessel functions of the first kind. In terms of $\boldsymbol{x}$, Equation (6.10) can be written in the more compact form

$$f_f(\Omega \neq 0) = \sum_{nk} \alpha_{nk} e^{i\boldsymbol{g}_{nk}\cdot\boldsymbol{x}} f_i(\boldsymbol{x} - \mathbf{N}_n) \tag{6.11}$$

where $\boldsymbol{g_{nk}} = (n + 2k, 0)$, $\boldsymbol{N}_n = (0, n/2)$, and $\alpha_{nk} = (-1)^n J_k J_{n+k}$.

The interferometer sequence is characterized by four unique operations separated in time. The first laser pulse at $t = 0$ operates on an initial Wigner distribution f_0 and transforms it to f_1, ($f_0 \rightarrow f_1$). There is then a propagation period from $t = 0$ to T, over which the distribution transforms $f_1 \rightarrow f_2$. The second laser pulse at $t = T$ transforms $f_2 \rightarrow f_3$. Lastly, another propagation to $t = 2T + \tau$ transforms the distribution to its final form $f_3 \rightarrow f_4$.

Near the end of the interferometer cycle, the cloud is illuminated with a short traveling wave laser pulse of duration τ_0, where $\tau_0 \ll T$. To determine the time dependence of the back-scattered light, the Wigner function must be found for times near the echo time, i.e., $t = 2T + \tau$. By direct substitution into Equations (6.9) and (6.11) for the interferometer cycle discussed in Figure 6.1, the Wigner function near the echo time is

$$\begin{aligned} f_4 &= \sum_{mlnk} \alpha_{ml}\alpha_{nk} \\ &\times \exp\left[i(\boldsymbol{g}_{ml}\cdot U_T + \boldsymbol{g}_{nk})\cdot U_{-2T-\tau}\cdot\boldsymbol{x} - i\boldsymbol{g}_{nk}\cdot U_{-T}\cdot\boldsymbol{N}_m\right] \\ &\times f_0(U_{-2T-\tau}\cdot\boldsymbol{x} - U_{-T}\cdot\boldsymbol{N}_m - \boldsymbol{N}_n). \end{aligned} \tag{6.12}$$

According to [93], the amplitude of the back-scattered light is proportional to

$$S = \int d^2x e^{i\boldsymbol{g}_{01}\cdot\boldsymbol{x}} f_4(\boldsymbol{x}) \tag{6.13}$$

For the rest of the chapter, the quantity S will be referred to as the signal of the interferometer. Changing the integration variable from $\boldsymbol{x}$ to $\boldsymbol{y}$, where

$$\boldsymbol{y} = U_{-2T-\tau}\boldsymbol{x} - U_{-T}\mathbf{N}_m - \mathbf{N}_n, \tag{6.14}$$

the signal can be written as

$$S = \sum_{mlnk} \alpha_{ml}\alpha_{nk} e^{i\Theta_{mlnk}} \int d^2y e^{i\boldsymbol{\Delta}_{mlnk}\cdot\boldsymbol{y}}, \tag{6.15}$$

where

$$\boldsymbol{\Delta}_{mlnk} = \boldsymbol{g}_{ml}\cdot U_T + \boldsymbol{g}_{nk} + \boldsymbol{g}_{10}\cdot U_{2T+\tau}, \tag{6.16}$$

and

$$\Theta_{mlnk} = \boldsymbol{\Delta}_{mlnk}\cdot(U_{-T}\cdot\boldsymbol{N}_m + \boldsymbol{N}_n) - \boldsymbol{g}_{nk}\cdot U_{-T}\cdot\boldsymbol{N}_m. \tag{6.17}$$

In what follows below, it will be assumed that both the echo duration is small as compared to the interferometer time $\tau \ll T$, and the residual trap curvature is $\beta \ll 1/T^2$. When these inequalities are fulfilled, only the linear contributions in both τ and β are retained. In this limit, the time propagation operator for small values of β is $U_T \approx U_T^{(0)} + \beta U_T^{(1)}$, where $U_t^{(0)} = \left(\begin{smallmatrix}1 & t\\ 0 & 1\end{smallmatrix}\right)$, and $U_t^{(1)} = \left(\begin{smallmatrix}t^2/2 & t^3/6\\ t & t^2/2\end{smallmatrix}\right)$, and for small values of time τ, $U_\tau = 1 + M^{(1)}\tau$, where $M^{(1)} = \left(\begin{smallmatrix}0 & 1\\ 0 & 0\end{smallmatrix}\right)$.

Equation (6.16) can now be written as

$$\boldsymbol{\Delta}_{mlnk} = \boldsymbol{\Delta}^{(0)}_{mlnk} + \beta\left(\boldsymbol{g}_{ml}\cdot U_T^{(1)} + \boldsymbol{g}_{10}\cdot U_{2T}^{(1)}\right) + \tau\left(\boldsymbol{g}_{10}U_{2T}^{(0)}M^{(1)}\right), \tag{6.18}$$

where $\Delta^{(0)}$ is given by Equation (6.16) where $\beta \to 0$ and $\tau \to 0$. In the limit where the distribution is slowly varying, the elements of the sum in Equation (6.13) are vanishingly small unless $\Delta^{(0)} = 0$. This implies that $\boldsymbol{g}_{ml} = -2\boldsymbol{g}_{10}$ and $\boldsymbol{g}_{nk} = \boldsymbol{g}_{10}$. Using the definition of $\boldsymbol{g}$, these relations can be written as $k = (1-n)/2$ and $l = -(2+m)/2$. In addition, only the terms where n, (m) are even (odd) contribute to the signal. Equation (6.18) becomes independent of the indices m, l, n, k.

Substituting the explicit matrix representations for Δ and Θ, the interferometer signal is given by

$$S = A\int dudv \exp\left[-i\beta T^2 u + i\tau' v\right] f_0(u,v), \tag{6.19}$$

where $\tau' = \tau - \beta T^3$ and u, v are the components of the vector $\mathbf{y}$. The parameter A in Equation (6.19) is the amplitude of the signal and can be expressed as the sum

$$A = \sum_{n,even} \sum_{m,odd} \frac{\gamma_{nm}}{2i} \exp\left[i \left(\frac{mT}{2} + \frac{m+n}{2}\tau' + \frac{5m}{12}\beta T^3 \right) \right], \tag{6.20}$$

where

$$\gamma_{nm} = 2(-1)^{(n-1)/2+m/2} J_{(1-n)/2} J_{(1+n)/2} J_{-(2+m)/2} J_{-(2-m)/2} \tag{6.21}$$

determines proportion of the atoms scattered into each mode.

Equation (6.19) is the primary result of this analysis and will be used for the case of a thermal atomic cloud in Section 6.4.

6.4 Discussion

By taking the limit where $\Xi \ll 1$, only the lowest order contributions to Equation (6.20) need to be retained. If we keep $n = \pm 1$ and $m = 0, \pm 2$ and use the limiting values of J_n for the small argument, $\gamma_{10} \approx -2\gamma_{12} \approx \Xi/4$, then

$$A = \sin\left(\frac{1}{2}\tau'\right) \frac{\Xi^3}{4} \left[1 + \cos\left(T + \frac{5\beta T^3}{6} + \tau' \right) \right]. \tag{6.22}$$

Assuming that the initial distribution is a thermal cloud of temperature $\mathcal{T}$ that is in equilibrium with the trap with frequency ω_0, the distribution f_0 becomes

$$f_0 = \frac{\omega_0}{2\pi\mathcal{T}} \exp\left(-\frac{p^2}{2\mathcal{T}} - \frac{\omega_0^2 x^2}{2\mathcal{T}} \right). \tag{6.23}$$

By comparison, the initial distribution of a condensate would be well approximated by the ground state of a harmonic oscillator. Using Equation (6.5), the pure state Wigner function is equivalent to Equation (6.23) when $\mathcal{T} = \omega_0/2$. During the transition from an incoherent thermal gas to a pure BEC, the distribution is a sum of f_0 and f_{pure}, weighted by the number of atoms in and out of the ground state, where $N_0/N = 1 - (\mathcal{T}/\mathcal{T}_c)^3$ and $\mathcal{T}_c = \bar{\omega}_0 (N/\zeta(3))^{1/3}$. N_0/N is the ratio of condensed atoms to the total, and ζ is the Riemann zeta function. This combined distribution can be used with Equation (6.19) to find the expected signal.

Returning focus to the incoherent thermal gas, substituting Equations (6.22) and (6.23) into Equation (6.19) and performing the integral yields

$$S = A \exp\left[-\frac{\mathcal{T}}{2}\left(\frac{\beta T^2}{\omega_0}\right)^2 - \frac{\mathcal{T}}{2}\tau'^2\right]. \tag{6.24}$$

To quantify the signal visibility, we define the echo strength as $\mathcal{I} = \Xi^6 \int d\tau' S^2$, which is proportional to the total number of photons (electromagnetic energy) of the backscattered light during the read-out pulse. In the limit where $\mathcal{T} \gg 1$, Equation (6.24) can be integrated, yielding

$$\mathcal{I} = \frac{\pi^{1/2}\mathcal{A}^2}{32\mathcal{T}^{3/2}} \exp\left[-\mathcal{T}\left(\frac{\beta T^2}{\omega_0}\right)^2\right], \tag{6.25}$$

where

$$\mathcal{A} = \frac{1}{4}\left[1 + \cos\left(T + \frac{5}{6}\beta T^3\right)\right]. \tag{6.26}$$

Equation (6.25) diverges in the limit $\mathcal{T} \to 0$, which is clearly an unphysical result. However, the numerical integration of Equation (6.24) remains finite.

Note that $\mathcal{I}$ is an oscillating function, and is well known in the $\beta = 0$ case [114]. Figure 6.2 shows a schematic of Equation (6.25) as a function of interferometer time T for $\beta > 0$. The dotted line is the envelope of the echo strength. Figure 6.3 shows a schematic of Equation (6.25) as a function of interferometer time T for $\beta < 0$.

The oscillation frequency increases when $\beta > 0$ and decreases when $\beta < 0$, and there is a maxima when $T + 5\beta T^3/6 = 2\pi n$. These oscillations depend only on the values of β and T. In a typical experiment, the oscillation frequency is much larger than depicted in Figure 6.2 or Figure 6.3. For the remainder of the chapter, it will be assumed that the interferometer time is tuned to be at the peak of an oscillation, which will be referred to as $\mathcal{I}_m$.

In order to maximize signal strength, it is also useful to release the atomic sample into the waveguide from the correct initial trap. Typically, the atomic gas is evaporatively cooled

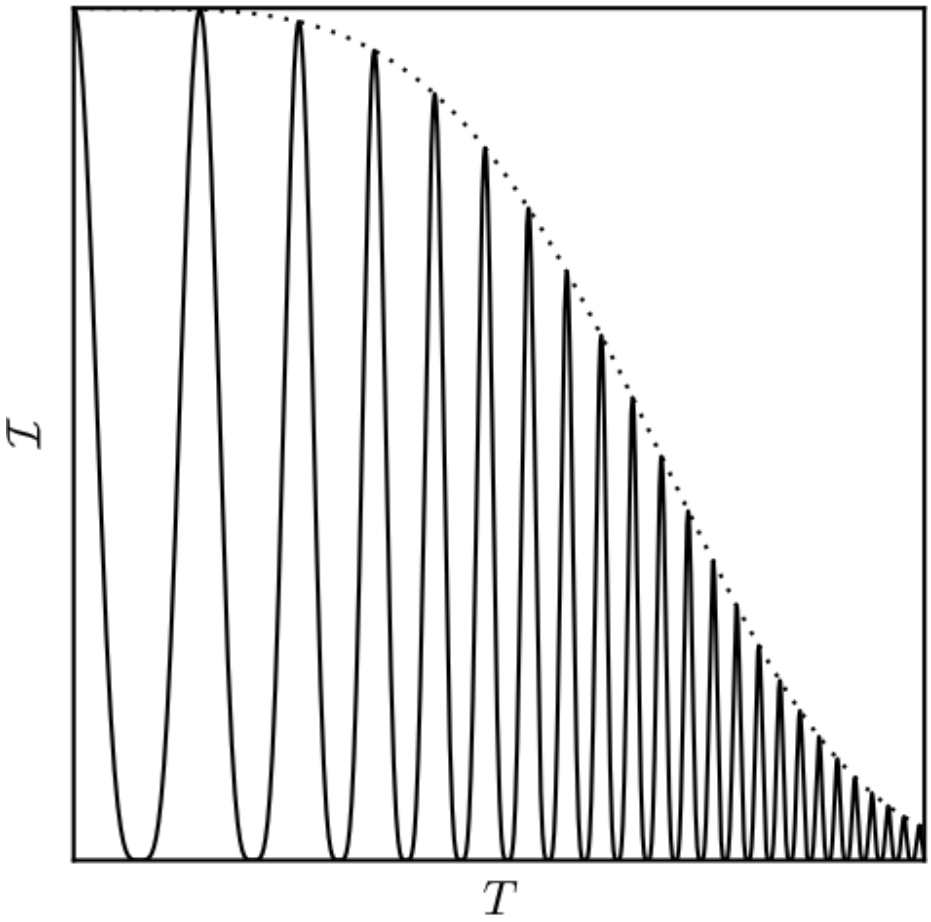

Figure 6.2: A schematic of the echo signal strength, $\mathcal{I}$, as a function of interferometer time, T, for an interferometer in a positive residual trapping potential, i.e., $\beta > 0$. The signal strength is proportional to the total number of backscattered photons during the readout laser pulse. $\mathcal{I}$ is periodic with an increasing frequency within an envelope defined by the dotted curve.

to a temperature $\mathcal{T}^{(e)}$ in a trap with frequency $\omega^{(e)}$. After cooling, the trap frequencies are adiabatically changed to a trap with frequency ω_0 and then released into a waveguide with residual potential curvature β. During the adiabatic transformation, the phase space density is constant. This condition implies $D = \mathcal{T}^3/\omega$ is held constant, assuming the radial trap

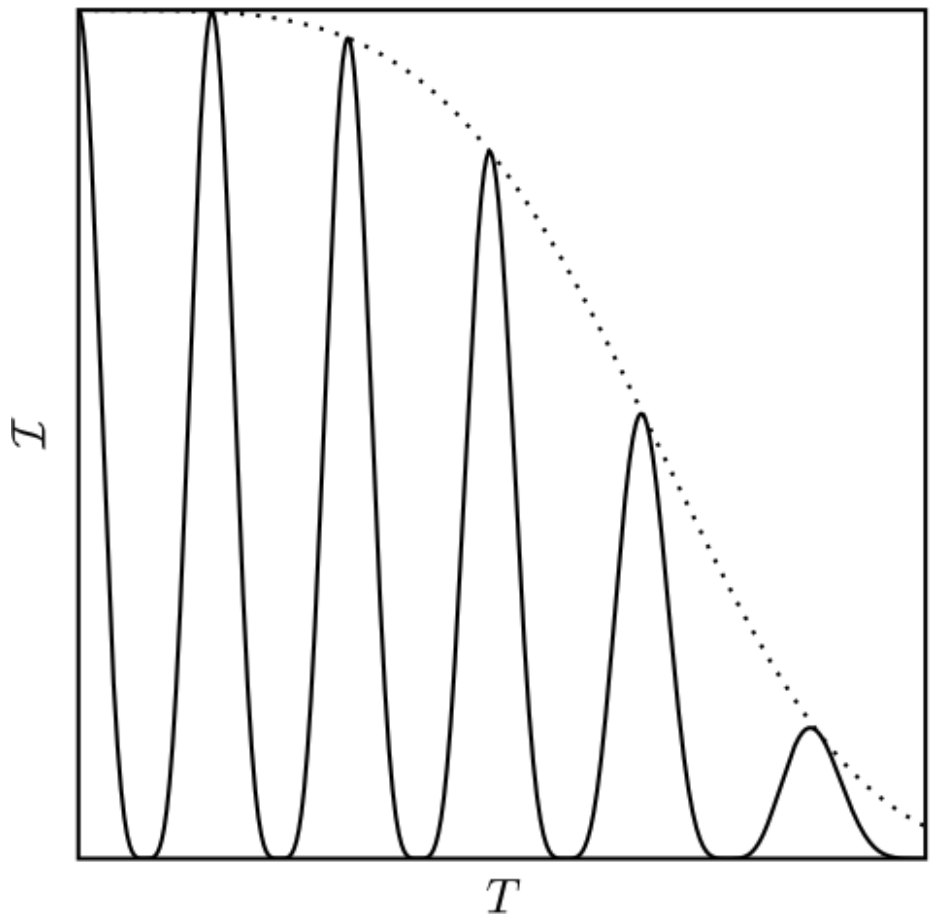

Figure 6.3: A schematic of the echo signal strength, $\mathcal{I}$, as a function of interferometer time, T, for an interferometer in a negative residual trapping potential, i.e., $\beta < 0$. Like the positive potential case, the signal strength is periodic and contained within a decaying envelope. However, the negative potential causes a decreasing frequency. Both positive and negative potentials have the same envelope.

frequencies $\omega_\perp$ are unchanged. Then Equation (6.25) can be recast as

$$\mathcal{I}_m = \frac{\pi^{1/2}}{32(D^{(e)})^2\omega_0^2} \exp\left[-\frac{(D^{(e)})^{1/3}}{\omega_0^{5/3}}(\beta T^2)^2\right], \tag{6.27}$$

where $D^{(e)} = (\mathcal{T}^{(e)})^3/\omega^{(e)}$ is proportional to the phase space density at the end of the evaporation.

For this analysis, assume the cloud is evaporatively cooled in a trap with frequency $\omega^{(e)} = 2\pi \times 10^{-4}$ and to a temperature $\mathcal{T} = 10$. For ^{87}Rb, these parameters correspond to a gas cooled in a trap with a frequency of 20 Hz to a temperature of 14 μK. The phase space density is proportional to $D^{(e)} = 10^{-6}/2\pi$. Figure 6.4 shows the echo strength, Equation (6.27), as a function of decompressed trap frequency ω_0. The remaining parameter $|\beta|^{1/2}T = 10^{-2}$, corresponds to a cycle time of 10 ms and a residual frequency of 0.3 Hz. In this case, the decompressed trap frequency is roughly half the evaporative trap frequency.

For small values of $\omega_0 \ll 1$, the echo strength vanishes because the weak trap creates a large cloud, which experiences more de-phasing due to the residual potential. On the other hand, when $\omega_0 \gg 1$, the echo strength vanishes because the tight trap increases the temperature of the cloud, resulting in a shorter echo duration.

The ratio of ideal starting trap frequency ω_0 and evaporation trap frequency $\omega^{(e)} = 2\pi \times 10^{-3}$ is shown as as a function of $|\beta|^{1/2}T$ in Figure 6.5. The dash-dot line is the ideal frequency if the gas is cooled to a temperature of $\mathcal{T} = 1$, the solid line is the ideal frequency when $\mathcal{T} = 10$, and the dashed line is when $\mathcal{T} = 20$.

For values where $\omega_0/\omega_e < 1$, the ideal starting frequency is lower than the evaporation frequency, i.e., the gas should be decompressed before the beginning of the interferometer cycle. At the cost of increasing the cloud size, it is more advantageous the lower the temperature. For the case where $\omega_0/\omega_e > 1$, the gas should be compressed, raising the temperature by reducing the size of the cloud.

6.5 Outlook

Tuning the interferometer time T and the injection trap frequency ω_0 allows for maximal signal visibility. However, these optimizations cannot overcome the $\exp(-\beta^2)$ dependence in Equation (6.25). Even a small residual potential dramatically reduces

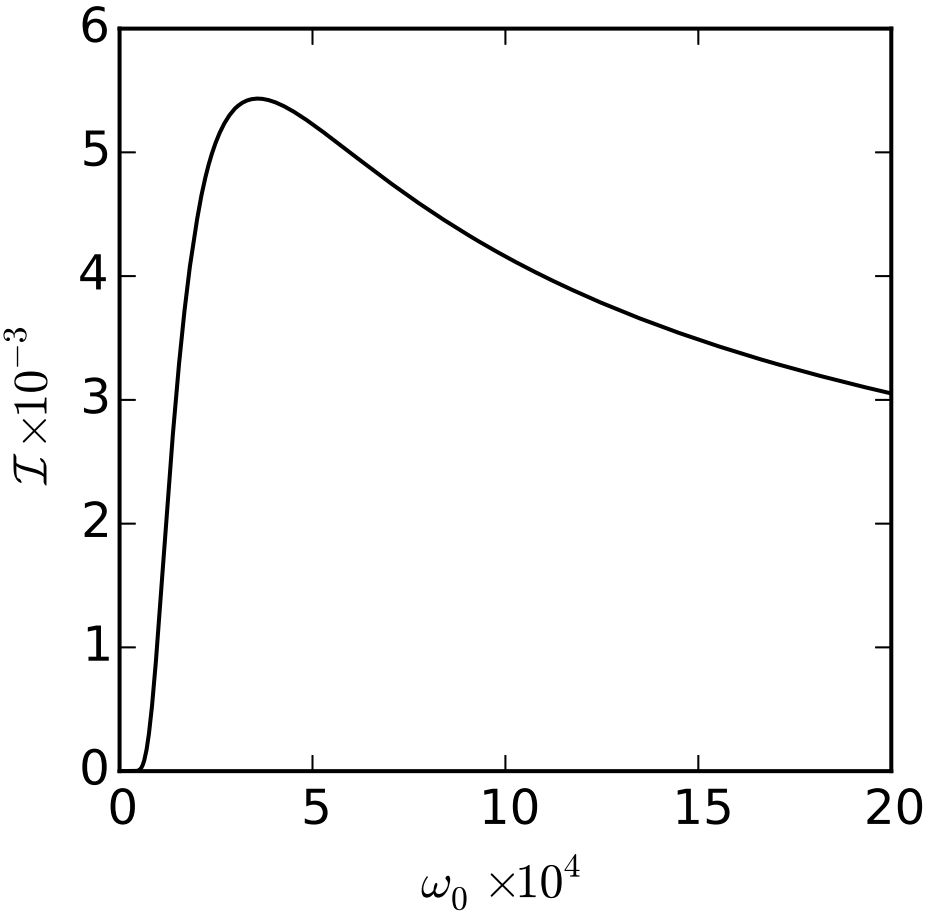

Figure 6.4: The signal strength as a function of injection trap frequency, ω_0. After evaporation in a trap with frequency $\omega^{(e)}$, the trap potential is adiabatically transformed to ω_0 before the interferometer cycle begins. At the start of the cycle, the trap is snapped to $\omega = \sqrt{\beta}$, where it stays. The signal strength peaks at a non-zero injection frequency ω_0. For this case, $\beta T^2 = 10^{-4}$ and $D^{(e)} = 10^6/2\pi$.

coherence times in this version of a trapped Talbot-Lau interferometer. Figure 6.6 shows the signal visibility, Equation (6.25), for several residual potentials. The dashed curve is $\beta = 5 \times 10^{-13}$, the solid line is 10^{-12}, and the dash-dot curve is 10^{-11}. For this plot, $\mathcal{I}_0 = \pi^{1/2}\mathcal{A}^2/32\mathcal{T}^{-3/2}$, with $\mathcal{A} = 1/2$ to correspond to maxima in the signal oscillation. For the time axis, $T \times 10^{-2}$ corresponds roughly to 1 ms.

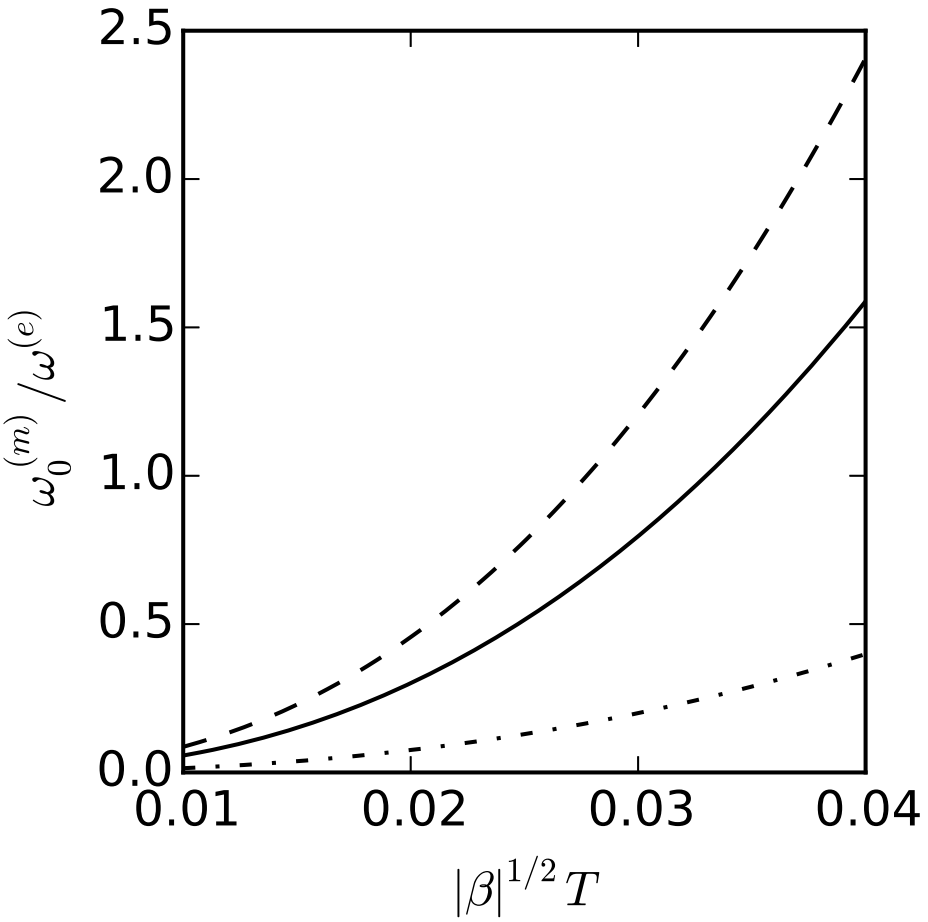

Figure 6.5: The ratio of the ideal injection trap frequency, ω_0, to the evaporation trap frequency, $\omega^{(e)}$, as a function of $|\beta|^{1/2}T$. Here, we use $\omega^{(e)} = 2\pi \times 10^{-3}$, and plot for temperatures $\mathcal{T} = 1$ (dash-dot), $\mathcal{T} = 10$ (solid), and $\mathcal{T} = 20$ (dash). As the ratio $\omega_0/\omega^{(e)}$ becomes greater than one, the gas should be compressed before being released into the interferometer. This compression step raises the temperature, but reduces the size of the cloud.

Clearly, the signal visibility has a strong dependence on residual potential, which must be extremely small for coherence times compared to free space interferometers. In future work, we will explore modifications to the trapped Talbot-Lau scheme with the potential to minimize the coherence time's sensitivity on residual field imperfections.

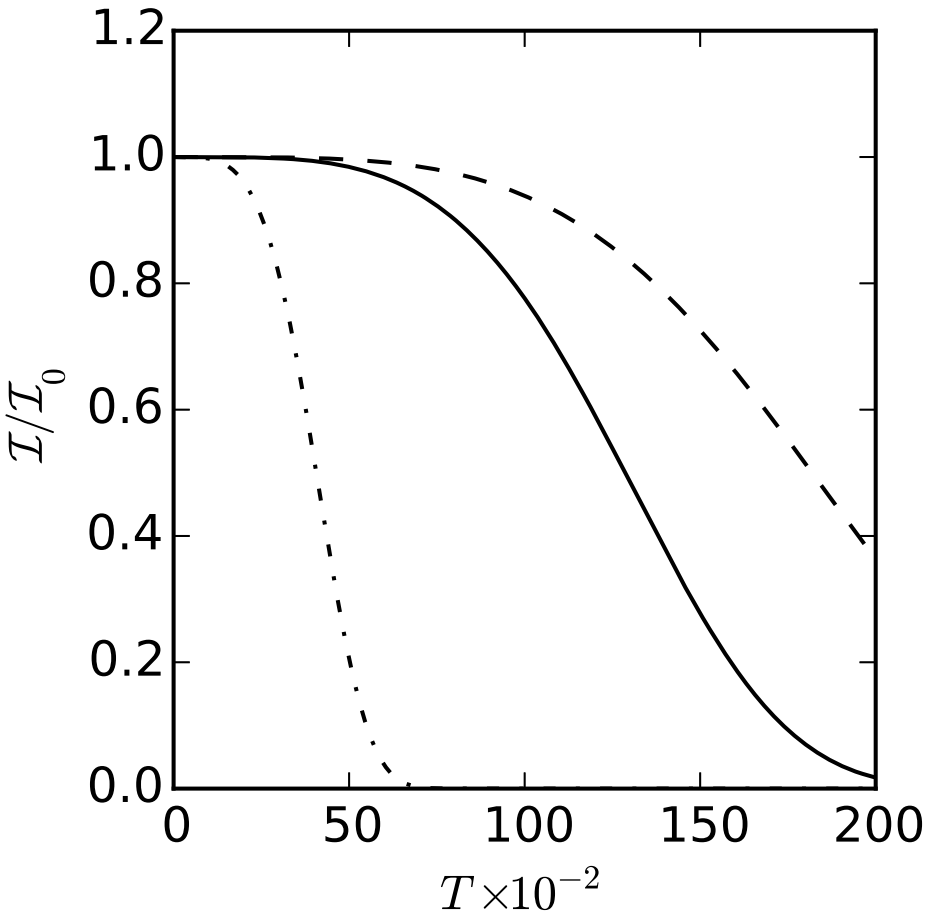

Figure 6.6: The signal visibility, i.e., the decaying envelope that limits the maximum possible signal strength for a given interferometer time T. The decay is proportional to $\exp(-\beta^2)$, causing rapid signal loss for even small residual potentials. Here, $\beta = 5 \times 10^{-13}$ (dashed), 10^{-12} (solid), and 10^{-11} (dash-dot). $T \times 10^{-2}$ corresponds roughly to 1 ms.

The Wigner function approach allows a straightforward way to model interference in an incoherent system such as a cold atomic gas. It can be readily applied to consider different pulse schemes such as those of [93], as well as propagation in more complex confining potentials. The Talbot-Lau interferometer's ability to operate at thermal temperatures is a significant enough benefit to a real-world device that further study is warranted.

Page intentionally left blank

VII. Conclusion and Outlook

7.1 Summary of Major Results

In this dissertation, I have detailed the production and characteristics of the first two-dimensional Grating Magneto-Optical Trap. The 2D GMOT theory was presented and analyzed, revealing the importance of beam intensity, polarization and grating efficiency. Using optimized parameters, the 2D GMOT was used to load a 3D GMOT in a lower pressure chamber.

The 2D GMOT flux ($\sim 10^8$ atoms/s) compares favorably to typical 2D MOTs, given our experiments short atom beam length and low optical power. By using pre-cooled atoms from the 2D GMOT and large-area gratings with substantial capture volume, our 3D GMOT trapped 2×10^8 atoms, the highest GMOT number so far reported. Standard improvements such as higher vacuum quality, more optical power, better beam shaping, and more stable lasers should enable the GMOT flux and trap number to compete with the other known MOT techniques.

Methods were analyzed to fabricate uniform bias and linear magnetic fields on planar structures so external coils would not be necessary. These methods were optimized via a genetic algorithm to account for finite wire length and a promising solution emerged. A chip was tested and showed strong agreement with simulations. Similar methods were used to design a magnetic trap conveyor that does not rely on an external bias.

The chips were shown to project 3 Gauss uniform magnetic fields 5 mm from their surface using a 15 A current. When compared to typical size Helmholtz coil pairs, these results demonstrate planar sources are an attractive alternative with increased optical access.

Finally, the effect of a small harmonic magnetic field along the splitting axis of a thermal Talbot-Lau interferometer was discussed. The non-condensed atoms were modeled

using the Wigner function and the interferometer's signal was derived. The model showed the signal decays rapidly as the remnant field increases.

To combat signal loss, the cold atom production sequence was considered. The magnetic trap used to inject atoms into the interferometer waveguide was shown to have a large impact on signal. In particular, if the injecting trap is too weak, the atom cloud is too large, causing de-phasing due to the residual potential. Alternatively, a strong trap heats the cloud, reducing the time for which the signal appears. Between these extremes, an ideal injection trap was identified for future experiments.

7.2 Future Directions

The flux and speed distribution of the 2D GMOT can be improved with a higher, more uniform cooling laser intensity. The Cold Atom Group is currently building models to predict how a new intensity profile will effect the trap, using theory presented here. The GMOT design enables a significantly smaller experimental footprint incorporating a vacuum chamber with a volume of only $\sim 9 \times 5 \times 1$ cm^3.

Besides scaling down in size, this new chamber will utilize a stack of chips designed using the magnetic field expansions of Chapter 5. Particularly, the 2D GMOT magnetic field will be similar to the optimized 2D guide of the magnetic conveyor, and the 3D GMOT will utilize a three layer chip stack to create a uniform field of arbitrary direction.

If these methods prove successful, the magnetic field control could enable significant suppression of the remnant field in a Talbot-Lau interferometer. Such suppression may result in an improved interference signal from confined thermal atoms on a chip.

7.3 Concluding Thoughts

As cold atom technologies are pushed to harsh environments, many of the traditional methods for cooling, trapping, manipulating, and measuring atoms must be improved. The contributions discussed here represent only a small fraction of the development needed

for a viable, deployable system. While I am convinced that the GMOT is a promising alternative to traditional MOT designs, I have little doubt that newer, better techniques lay on the horizon. Similarly, atom chips and the Talbot-Lau device are promising, but so are other techniques for confined matter interferometry, including optical traps and RF-dressed potentials.

The promise of cold atoms has been apparent for decades, with generations of scientists continually redefining leading-edge technology with increased sensitivity and robustness. I hope that my results contribute to that progress and accelerate cold atom advancements to more widespread applications.

Bibliography

[1] H. Müntinga, H. Ahlers, M. Krutzik, A. Wenzlawski, S. Arnold, D. Becker, K. Bongs, H. Dittus, H. Duncker, N. Gaaloul, C. Gherasim, E. Giese, C. Grzeschik, T. W. Hänsch, O. Hellmig, W. Herr, S. Herrmann, E. Kajari, S. Kleinert, C. Lämmerzahl, W. Lewoczko-Adamczyk, J. Malcolm, N. Meyer, R. Nolte, A. Peters, M. Popp, J. Reichel, A. Roura, J. Rudolph, M. Schiemangk, M. Schneider, S. T. Seidel, K. Sengstock, V. Tamma, T. Valenzuela, A. Vogel, R. Walser, T. Wendrich, P. Windpassinger, W. Zeller, T. van Zoest, W. Ertmer, W. P. Schleich, and E. M. Rasel. Interferometry with Bose-Einstein Condensates in Microgravity. *Physical Review Letters*, 110:093602, Feb 2013.

[2] Forschungsverbund Berlin e.V. Quantum Optical Sensor For The First Time Tested In Space. Phys.org, January 2017.

[3] V. Schkolnik, O. Hellmig, A. Wenzlawski, J. Grosse, A. Kohfeldt, K. Döringshoff, A. Wicht, P. Windpassinger, K. Sengstock, C. Braxmaier, M. Krutzik, and A. Peters. A Compact and Robust Diode Laser System for Atom Interferometry on a Sounding Rocket. *Applied Physics B*, 122(8):217, 2016.

[4] A. Kubelka-Lange, S. Herrmann, J. Grosse, C. Lämmerzahl, E. M. Rasel, and C. Braxmaier. A Three-Layer Magnetic Shielding for the MAIUS-1 Mission on a Sounding Rocket. *Review of Scientific Instruments*, 87(6):063101, 2016.

[5] J. Grosse, S. T. Seidel, D. Becker, M. D. Lachmann, M. Scharringhausen, C. Braxmaier, and E. M. Rasel. Design and Qualification of an UHV System for Operation on Sounding Rockets. *Journal of Vacuum Science & Technology A: Vacuum, Surfaces, and Films*, 34(3):031606, 2016.

[6] B. Barrett, L. Antoni-Micollier, L. Chichet, B. Battelier, T. Lévèque, A. Landragin, and P. Bouyer. Dual Matter-Wave Inertial Sensors in Weightlessness. *Nature Communications*, 7, Dec 2016.

[7] N. Yu. NASA Research Announcement: Research Opportunities in Fundamental Physics. Jet Propulsion Laboratory, October 2013.

[8] NASA. Physical Science Research Proposals Selected for Cold Atom Laboratory. Jet Propulsion Laboratory, January 2014.

[9] K. Bongs, V. Boyer, M. A. Cruise, A. Freise, M. Holynski, J. Hughes, A. Kaushik, Y.-H. Lien, A. Niggebaum, M. Perea-Ortiz, P. Petrov, S. Plant, Y. Singh, A. Stabrawa, D. J. Paul, M. Sorel, D. R. S. Cumming, J. H. Marsh, R. W. Bowtell, M. G. Bason, R. P. Beardsley, R. P. Campion, M. J. Brookes, T. Fernholz, T. M. Fromhold, L. Hackermuller, P. Krger, X. Li, J. O. Maclean, C. J. Mellor,

S. V. Novikov, F. Orucevic, A. W. Rushforth, N. Welch, T. M. Benson, R. D. Wildman, T. Freegarde, M. Himsworth, J. Ruostekoski, P. Smith, A. Tropper, P. F. Griffin, A. S. Arnold, E. Riis, J. E. Hastie, D. Paboeuf, D. C. Parrotta, B. M. Garraway, A. Pasquazi, M. Peccianti, W. Hensinger, E. Potter, A. H. Nizamani, H. Bostock, A. Rodriguez Blanco, G. Sinuco-Leon, I. R. Hill, R. A. Williams, P. Gill, N. Hempler, G. P. A. Malcolm, T. Cross, B. O. Kock, S. Maddox, and P. John. The UK National Quantum Technologies Hub in Sensors and Metrology (Keynote Paper), 2016.

[10] R. Geiger, V. Ménoret, G. Stern, N. Zahzam, P. Cheinet, B. Battelier, A. Villing, F. Moron, M. Lours, Y. Bidel, A. Bresson, A. Landragin, and P. Bouyer. Detecting Inertial Effects with Airborne Matter-Wave Interferometry. *Nature Communications*, 2, Sep 2011.

[11] J. Close. ANU Wins 3 Million for Research on Precision Navigation Device. *Australia National University News*, November 2016.

[12] M. R. Andrews, C. G. Townsend, H.-J. Miesner, D. S. Durfee, D. M. Kurn, W. Ketterle. Observation of Interference Between Two Bose Condensates. *Science*, 275, 1997.

[13] S. Bize, P. Laurent, M. Abgrall, H. Marion, I. Maksimovic, L. Cacciapuoti, J. Grünert, C. Vian, F. Pereira dos Santos, P. Rosenbusch, P. Lemonde, G. Santarelli, P. Wolf, A. Clairon, A. Luiten, M. Tobar, and C. Salomon. Cold Atom Clocks and Applications. *Journal of Physics B: Atomic, Molecular and Optical Physics*, 38(9):S449, 2005.

[14] F.-X. Esnault, E. Blanshan, E. N. Ivanov, R. E. Scholten, J. Kitching, and E. A. Donley. Cold-Atom Double-Λ Coherent Population Trapping Clock. *Physical Review A*, 88:042120, Oct 2013.

[15] A. Wicht, J. M. Hensley, E. Sarajlic, and S. Chu. A Preliminary Measurement of the Fine Structure Constant Based on Atom Interferometry. *Physica Scripta*, 2002(T102):82, 2002.

[16] P. Cladé, E. de Mirandes, M. Cadoret, S. Guellati-Khélifa, C. Schwob, F. Nez, L. Julien, and F. Biraben. Determination of the Fine Structure Constant Based on Bloch Oscillations of Ultracold Atoms in a Vertical Optical Lattice. *Physical Review Letters*, 96:033001, Jan 2006.

[17] J. E. Debs, N. P. Robins, and J. D. Close. Measuring Mass in Seconds. *Science*, 339(6119):532–533, 2013.

[18] J. E. Debs, P. A. Altin, T. H. Barter, D. Döring, G. R. Dennis, G. McDonald, R. P. Anderson, J. D. Close, and N. P. Robins. Cold-Atom Gravimetry with a Bose-Einstein Condensate. *Physical Review A*, 84:033610, Sep 2011.

[19] N. Poli, F.-Y. Wang, M. G. Tarallo, A. Alberti, M. Prevedelli, and G. M. Tino. Precision Measurement of Gravity with Cold Atoms in an Optical Lattice and Comparison with a Classical Gravimeter. *Physical Review Letters*, 106:038501, Jan 2011.

[20] G. Rosi, F. Sorrentino, L. Cacciapuoti, M. Prevedelli, and G. M. Tino. Precision Measurement of the Newtonian Gravitational Constant Using Cold Atoms. *Nature*, 510(7506):518–521, Jun 2014. Letter.

[21] J. M. Hogan, D. M. S. Johnson, S. Dickerson, T. Kovachy, A. Sugarbaker, S. Chiow, P. W. Graham, M. A. Kasevich, B. Saif, S. Rajendran, P. Bouyer, B. D. Seery, L. Feinberg, and R. Keski-Kuha. An Atomic Gravitational Wave Interferometric Sensor in Low Earth Orbit (AGIS-LEO). *General Relativity and Gravitation*, 43:1953–2009, Jul 2011.

[22] R. Lutwak. Micro-Technology for Positioning, Navigation, and Timing Towards PNT Everywhere and Always. Space-Based Positioning Navigation and Timing National Advisory Board Fourteenth Meeting, December 2014. http://www.gps.gov/governance/advisory/meetings/2014-12/lutwak.pdf.

[23] Chief Scientist of the Air Force. *Technology Horizons: A Vision for Air Force Science and Technology 2010-2030*. Air Force Headquarters, 2010.

[24] S. M. Dickerson, J. M. Hogan, A. Sugarbaker, D. M. S. Johnson, and M. A. Kasevich. Multiaxis Inertial Sensing with Long-Time Point Source Atom Interferometry. *Physical Review Letters*, 111:083001, Aug 2013.

[25] E. Imhof, J. Stickney, and M. Squires. A Wigner Function Approach to Coherence in a Talbot-Lau Interferometer. *Atoms*, 4(2), 2016.

[26] J. Stickney, B. Kasch, E. Imhof, B. Kroese, J. Crow, S. Olson, M. Squires. Tunable Axial Potentials for Atom Chip Waveguides. *Arxiv*, 1407.6398, 2014.

[27] M. B. Squires, S. E. Olson, B. Kasch, J. A. Stickney, C. J. Erickson, J. A. R. Crow, E. J. Carlson, and J. H. Burke. Ex Vacuo Atom Chip Bose-Einstein Condensate. *Applied Physics Letters*, 109(26):264101, 2016.

[28] G. della Porta. *Magiae Naturalis*. Naples, 1558.

[29] T. Shachtman. *Absolute Zero and the Conquest of Cold*. Houghton Mifflin Harcourt, 2000.

[30] R. Boyle. *New Experiments and Observations Touching Cold*. J. Crook, 1665.

[31] M. J. Wisniak. Guillaume Amontons. *Revista CENIC Ciencias Químicas*, 36(3):187–195, 2005.

[32] H. K. Onnes. Investigations into the Properties of Substances at Low Temperatures, Which Have Led, Amongst Other Things, to the Preparation of Liquid Helium. Nobel Lecture. Stockholm, 1913.

[33] H. E. Hall, P. J. Ford, and K. Thompson. A Helium-3 Dilution Refrigerator. *Cryogenics*, 6(2):80 – 88, 1966.

[34] A. Ashkin. Atomic-Beam Deflection by Resonance-Radiation Pressure. *Physical Review Letters*, 25:1321–1324, Nov 1970.

[35] C. S. Adams, E. Riis. Laser Cooling and Trapping of Neutral Atoms. *Progress in Quantum Electronics*, 21(1-79), 1997.

[36] D. Steck. Rubidium 87 D Line Data. http://steck.us/alkalidata, September 2001. Los Alamos National Laboratory.

[37] D. J. Griffiths. *Introduction to Quantum Mechanics*. Prentice Hall, 1995.

[38] C. Cohen-Tannoudji. *Quantum Mechanics*. Hermann and John Wiley and Sons, Inc., 1977.

[39] V. S. Letokhov, V. G. Minogin, and B. D. Pavlik. Cooling and Trapping of Atoms and Molecules by a Resonant Laser Field. *Optics Communications*, 19(1):72 – 75, 1976.

[40] W. D. Phillips and H. Metcalf. Laser Deceleration of an Atomic Beam. *Physical Review Letters*, 48:596–599, Mar 1982.

[41] J. V. Prodan, W. D. Phillips, and H. Metcalf. Laser Production of a Very Slow Monoenergetic Atomic Beam. *Physical Review Letters*, 49:1149–1153, Oct 1982.

[42] W. Phillips. Laser Cooling and Trapping of Neutral Atoms. Nobel Lecture. Stockholm, December 1997.

[43] T. W. Hänsch and A. L. Schawlow. Cooling of Gases by Laser Radiation. *Optics Communications*, 13(1):68 – 69, 1975.

[44] S. Chu, L. Hollberg, J. E. Bjorkholm, A. Cable, and A. Ashkin. Three-Dimensional Viscous Confinement and Cooling of Atoms by Resonance Radiation Pressure. *Physical Review Letters*, 55:48–51, Jul 1985.

[45] S. Chu. The Manipulation of Neutral Particles. Nobel Lecture. Stockholm, December 1997.

[46] K.-J. Kügler, W. Paul, and U. Trinks. A Magnetic Storage Ring for Neutrons. *Physics Letters B*, 72(3):422 – 424, 1978.

[47] M. Squires. *High Repetition Rate Bose-Einstein Condensate Production in a Compact, Transportable Vacuum*. PhD thesis, University of Colorado, Boulder, 2008.

[48] M. P. A. Jones. *Bose-Einstein Condensation on an Atom Chip*. PhD thesis, University of Sussex, 2002.

[49] E. Majorana. Atomi Orientati In Campo Magnetico Variabile. *Il Nuovo Cimento*, 9(43-50), 1932.

[50] A. Ashkin and J. P. Gordon. Stability of Radiation-Pressure Particle Traps: An Optical Earnshaw Theorem. *Optics Letters*, 8(10):511–513, Oct 1983.

[51] D. E. Pritchard, E. L. Raab, V. Bagnato, C. E. Wieman, and R. N. Watts. Light Traps Using Spontaneous Forces. *Physical Review Letters*, 57:310–313, Jul 1986.

[52] E. L. Raab, M. Prentiss, A. Cable, S. Chu, and D. E. Pritchard. Trapping of Neutral Sodium Atoms with Radiation Pressure. *Physical Review Letters*, 59:2631–2634, Dec 1987.

[53] P. D. Lett, R. N. Watts, C. I. Westbrook, W. D. Phillips, P. L. Gould, and H. J. Metcalf. Observation of Atoms Laser Cooled below the Doppler Limit. *Physical Review Letters*, 61:169–172, Jul 1988.

[54] C. Cohen-Tannoudji. Manipulating Atoms with Photons. Nobel Lecture. Stockholm, December 1997.

[55] C. Cohen-Tannoudji. Laser Cooling and Trapping of Neutral Atoms: Theory. *Physics Reports*, 219(3):153 – 164, 1992.

[56] M. S. Ioffe and R. I. Sobolev. Confinement of a Plasma in a Trap Formed by a Combined Magnetic Field. *Journal of Nuclear Energy. Part C, Plasma Physics, Accelerators, Thermonuclear Research*, 7(5):501, 1965.

[57] D. E. Pritchard. Cooling Neutral Atoms in a Magnetic Trap for Precision Spectroscopy. *Physical Review Letters*, 51:1336–1339, Oct 1983.

[58] H. F. Hess. Evaporative Cooling of Magnetically Trapped and Compressed Spin-Polarized Hydrogen. *Physical Review B*, 34:3476–3479, Sep 1986.

[59] C. C. Bradley, C. A. Sackett, J. J. Tollett, and R. G. Hulet. Evidence of Bose-Einstein Condensation in an Atomic Gas with Attractive Interactions. *Physical Review Letters*, 75:1687–1690, Aug 1995.

[60] N. Bose. Plancks Gesetz und Lichtquantenhypothese. *Zeitschrift fur Physik*, 26(1), 1924.

[61] A. Einstein. Quantentheorie des Einatomigen Idealen Gases. *Sitzungsberichte der Preussischen Akademie der Wissenschaften*, 1(3), 1925.

[62] M. H. Anderson, J. R. Ensher, M. R. Matthews, C. E. Wieman, and E. A. Cornell. Observation of Bose-Einstein Condensation in a Dilute Atomic Vapor. *Science*, 269, 1995.

[63] K. B. Davis, M. O. Mewes, M. R. Andrews, N. J. van Druten, D. S. Durfee, D. M. Kurn, and W. Ketterle. Bose-Einstein Condensation in a Gas of Sodium Atoms. *Physical Review Letters*, 75:3969–3973, Nov 1995.

[64] E. Cornell and C. Wieman. Bose-Einstein Condensation in a Dilute Gas; the First 70 Years and Some Recent Experiments. Nobel Lecture. Stockholm, December 2001.

[65] W. Ketterle. When Atoms Behave As Waves: Bose-Einstein Condensation and the Atom Laser. Nobel Lecture. Stockholm, December 2001.

[66] C. J. Bordé. Atomic Interferometry with Internal State Labelling. *Physics Letters A*, 140(1):10 – 12, 1989.

[67] A. Peters, K. Y. Chung, and S. Chu. High-Precision Gravity Measurements Using Atom Interferometry. *Metrologia*, 38(25-61), 2001.

[68] M. Kasevich, D. S. Weiss, E. Riis, K. Moler, S. Kasapi, and S. Chu. Atomic Velocity Selection Using Stimulated Raman Transitions. *Physical Review Letters*, 66:2297–2300, May 1991.

[69] M. Kasevich and S. Chu. Atomic Interferometry Using Stimulated Raman Transitions. *Physical Review Letters*, 67:181–184, Jul 1991.

[70] J. M. McGuirk. *High Precision Absolute Gravity Gradiometry with Atom Interferometry*. PhD thesis, Stanford University, 2001.

[71] M. A. Kasevich. *Atom Interferometry in an Atomic Fountain*. PhD thesis, Stanford University, 1992.

[72] K. Moler, D. S. Weiss, M. Kasevich, and S. Chu. Theoretical Analysis of Velocity-Selective Raman Transitions. *Physical Review A*, 45(1), 1991.

[73] P. A. Altin, M. T. Johnsson, V. Negnevitsky, G. R. Dennis, R. P. Anderson, J. E. Debs, S. S. Szigeti, K. S. Hardman, S. Bennetts, G. D. McDonald, L. D. Turner, J. D. Close, and N. P. Robins. Precision Atomic Gravimeter Based on Bragg Diffraction. *New Journal of Physics*, 15(023009), 2013.

[74] G. W. Biedermann, X. Wu, L. Deslauriers, S. Roy, C. Mahadeswaraswamy, and M. A. Kasevich. Testing Gravity with Cold-Atom Interferometers. *Physical Review A*, 91(033629), 2015.

[75] J. M. McGuirk, G. T. Foster, J. B. Fixler, M. J. Snadden, and M. A. Kasevich. Sensitive Absolute-Gravity Gradiometry Using Atom Interferometry. *Physical Review A*, 65(033608), 2002.

[76] S. Chu. Cooling and Trapping of Atoms and Particles: Technical Report for AFOSR Grant 91-0395. Technical report, Stanford University, Washington, DC, 1991.

[77] C. Wieman and E. Cornell. Spontaneous Force Optical Traps: Technical Report for ONR Grant N00014-91-J-1006. Technical report, University of Colorado at Boulder, Washington, DC, 1996.

[78] S. Chiow, T. Kovachy, H. Chien, and M. A. Kasevich. $102\hbar k$ Large Area Atom Interferometers. *Physical Review Letters*, 107:130403, Sep 2011.

[79] Y. Wang, D. Anderson, V. Bright, E. Cornell, Q. Diot, T. Kishimoto, M. Prentiss, R. Saravanan, S. Segal, S. Wu. Atom Michelson Interferometer on a Chip Using a Bose-Einstein Condensate. *Physical Review Letters*, 94(090405), 2005.

[80] S. Du, M. B. Squires, Y. Imai, L. Czaia, R. A. Saravanan, V. Bright, J. Reichel, T. W. Hänsch, D. Anderson. Bose-Einstein Condensation in a Gas of Sodium Atoms. *Physical Review A*, 70(053606), 2004.

[81] J. Fortágh and C. Zimmermann. Magnetic Microtraps for Ultracold Atoms. *Reviews of Modern Physics*, 79:235–289, Feb 2007.

[82] M. Vangeleyn, P. F. Griffin, E. Riis, and A. S. Arnold. Laser Cooling with a Single Laser Beam and a Planar Diffractor. *Optics Letters*, 35(20):3453–3455, Oct 2010.

[83] J. Esteve. Cold Atoms: Trapped by Nanostructures. *Nature Nanotechnology*, 8(5):317–318, May 2013.

[84] C.C. Nshii, M. Vangeleyn, J.P. Cotter, P.F. Griffin, E. A. Hinds, C. N. Ironside, P. See, A. G. Sinclair, E. Riis, and A.S. Arnold. A Surface-Patterned Chip as a Strong Source of Ultracold Atoms for Quantum Technologies. *Nature Nanotechnology*, 8(5):321–324, May 2013.

[85] J. Lee, J. A. Grover, L. A. Orozco, and S. L. Rolston. Sub-Doppler Cooling of Neutral Atoms in a Grating Magneto-Optical Trap. *Journal of the Optical Society of America B*, 30(11):2869–2874, Nov 2013.

[86] T. Schumm, P. Kruger, S. Hofferberth, I. Lesanovsky, S. Wildermuth, S. Groth, I. Bar-Joseph, L. M. Andersson, and J. Schmiedmayer. A Double Well Interferometer on an Atom Chip. *Quantum Information Processing*, 5(6), 2006.

[87] A. Hilico, C. Solaro, M.K. Zhou, M. Lopez, and F. Pereira dos Santos. Contrast Decay in a Trapped-Atom Interferometer. *Physical Review A*, 91(053616), 2015.

[88] M. Horikoshi and K. Nakagawa. Dephasing Due to Atom-Atom Interaction in a Waveguide Interferometer Using a Bose-Einstein Condensate. *Physical Review A*, 74(031602(R)), 2006.

[89] J. Burke, C. Sackett. Scalable Bose-Einstein-Condensate Sagnac Interferometer in a Linear Trap. *Physical Review A*, 80(061603(R)), 2009.

[90] S. Wu, E. Su, M. Prentiss. Time Domain de Broglie Wave Interferometry Along a Magnetic Guide. *European Physical Journal D*, 35(DOI: 10:1140/epjd/e2005-00212-8), 2005.

[91] W. Xiong, X. Zhou, X. Yue, X. Chen, B. Wu, and H. Xiong. Critical Correlations in an Ultra-Cold Bose Gas Revealed By Means of a Temporal Talbot-Lau Interferometer. *Laser Physics Letters*, 10(125502), 2013.

[92] C. Mok, B. Barrett, A. Carew, R. Berthiaume, S. Beattie, and A. Kumarakrishnan. Demonstration of Improved Sensitivity of Echo Interferometers to Gravitational Acceleration. *Physical Review A*, 88(023614), 2013.

[93] S. Wu. *Light Pulse Talbot-Lau Interferometry with Magnetically Guided Atoms*. PhD thesis, Harvard University, 2007.

[94] E. Su, S. Wu, M. Prentiss. Atom Interferometry Using Wave Packets with Constant Spatial Displacements. *Physical Review A*, 81(043631), 2010.

[95] C. Wieman, G. Flowers, S. Gilbert. Inexpensive Laser Cooling and Trapping Experiment for Undergraduate Laboratories. *American Journal of Physics*, 63(4), 1994.

[96] Alkali Metal Dispensers. SAES Group Promotional Materials.

[97] RMCybernetics. A DIY Induction Heater. http://www.rmcybernetics.com/.

[98] M. B. Squires, J. A. Stickney, E. J. Carlson, P. M. Baker, W. R. Buchwald, S. Wentzell, and S. M. Miller. Atom Chips on Direct Bonded Copper Substrates. *Review of Scientific Instruments*, 82(2):023101, 2011.

[99] K. Dieckmann, R. J. C. Spreeuw, M. Weidemüller, and J. T. M. Walraven. Two-Dimensional Magneto-Optical Trap as a Source of Slow Atoms. *Physical Review A*, 58:3891–3895, Nov 1998.

[100] M. Vangeleyn. *Atom Trapping in Non-Trivial Geometries for Micro-Fabrication Applications*. PhD thesis, University of Strathclyde, 2011.

[101] J. P. McGilligan, P. F. Griffin, E. Riis, and A. S. Arnold. Phase-Space Properties of Magneto-Optical Traps Utilising Micro-Fabricated Gratings. *Optics Express*, 23(7):8948–8959, Apr 2015.

[102] J. P. McGilligan, P. F. Griffin, E. Riis, and A. S. Arnold. Diffraction-Grating Characterization for Cold-Atom Experiments. *Journal of the Optical Society of America B*, 33(6):1271–1277, Jun 2016.

[103] J. P. Cotter, J. P. McGilligan, P. F. Griffin, I. M. Rabey, K. Docherty, E. Riis, A. S. Arnold, and E. A. Hinds. Design and fabrication of diffractive atom chips for laser cooling and trapping. *Applied Physics B*, 122(6):172, 2016.

[104] J. Schoser, A. Batär, R. Löw, V. Schweikhard, A. Grabowski, Yu. B. Ovchinnikov, and T. Pfau. Intense Source of Cold Rb atoms from a Pure Two-Dimensional Magneto-Optical Trap. *Physical Review A*, 66:023410, Aug 2002.

[105] J. Ramirez-Serrano, N. Yu, J. M. Kohel, J. R. Kellogg, and L. Maleki. Multistage Two-Dimensional Magneto-Optical Trap as a Compact Cold Atom Beam Source. *Optics Letters*, 31(6):682–684, Mar 2006.

[106] J. R. Kellogg, D. Schlippert, J. M. Kohel, R. J. Thompson, D. C. Aveline, and N. Yu. A Compact High-Efficiency Cold Atom Beam Source. *Applied Physics B*, 109(1):61–64, 2012.

[107] M. W. Garrett. Axially Symmetric Systems for Generating and Measuring Magnetic Fields. Part I. *Journal of Applied Physics*, 22(9), 1951.

[108] E. Boridy. Magnetic Fields Generated by Axially Symmetric Systems. *Journal of Applied Physics*, 66(5691), 1989.

[109] J. C. Maxwell. *Treatise on Electricity and Magnetism, Vol. II*. Dover, NY, 1954.

[110] L. W. McKeehan. Combinations of Circular Currents for Producing Uniform Magnetic Fields. *Review of Scientific Instruments*, 7(3):150–153, 1936.

[111] A. Sauter and F. Sauter. Die Erzeugung von Möglichst Homogenen Magnetfeldern durch Stromsysteme. *Zeitschrift für Physik*, 122(1):120–136, 1944.

[112] P. Hommelhoff, W. Hansel, T. Steinmetz, T. W. Hansch, and J. Reichel. Transporting, Splitting and Merging of Atomic Ensembles in a Chip Trap. *New Journal of Physics*, 7(3), 2005.

[113] J. Stickney, M. Squires, J. Scoville, P. Baker, S. Miller. Collisional Decoherence in Trapped-Atom Interferometers That Use Nondegenerate Sources. *Physical Review A*, 79(013618), 2009.

[114] S. B. Cahn, A. Kumarakrishnan, U. Shim, T. Sleator, P. R. Berman, and B. Dubetsky. Time-Domain de Broglie Wave Interferometry. *Physical Review Letters*, 79:784–787, Aug 1997.

[115] H. J. Lewandowski. *Coherences and Correlations in an Ultracold Bose Gas*. PhD thesis, University of Colorado, Boulder, 2002.

Appendix A: GMOT Theory

A.1 Linear Approximation of the MOT Force

A beam with intensity I_j and detuning Δ drives $F = 0 \rightarrow F' = 1$ transitions from the ground state $m_F = 0$ to three excited states $m_F = -1, 0, +1$. If the beam has right circular polarization, define $s = +1$. If the beam has left circular polarization, define $s = -1$. The beam's wavevector $\mathbf{k}_j$ makes an angle φ with the local magnetic field $\mathbf{B}$ such that $\cos\varphi = \hat{\mathbf{k}}_j \cdot \hat{\mathbf{B}}$. The beam drives transitions to state m_F with fractional intensities I_{m_F} given by

$$\begin{aligned} I_{-1} &= I_j \left(\frac{1 + s\cos\varphi}{2} \right)^2, \\ I_0 &= I_j \left(\frac{\sin^2\varphi}{2} \right), \\ I_{+1} &= I_j \left(\frac{1 - s\cos\varphi}{2} \right)^2. \end{aligned} \tag{A.1}$$

Then, defining $\alpha_{m_F} = I_{m_F}/I_j$, the average force on an atom with velocity $\mathbf{v}$ located within $\mathbf{B}$ is

$$\mathcal{F}_j = \hbar \mathbf{k}_j \frac{\Gamma}{2} \frac{I_j}{I_{sat}} \sum_{m_F=-1,0,1} \frac{\alpha_{m_F}}{1 + \frac{\sum_j I_j}{I_{sat}} + \frac{4(\Delta - \mathbf{k}_j \cdot \mathbf{v} - \mu_F m_F B/\hbar)^2}{\Gamma^2}}, \tag{A.2}$$

where $\mu_F = g_F \mu_B$ for the excited state.

Expand for the case of small Doppler and Zeeman shifts with respect to the detuning (i.e. $\mathbf{k}_j \cdot \mathbf{v} + \mu_F m_F B/\hbar << \Delta$). To prepare, pull the Δ out,

$$\mathcal{F}_j = \hbar \mathbf{k}_j \frac{\Gamma}{2} \frac{I_j}{I_{sat}} \sum_{m_F=-1,0,+1} \frac{\alpha_{m_F}}{1 + \frac{\sum_j I_j}{I_{sat}} + \frac{4\Delta^2}{\Gamma^2}(1 - \frac{\mathbf{k}_j \cdot \mathbf{v}}{\Delta} - \frac{\mu_F m_F B}{\hbar\Delta})^2}, \tag{A.3}$$

and call

$$x = \frac{\mathbf{k}_j \cdot \mathbf{v}}{\Delta} + \frac{\mu_F m_F B}{\hbar\Delta}.$$

Then,

$$\boldsymbol{\mathcal{F}}_j = \hbar \mathbf{k}_j \frac{\Gamma}{2} \frac{I_j}{I_{sat}} \sum_{m_F=-1,0,+1} \frac{\alpha_{m_F}}{1 + \frac{\sum_j I_j}{I_{sat}} + \frac{4\Delta^2}{\Gamma^2}(1-x)^2}. \tag{A.4}$$

The Taylor expansion says $f(x) = f(0) + f'(0)x + \cdots$, so

$$\boldsymbol{\mathcal{F}}_j \approx \hbar \mathbf{k}_j \frac{\Gamma}{2} \frac{I_j}{I_{sat}} \sum_{m_F=-1,0,+1} \alpha_{m_F} \left(\frac{1}{1 + \frac{\sum_j I_j}{I_{sat}} + \frac{4\Delta^2}{\Gamma^2}} + \frac{\frac{8\Delta^2}{\Gamma^2}(1-x)}{\left(1 + \frac{\sum_j I_j}{I_{sat}} + \frac{4\Delta^2}{\Gamma^2}(1-x)^2\right)^2} \bigg|_{x=0} x \right) \tag{A.5}$$

$$\boldsymbol{\mathcal{F}}_j \approx \hbar \mathbf{k}_j \frac{\Gamma}{2} \frac{I_j}{I_{sat}} \sum_{m_F=-1,0,+1} \alpha_{m_F} \left(\frac{1}{1 + \frac{\sum_j I_j}{I_{sat}} + \frac{4\Delta^2}{\Gamma^2}} + \frac{\frac{8\Delta^2}{\Gamma^2}}{\left(1 + \frac{\sum_j I_j}{I_{sat}} + \frac{4\Delta^2}{\Gamma^2}\right)^2} x \right). \tag{A.6}$$

Now identify the constant $K = 1/\left(1 + \frac{\sum_j I_j}{I_{sat}} + \frac{4\Delta^2}{\Gamma^2}\right)$. Then,

$$\boldsymbol{\mathcal{F}}_j \approx \hbar \mathbf{k}_j \frac{\Gamma}{2} \frac{I_j}{I_{sat}} \sum_{m_F=-1,0,+1} \alpha_{m_F} \left(K + \frac{8\Delta^2 K^2}{\Gamma^2} x \right). \tag{A.7}$$

Identify $C = 8K^2\Delta/\Gamma^2$. Then,

$$\boldsymbol{\mathcal{F}}_j \approx \hbar \mathbf{k}_j \frac{\Gamma}{2} \frac{I_j}{I_{sat}} \sum_{m_F=-1,0,+1} \alpha_{m_F} \left(K + C\Delta x \right). \tag{A.8}$$

Reinserting x,

$$\boldsymbol{\mathcal{F}}_j \approx \hbar \mathbf{k}_j \frac{\Gamma}{2} \frac{I_j}{I_{sat}} \sum_{m_F=-1,0,+1} \alpha_{m_F} \left(K + C\Delta \left(\frac{\mathbf{k}_j \cdot \mathbf{v}}{\Delta} + \frac{\mu_F m_F B}{\hbar \Delta} \right) \right). \tag{A.9}$$

We arrive at

$$\boldsymbol{\mathcal{F}}_j \approx \hbar \mathbf{k}_j \frac{\Gamma}{2} \frac{I_j}{I_{sat}} \sum_{m_F=-1,0,+1} \alpha_{m_F} \left(K + C \left(\mathbf{k}_j \cdot \mathbf{v} + \frac{\mu_F m_F B}{\hbar} \right) \right). \tag{A.10}$$

Now insert the transition strengths α_{m_F},

$$\begin{aligned} \boldsymbol{\mathcal{F}}_j \approx \hbar \mathbf{k}_j \frac{\Gamma}{2} \frac{I_j}{I_{sat}} \Bigg[& \frac{(1 - s\cos\varphi)^2}{4} \left(K + C \left(\mathbf{k}_j \cdot \mathbf{v} + \frac{\mu_F B}{\hbar} \right) \right) \\ & + \frac{\sin^2\varphi}{4} \left(K + C \left(\mathbf{k}_j \cdot \mathbf{v} \right) \right) + \frac{(1 + s\cos\varphi)^2}{4} \left(K + C \left(\mathbf{k}_j \cdot \mathbf{v} - \frac{\mu_F B}{\hbar} \right) \right) \Bigg]. \end{aligned} \tag{A.11}$$

Note that $\sin^2\varphi/4 + (1 + s\cos\varphi)^2/4 + (1 - s\cos\varphi)^2/4 = 1$ and $(1 + s\cos\varphi)^2/4 - (1 - s\cos\varphi)^2/4 = s\cos\varphi$. Then,

$$\mathcal{F}_j \approx \hbar \mathbf{k}_j \frac{\Gamma}{2} \frac{I_j}{I_{sat}} \left(K + C \left(\mathbf{k}_j \cdot \mathbf{v} - s \frac{\mu_F B}{\hbar} \cos\varphi \right) \right). \tag{A.12}$$

Recalling the definition of $\cos\varphi$,

$$\mathcal{F}_j \approx \hbar \mathbf{k}_j \frac{\Gamma}{2} \frac{I_j}{I_{sat}} \left(K + C \left(\mathbf{k}_j \cdot \mathbf{v} - s \frac{\mu_F}{\hbar} \frac{\mathbf{k}_j \cdot \mathbf{B}}{k_j} \right) \right). \tag{A.13}$$

A.2 2D GMOT Forces

The average force from the j^{th} beam is

$$\mathcal{F}_j \approx \hbar \mathbf{k}_j \frac{\Gamma}{2} \frac{I_j}{I_{sat}} \left[K + C \left(\mathbf{k}_j \cdot \mathbf{v} - \frac{\mu_F s}{\hbar} \frac{\mathbf{k}_j \cdot \mathbf{B}}{|\mathbf{k}_j|} \right) \right]. \tag{A.14}$$

The magnetic field is $\mathbf{B} = G\,(x\hat{\mathbf{x}} - y\hat{\mathbf{y}})$. The three beams have $\mathbf{k}$ vectors,

$$\mathbf{k}_1 = -k\hat{\mathbf{y}}$$

with polarization $s = +1$ and

$$\mathbf{k}_2 = k\,(\sin\theta\hat{\mathbf{x}} + \cos\theta\hat{\mathbf{y}})$$

$$\mathbf{k}_3 = k\,(-\sin\theta\hat{\mathbf{x}} + \cos\theta\hat{\mathbf{y}})$$

with fraction P_+ in the $s = +1$ polarization and the remainder P_- in the $s = -1$ polarization, where θ is the diffraction angle from the $+\hat{\mathbf{y}}$ axis.

A.2.1 Beam 1

For the input beam,

$$\begin{aligned} \mathcal{F} &\approx \hbar \mathbf{k}_1 \frac{\Gamma}{2} \frac{I_1}{I_{sat}} \left[K + C \left(\mathbf{k}_1 \cdot \mathbf{v} - \frac{\mu_F s}{\hbar} \frac{\mathbf{k}_1 \cdot \mathbf{B}}{|\mathbf{k}_1|} \right) \right] \\ &\approx -\hbar k \frac{\Gamma}{2} \frac{I_1}{I_{sat}} \left[K + C \left(-k v_y - \frac{\mu_F G}{\hbar} y \right) \right] \hat{\mathbf{y}}. \end{aligned} \tag{A.15}$$

A.2.2 Beam 2

For the $s = +1$ fraction of the second beam,

$$\mathcal{F} \approx \hbar k\langle \sin\theta, \cos\theta\rangle \frac{\Gamma}{2}\frac{P_+ I_2}{I_{sat}}\Big[K + C\Big(kv_x \sin\theta + kv_y \cos\theta - \frac{\mu_F G}{\hbar}x\sin\theta + \frac{\mu_F G}{\hbar}y\cos\theta\Big)\Big]. \tag{A.16}$$

For the $s = -1$ fraction of the second beam,

$$\mathcal{F} \approx \hbar k\langle \sin\theta, \cos\theta\rangle \frac{\Gamma}{2}\frac{P_- I_2}{I_{sat}}\Big[K + C\Big(kv_x \sin\theta + kv_y \cos\theta + \frac{\mu_F G}{\hbar}x\sin\theta - \frac{\mu_F G}{\hbar}y\cos\theta\Big)\Big]. \tag{A.17}$$

A.2.3 Beam 3

For the $s = +1$ fraction of the third beam,

$$\mathcal{F} \approx \hbar k\langle -\sin\theta, \cos\theta\rangle \frac{\Gamma}{2}\frac{P_+ I_3}{I_{sat}}\Big[K + C\Big(-kv_x \sin\theta + kv_y \cos\theta + \frac{\mu_F G}{\hbar}x\sin\theta + \frac{\mu_F G}{\hbar}y\cos\theta\Big)\Big]. \tag{A.18}$$

For the $s = -1$ fraction of the third beam,

$$\mathcal{F} \approx \hbar k\langle -\sin\theta, \cos\theta\rangle \frac{\Gamma}{2}\frac{P_- I_3}{I_{sat}}\Big[K + C\Big(-kv_x \sin\theta + kv_y \cos\theta - \frac{\mu_F G}{\hbar}x\sin\theta - \frac{\mu_F G}{\hbar}y\cos\theta\Big)\Big]. \tag{A.19}$$

A.2.4 Total Forces

Combining the contributions of each beam in the $\hat{\mathbf{x}}$ direction with $I_{up} = I_1 = I_2$ and $P_+ + P_- = 1$,

$$\mathcal{F}_{tot,x} \approx \hbar k C \Gamma \sin^2\theta \frac{I_{up}}{I_{sat}} \Big(k v_x + (P_- - P_+) \frac{\mu_F G}{\hbar} x \Big). \tag{A.20}$$

Similarly,

$$\begin{aligned} \mathcal{F}_{tot,y} \approx \hbar k \cos\theta \frac{\Gamma}{2} \frac{I_{up}}{I_{sat}} \Big(2K + \Big[2C \Big(k v_y \cos\theta \\ + 2(P_+ - P_-) \frac{\mu_F G}{\hbar} y \cos\theta \Big) \Big] \Big) \\ - \hbar k \frac{\Gamma}{2} \frac{I_1}{I_{sat}} \Big[K + C \Big(- k v_y - \frac{\mu_F G}{\hbar} y \Big) \Big]. \end{aligned} \tag{A.21}$$

For the constant terms (i.e. those $\propto K$) to cancel, $I_{up} = I_1/2\cos\theta$. Then,

$$\mathcal{F}_{tot,y} \approx \hbar k C \frac{\Gamma}{2} \frac{I_1}{I_{sat}} \Big(k v_y (1 + \cos\theta) + \frac{\mu_F G}{\hbar} y (1 + (P_+ - P_-)\cos\theta) \Big). \tag{A.22}$$

Appendix B: Measuring the GMOT

B.1 3D GMOT Atom Number

The 3D GMOT was measured using scattered light from the main laser to a side-viewing photodiode, a Thorlabs PDA100A with gain set at 40 dB. A $2f$ imaging system was used, in which a $f = 25.4$mm lens with diameter $D = 25.4$mm was placed in a 50.8mm lens tube such that the lens was $2f$ from the MOT and the detector, as shown in Fig. B.1.

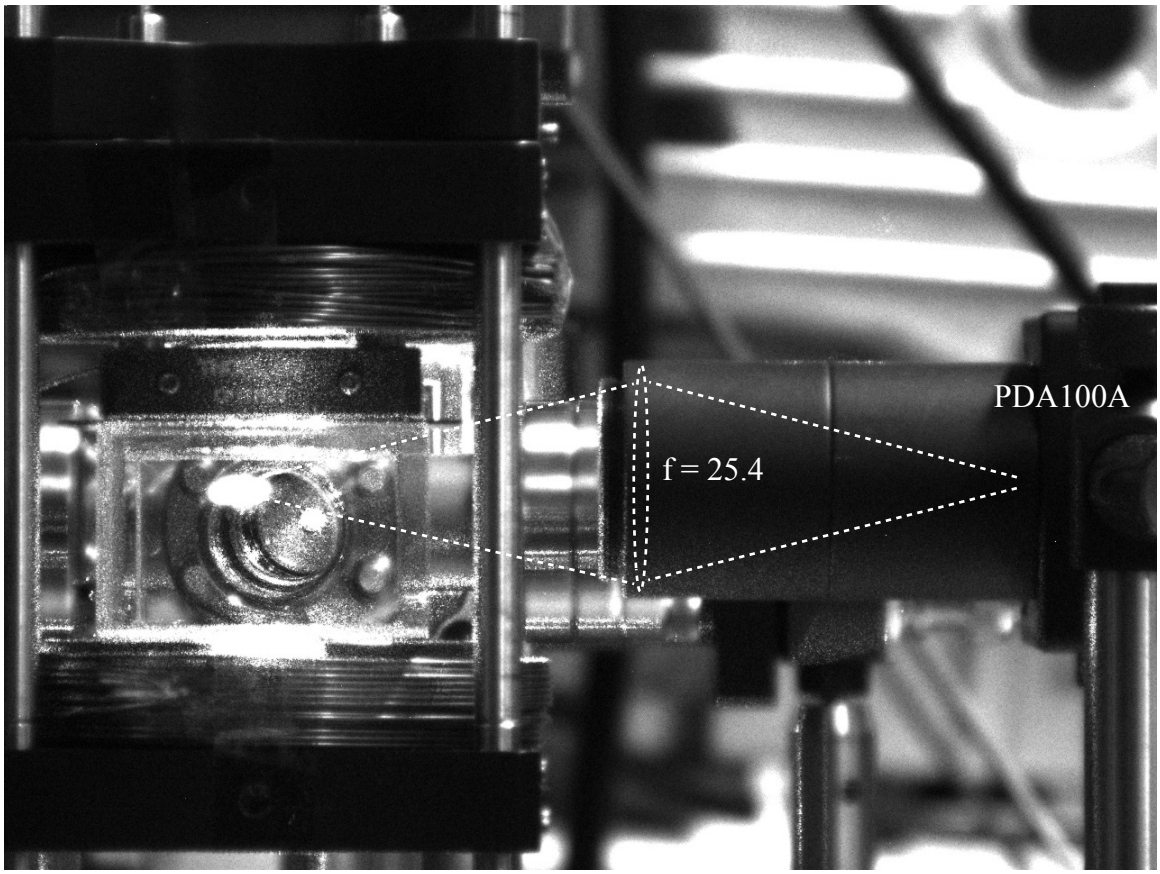

Figure B.1: The $2f$ imaging setup to measure fluorescence of a 3D GMOT.

According to [115], pg. 26, the atom number is given by

$$N = \frac{4\pi(\text{photodiode current})}{(\text{solid angle})(\text{responsivity})(\text{energy of the photon})(\text{scattering rate})(\text{surface transmissivity})^k}, \tag{B.1}$$

where k is the number of reflective surfaces in the imaging setup.

B.1.1 Photodiode Current

The photodiode current is related to the measured output voltage of the PDA100A, which Thorlabs says is 150 kV/A for 40 dB of gain on a high impedance load, i.e. a 1 MΩ oscilloscope. So, the photodiode current is

$$I_{signal} = \frac{V_{signal}}{150\frac{\text{kV}}{\text{A}}}.$$

A typical florescence signal is shown in Fig. B.2. The 3D coils were pulsed off and then on, showing a difference in voltage of $V_{signal} = 150\text{mV}$. This corresponds to 1.0×10^{-6} A of photodiode current.

B.1.2 Solid Angle

The solid angle is defined as

$$\Omega = \int\int \sin\theta d\theta d\phi = (\phi_2 - \phi_1)\cos\theta_1 - (\phi_2 - \phi_1)\cos\theta_2, \tag{B.2}$$

where θ is the angle from the north pole and ϕ is the longitudinal angle.

The solid angle of the imaging system is limited by the retaining ring in the 1 inch lens tube. The ring has a clear aperture of 0.9 inches or 22.9mm. The angle from the MOT to the edge of this ring, from horizontal is

$$\frac{\theta}{2} = \arctan\frac{0.45}{2} = 0.221 \text{ radians}.$$

So, the solid angle is

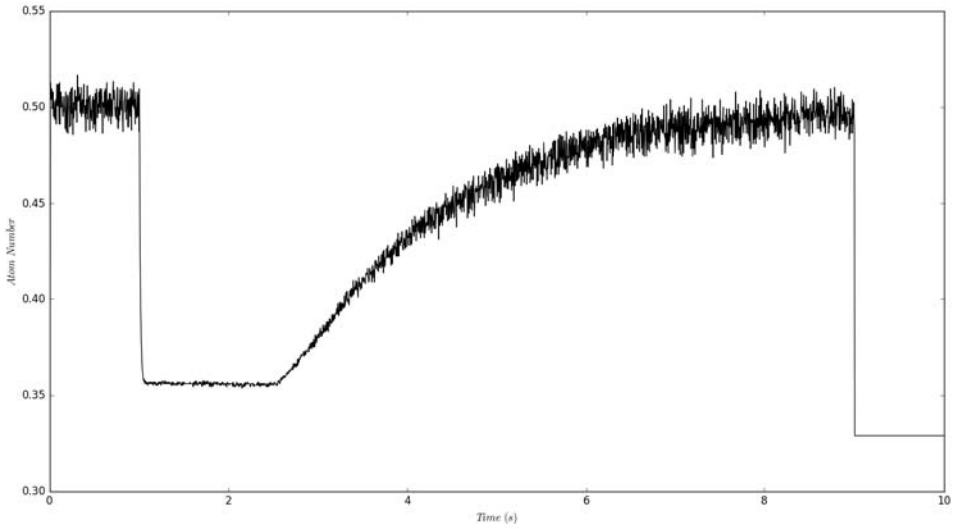

Figure B.2: Typical photodiode signal when the 3D GMOT magnetic field is pulsed off and then on.

$$\Omega_{full} = (0.44)\cos(0) - (0.44)\cos(0.44) = 0.042$$

However, viewing Fig. B.1, it is clear the upper portion of the solid angle is cut off by the top wall of the vacuum chamber. Comparing pixels in the image, only 95.32% passes unclipped by the top wall. Then, the actual solid angle is

$$\Omega_{actual} = 0.042(0.9532) = 0.04.$$

B.1.3 Responsivity

The responsivity of the photodiode at λ =780nm is 0.51 A/W.

B.1.4 Energy of the Photon

The energy of the photon is given by

$$E_\gamma = \frac{hc}{\lambda} = 2.546 \times 10^{-19} \text{ J}.$$

B.1.5 Scattering Rate

Using the scattering rate from [36],

$$R_{sc} = \left(\frac{\Gamma}{2}\right) \frac{I/I_{sat}}{1 + 4\left(\frac{\Delta}{\Gamma}\right)^2 + \frac{I}{I_{sat}}}. \tag{B.3}$$

$I_{sat} = 1.669$ mW/cm^2 for σ polarized light [36]. The lifetime $\Gamma = 38.11 \times 10^6$ Hz. The detuning $\Delta = 49.245 \times 10^6$ Hz. The intensity of the cooling beam was measured to be 7.5 mW/cm^2. Assuming the same amount of intensity going up as going down, this is doubled to 15 mW/cm^2. This measurement used 50 mW of power, implying $I = 22$ mW/cm^2. Then,

$$R_{sc} = \left(\frac{38.11 \times 10^6}{2}\right) \frac{22/1.669}{1 + 4\left(\frac{49.245 \times 10^6}{38.11 \times 10^6}\right)^2 + \frac{22}{1.669}} = 1.204 \times 10^7 \text{ Hz}.$$

B.1.6 Reflective Surfaces

There are four AR-coated surfaces in the imaging train, two chamber walls and two lens surfaces. These are 99.7% transmissive.

B.1.7 Resulting Atom Number

Combining the above data, the atom number measured is

$$N = \frac{4\pi(1.0 \times 10^{-6})}{(0.04)(0.51)(2.546 \times 10^{-19})(1.204 \times 10^7)(0.997)^4} = 2.03 \times 10^8 \text{ atoms}.$$

More generally, 40 dB voltages to atom number,

$$\begin{aligned} N &= \frac{4\pi(V_{signal})}{(150 \times 10^3)(0.04)(0.51)(2.546 \times 10^{-19})(1.204 \times 10^7)(0.997)^4} \\ &= (1.355885193 \times 10^9) V_{signal}. \end{aligned} \tag{B.4}$$

B.2 3D GMOT Loading Rate

B.2.1 Beam Distribution

When the plug beam is pulsed off for a short period, a small packet of atoms from the $2D^+$ GMOT is allowed to pass through the pinhole, across a distance L, to the 3D GMOT trapping region. If the atoms from the beam packet are slower than the capture velocity v_c, they will be collected into the 3D GMOT, which will grow with increased atom number. The process is illustrated in Fig. 4.7.

Define the pinhole to be at $x = 0$. Assume that at $t = 0$, the atoms are distributed uniformly behind the pinhole ($x < 0$) with no atoms past the pinhole ($x > 0$). Assume the atoms have a Gaussian distribution in velocity. The number of atoms between x and $x + dx$ with velocities between v and $v + dv$ is given by

$$\eta(x, v)\, dx\, dv = \frac{A}{\sigma\sqrt{2\pi}} \exp\left(-\frac{(v - v_0)^2}{2\sigma^2}\right) dx\, dv \tag{B.5}$$

where v_0 is the peak velocity of the distribution and σ is the velocity spread. A represents the number of atoms/m, which is weighted by a normal distribution in velocity. The total number of atoms with initial positions between x_1 and x_2 with velocities between v_1 and v_2 is

$$N = \int_{x_2}^{x_1} \int_{v_1}^{v_2} \eta(x, v)\, dv\, dx\,. \tag{B.6}$$

The 3D GMOT size at time t is proportional to the number of atoms that reach the point $x = L$ with velocities less than v_c at or before time t. In other words, an atom at position x must travel at least $L + |x|$ in time t. Accordingly, the minimum velocity that reaches the 3D GMOT by time t is $v_1 = (L + |x|)/t$. The velocity range that can effect the 3D GMOT at time t is then $[v_1, v_2] = [(L - x)/t, v_c]$.

At $t = 0$, no atoms exist past the pinhole, so $x_2 = 0$. The fastest atom capable of being trapped is v_c and it can only travel a distance $v_c t$ in time t. The fastest atom can have an

initial position no further behind the pinhole than $x_1 = L - v_c t$. Using these limits, the total number of atoms that reach the 3D GMOT by time t is

$$\begin{aligned}
N(t) &= \int_{L-v_c t}^{0} \int_{(L-x)/t}^{v_c} \eta(x,v)\, dv\, dx \\
&= \frac{A}{\sigma\sqrt{2\pi}} \int_{L-v_c t}^{0} \int_{(L-x)/t}^{v_c} \exp\left(-\frac{(v-v_0)^2}{2\sigma^2}\right) dv\, dx \\
&= \frac{A}{2} \int_{L-v_c t}^{0} \operatorname{erf}\left[\frac{v_0 - \frac{L-x}{t}}{\sigma\sqrt{2}}\right] dx - \frac{A}{2} \int_{L-v_c t}^{0} \operatorname{erf}\left[\frac{v_0 - v_c}{\sigma\sqrt{2}}\right] dx. \\
&= A\frac{\sigma t}{\sqrt{2\pi}} \left(\exp\left[-\frac{(\frac{L}{t} - v_0)^2}{2\sigma^2}\right] - \exp\left[-\frac{(v_0 - v_c)^2}{2\sigma^2}\right]\right) \\
&+ \frac{A}{2}(v_0 t - L) \operatorname{erf}\left[\frac{v_0 - \frac{L}{t}}{\sigma\sqrt{2}}\right] - \frac{A}{2} t (v_0 - v_c) \operatorname{erf}\left[\frac{v_0 - v_c}{\sigma\sqrt{2}}\right] \\
&+ \frac{A}{2}(L - v_c t) \operatorname{erf}\left[\frac{v_0 - v_c}{\sigma\sqrt{2}}\right].
\end{aligned} \tag{B.7}$$

B.2.2 Flux Distribution

Define the total flux, in atoms/second at speeds between v_1 and v_2, as $\int_{v_1}^{v_2} \Phi(v) dv$. $\Phi(v)$ can be derived knowing $\eta(x, v)$. The number of atoms at speed v' in the $2D^+$ GMOT distribution that exit the pinhole in time t is given by

$$\begin{aligned}
N(v', t) &= \int_{-v't}^{0} \int_{v'}^{v'+dv} \eta(x,v)\, dv\, dx \\
&= \int_{-v't}^{0} [\eta(x, v') dv]\, dx \\
&= A \int_{-v't}^{0} \left[\frac{1}{\sigma\sqrt{2\pi}} \exp\left(-\frac{(v'-v_0)^2}{2\sigma^2}\right) dv\right] dx \\
&= \frac{A v' t}{\sigma\sqrt{2\pi}} \exp\left(-\frac{(v'-v_0)^2}{2\sigma^2}\right) dv.
\end{aligned} \tag{B.8}$$

Thus, the flux of atoms in a narrow range of velocities between v and $v + dv$ is

$$\Phi(v)dv = \frac{N(v,t)}{t} = \frac{A}{\sigma\sqrt{2\pi}}\, v \exp\left(-\frac{(v-v_0)^2}{2\sigma^2}\right) dv, \tag{B.9}$$

which peaks when $v = (v_0 \pm \sqrt{v_0^2 + 4\sigma^2})/2$. The total flux that was blocked by the plug beam is

$$\int_{-\infty}^{\infty} \Phi(v)\, dv = A v_0. \tag{B.10}$$

Appendix C: Conveyor Guide Field

C.1 Setting up the Problem

For an $\hat{\mathbf{x}}$ wire at position $(y, z) = (0, 0)$, the magnetic field is

$$\mathbf{B} = \frac{\mu_0 I}{2\pi}\left[\frac{-z}{y^2+z^2}\hat{\mathbf{y}} + \frac{y}{y^2+z^2}\hat{\mathbf{z}}\right]. \tag{C.1}$$

A guide field is made with four wires in the $\hat{\mathbf{x}}$ direction. The wires are located in the $z = d$ plane and spaced at $y = \pm P$ and $y = \pm Q$. The exact field of the guide wires is

$$\mathbf{B}_G = \mathbf{B}_1 + \mathbf{B}_2 + \mathbf{B}_3 + \mathbf{B}_4, \tag{C.2}$$

where

$$\begin{aligned}
\mathbf{B}_1 &= \frac{\mu_0 I_1}{2\pi}\left[\frac{-(z-d)}{(y+P)^2+(z-d)^2}\hat{\mathbf{y}} + \frac{y+P}{(y+P)^2+(z-d)^2}\hat{\mathbf{z}}\right],\\
\mathbf{B}_2 &= \frac{\mu_0 I_2}{2\pi}\left[\frac{-(z-d)}{(y+Q)^2+(z-d)^2}\hat{\mathbf{y}} + \frac{y+Q}{(y+Q)^2+(z-d)^2}\hat{\mathbf{z}}\right],\\
\mathbf{B}_3 &= \frac{\mu_0 I_3}{2\pi}\left[\frac{-(z-d)}{(y-Q)^2+(z-d)^2}\hat{\mathbf{y}} + \frac{y-Q}{(y-Q)^2+(z-d)^2}\hat{\mathbf{z}}\right],\\
\mathbf{B}_4 &= \frac{\mu_0 I_4}{2\pi}\left[\frac{-(z-d)}{(y-P)^2+(z-d)^2}\hat{\mathbf{y}} + \frac{y-P}{(y-P)^2+(z-d)^2}\hat{\mathbf{z}}\right].
\end{aligned}$$

Break the total field into its components

$$\mathbf{B}_G = B_y\hat{\mathbf{y}} + B_z\hat{\mathbf{z}}, \tag{C.3}$$

such that

$$\begin{aligned}
B_y(y,z) &= \frac{\mu_0}{2\pi}\left[\frac{-(z-d)I_1}{(y+P)^2+(z-d)^2} + \frac{-(z-d)I_2}{(y+Q)^2+(z-d)^2} + \frac{-(z-d)I_3}{(y-Q)^2+(z-d)^2} + \frac{-(z-d)I_4}{(y-P)^2+(z-d)^2}\right],\\
B_z(y,z) &= \frac{\mu_0}{2\pi}\left[\frac{(y+P)I_1}{(y+P)^2+(z-d)^2} + \frac{(y+Q)I_2}{(y+Q)^2+(z-d)^2} + \frac{(y-Q)I_3}{(y-Q)^2+(z-d)^2} + \frac{(y-P)I_4}{(y-P)^2+(z-d)^2}\right].
\end{aligned}$$

To simplify the above expressions for the field, Taylor expand in two dimensions according to

$$T(x,y) \approx T(a,b) + (x-a)T_x(a,b) + (y-b)T_y(a,b) + O(x^2, y^2)$$

where (a,b) is the expansion point and T_x, T_y are partial derivatives of f in x and y, respectively. In our case, the beam is confined to travel along the origin, so $(a,b) = (0,0)$. However, B_y and B_z have many terms. These can be expanded all at once by noticing that all the B_y terms have the generic form

$$f_{\hat{\mathbf{y}}} = \frac{-(z-r)}{(y-s)^2 + (z-r)^2}$$

for different values of r and s. Meanwhile, all the B_z terms have the generic form

$$f_{\hat{\mathbf{z}}} = \frac{(y-s)}{(y-s)^2 + (z-r)^2}.$$

Then the generic partial derivatives, evaluated at $(y,z) = (0,0)$ are

$$\begin{aligned}
(f_{\hat{\mathbf{y}}})_y &= \frac{(z-r)2(y-s)}{[(y-s)^2 + (z-r)^2]^2} \to \frac{2rs}{(s^2+r^2)^2}, \\
(f_{\hat{\mathbf{y}}})_z &= \frac{-[(y-s)^2 + (z-r)^2] + (z-r)2(z-r)}{[(y-s)^2 + (z-r)^2]^2} = \frac{-(y-s)^2 + (z-r)^2}{[(y-s)^2 + (z-r)^2]^2} \to \frac{r^2-s^2}{(s^2+r^2)^2}, \\
(f_{\hat{\mathbf{z}}})_y &= \frac{[(y-s)^2 + (z-r)^2] - (y-s)2(y-s)}{[(y-s)^2 + (z-r)^2]^2} = \frac{(z-r)^2 - (y-s)^2}{[(y-s)^2 + (z-r)^2]^2} \to \frac{r^2-s^2}{(s^2+r^2)^2}, \\
(f_{\hat{\mathbf{z}}})_z &= \frac{-(y-s)2(z-r)}{[(y-s)^2 + (z-r)^2]^2} \to \frac{-2rs}{(s^2+r^2)^2}.
\end{aligned}$$

Finally, assume the currents are

$$\begin{aligned}
I_1 &= I_G(1 - \Delta_I + \delta_I) \\
I_2 &= -I_G(1 + \Delta_I + \delta_I) \\
I_3 &= I_G(1 + \Delta_I - \delta_I) \\
I_4 &= -I_G(1 - \Delta_I - \delta_I).
\end{aligned} \tag{C.4}$$

C.2 Performing the Taylor Expansion

C.2.1 The Zeroth Order Terms

Collecting all the zeroth order terms of B_y,

$$\begin{aligned} B_y^0 &= \frac{\mu_0}{2\pi}\left(I_1\frac{d}{d^2+P^2} + I_2\frac{d}{d^2+Q^2} + I_3\frac{d}{d^2+Q^2} + I_4\frac{d}{d^2+P^2}\right) \\ &= \frac{\mu_0}{2\pi d}\left((I_1+I_4)\frac{1}{1+p^2} + (I_2+I_3)\frac{1}{1+q^2}\right) \\ &= \frac{\mu_0 I_G}{\pi d}\left(\frac{\delta_I}{1+p^2} + \frac{-\delta_I}{1+q^2}\right), \end{aligned} \tag{C.5}$$

where $p = P/d$ and $q = Q/d$. Similarly, the four zeroth order terms of B_z reduce to

$$B_z^0 = \frac{\mu_0 I_G}{\pi d}\left((1-\Delta_I)\frac{p}{1+p^2} + (-1-\Delta_I)\frac{q}{1+q^2}\right). \tag{C.6}$$

C.2.2 The First Order Terms in y

Collecting the terms of B_y that are multiplied by y,

$$\begin{aligned} B_y^{1,y} &= \frac{\mu_0}{2\pi}\left(I_1\frac{-2Pd}{(d^2+P^2)^2} + I_2\frac{-2Qd}{(d^2+Q^2)^2} + I_3\frac{2Qd}{(d^2+Q^2)^2} + I_4\frac{2Pd}{(d^2+P^2)^2}\right) \\ &= \frac{2\mu_0 I_G}{\pi d^2}\left((-1+\Delta_I)\frac{p}{(1+p^2)^2} + (1+\Delta_I)\frac{q}{(1+q^2)^2}\right). \end{aligned} \tag{C.7}$$

Similarly, collect the terms of B_z that depend on y,

$$\begin{aligned} B_z^{1,y} &= \frac{\mu_0}{2\pi}\left(I_1\frac{d^2-P^2}{(d^2+P^2)^2} + I_2\frac{d^2-Q^2}{(d^2+Q^2)^2} + I_3\frac{d^2-Q^2}{(d^2+Q^2)^2} + I_4\frac{d^2-P^2}{(d^2+P^2)^2}\right) \\ &= \frac{\mu_0 I_G \delta_I}{\pi d^2}\left(\frac{1-p^2}{(1+p^2)^2} - \frac{1-q^2}{(1+q^2)^2}\right). \end{aligned} \tag{C.8}$$

C.2.3 The First Order Terms in z

Collect the four terms of the expansion of B_y that are multiplied by z,

$$\begin{aligned} B_y^{1,z} &= \frac{\mu_0}{2\pi}\left(I_1\frac{d^2-P^2}{(d^2+P^2)^2} + I_2\frac{d^2-Q^2}{(d^2+Q^2)^2} + I_3\frac{d^2-Q^2}{(d^2+Q^2)^2} + I_4\frac{d^2-P^2}{(d^2+P^2)^2}\right) \\ &= \frac{\mu_0 I_G \delta_I}{\pi d^2}\left(\frac{1-p^2}{(1+p^2)^2} - \frac{1-q^2}{(1+q^2)^2}\right). \end{aligned} \tag{C.9}$$

Similarly, the four terms of the expansion of B_z that are multiplied by z are

$$\begin{aligned} B_z^{1,z} &= \frac{\mu_0}{2\pi}\left(I_1\frac{2Pd}{(d^2+P^2)^2} + I_2\frac{2Qd}{(d^2+Q^2)^2} + I_3\frac{-2Qd}{(d^2+Q^2)^2} + I_4\frac{-2Pd}{(d^2+P^2)^2}\right) \\ &= \frac{2\mu_0 I_G}{\pi d^2}\left((1-\Delta_I)\frac{p}{(1+p^2)^2} - (1+\Delta_I)\frac{q}{(1+q^2)^2}\right). \end{aligned} \tag{C.10}$$

C.3 Putting It All Together

We now have the terms of the Taylor expansion for the four guide wire field. The approximate field for small y and z around the origin is

$$\mathbf{B}_{tot} = \left((B_y^0 + B_y^{1,y}y + B_y^{1,z}z)\hat{\mathbf{y}} + (B_z^0 + B_z^{1,y}y + B_z^{1,z}z)\hat{\mathbf{z}}\right). \tag{C.11}$$

The $\hat{\mathbf{y}}$ term is

$$B_y = B_y^0 + B_y^{1,y}y + B_y^{1,z}z,$$

so

$$\frac{\pi d}{\mu_0 I_G}B_y = \left(\frac{\delta_I}{1+p^2} + \frac{-\delta_I}{1+q^2}\right) + \frac{2}{d}\left((-1+\Delta_I)\frac{p}{(1+p^2)^2} + (1+\Delta_I)\frac{q}{(1+q^2)^2}\right)y + \frac{\delta_I}{d}\left(\frac{1-p^2}{(1+p^2)^2} - \frac{1-q^2}{(1+q^2)^2}\right)z.$$

Assuming Δ_I and δ_I are small, and recalling that y and z are small, then their products (i.e. $z\delta_I$ or $y\Delta_I$) are negligible. Then,

$$\frac{2\pi d B_y}{\mu_0 I_G} = \frac{2\delta_I}{1+p^2} + \frac{-2\delta_I}{1+q^2} - \frac{4}{d}\frac{py}{(1+p^2)^2} + \frac{4}{d}\frac{qy}{(1+q^2)^2}, \tag{C.12}$$

which can be written in the form

$$B_y = G_y(y - y_0),$$

by setting $p = 1/q$. Then,

$$B_y = \frac{\mu_0 I_G}{2\pi d}\left[\frac{2\delta_I q^4 - 2\delta_I - 4yq^3/d + 4yq/d}{(1+q^2)^2}\right]. \tag{C.13}$$

Similarly, the $\hat{\mathbf{z}}$ term is

$$B_z = B_z^0 + B_z^{1,y} y + B_z^{1,z} z,$$

which becomes

$$\frac{2\pi d B_z}{\mu_0 I_G} = 4\frac{q(-\Delta_I - \Delta_I q^2 + \frac{z}{d}q^2 - \frac{z}{d})}{(1+q^2)^2}, \tag{C.14}$$

for $p = 1/q$.

C.4 Maximizing the Gradient

The gradient of $|\mathbf{B}|$ is then

$$\begin{aligned}\vec{\nabla}|\mathbf{B}| &= \frac{\mu_0 I_G}{2\pi d}\vec{\nabla}\left(\sqrt{\left(-2\frac{(q-1)(q+1)(-\delta_I q^2 - \delta_I + \frac{2}{d}qy)}{(1+q^2)^2}\right)^2 + \left(4\frac{q(-\Delta_I - \Delta_I q^2 + \frac{z}{d}q^2 - \frac{z}{d})}{(1+q^2)^2}\right)^2}\right) \\ &= \frac{\mu_0 I_G}{2\pi d}\vec{\nabla}\left(\sqrt{\frac{4}{(1+q^2)^4}\left[(C-Dy)^2 + 4\,(F-Gz)^2\right]}\right),\end{aligned} \tag{C.15}$$

where $C = \delta_I q^4 - \delta_I$, $D = \frac{2q^3}{d} - \frac{2q}{d}$, $F = q\Delta_I + \Delta_I q^3$, and $G = \frac{1}{d}q^3 - \frac{1}{d}q$.

Then,

$$\vec{\nabla}|\mathbf{B}| = \frac{\mu_0 I_G}{\pi d}\frac{1}{(1+q^2)^2}\left[\frac{-CD + D^2 y}{\sqrt{(C-Dy)^2 + 4\,(F-Gz)^2}}\hat{\mathbf{y}} + \frac{-4FG + 4G^2 z}{\sqrt{(C-Dy)^2 + 4\,(F-Gz)^2}}\hat{\mathbf{z}}\right]. \tag{C.16}$$

We know that the divergence of a magnetic field is zero, so the magnitude of the gradient in $\hat{\mathbf{y}}$ and $\hat{\mathbf{z}}$ will be equal for this 2D problem. Arbitrarily choosing to maximize z,

$$\frac{\partial}{\partial q}\left[\frac{1}{(1+q^2)^2}\frac{-4G(F-Gz)}{\sqrt{(C-Dy)^2+4\,(F-Gz)^2}}\right]=0. \tag{C.17}$$

Notice C and F contain δ_I and Δ_I, which were assumed to be small. For the purpose of mass-simplification, these terms are set to zero. Then

$$\frac{(1+q^2)^2(3q^2-1)-(q^3-q)(4q(1+q^2))}{(1+q^2)^4}=0, \tag{C.18}$$

which yields

$$q\approx 2.413 \text{ OR } 0.414.$$

Using $q = 0.414 = \sqrt{2}-1$ and Eq.'s C.13 and C.14, we find the maximized field for small y, z around the origin is

$$\begin{aligned}\mathbf{B}_y &= \frac{\mu_0 I_G}{2\pi d^2}(y-y_0)\hat{\mathbf{y}}\\ \mathbf{B}_z &= -\frac{\mu_0 I_G}{2\pi d^2}(z-z_0)\hat{\mathbf{z}}\end{aligned} \tag{C.19}$$

with $y_0 = \sqrt{2}\delta_I d$ and $z_0 = -\sqrt{2}\Delta_I d$.

Appendix D: Conveyor Crossing Wire Field

D.1 The Magnetic Field

For $\hat{\mathbf{y}}$ wire at position $(x, z) = (0, 0)$, the magnetic field is

$$\mathbf{B} = \frac{\mu_0 I_y}{2\pi}\left[\frac{-z}{x^2+z^2}\hat{\mathbf{x}} + \frac{x}{x^2+z^2}\hat{\mathbf{z}}\right]. \tag{D.1}$$

The atom beam is taken to travel in $\hat{\mathbf{x}}$ with transverse position $(y, z) = (0, 0)$ and will interact with a series of $\hat{\mathbf{y}}$ wires running alternating currents. Those wires are at positions $(x, z) = (nl, h)$ with currents $I_{n,1} = I_y(-1)^n$. To find the the field due to the alternating currents, use Eq. D.1, plugging in $z = 0$ and offsetting the x positions by nl,

$$\mathbf{B}(z=0) = \frac{\mu_0 I_y(-1)^n}{2\pi}\left[\frac{h}{(x-nl)^2+h^2}\hat{\mathbf{x}} + \frac{x-nl}{(x-nl)^2+h^2}\hat{\mathbf{z}}\right]. \tag{D.2}$$

The field can be written

$$\mathbf{B} = \frac{\mu_0 I_j}{2\pi}\left[\beta_x(x)\hat{\mathbf{x}} + \beta_z(x)\hat{\mathbf{z}}\right], \tag{D.3}$$

having defined

$$\beta_x(x) = \sum_{n=-\infty}^{\infty}(-1)^n\frac{h}{h^2+(x-nl)^2}, \tag{D.4}$$

and

$$\beta_z(x) = \sum_{n=-\infty}^{\infty}(-1)^n\frac{x-nl}{h^2+(x-nl)^2}, \tag{D.5}$$

where $k_n = \pi\frac{2n+1}{l}$. We will now derive that

$$\beta_x(x) = \frac{2\pi}{l}\sum_{n=0}^{\infty}e^{-k_n h}\cos(k_n x), \tag{D.6}$$

and

$$\beta_z(x) = -\frac{2\pi}{l}\sum_{n=0}^{\infty}e^{-k_n h}\sin(k_n x). \tag{D.7}$$

D.2 Deriving the Fourier Series Expressions for β_x and β_z

Equations D.6 and D.7 are not trivial to achieve from equations D.4 and D.5. The derivation of $\beta_x(x)$ is shown here. First, recall the Poisson Sum Formula, which states that, given some $f(t)$ which has a Fourier transform $\hat{f}(s)$ defined as

$$\hat{f}(s) = \int_{-\infty}^{\infty} e^{-2\pi i s t} f(t) dt,$$

then

$$\sum_{n=-\infty}^{\infty} f(n) = \sum_{s=-\infty}^{\infty} \hat{f}(s). \tag{D.8}$$

So, for this specific problem, substitute $f(n)$ to write

$$\beta_x(x) = \sum_{n=-\infty}^{\infty} (-1)^n \frac{h}{h^2 + (x - nl)^2} = \sum_{s=-\infty}^{\infty} \hat{f}(s).$$

Therefore, $\beta_x(x)$ is found through the Fourier transform

$$\hat{f}(s) = \int_{-\infty}^{\infty} e^{-2\pi i s t} (-1)^t \frac{h}{h^2 + (x - tl)^2} dt.$$

Note that here t replaces n, not x. Rewriting $(-1)^t = e^{i\pi t}$, then

$$\begin{aligned} \hat{f}(s) &= \int_{-\infty}^{\infty} e^{-2\pi i s t} e^{i\pi t} \frac{h}{h^2 + (x - tl)^2} dt \\ &= \int_{-\infty}^{\infty} e^{-i\pi(2s-1)t} \frac{h}{h^2 + (x - tl)^2} dt. \end{aligned} \tag{D.9}$$

D.2.1 Sidebar - Required Residue Calculus

Evaluating this integral for $\hat{f}(s)$ from Eq. (D.9) requires residue calculus. The Cauchy Residue Theorem states that the integral of a complex function over a closed path in the complex plane is equal to $2\pi i$ times sum of the function's residues evaluated at each of its poles. Explicitly,

$$\oint_\gamma f(z)dz = 2\pi i \sum_k \text{Res}(f, a_k),$$

where $f(z)$ is said to have a pole at point a if $f(z) \to \infty$ as $z \to a$. In this problem, the poles are located at

$$t = \frac{x}{l} \pm i\frac{h}{l},$$

which is verified by plugging into the denominator

$$h^2 + (x - tl)^2 \to h^2 + (x - x \mp ih)^2 \to h^2 - h^2 = 0,$$

meaning

$$f(t) \to \frac{g(t)}{0} = \infty.$$

For simple poles, if

$$f(z) = \frac{g(z)}{h(z)},$$

then the residue is given by

$$\text{Res}(f, a) = \frac{g(a)}{h'(a)}.$$

D.2.2 Resuming the Derivation - Decomposing the Integral and Jordan's Lemma

We seek a solution to Eq. (D.9),

$$\hat{f}(s) = \int_{-\infty}^{\infty} e^{-i\pi(2s-1)t} \frac{h}{h^2 + (x - tl)^2} dt,$$

which is along the real axis of t. To use residue calculus, notice that if we integrate in the complex plane

$$\oint_\gamma f(z)dz = \int_{C_1} f(z)dz + \int_{C_2} f(z)dz,$$

where C_1 extends on the real axis of t from $-R$ to R and C_2 is a path which closes the curve through the imaginary part of the t plane as a half-circle, then

$$\int_{C_1} f(z)dz = \int_{-R}^{R} f(t)dt.$$

Meanwhile, Jordan's Lemma states that for functions $f(z)$ of the form

$$f(z) = e^{ibz}g(z)$$

with $b > 0$, then $\int_{C_2} f(z)dz \to 0$ as $R \to \infty$. In our integral, $b = -\pi(2s-1)$. Thus, for positive b and $R \to \infty$, the complex contour integral reduces to

$$\oint_{\gamma} f(z)dz = \int_{-\infty}^{\infty} f(t)dt = 2\pi i \text{Res}(f, a_+), \quad \text{for } (2s-1) < 0.$$

Only the positive pole is evaluated, as the curve encloses the positive half circle above the $Re(t)$ axis.

Meanwhile, for those values of s in the sum such that $(2s-1) > 0$, we must integrate in the opposite direction along $Re(t)$ to still use Jordan's Lemma, from ∞ to $-\infty$. Integrating in this direction uses the lower half circle below the $Re(t)$ axis, and thus encloses the negative pole, a_-. Therefore,

$$\oint_{\gamma} f(z)dz = \int_{\infty}^{-\infty} f(t)dt = 2\pi i \text{Res}(f, a_-), \quad \text{for } (2s-1) < 0.$$

D.2.3 Evaluating the Integral

If $(2s-1) < 0$, then

$$\int_{-\infty}^{\infty} f(t)dt = 2\pi i \text{Res}(f, a_+) = 2\pi i \frac{g(a_+)}{h'(a_+)}.$$

Note that

$$g(t) = he^{-i\pi(2s-1)t},$$

and

$$h(t) = h^2 + (x - tl)^2,$$

so

$$h'(t) = -2l(x - tl).$$

Thus, the integral becomes

$$\begin{aligned}\int_{-\infty}^{\infty} f(t)dt &= 2\pi i \frac{g(a_+)}{h'(a_+)} = -2\pi i \frac{he^{-i\pi(2s-1)t}}{2l(x-tl)} \\ &= -2\pi i \frac{he^{-i\pi(2s-1)(\frac{x}{l}+i\frac{h}{l})}}{2l(x-(x+ih))} \\ &= \frac{\pi}{l} e^{-i\pi(2s-1)(\frac{x}{l}+i\frac{h}{l})}. \end{aligned} \tag{D.10}$$

Employing similar logic, the integral can be evaluated at the negative pole, using the negative half circle as C_2 to close the curve. Because we must integrate counterclockwise on this curve, integration occurs from $t = \infty$ to $-\infty$, picking up an extra minus sign.

$$\begin{aligned}\int_{-\infty}^{\infty} f(t)dt &= -\int_{\infty}^{-\infty} f(t)dt = -2\pi i \text{Res}(f, a_-) = -2\pi i \frac{g(a_-)}{h'(a_-)} \\ &= 2\pi i \frac{he^{-i\pi(2s-1)(\frac{x}{l}-i\frac{h}{l})}}{2l(x-(x-ih))} \\ &= \frac{\pi}{l} e^{-i\pi(2s-1)(\frac{x}{l}-i\frac{h}{l})}. \end{aligned} \tag{D.11}$$

D.2.4 Putting It All Back Together

Recall the Poisson Sum Formula states

$$\sum_{n=-\infty}^{\infty} f(n) = \sum_{s=-\infty}^{\infty} \hat{f}(s),$$

so

$$\beta_x(x) = \sum_{n=-\infty}^{\infty} (-1)^n \frac{h}{h^2 + (x-nl)^2} = \sum_{s=-\infty}^{\infty} \hat{f}(s).$$

Breaking the sum apart for the $(2s-1) > 0$ and $(2s-1) < 0$ cases and using Eq.'s (D.10) and (D.11),

$$\begin{aligned}\beta_x(x) &= \frac{\pi}{l}\left(\sum_{s=-\infty}^{0} e^{-i\pi(2s-1)(\frac{x}{l}+i\frac{h}{l})} + \sum_{s=1}^{\infty} e^{-i\pi(2s-1)(\frac{x}{l}-i\frac{h}{l})}\right) \\ &= \frac{\pi}{l}\sum_{s=-\infty}^{\infty} e^{-\frac{\pi h}{l}|2s-1|} e^{-i\frac{\pi x}{l}(2s-1)}. \end{aligned} \tag{D.12}$$

If this sum is evaluated for the $s = -1, 0, 1, 2$ cases, a pattern emerges

$$= \frac{\pi}{l}\left(\cdots + e^{-\frac{3\pi h}{l}} e^{3i\frac{\pi x}{l}} + e^{-\frac{\pi h}{l}} e^{i\frac{\pi x}{l}} + e^{-\frac{\pi h}{l}} e^{-i\frac{\pi x}{l}} + e^{-\frac{3\pi h}{l}} e^{-3i\frac{\pi x}{l}} + \ldots\right).$$

The matching exponent parts of the series can be combined by the relation

$$\frac{e^{ix} + e^{-ix}}{2} = \cos(x),$$

so that

$$\beta_x(x) = \frac{2\pi}{l}\sum_{n=0}^{\infty} e^{-k_n h}\cos(k_n x),$$

where $k_n = \frac{\pi}{l}(2n+1)$. Deriving $\beta_z(x)$ follows a similar procedure and is left to the reader.

Appendix E: Full Conveyor Analysis

E.1 Two Sets of Crossing Wires

The results of Appendices C and D allow consideration of the total magnetic field of the atom conveyor.

Consider two sets of alternating $\hat{\mathbf{y}}$ wires, the first at positions $x = nl$, as before, and a second set at positions $x = nl + l/2$. The first set has current $I_{n,1} = I_y(-1)^n\mathcal{U}(t)$ and the second set has current $I_{n,2} = I_y(-1)^n\mathcal{V}(t)$. Then the total field from both sets will be

$$B_x = \frac{\mu_0 I_y}{l}\left[\mathcal{U}(t)\sum_{n=0}^{\infty} e^{-k_n h}\cos(k_n x) + \mathcal{V}(t)\sum_{n=0}^{\infty} e^{-k_n h}\cos(k_n(x - l/2))\right], \tag{E.1}$$

and

$$B_z = -\frac{\mu_0 I_y}{l}\left[\mathcal{U}(t)\sum_{n=0}^{\infty} e^{-k_n h}\sin(k_n x) + \mathcal{V}(t)\sum_{n=0}^{\infty} e^{-k_n h}\sin(k_n(x - l/2))\right]. \tag{E.2}$$

In the limit that $\pi h/l << 1$, then $e^{-k_n h} \to 0$ for $n \neq 0$. Keeping only the $n = 0$ terms, noting $k_0 = \pi/l$,

$$B_x = \frac{\mu_0 I_y}{l} e^{-\frac{\pi h}{l}}\left[\mathcal{U}(t)\cos\left(\frac{\pi x}{l}\right) + \mathcal{V}(t)\sin\left(\frac{\pi x}{l}\right)\right], \tag{E.3}$$

and

$$B_z = -\frac{\mu_0 I_y}{l} e^{-\frac{\pi h}{l}}\left[\mathcal{U}(t)\sin\left(\frac{\pi x}{l}\right) - \mathcal{V}(t)\cos\left(\frac{\pi x}{l}\right)\right]. \tag{E.4}$$

If

$$\mathcal{U}(t) = \cos(\frac{\pi x_0(t)}{l}),$$

and

$$\mathcal{V}(t) = \sin(\frac{\pi x_0(t)}{l}),$$

simple trigonometry allows us to write,

$$B_x = \frac{\mu_0 I_y}{l} e^{-\frac{\pi h}{l}}\cos\left(\frac{\pi}{l}(x - x_0)\right), \tag{E.5}$$

$$B_z = -\frac{\mu_0 I_y}{l} e^{-\frac{\pi h}{l}} \sin\left(\frac{\pi}{l}(x - x_0)\right). \tag{E.6}$$

E.2 Finding the Position of the Full Conveyor's Potential Minimum

Combining the conveyor guide and crossing wires, the magnitude of the magnetic field is given by

$$|\mathbf{B}_{tot}| = \sqrt{\left(C_1 \cos\left[\frac{\pi}{l}(x - x_0)\right]\right)^2 + (C_2(y - y_0))^2 + \left(C_1 \sin\left[\frac{\pi}{l}(x - x_0)\right] + C_2(z - z_0)\right)^2}, \tag{E.7}$$

where $C_1 = (\mu_0 I_y / l) e^{-\pi h/l}$ and $C_2 = -\mu_0 I_G / (2\pi d^2)$. Expanding and simplifying,

$$|\mathbf{B}_{tot}| = \sqrt{C_1^2 + C_2^2(y - y_0)^2 + C_2^2(z - z_0)^2 + 2C_2 C_1 (z - z_0) \sin\left[\frac{\pi}{l}(x - x_0)\right]}. \tag{E.8}$$

To find the position of the minimum, we seek (x, y, z) such that

$$\begin{aligned} \frac{\partial |\mathbf{B}_{tot}|}{\partial x} &= 0, \\ \frac{\partial |\mathbf{B}_{tot}|}{\partial y} &= 0, \\ \frac{\partial |\mathbf{B}_{tot}|}{\partial z} &= 0. \end{aligned} \tag{E.9}$$

These are three equations for three unknowns,

$$\begin{aligned} \frac{\partial |\mathbf{B}_{tot}|}{\partial x} &= \frac{1}{2|\mathbf{B}_{tot}|}\left(\frac{2\pi C_2 C_1}{l}(z - z_0) \cos\left[\frac{\pi}{l}(x - x_0)\right]\right) = 0, \\ \frac{\partial |\mathbf{B}_{tot}|}{\partial y} &= \frac{2C_2^2(y - y_0)}{2|\mathbf{B}_{tot}|} = 0, \\ \frac{\partial |\mathbf{B}_{tot}|}{\partial z} &= \frac{1}{2|\mathbf{B}_{tot}|}\left(2C_2^2(z - z_0) + 2C_2 C_1 \sin\left[\frac{\pi}{l}(x - x_0)\right]\right) = 0. \end{aligned} \tag{E.10}$$

Note that $|\mathbf{B}_{tot}|$ is always positive and non-zero, so solutions are found by setting the numerators equal to zero. Not surprisingly, the y equation implies the zero occurs at

$$y = y_0.$$

For x and z, two numerators are set equal,

$$z - z_0 = \frac{l\sin\left[\frac{\pi}{l}(x - x_0)\right]}{\pi\cos\left[\frac{\pi}{l}(x - x_0)\right] - \frac{C_2 l}{C_1}}. \tag{E.11}$$

Then, using the $\partial|\mathbf{B}_{tot}|/\partial z = 0$ condition with Eq. (E.11),

$$x - x_0 = \frac{(2n + 1)l}{2}, \tag{E.12}$$

where n is an integer. Taking that result and substituting back into Eq. (E.11) gives

$$z - z_0 = -\frac{2\pi d^2}{l} e^{-\frac{\pi h}{l}} \frac{I_y}{I_G} (-1)^n. \tag{E.13}$$

The position of the zero of the minimum field is then given by $(x_{min}, y_{min}, z_{min})$ where

$$\begin{aligned} x_{min} &= \frac{(2n + 1)l}{2} + x_0(t), \\ y_{min} &= \sqrt{2}\delta_I d, \\ z_{min} &= -\sqrt{2}\Delta_I d - \frac{2\pi d^2}{l} e^{-\frac{\pi h}{l}} \frac{I_y}{I_G} (-1)^n. \end{aligned} \tag{E.14}$$

Appendix F: Understanding the Wigner Function

F.1 Let's Start From the Very Beginning...

The Wigner function allows for tracking the time evolution of a gas with many quantum states using the density operator

$$\hat{\rho} = |\psi\rangle\langle\psi|. \tag{F.1}$$

The time evolution of $\hat{\rho}$ is

$$i\hbar\frac{\partial}{\partial t}\hat{\rho} = i\hbar\frac{\partial}{\partial t}|\psi\rangle\langle\psi|. \tag{F.2}$$

Performing the product rule and recognizing the Schrödinger equation $i\hbar\frac{\partial}{\partial t}|\psi\rangle = \hat{H}|\psi\rangle$,

$$\begin{aligned} i\hbar\frac{\partial}{\partial t}\hat{\rho} &= i\hbar\left(\frac{\partial}{\partial t}|\psi\rangle\right)\langle\psi| + i\hbar|\psi\rangle\left(\frac{\partial}{\partial t}\langle\psi|\right) \\ &= i\hbar\left(\frac{\partial}{\partial t}|\psi\rangle\right)\langle\psi| - |\psi\rangle\left(-i\hbar\frac{\partial}{\partial t}\langle\psi|\right) \\ &= \hat{H}|\psi\rangle\langle\psi| - |\psi\rangle\langle\psi|\hat{H}^{\dagger} \\ &= \hat{H}|\psi\rangle\langle\psi| - |\psi\rangle\langle\psi|\hat{H} \\ &= \hat{H}\hat{\rho} - \hat{\rho}\hat{H} \\ \rightarrow i\hbar\frac{\partial}{\partial t}\hat{\rho} &= [\hat{H}, \hat{\rho}]. \end{aligned} \tag{F.3}$$

F.2 When You Sing You Begin with $f(x, p)$...

The following basic relations from elementary quantum mechanics are needed,

$$\langle x|p\rangle = \frac{e^{ipx/\hbar}}{\sqrt{2\pi\hbar}}. \tag{F.4}$$

$$\int dx|x\rangle\langle x| = \int dp|p\rangle\langle p| = \hat{1}. \tag{F.5}$$

$$\delta(x) = \frac{1}{2\pi}\int dp\, e^{ipx}. \tag{F.6}$$

The Wigner function is defined (with no explanation yet) as

$$f(x,p) = \frac{1}{\pi\hbar}\int dq \langle p+q|\hat{\rho}|p-q\rangle e^{2iqx/\hbar}. \tag{F.7}$$

We will now show that there is an equivalent definition for the position coordinate,

$$f(x,p) = \frac{1}{\pi\hbar}\int d\epsilon \langle x+\epsilon|\hat{\rho}|x-\epsilon\rangle e^{-2ip\epsilon/\hbar}. \tag{F.8}$$

Beginning with Eq. (F.7),

$$f(x,p) = \frac{1}{\pi\hbar}\int dq \langle p+q|\hat{\rho}|p-q\rangle e^{2iqx/\hbar}.$$

Operate on both sides of $\hat{\rho}$ with $\hat{1}$ from Eq. (F.5),

$$= \frac{1}{\pi\hbar}\int\int\int dq dx' dx'' \langle p+q|x'\rangle\langle x'|\hat{\rho}|x''\rangle\langle x''|p-q\rangle e^{2iqx/\hbar}.$$

Evaluate using Eq. (F.4),

$$\begin{aligned}
&= \frac{1}{\pi\hbar}\frac{1}{2\pi\hbar}\int\int\int dq dx' dx'' e^{-i(p+q)x'/\hbar}\langle x'|\hat{\rho}|x''\rangle e^{-i(p-q)x''/\hbar}e^{2iqx/\hbar} \\
&= \frac{1}{2\pi^2\hbar^2}\int\int\int dq dx' dx'' \langle x'|\hat{\rho}|x''\rangle \exp\left(\frac{iq}{\hbar}(-x''-x'+2x)+\frac{ip}{\hbar}(x''-x')\right).
\end{aligned}$$

Using the definition of the δ function from Eq. (F.6),

$$= \frac{1}{\pi\hbar}\int\int dx' dx'' \langle x'|\hat{\rho}|x''\rangle \exp\left(\frac{ip}{\hbar}(x''-x')\right)\delta(2x-x'-x'').$$

Integrating across x'' using the δ function,

$$= \frac{1}{\pi\hbar}\int dx' \langle x'|\hat{\rho}|2x-x'\rangle \exp\left(\frac{ip}{\hbar}(2x-x'-x')\right).$$

Performing a change of variables $x' = x+\epsilon \rightarrow dx' = d\epsilon$,

$$= \frac{1}{\pi\hbar}\int d\epsilon \langle x+\epsilon|\hat{\rho}|x-\epsilon\rangle \exp\left(\frac{-2ip\epsilon}{\hbar}\right).$$

F.3 Why Do All That?

The Wigner function is useful because when integrated across x or p, it gives the position density or momentum density, respectively. In other words,

$$\int dp f(x,p) = \langle x|\hat{\rho}|x\rangle = n(x). \tag{F.9}$$

$$\int dx f(x,p) = \langle p|\hat{\rho}|p\rangle = \eta(p). \tag{F.10}$$

We now show Eq. (F.9). Using the definition of the Wigner function from Eq. (F.8),

$$\int dp f(x,p) = \frac{1}{\pi\hbar}\int\int dp d\epsilon \langle x+\epsilon|\hat{\rho}|x-\epsilon\rangle e^{-2ip\epsilon/\hbar}. \tag{F.11}$$

Using the definition of the δ function from Eq. (F.6), with the change of variables that $x = -\epsilon$ and $p' = \hbar p/2$, then $dp' = (\hbar/2)dp$. $\delta(\epsilon) = \frac{1}{\pi\hbar}\int dp'\, e^{-2ip'\epsilon/\hbar}$. So,

$$\int dp f(x,p) = \int d\epsilon \langle x+\epsilon|\hat{\rho}|x-\epsilon\rangle \delta(-\epsilon). \tag{F.12}$$

Evaluating the δ function integral picks out the value at $-\epsilon = 0$,

$$= \langle x|\hat{\rho}|x\rangle = n(x). \tag{F.13}$$

F.4 Time Evolution

Thus, to model the density as a function of time, we only need the time evolution of the Wigner function. Using Eq. (F.3),

$$i\hbar\frac{\partial}{\partial t}\hat{\rho} = [\hat{H},\hat{\rho}]$$

$$\langle p+q|i\hbar\frac{\partial}{\partial t}\hat{\rho}|p-q\rangle = \langle p+q|[\hat{H},\hat{\rho}]|p-q\rangle. \tag{F.14}$$

Multiply both sides by $\frac{1}{\pi\hbar}e^{2iqx/\hbar}$ and integrate both sides in q,

$$\begin{aligned}
\frac{1}{\pi\hbar}\int dq\langle p+q|i\hbar\frac{\partial}{\partial t}\hat{\rho}|p-q\rangle e^{2iqx/\hbar} &= \frac{1}{\pi\hbar}\int dq\langle p+q|[\hat{H},\hat{\rho}]|p-q\rangle e^{2iqx/\hbar} \\
\frac{i}{\pi}\int dq\langle p+q|\frac{\partial}{\partial t}\hat{\rho}|p-q\rangle e^{2iqx/\hbar} &= \frac{1}{\pi\hbar}\int dq\langle p+q|[\hat{H},\hat{\rho}]|p-q\rangle e^{2iqx/\hbar} \\
i\hbar\frac{\partial}{\partial t}f &= \frac{1}{\pi\hbar}\int dq\langle p+q|[\hat{H},\hat{\rho}]|p-q\rangle e^{2iqx/\hbar}, \qquad \text{(F.15)}
\end{aligned}$$

because $\frac{\partial}{\partial t}f = \frac{1}{\pi\hbar}\int dq\langle p+q|\frac{\partial}{\partial t}\hat{\rho}|p-q\rangle e^{2iqx/\hbar}$.

F.5 Use the Wigner Function To Do Something Real

Now we can model the density distribution as a function of time under the influence of some Hamiltonian

$$\hat{H} = \frac{\hat{p}^2}{2m} + \hat{V}.$$

The time evolution of the Wigner function depends on $[\hat{H},\hat{\rho}] = [\hat{T}+\hat{V},\rho] = [\hat{T},\hat{\rho}] + [\hat{V},\hat{\rho}]$. Thus, each component of the Hamiltonian can be considered independently.

F.5.1 Free Particle

A free particle (i.e. $\hat{V} = 0$) can be solved using Eq. (F.15),

$$i\hbar\frac{\partial}{\partial t}f = \frac{1}{2m\pi\hbar}\int dq e^{2iqx/\hbar}\left[\langle p+q|\hat{p}^2\hat{\rho}|p-q\rangle - \langle p+q|\hat{\rho}\hat{p}^2|p-q\rangle\right]$$

$$= \frac{1}{2m\pi\hbar}\int dq e^{2iqx/\hbar}\left[(p+q)^2 - (p-q^2)\right]\langle p+q|\hat{\rho}|p-q\rangle$$

$$= \frac{4p}{2m\pi\hbar}\int dq e^{2iqx/\hbar} q\langle p+q|\hat{\rho}|p-q\rangle$$

$$= \frac{\hbar}{i}\frac{p}{m}\frac{\partial}{\partial x}f$$

$$\frac{\partial}{\partial t}f = -\frac{p}{m}\frac{\partial}{\partial x}f \qquad \text{(F.16)}$$

F.5.2 Harmonic Trap

What if a harmonic potential contributes $\hat{V} = \beta\hat{X}^2/2$ to our Hamiltonian?

$$\begin{aligned}
i\hbar\frac{\partial}{\partial t}f &= \frac{\beta}{2\pi\hbar}\int d\epsilon\langle x+\epsilon|[\hat{X}^2\rho]|x-\epsilon\rangle - \langle x+\epsilon|[\rho\hat{X}^2]|x-\epsilon\rangle e^{-2ip\epsilon/\hbar} \\
&= \frac{\beta}{2\pi\hbar}\int d\epsilon[(x+\epsilon)^2-(x-\epsilon)^2]\langle x+\epsilon|\rho|x-\epsilon\rangle e^{-2ip\epsilon/\hbar} \\
&= \frac{4x\beta}{2\pi\hbar}\int d\epsilon\ \epsilon\langle x+\epsilon|\rho|x-\epsilon\rangle e^{-2ip\epsilon/\hbar} \\
&= -\frac{\hbar}{i}\beta x\frac{\partial}{\partial p}f \\
\rightarrow \frac{\partial}{\partial t}f &= \beta x\frac{\partial}{\partial p}f
\end{aligned} \tag{F.17}$$

F.5.3 Light Pulse

What about a potential $\hat{V} = \hbar\Omega\cos(x) = \frac{\hbar\Omega}{2}(e^{ix}+e^{-ix})$? Here, we operate on $|x\rangle$ eigenstates using the version of the Wigner function from Eq. (F.8).

$$\begin{aligned}
i\hbar\frac{\partial}{\partial t}f &= \frac{\Omega}{2\pi}\int d\epsilon e^{-2ip\epsilon/\hbar}\left(\langle x+\epsilon|e^{i\hat{x}}\hat{\rho}|x-\epsilon\rangle - \langle x+\epsilon|\hat{\rho}e^{i\hat{x}}|x-\epsilon\rangle + \langle x+\epsilon|e^{-i\hat{x}}\hat{\rho}|x-\epsilon\rangle - \langle x+\epsilon|\hat{\rho}e^{-i\hat{x}}|x-\epsilon\rangle\right) \\
i\hbar\frac{\partial}{\partial t}f &= \frac{\Omega}{2\pi}\int d\epsilon e^{-2ip\epsilon/\hbar}\left[e^{i(x+\epsilon)} - e^{i(x-\epsilon)} + e^{-i(x+\epsilon)} - e^{-i(x-\epsilon)}\right]\langle x+\epsilon|\hat{\rho}|x-\epsilon\rangle \\
i\hbar\frac{\partial}{\partial t}f &= \frac{\Omega}{2\pi}\int d\epsilon\left[e^{ix}e^{i\epsilon(-\frac{2p}{\hbar}+1)} - e^{ix}e^{i\epsilon(-\frac{2p}{\hbar}-1)} + e^{-ix}e^{i\epsilon(-\frac{2p}{\hbar}-1)} - e^{-ix}e^{i\epsilon(-\frac{2p}{\hbar}+1)}\right]\langle x+\epsilon|\hat{\rho}|x-\epsilon\rangle \\
i\hbar\frac{\partial}{\partial t}f &= \frac{\Omega}{2\pi}\int d\epsilon\left[(e^{ix}-e^{-ix})\left(e^{i\epsilon(-\frac{2p}{\hbar}+1)} - e^{i\epsilon(-\frac{2p}{\hbar}-1)}\right)\right]\langle x+\epsilon|\hat{\rho}|x-\epsilon\rangle \\
\frac{\partial}{\partial t}f &= \frac{\Omega}{\pi\hbar}\sin(x)\int d\epsilon\left(e^{i\epsilon(-\frac{2p}{\hbar}+1)} - e^{i\epsilon(-\frac{2p}{\hbar}-1)}\right)\langle x+\epsilon|\hat{\rho}|x-\epsilon\rangle \\
\frac{\partial}{\partial t}f &= \frac{\Omega}{\pi\hbar}\sin(x)\int d\epsilon\left(e^{-2i\epsilon(p-\hbar/2)/\hbar} - e^{-2i\epsilon(p+\hbar/2)/\hbar}\right)\langle x+\epsilon|\hat{\rho}|x-\epsilon\rangle \\
\frac{\partial}{\partial t}f &= \Omega\sin(x)\Big[f(x,p-\hbar/2) - f(x,p+\hbar/2)\Big]
\end{aligned} \tag{F.18}$$

Appendix G: Wigner Function Analysis of the Talbot-Lau Interferometer with a Small Harmonic Potential

G.1 Equations of Motion

As shown in Appendix F, the interferometer is described by the density operator $\hat{\rho}$ that is governed by the equation of motion

$$i\frac{\partial}{\partial t}\rho = [\hat{H}, \hat{\rho}], \tag{G.1}$$

where we have moved to a unitless expression. Accordingly, in our model of the interferometer, the unitless Hamiltonian is

$$H = \frac{P^2}{2} + \frac{1}{2}\beta X^2 + \Omega \cos X. \tag{G.2}$$

G.1.1 Solving the Full Equation of Motion

Using the results of Appendix F, the three contributions to the Hamiltonian are combined to find the full equation of motion for the interferometer

$$\left(\frac{\partial}{\partial t} + p\frac{\partial}{\partial x} - \beta\frac{\partial}{\partial p}\right) f(x, p, t) = \Omega \sin x \left[f\left(x, p - \frac{1}{2}\right) - f\left(x, p + \frac{1}{2}\right)\right]. \tag{G.3}$$

At $t = 0$, a laser pulse is applied. The laser pulses used in this type of interferometer are in the Kapitza-Dirac regime, which occurs in the Raman-Nath limit. In this limit, the coordinate and momentum derivatives in Eq. (6.6) may be neglected. If f_0 is the Wigner function just before the laser pulse, it can be shown that just after the laser pulse the Wigner function is

$$f_1 = \sum_{nk=-\infty}^{\infty} (-i)^n J_k(\Xi) J_{n+k}(\Xi) e^{i(n+2k)x} f_0\left(x, p - \frac{n}{2}\right), \tag{G.4}$$

for the pulse power $\Xi = \int d\tau \Omega(\tau)$, where the functions J_n are the Bessel functions of the first kind.

After the first laser pulse, the atoms are free to propagate in the harmonic potential. During this time, the right hand side of Eq. (6.6) is zero. The remaining part of this equation can be solved by substution. If f_2 is the Wigner function after open propagation for time t,

$$f_2(x, p, t) = f_1(x\cos\omega t - \frac{p}{\omega}\sin\omega t, \omega x\sin\omega t + p\cos\omega t), \tag{G.5}$$

where $\omega^2 = \beta$. Note that when $\beta < 0$, ω becomes imaginary and the cosine and sine functions are replaced by hyperbolic functions.

If only a small residual potential to lowest order in β is considered, the equations of motion become

$$f_2 = f_1\left[x - pt - \beta\left(\frac{xt^2}{2} - \frac{pt^3}{3}\right), p + \beta\left(xt - \frac{pt^2}{2}\right)\right]. \tag{G.6}$$

These equations are used again for the laser pulse at $t = T$, and for the final propagation until time $t = 2T + \tau$.

G.2 Recasting in Matrix Notation

Matrix notation is useful in order to better track the many terms involved in the evolution of equations (G.4) and (G.6). We define

$$\mathbf{x} = \begin{pmatrix} x \\ p \end{pmatrix}$$

and

$$\dot{\mathbf{x}} = \begin{pmatrix} \dot{x} \\ \dot{p} \end{pmatrix} = M\mathbf{x} = \begin{pmatrix} 0 & 1 \\ -\beta & 0 \end{pmatrix}\mathbf{x} = \begin{pmatrix} p \\ -\beta x \end{pmatrix}.$$

Note that with this definition

$$\mathbf{x}(t) = \exp(Mt)\mathbf{x}_0 = U(t)\mathbf{x}_0, \tag{G.7}$$

and that $U(t + \tau) = U(t)U(\tau)$. Using this notation, the effect of the first laser pulse at $t = 0$ (given by Eq. G.4) is

$$f_1 = \sum_{nk} \alpha_{nk} e^{\mathbf{g}_{nk}\cdot\mathbf{x}} f_0(\mathbf{x} - \mathbf{N}_n), \tag{G.8}$$

where

$$\mathbf{g} = \begin{pmatrix} i(n+2k) & 0 \end{pmatrix} \text{ and } \mathbf{N}_n = \begin{pmatrix} 0 \\ n/2 \end{pmatrix}. \tag{G.9}$$

The effect of a propagation until time $t = T$ is given by

$$\begin{aligned} f_2 &= f_1(U(-T)\mathbf{x}) = f_1(U_{-T}\mathbf{x}) \\ &= \sum_{nk} \alpha_{nk} e^{\mathbf{g}_{nk}\cdot U_{-T}\mathbf{x}} f_0(U_{-T}\mathbf{x} - \mathbf{N}_n). \end{aligned} \tag{G.10}$$

The effect of the second laser pulse at $t = T$ is given by

$$\begin{aligned} f_3 &= \sum_{ml} \alpha_{ml} e^{\mathbf{g}_{ml}\cdot\mathbf{x}} f_2(\mathbf{x} - \mathbf{N}_m) \\ &= \sum_{ml} \alpha_{ml} e^{\mathbf{g}_{ml}\cdot\mathbf{x}} \sum_{nk} \alpha_{nk} e^{\mathbf{g}_{nk}\cdot U_{-T}(\mathbf{x}-\mathbf{N}_m)} f_0(U_{-T}(\mathbf{x} - \mathbf{N}_m) - \mathbf{N}_n) \\ &= \sum_{mlnk} \alpha_{ml}\alpha_{nk} \exp\left(\mathbf{g}_{ml}\cdot\mathbf{x} + \mathbf{g}_{nk}\cdot U_{-T}\mathbf{x} - \mathbf{g}_{nk}\cdot U_{-T}\mathbf{N}_m\right) f_0(U_{-T}\mathbf{x} - U_{-T}\mathbf{N}_m - \mathbf{N}_n). \end{aligned} \tag{G.11}$$

The final propagation until time $t = 2T + \tau$ is given by

$$\begin{aligned} f_4 &= f_3(U_{-(T+\tau)}\mathbf{x}) \\ &= \sum_{mlnk} \alpha_{ml}\alpha_{nk} \exp\left(\mathbf{g}_{ml}\cdot U_{-(T+\tau)}\mathbf{x} + \mathbf{g}_{nk}\cdot U_{-T}U_{-(T+\tau)}\mathbf{x} - \mathbf{g}_{nk}\cdot U_{-T}\mathbf{N}_m\right) f_0(U_{-T}U_{-(T+\tau)}\mathbf{x} - U_{-T}\mathbf{N}_m - \mathbf{N}_n). \end{aligned} \tag{G.12}$$

G.3 The Interferometer Signal

The interferometer signal is given by

$$S = \int d^2x e^{ix} f_4(\mathbf{x}). \tag{G.13}$$

At this point, it is useful to define,

$$\mathbf{y} = U_{-(2T+\tau)}\mathbf{x} - U_{-T}\mathbf{N}_m - \mathbf{N}_n$$

and

$$\mathbf{i} = \begin{pmatrix} , i & 0 \end{pmatrix}$$

which allows the signal to be written as

$$\begin{aligned} S =& \sum_{mlnk} \alpha_{ml}\alpha_{nk} \exp\left[\mathbf{i}U_{2T+\tau}\mathbf{N}_n + \mathbf{i}U_{T+\tau}N_m + \mathbf{g}_{ml}\cdot\mathbf{N}_m + \mathbf{g}_{ml}\cdot U_T\mathbf{N}_n + \mathbf{g}_{nk}\cdot\mathbf{N}_n\right] \\ & \times \int d^2\mathbf{y} \exp\Big[(\mathbf{i}U_{2T+\tau} + \mathbf{g}_{ml}U_T + \mathbf{g}_{nk})\mathbf{y}\Big] f_0(\mathbf{y}). \end{aligned} \tag{G.14}$$

If $\tau << T$, we approximate

$$\begin{aligned} U(\tau) &\approx \mathbf{1} + M\tau, \\ U_{2T+\tau} &\approx U_{2T} + U_{2T}M\tau, \\ U_{T+\tau} &\approx U_T + U_T M\tau. \end{aligned} \tag{G.15}$$

Under these approximations, note that $U(T+\tau) \neq U(T)U(\tau)$ as before. The approximated signal is now

$$\begin{aligned} S =& \sum_{mlnk} \alpha_{ml}\alpha_{nk} \exp\left[\mathbf{i}U_{2T}\mathbf{N}_n + \mathbf{i}U_{2T}M\tau\mathbf{N}_n + \mathbf{i}U_T N_m + \mathbf{i}U_T M\tau N_m + \mathbf{g}_{ml}\cdot\mathbf{N}_m + \mathbf{g}_{ml}\cdot U_T\mathbf{N}_n + \mathbf{g}_{nk}\cdot\mathbf{N}_n\right] \\ & \times \int d^2\mathbf{y} \exp\Big[(\mathbf{i}U_{2T} + \mathbf{i}U_{2T}M\tau + \mathbf{g}_{ml}U_T + \mathbf{g}_{nk})\mathbf{y}\Big] f_0(\mathbf{y}). \end{aligned} \tag{G.16}$$

Assume that β is small. By expanding $U(t)$ in a Taylor series and keeping all the lowest orders of β, we express

$$U_t \approx U_t^{(0)} - \beta U_t^{(1)}, \tag{G.17}$$

where

$$U_t^{(0)} = \begin{pmatrix} 1 & t \\ 0 & 1 \end{pmatrix} \text{ and } U_t^{(1)} = \begin{pmatrix} t^2/2 & t^3/6 \\ t & t^2/2 \end{pmatrix},$$

and

$$M = \begin{pmatrix} 0 & 1 \\ -\beta & 0 \end{pmatrix} = M^{(0)} - \beta M^{(1)},$$

where

$$M^{(0)} = \begin{pmatrix} 0 & 1 \\ 0 & 0 \end{pmatrix} \text{ and } M^{(1)} = \begin{pmatrix} 0 & 0 \\ 1 & 0 \end{pmatrix}.$$

Applying this approximation and eliminating terms that go as $\beta\tau$ and β^2, the signal becomes

$$\begin{aligned} S = & \sum_{mlnk} \alpha_{ml}\alpha_{nk} \exp\Big[(\mathbf{i}U_{2T}^0\mathbf{N}_n + \mathbf{i}U_T^0\mathbf{N}_m + \mathbf{g}_{ml}\mathbf{N}_m + \mathbf{g}_{ml}U_T^0\mathbf{N}_n + \mathbf{g}_{nk}\mathbf{N}_n) \\ & - \beta(\mathbf{i}U_{2T}^1\mathbf{N}_n + \mathbf{i}U_T^1\mathbf{N}_m + \mathbf{g}_{ml}U_T^1\mathbf{N}_n) + \tau(\mathbf{i}U_{2T}^0M^0\mathbf{N}_n + \mathbf{i}U_T^0M^0\mathbf{N}_m)\Big] \\ & \times \int d^2\mathbf{y} \exp\Big[(\mathbf{i}U_{2T}^0 + \mathbf{g}_{ml}U_T^0 + \mathbf{g}_{nk})\mathbf{y} - \beta(\mathbf{i}U_{2T}^1 + \mathbf{g}_{ml}U_T^1)\mathbf{y} + \tau(\mathbf{i}U_{2T}^0M^0)\mathbf{y}\Big] f_0(\mathbf{y}). \end{aligned} \quad \text{(G.18)}$$

The exponential in the integral has three terms, proportional to $1, \beta$, and τ. The term proportional to 1 will oscillate quickly and only contribute when

$$\mathbf{i}U_{2T}^0 + \mathbf{g}_{ml}U_T^0 + \mathbf{g}_{nk} = 0, \quad \text{(G.19)}$$

which forces $l = -m/2 - 1$ and $k = (1 - n)/2$. Under this condition,

$$\begin{aligned} S = & \sum_{mn} \alpha_{m,-m/2-1}\alpha_{n,(1-n)/2} \\ & \times \exp\Big[(\mathbf{i}U_T^0\mathbf{N}_m + \mathbf{g}_{ml}\mathbf{N}_m) - \beta(\mathbf{i}U_{2T}^1\mathbf{N}_n + \mathbf{i}U_T^1\mathbf{N}_m + \mathbf{g}_{ml}U_T^1\mathbf{N}_n) + \tau(\mathbf{i}U_{2T}^0M^0\mathbf{N}_n + \mathbf{i}U_T^0M^0\mathbf{N}_m)\Big] \\ & \times \int d^2\mathbf{y} \exp\Big[-\beta(\mathbf{i}U_{2T}^1 + \mathbf{g}_{ml}U_T^1)\mathbf{y} + \tau(\mathbf{i}U_{2T}^0M^0)\mathbf{y}\Big] f_0(\mathbf{y}). \end{aligned} \quad \text{(G.20)}$$

Evaluating the expression back from matrix form gives

$$S = A \int du dv \exp\left[-i\beta\left(T^2 u + T^3 v\right) + i\tau v\right] f_0(u, v), \tag{G.21}$$

where

$$(u, v) = \left(x - (2T + \tau)p + \frac{mT}{2}, p - \frac{m+n}{2}\right),$$
$$A = \sum_{nm=-\infty}^{\infty} \alpha_{m,-m/2-1}\alpha_{n,(1-n)/2} \exp\left[i\left(\frac{mT}{2} - \beta[6n + m]\frac{T^3}{12} + \frac{m+n}{2}\tau\right)\right],$$

and

$$\alpha_{ab} = (-i)^n J_b(\Xi) J_{a+b}(\Xi), \tag{G.22}$$

for whole integer indices a, b.

REPORT DOCUMENTATION PAGE

Form Approved
OMB No. 0704–0188

1. REPORT DATE *(DD–MM–YYYY)*	2. REPORT TYPE	3. DATES COVERED *(From — To)*
15–06–2017	Doctoral Dissertation	Jun 2013–Jun 2017

4. TITLE AND SUBTITLE

Development Of Compact, Deployable Sensors
Using Cold Atom Interference

5a. CONTRACT NUMBER

5b. GRANT NUMBER

5c. PROGRAM ELEMENT NUMBER

6. AUTHOR(S)

Imhof, Eric A.,

5d. PROJECT NUMBER

5e. TASK NUMBER

5f. WORK UNIT NUMBER

7. PERFORMING ORGANIZATION NAME(S) AND ADDRESS(ES)

Air Force Institute of Technology
Graduate School of Engineering and Management (AFIT/EN)
2950 Hobson Way
WPAFB, OH 45433-7765

8. PERFORMING ORGANIZATION REPORT NUMBER

AFIT-ENP-DS-17-J-073

9. SPONSORING / MONITORING AGENCY NAME(S) AND ADDRESS(ES)

Cold Atom Group
Air Force Research Laboratory
Bldg. 570, Kirtland AFB, NM

10. SPONSOR/MONITOR'S ACRONYM(S)

AFRL/RVBYE

11. SPONSOR/MONITOR'S REPORT NUMBER(S)

12. DISTRIBUTION / AVAILABILITY STATEMENT

DISTRIBUTION STATEMENT A: APPROVED FOR PUBLIC RELEASE; DISTRIBUTION UNLIMITED

13. SUPPLEMENTARY NOTES

14. ABSTRACT

This dissertation makes three distinct contributions to the field of compact cold atom interferometry.
First, a two-dimensional grating magneto-optical trap (2D GMOT) is demonstrated, in which a single laser and a planar diffraction grating produce a slow, high flux beam of ^{87}Rb atoms. This configuration increases experimental access when compared with a traditional 2D MOT. The output flux is several hundred million rubidium atoms/s at a mean velocity of 19.0(2) m/s. The velocity distribution has a 3.3(17) m/s standard deviation. The atomic beam from the 2D GMOT is used to demonstrate loading of a three-dimensional grating MOT (3D GMOT) with $2.02(3) \times 10^8$ atoms. Methods to improve flux output are discussed.
Second, a method to produce uniform magnetic fields of arbitrary direction from a single planar microchip is developed. Chip-based fields reduce the dependence of cold atom devices on large current-carrying coils external to the vacuum chamber. A chip is fabricated that demonstrates equivalent magnetic field uniformity to the widely-used Helmholtz coil pair. These results are used to propose a novel magnetic trap conveyor to move atoms along the surface of the chip without the use of an externally-supplied field.
Third, using a thermal gas, the signal of a trapped atom interferometer is modeled. This interferometer uses two short laser pulses, separated by time T, which act as phase gratings for the matter waves. Near time $2T$, there is an echo in the cloud's density due to the Talbot-Lau effect. The model uses the Wigner function approach and includes a weak residual harmonic trap. The analysis shows that the residual potential limits the interferometer's visibility, shifts the echo time, and alters its time dependence. Loss of visibility can be mitigated by optimizing the initial trap frequency just before the interferometer cycle begins.

15. SUBJECT TERMS

Atomic Sources, Cold Atoms, Magneto-Optical Trap, Bose-Einstein Condensate

16. SECURITY CLASSIFICATION OF:			17. LIMITATION OF ABSTRACT	18. NUMBER OF PAGES	19a. NAME OF RESPONSIBLE PERSON
a. REPORT	b. ABSTRACT	c. THIS PAGE			Dr. Glen P. Perram (ENP)
U	U	U	UU	204	19b. TELEPHONE NUMBER *(include area code)* (937) 255-3636 x4504, glen.perram@afit.edu